
Engineering site-isolated reactive metal complexes within a Metal-organic Framework

A thesis presented to

The School of Physical Sciences

at

The University of Adelaide

in fulfilment of the requirements for

The Degree of

Doctor of Philosophy in Chemical Science

by

Ricardo Peralta



THE UNIVERSITY
of ADELAIDE

Adelaide, Australia

March 2021

Declaration

I certify that this work contains no material which has been accepted for the award of any other degree or diploma in my name, in any university or other tertiary institution and, to the best of my knowledge and belief, contains no material previously published or written by another person, except where due reference has been made in the text. In addition, I certify that no part of this work will, in the future, be used in a submission in my name, for any other degree or diploma in any university or other tertiary institution without the prior approval of the University of Adelaide and where applicable, any partner institution responsible for the joint-award of this degree.

I acknowledge that copyright of published works contained within this thesis resides with the copyright holder(s) of those works.

I also give permission for the digital version of my thesis to be made available on the web, via the University's digital research repository, the Library Search and also through web search engines, unless permission has been granted by the University to restrict access for a period of time.

Ricardo Peralta

Publications

- 1) **Ricardo A. Peralta**, Michael T. Huxley, Rosemary Young, Oliver M. Linder-Patton, Jack D. Evans, Christian J. Doonan and Christopher J. Sumbly, *Faraday Discussions*, 2020, 0–9, MOF Matrix Isolation: Cooperative Conformational Mobility Enables Reliable Single Crystal Transformations.

- 2) **Ricardo A. Peralta**, Michael T. Huxley, Jack D. Evans, Thomas Fallon, Haijie Cao, Maoxia He, Xiu Song Zhao, Stefano Agnoli, Christopher J. Sumbly and Christian J. Doonan, *Journal of the American Chemical Society*, 2020, Highly Active Gas Phase Organometallic Catalysis Supported Within Metal-organic Framework Pores.

- 3) **Ricardo A. Peralta**, Michael Huxley, Zhaolin Shi, Yue-Biao Zhang, Christopher J. Sumbly and Christian J. Doonan, *Chem. Commun.*, 2020, A Metal-organic Framework Supported Iridium Catalyst for the Gas Phase Hydrogenation of Ethylene.

- 4) **Ricardo A. Peralta**, Michael Huxley, Jorge Albalad, Christopher J. Sumbly and Christian J. Doonan, Single-crystal to Single-crystal transformations of MOF-supported, site-isolated trigonal planar Cu(I) complexes with labile ligands. Submitted for Publication in *Inorganic Chemistry*

Acknowledgements

I would like to thank both of my supervisors for all their help and advice during my PhD. Firstly, I would like to thank Prof. Christian Doonan for believing in me and give me the opportunity to know this wonderful part of the world. It has been a privilege to work under his supervision, his encouragement and constant motivation has pushed me to grow as a person. Also, to Prof. Christopher Sumbly who has been a guide and always easy-going to speak during the three years of my PhD. I will always be grateful for all the time he spent discussing and interpreting the research outcomes. This thesis would not be possible without the help of Dr. Michael Huxley, he was there during all the dark times of my PhD, always willing to help with the best attitude. I will never forget his kindness and as I promised to him, I will build a statue of him in Mexico. To Dr Ilich Ibarra, I will be forever thankful for being one of the first person who believed in me, for encouraging me in all my pursuits and inspiring me to follow my dreams.

I would like to express my gratitude to each member of the Sumbly-Doonan group, past and present; every interaction has been invaluable. I would like to particularly acknowledge the guidance I have received from Dr Alexandre Burgun, Dr Natasha Zaitseva, Dr Kenji Sumida, Dr Jorge Albalad, Steven Tsoukatos, Rosemary Young, Pol Gimeno, Kate Flint, Dr Oliver Linder-Patton, Dr Andrew Tarzia, Em. Prof. Richard Keene and Dr Witold Bloch. Thanks also to Peter Apoeffis, Philip Clements and Matthew Bull for all the technical support and assistance in plenty of the experiments, without their knowledge some of the projects would never have come to fruition. Additionally, I would like to thank the staff at Adelaide Microscopy, especially Ken Neubauer for all his technical support.

All the crystallography work conducted in this thesis was performed at the Australian Synchrotron using the MX1 and MX2 beamlines. The synchrotron radiation was essential to elucidate the coordination environment of the allocated reactive metal complexes studied in this thesis and thereby, access to the facilities been pivotal to the success of this thesis. I expressed my sincere gratitude to the MX beamline team, particularly Dr Alan Riboldi-Tunncliffe, Dr Rachel Williamson and Dr Jason Price for all their technical support and to accommodate new experiments in the beamlines.

This entire journey would not have been possible without the support of my friends. To my housemate and friend Dipti, you made me feel like home every day. Min, Hedda, Po-Wei, Kwonil, Charles, Reshma and Diana thank for your friendship and encouragement, you made my stay in Australia more enjoyable. To my friends in Mexico, for being a pillar of support and inspiration. Carlos, I am sorry that I miss the birth of Sofi. Cynthia, I will always be indebted to you.

Acknowledgments

Last but not least, thank you to my family for their endless support and patience. To my parents, Antonia and Ricardo, for never losing faith in me, I hope I've made you proud. Pola and Voltar, I wish you can forgive me for leaving you to come to Australia. To Chaparro, thank you for all the happiness that you provided, we will always miss you, see you soon my friend.

Table of Contents

Chapter 1: Introduction	1
Importance of bulky ligands in homogenous catalysis	2
Importance of heterogenous catalysts as useful materials.....	3
Heterogenization by crystallisation	5
Advantages of crystallinity in molecular crystal based catalysts.....	8
Metal-organic Frameworks (MOFs)	12
Heterogenous catalysis in MOFs.....	13
Metal-Organic Frameworks: X-ray crystallographic insights into catalysis	22
Contextual Statement	27
References.....	29
Chapter 2. MOF Matrix Isolation: Cooperative Conformational Mobility Enables Reliable Single Crystal Transformations	38
2.1 Abstract	43
2.2 Introduction.....	43
2.3 Results and discussion.....	45
2.4 Conclusions.....	54
2.5 Experimental	55
2.6 Associate content	59
2.7 Acknowledgements	59
2.8 References.....	59
Chapter 3. Highly Active Gas Phase Organometallic Catalysis Supported Within Metal-organic Framework Pores	63
3.1 Abstract	68
3.2 Introduction.....	68
3.3 Results and discussion.....	70
3.4 Conclusion	80
3.5 Experimental.....	81
3.6 Molecular simulations	86
3.7 Associated content.....	87
3.8 Acknowledgment.....	87
3.9 References.....	88

Chapter 4. A Metal-organic Framework Supported Iridium Catalyst for the Gas Phase Hydrogenation of Ethylene	97
4.1 Abstract.....	101
4.2 Introduction.....	101
4.3 Results and discussion.....	102
4.4 Conclusions.....	107
4.5 Associated content.....	108
4.6 Acknowledgment.....	108
4.7 References.....	108
Chapter 5: Single-crystal to Single-crystal transformations of MOF-supported, site-isolated trigonal planar Cu(I) complexes with labile ligands	111
5.1 Abstract.....	114
5.2 Introduction.....	114
5.3 Results and Discussion.....	116
5.4 Conclusions.....	124
5.5 Experimental.....	125
5.6 Associated content.....	128
5.7 Acknowledgements.....	128
5.8 References.....	129
Chapter 6: Conclusion and Future outlook	138
Chapter 7: Appendices	143
7.1. Supplementary information for Chapter 2.....	143
7.2. Supplementary information for Chapter 3.....	162
7.3. Supplementary information for Chapter 4.....	203
7.4. Supplementary information for Chapter 5.....	221

Thesis abstract

Metal-organic frameworks (MOFs) are a comparatively new, fascinating class of porous materials. They are organic-inorganic hybrid compounds consisting of organic ligands acting as linkers/spacers and metal ions or clusters as nodes/vertices. Combinations of these building blocks allow formation of three-dimensional periodic lattices with different pore shapes and sizes. In the development of MOF chemistry, different methodologies have emerged to imbue MOFs with catalytically active metal centers. One of the most attractive approaches is immobilizing well-defined homogeneous catalysts via postsynthetic modification (PSM). The well-defined architecture of MOFs in combination with the isolation that the framework provides to the guest metal complex allows the elucidation of the coordination environment by X-ray crystallography. This excellent combination of properties provides the opportunity to structurally characterize organometallic species isolated within MOF architectures and explore the potential of these unique systems for application in commercially attractive processes.

The Mn-based MOF ($[\text{Mn}_3\text{L}_2\text{L}']$) where $\text{L} = (\text{bis}(4\text{-(4-carboxyphenyl)-1H-3,5-dimethylpyrazolyl})\text{methane})$ (MnMOF-1) has proven to be an exceptional platform for showcasing these properties. This high crystalline MOF has demonstrated a degree of flexibility and possesses free chelating sites capable of binding reactive metal complexes. In Chapter 2, the underlying conformational flexibility of the framework was demonstrated to be solvent dependent and to influence the outcome of postsynthetic metalation.

Most of the investigations in heterogeneous catalysis using MOFs have focused on reactions for the synthesis of fine chemicals. Generally, this chemistry is carried out in solution and therefore does not take full advantage of the MOF's intrinsic characteristics such as high surface area, crystallinity, and permanent porosity. Thus, the judicious choice of chemistry and reaction conditions can showcase the unique properties of MOFs. In Chapter 3 and 4, gas-phase reactions with cationic rhodium(I) and iridium(I) bis-ethylene complexes immobilized within MnMOF-1 are reported. The mononuclear Rh(I) species were demonstrated to be highly active towards 1-butene isomerization, while both the Rh(I) and Ir(I) complexes

Thesis abstract

successfully catalyze gas-phase ethylene hydrogenation. The gas phase reactions carried out in these Chapters are an important step towards fully exploiting the capacity of MOFs to act as supports for highly reactive metal centers. Finally in Chapter 5, the concept of isolating reactive metal complexes within MOFs was expanded to include the metalation of MnMOF-1 with a Cu(I) chloride complex. A new methodology was developed to convert the Cu(I) chloride moiety into a series of labile Cu(I) complexes which are otherwise difficult to characterize and which are of interest in copper-centered catalysis. In accordance with the porous nature of the host framework, the weakly bound 'place-holder' ligands readily undergo substitution with a broad repertoire of small guest molecules and weakly coordinating anions. Due to the highly crystalline and robust host framework, these sequential processes are mapped via X-ray crystallography, providing exquisite insight into the exchange processes of site-isolated Cu(I) moieties within MnMOF-1, pertinent to Cu-centered catalysis.

Chapter 1: Introduction

Chemical reactions with a half-life as long as centuries can be accomplished in minutes by the use of a catalyst.¹ The general feature of a catalyst is that it provides a reaction pathway in which the rate limiting transition state has a lower energy than that of the non-catalyzed reaction, thus increasing the rate of a reaction.² A catalyst is defined as a substance that increases the rate of a chemical reaction without being consumed in the process and were first developed in the early 19th century due to the need to improve old inefficient processes.³ Catalysts systems can be grouped into two different categories, homogeneous or heterogeneous, based on whether the reactants and the catalyst are in the same or a different phase. Homogeneous catalysts are those which exist in a single phase (typically liquid), while heterogeneous catalysts occur in two or more different phases.⁴ The first large scale catalytic process was the production of ammonia from nitrogen and hydrogen (Haber process) in 1913.⁵

Following this development, intense competition in chemical industry has encouraged development of new catalysts and further investigation to improve the selectivity, activity and stability of existing catalysts for novel and established reaction processes.⁶ These enhancements rely on concurrent developments in organometallic chemistry, such as better understanding of catalytically active species and reaction mechanisms.⁷ For instance, many reactive metal complexes are coordinatively unsaturated species which are considered key intermediates for fundamental chemical transformations involved in catalytic cycles. Despite their importance, characterizing these species is challenging due to their short solution lifetimes and they are frequently limited to study by fast time-resolved infrared spectroscopy methods^{8,9} or nuclear magnetic resonance (NMR),¹⁰ mostly at low temperatures. One common strategy to stabilize reactive species, and to structurally characterize the complexes, is via matrix isolation or by using bulky, protective ligands that limit dimerization and facilitate isolation of the catalyst.^{11,12} An increased understanding of the mechanism of a given catalytic process is essential for developing catalysts with improved performance and stability.

Importance of bulky ligands in homogenous catalysis

Homogeneous catalysts, which are often organometallic complexes of transition metals, have the advantage that they can easily be modified by changing the ligand, facilitating systematic optimization of the catalyst.¹³ Despite these advantages, preventing the degradation of the metal catalyst is still challenging. Isolating metal complexes has proven to be an effective tool to avoid decomposition, characterize transient intermediates and enhance the catalytic activity.^{14–18} Bulky substituents are commonly introduced into these systems to suppress bimolecular decomposition and dimerization of the metal centers via steric hindrance.¹⁹ A common example in industry is the system based on zirconocene (homogeneous Ziegler-Natta catalysts based on complexes of Zr), that is highly active towards the preparation of several ethylene- α -olefin copolymers.²⁰ Besides being good systems to isolate active catalyst, sterically bulky ligands have also been employed to structurally characterize transient intermediates. Recently, Betley and co-workers reported the characterization of a Cu(I) nitrene complex, the key intermediates in organic reactions such as aziridination and C-H functionalization.²¹ The reaction between the Cu(I) complex and organic azides lead to the rapid formation of aziridination and amination products, forbidding the isolation of the putative intermediate (Figure 1.1).²² In order to stop the catalytic cycle, a bulky, sterically demanding ligand was introduced, facilitating the isolation of the reactive metal complex and preventing the secondary reaction, thereby allowing the crystallization of the intermediate complex. Single-crystal X-ray Diffraction (SCXRD) revealed a linear M–N–R structure and in agreement with X-ray Absorption Spectroscopy (XAS) studies, this was formulated to be a Cu-triplet nitrene intermediate. This remarkable work highlights the role bulky ligands in providing the required encumbrance to isolate reactive intermediates.

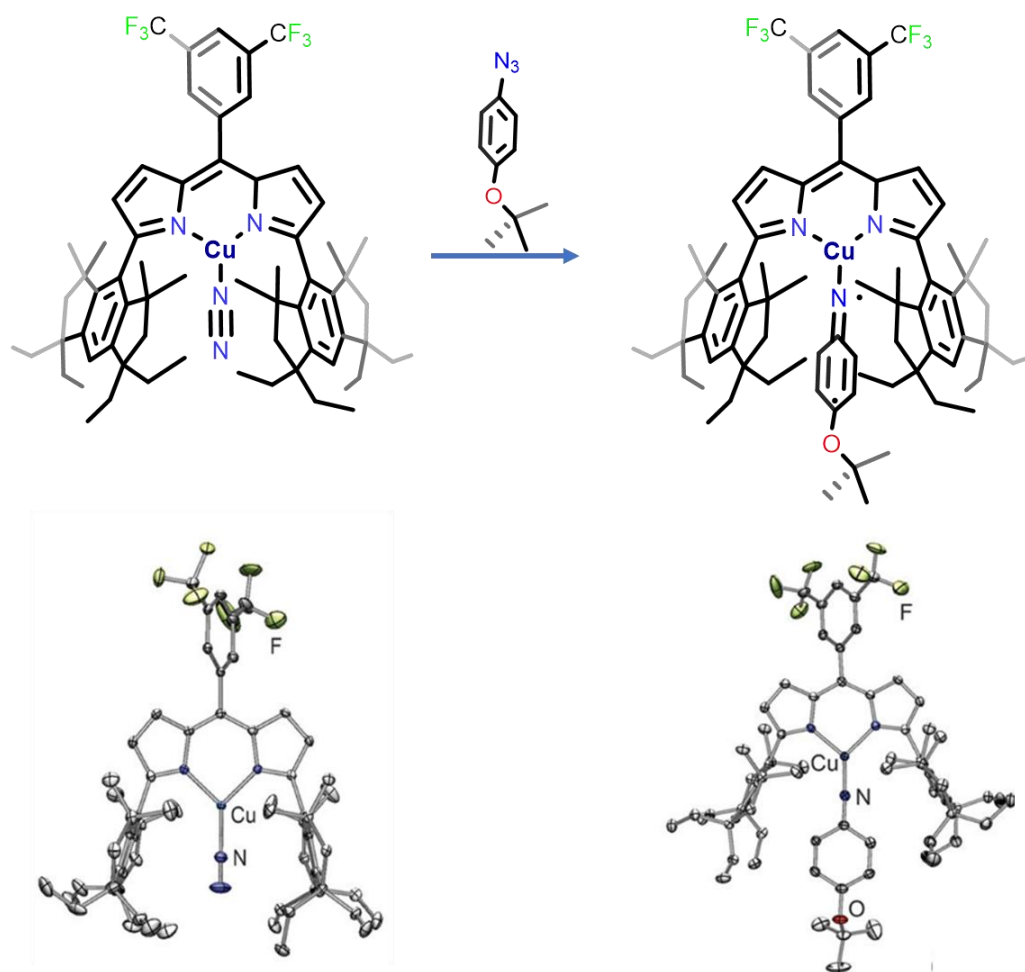


Figure 1.1. Reaction scheme of the Cu(I) nitrogen complex forming copper nitrene with the corresponding crystal structures. Color scheme: Cu (light blue), F (green), N (blue), and O (red). Figure adapted from reference 22.

Importance of heterogenous catalysts as useful materials

As outlined above, steric protection can be an effective way to stabilize and isolate reactive species in homogenous systems; however, this can attenuate the catalytic activity of the metal centre.¹⁹ Furthermore, the synthesis of such catalysts requires multiple-step elaboration, reducing the practicality of employing these types of catalysts in industry. Finally, the often exorbitant costs involved in product separation from the catalyst can make homogenous catalysis processes unattractive.²³ As a consequence, heterogeneous catalysis has been dominant in the industrial sector, particularly in the synthesis of materials²⁴ and manufacture of chemicals.²⁵ Traditionally, solid state materials have been employed as heterogeneous

catalysts for gas-solid (GS) reactions, due to the improved chemical stability, easy separation of products from the catalysts and ability to avoid large volumes of organic solvent that present health and environmental hazards. Typical heterogeneous systems are composed of metal particles supported on metal oxides (MMOs),²⁶ but, single-crystals of transition metals (solid-state catalyst)¹⁵ and porous material (i.e. zeolites and Metal-organic Frameworks MOFs)²⁷ have shown potential for industrial applications.

MMOs became prominent during the mid-1950s after they were found to effectively catalyze an extensive variety of reactions, in particular, acid-base and oxidation reactions. Nowadays, the research and use of these materials has been expanded to applications in the petrochemical and pharmaceutical industry.²⁶ In addition, metal oxide surfaces have been employed to support isolated catalytically active metals by decorating the surface with bulky ligands on dehydroxylated surfaces.^{28,29} The main limitation of these systems is the nonuniform distribution of catalytic sites, providing limited scope to structurally characterize the host metals and explore the catalytic mechanism (i.e., the interaction between the catalyst and the reactants, catalytic intermediates and deactivation process), inhibiting the development of superior and more cost-effective materials. Furthermore, the nature and the chemical surroundings of the catalytically active single sites are key properties which can be modulated to obtain catalytic systems with enhanced chemo-, regio- and stereo-selectivity. Therefore, reactive transition metals complexes have been supported/immobilized on solid matrixes with defined binding sites (Figure 1.2),¹⁵ thereby combining in this way the merits of homogeneous and heterogeneous catalysts.

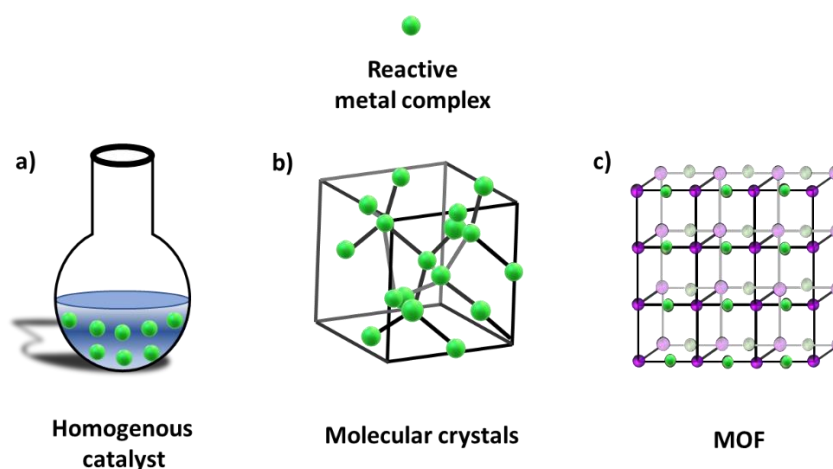


Figure 1.2. Comparison of different environments for reactive metal complexes namely in **a)** solution; **b)** molecular crystals in the solid-state; **c)** isolated in a MOF support.

Heterogenization by crystallization

With respect to recovery and recycle strategies, some authors have immobilized catalysts on soluble polymers, but as mentioned above the main limitation of these systems is the nonuniform distribution of catalytic sites which makes it difficult to structurally characterize the active metal sites and therefore undertake structure-function analysis.³⁰ One approach to solving this conundrum is to heterogenize well-defined homogeneous catalysts by crystallization, which, under appropriate conditions, can form molecular crystals with a degree of porosity towards small gaseous reagents.³¹ Such solid-state molecular catalysts have been explored in recent years but remain a remarkably undeveloped field with tremendous potential.¹⁸ Well-defined transition metal complexes immobilized in the solid-state can partake in the same processes observed for homogenous catalysts, such as ligand substitution, reductive elimination, oxidative addition, and insertion reactions, while providing insights into these processes through techniques such as X-ray crystallography,^{15,32} which are not accessible for their homogenous or 'supported' counterparts.

In the late 1960's, one of the earliest examples of a well-defined organometallic solid-gas phase reactions was reported by Vaska and co-workers. The reaction between $[\text{IrX}(\text{CO})(\text{PPh}_3)_2]$ ($\text{X} = \text{Cl}, \text{Br}$ etc) with gaseous alkyl halides lead to an oxidative addition to produce $[\text{IrX}(\text{H})(\text{Y})(\text{CO})(\text{PPh}_3)_2]$ ($\text{Y} = \text{Cl}, \text{Br}$ etc.).³³ Analogous reactions were reported in the 1980s by Siedle and Newmark.³⁴ Similarly, at high temperatures and high CO pressures, nickel metal converts to $[\text{Ni}(\text{CO})_4]$; and numerous other metal carbonyl complexes have been prepared via solid-state reaction of metal with CO without a solvent.³⁵

The solid-gas reaction between $[\text{Rh}(\text{PPh}_3)_3\text{Cl}]$ and CO results in the formation of $[\text{Rh}(\text{PPh}_3)_3(\text{CO})\text{Cl}]$. The carbonylation reaction was confirmed by IR spectroscopy and, subsequently, the powder was washed with diethyl ether to yield $[\text{Rh}(\text{PPh}_3)_2(\text{CO})\text{Cl}]$ and a free PPh_3 . This led to the conclusion that formation of $[\text{Rh}(\text{PPh}_3)_2(\text{CO})\text{Cl}]$ is via association of CO into the primary coordination sphere of $[\text{Rh}(\text{PPh}_3)_3\text{Cl}]$ followed by dissociation of the PPh_3 ligand. In solution, the reaction gave two isomers; one in which the PPh_3 ligands are trans to each other but staggered and the other in which the PPh_3 ligand are trans but eclipsed. In the solid-state the reaction gave only one product in which all three PPh_3 ligands are staggered

since the dissociative process of the PPh_3 was impossible without the presence of a solvent.³⁶ A similar carbonylation reaction, in the solid state, on $[\text{RuCl}_2(\text{PPh}_3)_3]$ gave $[\text{RuCl}_2(\text{CO})_2(\text{PPh}_3)_2]$.³⁷ In this particular case, the solid-state reaction took place at relatively low temperature and offered the advantage that the crystallinity was retained in the transformation from reactant to product. These are good examples of how, in the solid-state, new complexes including metastable species or selective isomers may be prepared and studied, shedding light on key catalytic processes.^{38,39}

In 1991 Zanobini and co-workers explored the reactions of a cobalt complex with small gaseous molecules. Purple-red crystals of a monomeric tripodal tetraphosphine Co(II) complex, $[(\text{P}(\text{CH}_2\text{CH}_2\text{PPh}_2)_3)\text{Co}(\text{N}_2)]\text{BPh}_4$ were reacted with different gases and vapors such as carbon monoxide, ethylene, acetylene, and vapors of formaldehyde and acetaldehyde (Figure 1.3). The dinitrogen ligand was substituted by CO, C_2H_4 , and C_2H_2 to form the corresponding carbonyl, π -ethylene and vinylidene complexes. Formaldehyde decomposes to H_2 and CO, which is bound as a terminal ligand. In contrast, aldehyde vapor gave a paramagnetic Co(II)-acyl complex $[(\text{P}(\text{CH}_2\text{CH}_2\text{PPh}_2)_3)\text{Co}(\text{C}\{\text{O}\}\text{Me})]\text{BPh}_4$. When the BPh_4^- anion is replaced by BF_4^- , PF_6^- or SO_3CF_3^- anions the solid-gas reaction does not proceed completely in MeCHO and C_2H_2 probably due to the comparatively small channels present in the solid-state structures formed using the smaller anions.⁴⁰ The importance of anion size on the cavities in the solid-state system highlights the subtle effect of the structure elements on the mass transport properties. This example shows that a labile ligand like N_2 can be displaced by small molecules in the solid-state.

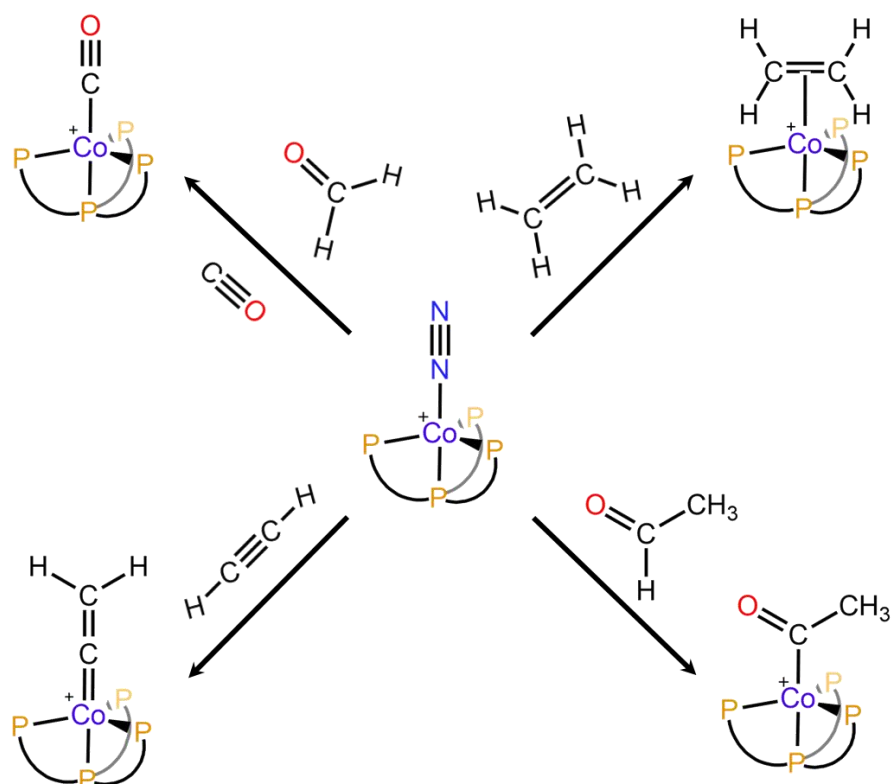


Figure 1.3. Molecular structures of a monomeric Co(II) complex and the substitution of nitrogen for different small molecules. Figure adapted from reference 40.

Addition of alkynes and alkenes to a metal complex may result in olefin oligomerization through C–H and C–C coupling processes, which are important transformations in solution-phase organometallic chemistry.^{41–44} Recently, Goldman *et al.* reported a well-defined phebox iridium complex ($[(\text{Phebox})\text{Ir}(\text{C}_2\text{H}_4)_2]$ [Phebox = 3,5-dimethylphenyl-2,6-bis(oxazolonyl)]) which promotes the selective formation of butadiene from ethylene.⁴⁵ The steric effect and hemilabile nature of the phebox ligand provided stability and allowed the formation of a vacant site, facilitating the selective reaction. Similarly, gas-phase alkene hydrogenation reactions were observed using a solid-state triphos iridium complex ($[\text{Ir}(\text{triphos})(\text{C}_2\text{H}_4)(\text{H})_2][\text{BPh}_4]$ [triphos = $(\text{Ph}_2\text{PCH}_2)_3\text{CCH}_3$]).^{46,47} The material catalyzed the gas-phase dehydrogenation of light alkanes (butane, pentane) and subsequently an isomerization of the alkenes, when ethylene and propane were used as hydrogen acceptors at a relatively high temperature. The results showed that the regioselectivity of the reaction under these conditions was comparable to the homogenous catalyst; however, the dehydrogenation activity was superior. This is a remarkable result considering the typically superior selectivity

of homogeneous systems. The first comprehensive review of reactions in solid-gas phase on well-defined organometallic species was reported in 1998,⁴⁸ while a more recent review on this topic was conducted by Weller and co-workers was published in 2015.¹⁵ These reviews highlighted the limited research conducted on these systems and the enormous challenges needing to be addressed for their industrial application.

Advantages of crystallinity in molecular crystal based catalysts

When single crystals undergo chemical transformation whilst retaining crystallinity, the process is called a single crystal to single crystal (SCSC) transformation.⁴⁹ Direct observation of chemical processes in the lattice during SCSC processes allow mechanistic details of the chemical process to be derived, potentially including direct characterization of transient intermediates.⁵⁰ These transformations can be triggered by external stimuli, such as a chemical reaction with guest molecules (solid-gas phase), light, heat, uptake or exchange of solvent.

In a classic example of using SCSC transformations to study organometallic transformations, Brookhart *et al.* reported a square-planar pincer Ir(I) complex underwent multiple SCSC transformations involving the exchange coordinated dinitrogen by the small gaseous ligands CO, NH₃, C₂H₄, H₂ and O₂ at an iridium(I) metal center (Figure 1.4).⁵¹ Furthermore, the restricted environment within the crystal lattice can tune the catalytic activity of the iridium pincer complex allowing it to act as an alkene hydrogenation catalyst. Selective hydrogenation of ethylene over propylene (using a 1:25 mixture) was observed when the surface iridium sites were occupied by CO. This selectivity occurred because the internal cavities of the crystals are small enough to only permit ethylene into the lattice of the crystal; while coordinated CO prevents the sites on the crystal surface from participating. This work demonstrates that complexes bearing weak ligands, such as nitrogen, can be isolated in the solvent-free environment and undergo controlled substitution within single crystals while maintaining crystallinity.

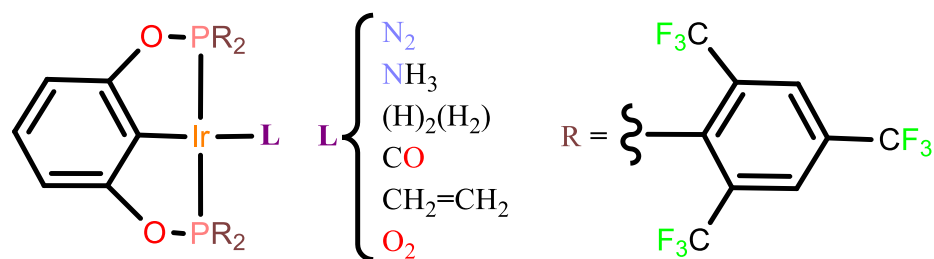


Figure 1.4. Molecular structures of a square-planar pincer Ir(I) complex and the substitution for different small molecules. Figure adapted from reference 51.

In a remarkable culmination of these attributes, in 2012 Weller *et al.* reported a unique SCSC transformation in which an extremely reactive Rh(I) σ -alkane complex was generated in-situ and characterized by SCXRD within the crystal lattice. The addition of H₂ to a single crystal of a cationic, phosphine-chelated Rh(I) norbornadiene (NBD) complex, resulted in a solid-state transformation of the norbornadiene ligand to norbornane, facilitating the isolation and structural characterization of a durable Rh σ -alkane complex via crystallography.³¹ The presence of a bulky anion in the system creates octahedral cavities around the Rh center allowing H₂ to interact with the metal complex in a solvent-free environment without compromising crystallinity. Despite being posited as transient intermediates in catalytic processes, very few examples of σ -alkane complexes have been characterized by X-ray crystallography due their instability. Outside the protective crystal lattice, the σ -alkane complex is rapidly displaced by the anion to yield the corresponding arene complex (Figure 1.5). Recently, this methodology has been expanded to a cationic Co(I) NBD complex in which a transient of σ -alkane complexes was characterized by X-ray crystallography.⁵²

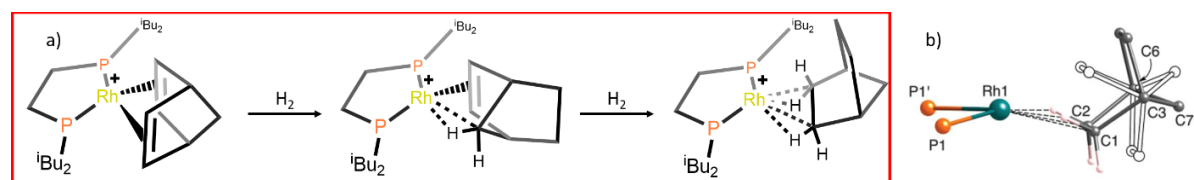


Figure 1.5. a) Reaction scheme of the cationic Rh(I) complex which furnishes the long-lived stable σ -complex intermediate; b) Crystal structure of the Rh σ -alkane complex. Figure adapted from reference 31.

The Rh σ -alkane complex formed in the hydrogenation process can be displaced by ethylene, to yield a Rh bis(ethylene) complex. In the solid-state the complex proved to be more stable given that in solution the complex underwent decomposition, even in the presence of ethylene, highlighting the importance of heterogenizing the complex. Recrystallization of this compound, from pentane at low temperature, generated a porous polymorph of the starting material in which the arrangement of the Rh center and the anion changed, resulting in the serendipitous formation of a porous material (Figure 1.6). Both the porous and non-porous materials were utilized in the gas-phase isomerization of 1-butene at room temperature (RT), the porous polymorph vastly outperformed the non-porous analogue with an outstanding Turnover Frequency TOF (90%) = 1160 h⁻¹ (TOF (95%) = 3100 h⁻¹ using crushed samples). It is worth mentioning that a second cycle revealed a loss in activity, suggesting the partial collapse of the lattice and confirming the importance of maintaining the crystal lattice over multiple cycles.⁵³ More recently, these crystals were used in a flow-reactor to carry out the isomerization of 1-butene; on-stream conversion is retained up to 90 hours at 298 K.⁵⁴ These conditions are industrially attractive, and the deactivation only occurs when the structure partially collapses. It is worth noting, this is the first reported study employing flow-reactor conditions for these unique systems, highlighting the potential for industrial applications. However, the stability and innately non-porosity nature of these materials make their use challenging in real-world application.

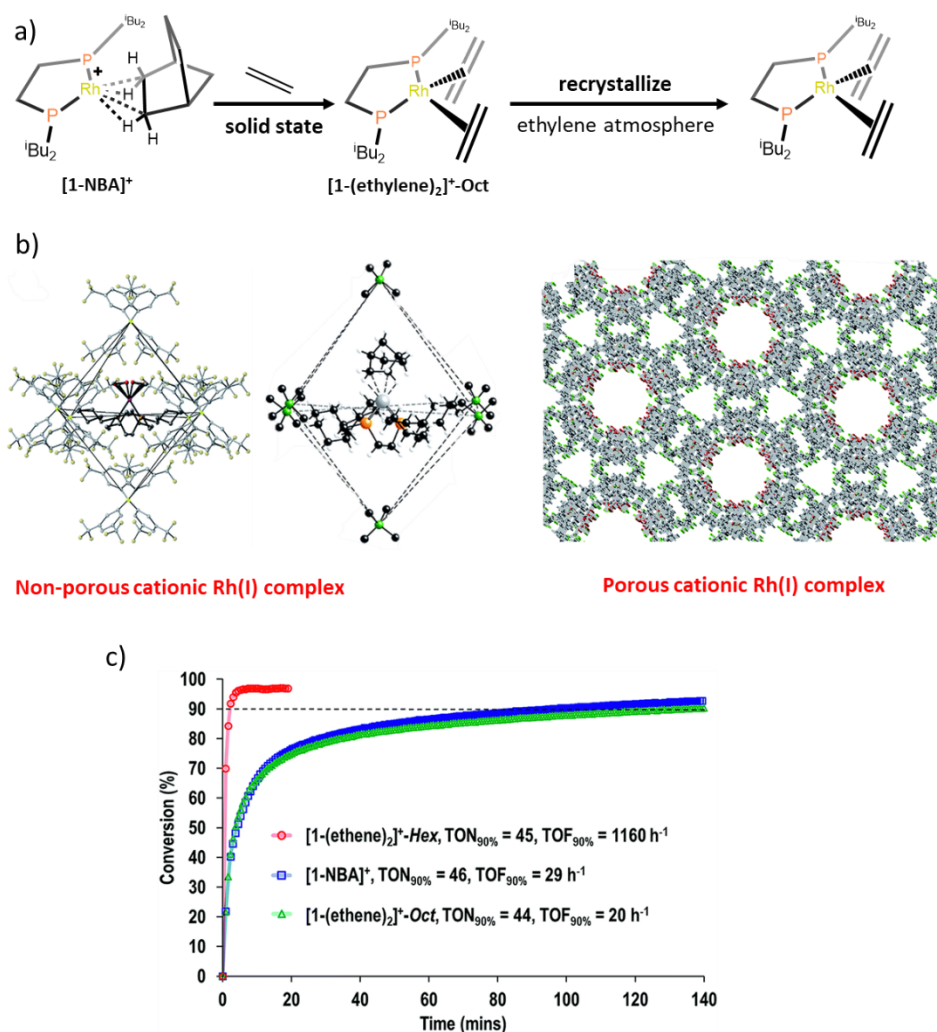


Figure 1.6. a) Schematic structures of cationic Rh(I) complex possessing different polymorphs; b) View of the extended structure of the porous and non-porous systems; c) Comparison for the isomerization of 1-butene to 2-butene. Figure adapted from reference 53.

In some instances, more than one SCSC transformation can be performed without compromising crystallinity. Crudden and co-workers reported a double SCSC transformation of a rhodium complex, in which sequential exchanges with oxygen and CO were carried out. The $[(\text{SIPr})_2\text{RhCl}(\text{N}_2)]$ complex ($\text{SIPr} = \text{N,N}-(2,6\text{-iPr}_2\text{C}_6\text{H}_3)_2\text{C}_3\text{H}_4\text{N}_2$) underwent exchange of η^1 -coordinated N_2 for O_2 to give an dioxygen adduct. Afterwards, the O_2 was readily and irreversibly substituted by CO (Figure 1.7). The transformations were accompanied with a change of color, from yellow, to blue and finally to brown, without losing crystallinity. The rhodium complex did not suffer an oxidation from Rh(I) to Rh(III) in the presence of O_2 , which is probably due to the considerable steric bulk in the coordination environment of the rhodium

complex preventing formation of the higher coordinate species.⁵⁵ This example highlights the importance of characterization by SCXRD, which elucidate the transformations that take place in the coordination environment and the geometry of the crystal, which is intimately related with the oxidation state of the metal.

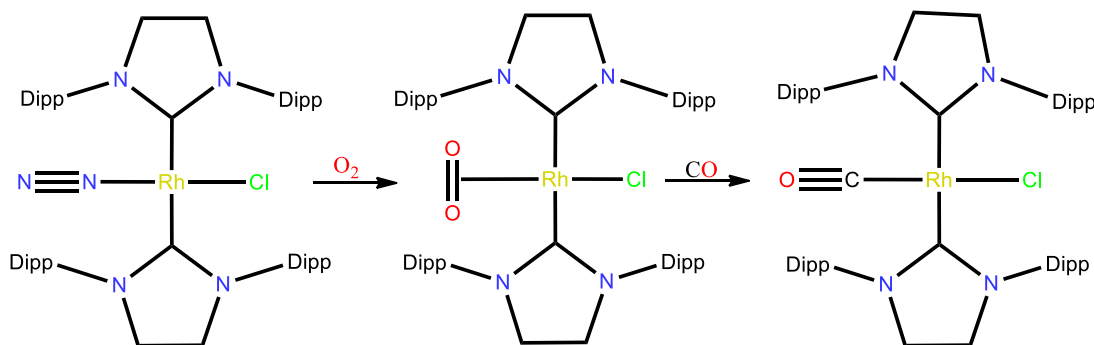


Figure 1.7. Sequence of SCSC substitution in a Rhodium (I) complex with different gases. Figure adapted from reference 55.

Despite their potential as matrices for isolating transient organometallic species, the application of crystallized organometallic complexes to industrial catalysis has thus far been limited by their low mechanical stability due to the lack of covalent bonds between the network components.⁵⁶ This limits the long-term site-isolation of the metallic centers while the innately non-porous nature of the molecular crystals makes it difficult for larger reagents to access the active sites. Therefore, in real word applications, the intrinsic characteristics of crystalline porous 3D materials such as Metal-organic-Framework (MOF)s makes them especially interesting as platform to perform heterogenous catalysis (i.e., stability, recyclability and easy removal from the reaction mixture).

Metal-organic Frameworks (MOFs)

Metal-organic frameworks (MOFs) are a comparatively new, fascinating class of porous materials. They are organic-inorganic hybrid compounds consisting of organic ligands acting as linkers/spacers and metal ions or clusters as nodes/vertices. Combinations of these building

blocks allow formation of three-dimensional periodic lattices with different pore shapes and sizes.

MOFs possess well-defined framework structures due to the strong metal-ligand coordination bonds. The possible combinations of organic and inorganic building blocks offer a nearly infinite number of structural variants,^{57–59} resulting in unique nets, such as those shown in Figure 1.8. This extraordinary diversity is an important feature that differentiates these materials from conventional porous materials, for instance zeolites⁶⁰ and activated carbon.⁶¹ Furthermore, subtle changes in the structure metrics of the building blocks allows the optimization of the pore dimensions and surface chemistry within the porous material. These fascinating characteristics endear MOFs towards a wide range of applications, for example gas adsorption/separation,^{62–64} sensing,^{65,66} microelectronics,^{67,68} heterogeneous catalysis^{69,70} and biotechnology.^{71,72}

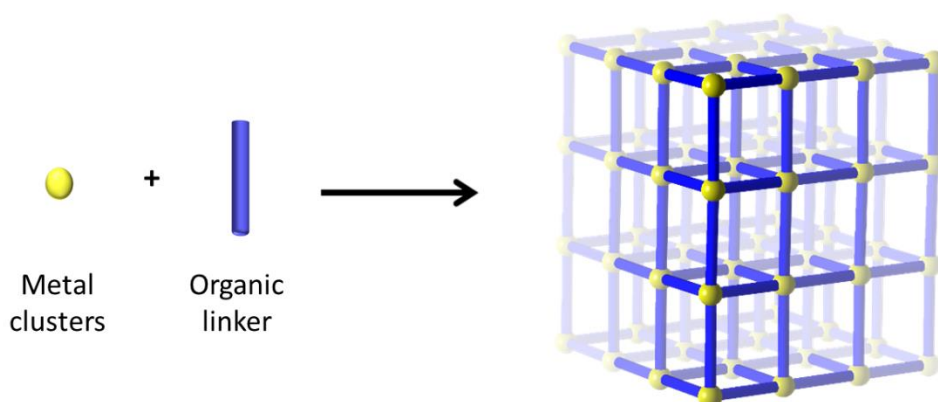


Figure 1.8. Schematic representation of a MOF consisting of organic linkers and metal clusters to form 3D structures.

Heterogeneous catalysis in MOFs

The application of MOFs as heterogeneous catalyst has expanded in the last two decades since Fujita *et al.* confirmed the catalytic activity of a MOF, the 2D square network $[\text{Cd}(4,4'\text{-bpy})_2](\text{NO}_3)_2$ which was used for aldehyde cyanosilylation.⁷³ In the development of MOF chemistry, three different methodologies have emerged to imbue MOFs with catalytically active metal centres (Figure 1.9):

- 1) The metal ions/node being the catalytically active site.^{74,75}
- 2) Loading the MOF with active constituents (i.e. metallic nanoparticles (MNPs)).^{76,77}
- 3) Postsynthetic modification (PSM) of the MOF by incorporating active metal catalysis.^{78–80}

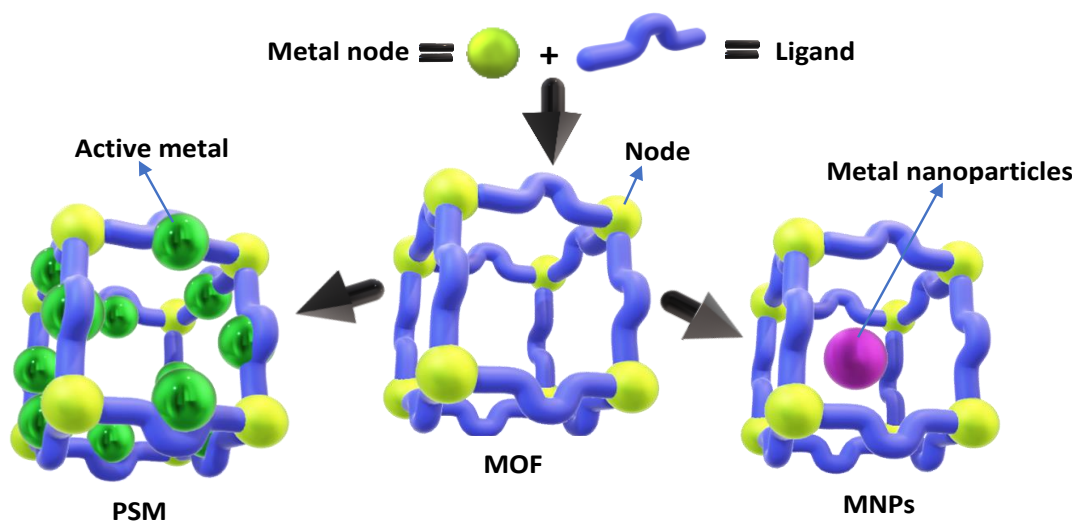


Figure 1.9. Representation of the different approaches to incorporate reactive metals within MOFs, including postsynthetic modification (PSM) and metal nanoparticles (MNPs), or utilising the metal ion/node of the framework.

One of the most attractive approaches to preparing MOFs featuring catalytically active metal sites is via PSM. Two common methods are employed to introduce catalytically active metal sites in MOFs via PSM:

- 1) The metal cations that compose the MOF nodes can undergo direct exchange with catalytically active metal cations, imparting activity to the MOF nodes (i.e. cation exchange).⁸¹
- 2) If the organic linker contains Lewis basic sites (preferably chelating) that do not coordinate with the structural metal ions and remain 'free' during MOF synthesis, they can undergo subsequent reaction with the catalytic metal.⁷⁹

Installing active sites in MOFs by cation exchange of metal centers in MOFs is a strategy that has been the subject of several reviews.^{82,83} PSM by cation exchange can give access to coordination environments unfeasible in solution or during the synthesis of the material. In 2012, Dincă *et al.* reported a pioneering work in this field by trapping a uncommon pseudo-tetrahedral Ni(II) oxygen complex via cation exchange with Zn(II) in MOF 5 [(Zn₄O(BDC)₃)] (BDC

= benzenedicarboxylate).⁸⁴ Characterization of the resultant material by X-ray crystallography was not possible due to the high symmetry of the material and therefore it was characterized by various spectroscopic techniques. Structural characterization of MOFs after cationic exchange is challenging due to only partial exchange or the location of metal clusters on high symmetry sites. Therefore, characterization is typically limited to spectroscopic techniques. Nevertheless, this method is a unique way for accessing rare coordination environments which can be used as catalytically active metal sites.

In an extension of this work, Dincă *et al.* employed a similar strategy to introduced Ni(II) within MFU- 4l⁸⁵ (Metal–Organic Framework Ulm University-4l = $[Zn_5Cl_4(BTDD)_3]$ (BTDD = bis(1 H-1,2,3-triazolo[4,5-b],[4',5'- i])dibenzo[1,4]dioxin)). The Zn(II) was partially exchange for Ni(II) (1-30%) in which the resultant materials were demonstrated to be highly active for ethylene dimerization to 1-butene.⁸⁶ This result highlights the importance of this methodology for PSM and how Dincă and co-workers took advantage to install reactive species. However, a better understanding of the mechanism and scope of the technique is still required in order to fully exploit the potential of cation exchange in developing future catalysts.

Heterogenization of well-defined homogeneous catalysts by post-synthetically immobilizing them on suitably functionalized MOF linkers is a convenient way of isolating reactive species due the controlled spacing of ligand-based binding sites. Compared to molecular crystals, the mechanical stability of MOF crystals promotes the retention of crystallinity during PSM; sometimes this allows the coordination sphere of the active metal center to be studied via X-ray crystallography. Unlike the well-defined heterogenous systems described above, MOF materials are generally robust towards chemical processing, including solvent removal, and maintain structural integrity that is critical for transporting guest molecules. Thus far, one of the most widely studied frameworks for PSM is the Zr-UiO-type (University of Oslo) MOFs since they are robust and easily functionalized with different types of bidentate ligands, for instance N,N-chelating,^{87–90} diol,⁹¹ salicylaldimine,⁹² 2,2'-bis(diphenylphosphino)-1,1'-binaphthyl (BINAP)⁹³ and NHC based binding sites (Figure 1.10).⁹⁴ Following PSM, these coordinating groups can stabilize the active metal and prevent them from leaching during catalysis.⁹⁵

Despite the tunability of the UiO MOFs and their popularity as platforms for PSM, structural characterization of the catalytically active metals located in this framework have proven

challenging and few examples have been reported.^{96–98} This is mostly attributed to the difficulty of growing larger crystals for SCXRD and the higher symmetry of UiO family of materials that leads to crystallographic disorder of the active metals. Nonetheless, metalated UiO materials have proven to be excellent matrices in which to isolate active metal catalysts and their activity.

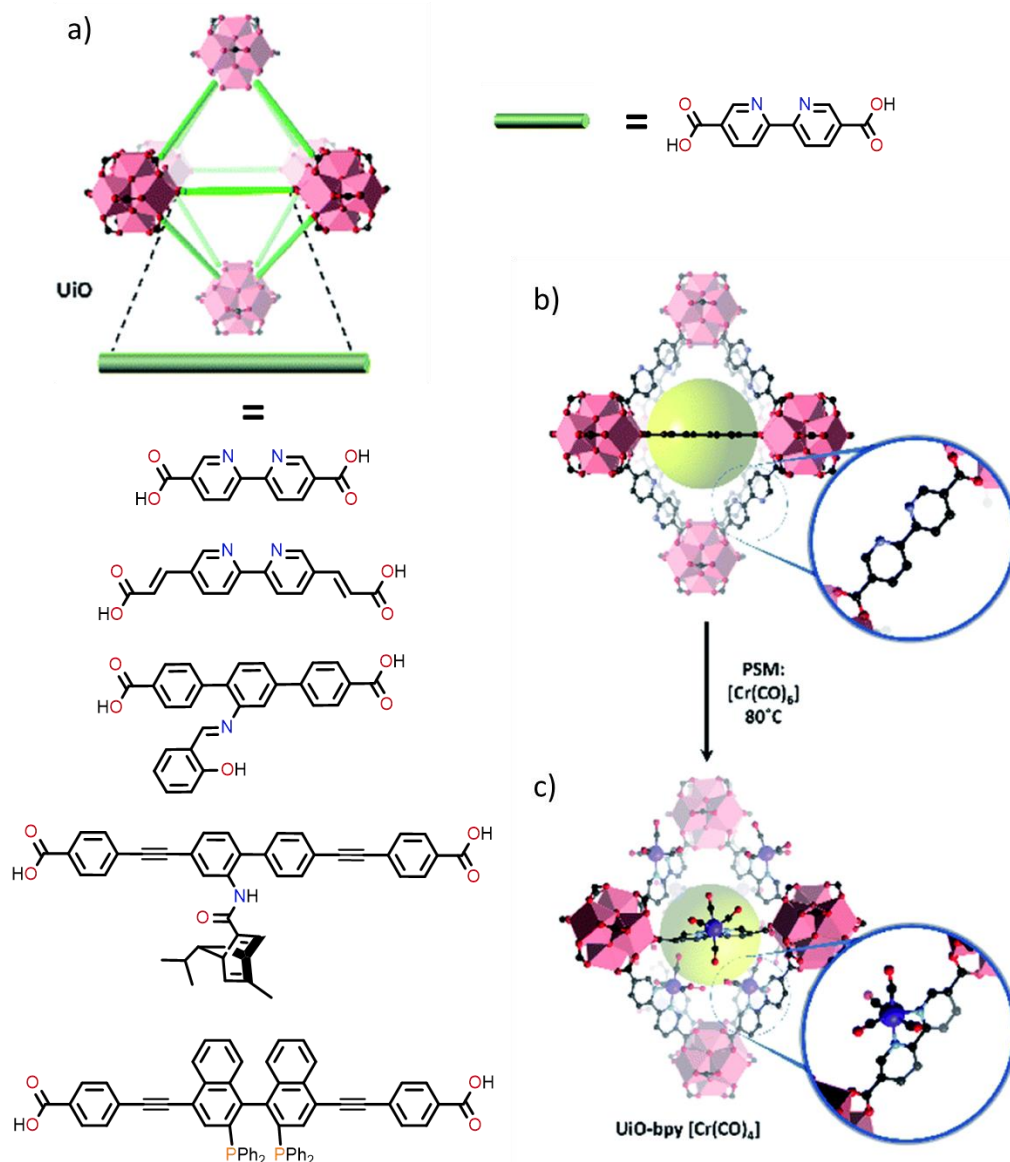


Figure 1.10. a) Different free-coordination sites for PSM in MOFs, including numerous derivatives of the UiO structure; b) Non-metalated UiO framework; c) Metalated UiO framework. Figure adapted from reference 14.

A prominent example of the UiO series being employed as catalysts was reported by Manna *et al.* Salicylaldimine (Sal) ligand derivatives of a UiO MOF underwent for PSM to incorporate

nickel or zirconium complexes that can perform olefin polymerization reactions. Typical molecular catalysts of this Sal ligands need the presence of bulky substituents to prevent ligand migration and formation of inactive metal complexes $M(\text{Sal})_2$ or $M(\text{Sal})_3$,⁹⁹ and loss of catalytic activity. In 2014, Manna *et al.* synthesized Sal-UiO-type MOF which was metalated with $[\text{FeCl}_2]$ or $[\text{CoCl}_2]$. Subsequently, the Fe(II) complex was reduced with NaBEt_3H in THF to afford an active Fe(0) catalyst for alkene hydrogenation that can be easily recycled and reused.⁹² In the homogenous phase, the ligand migrated forming an inactive $[\text{Fe}_4(\text{Sal})_4\text{Cl}_4(\text{THF})_2]$ cluster, highlighting the importance of the isolated metal sites offered by MOFs as a powerful tool to support highly active catalyst for important organometallic reactions (Figure 1.11).

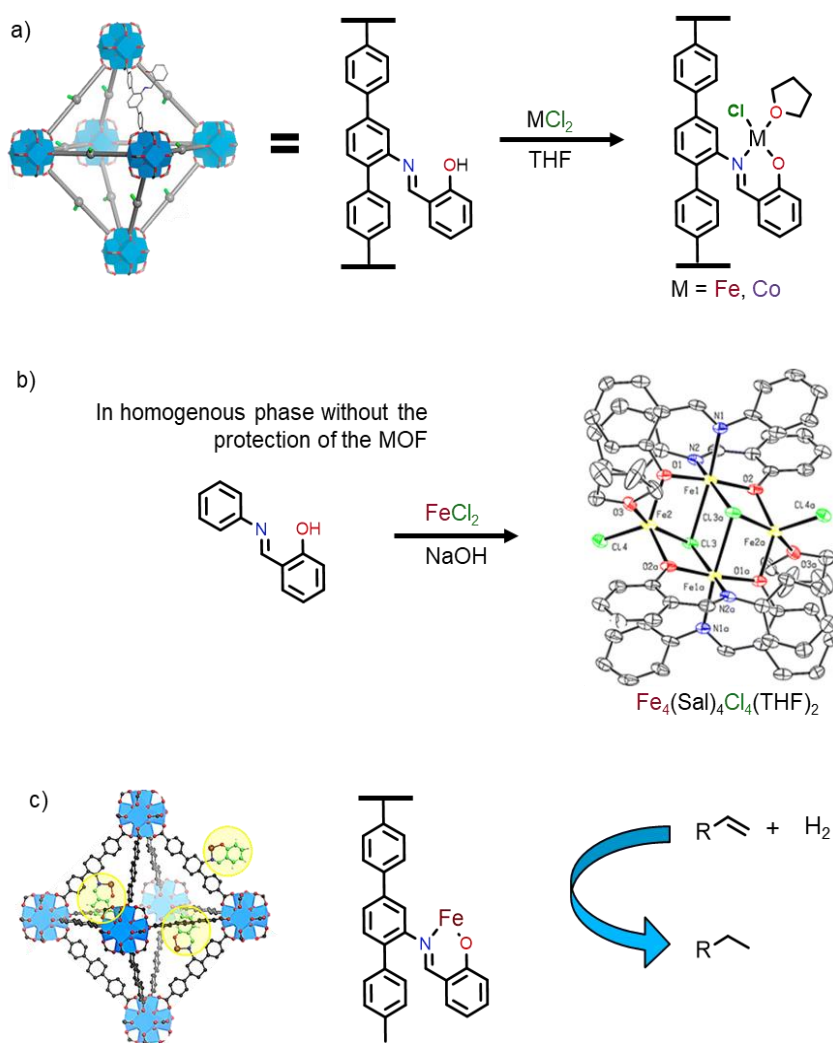


Figure 1.11. a) PSM of a Sal-UiO-type MOF with FeCl_2 and CoCl_2 ; b) In homogenous phase, Fe complex migrated from the ligand to form the inactive $\text{Fe}_4(\text{Sal})_4\text{Cl}_4(\text{THF})_2$ clusters; c) Fe-Sal-UiO-type MOF is a powerful catalyst for alkene hydrogenation. Figure adapted from reference 92.

Transition metal complexes in low oxidation states are highly active catalytic complexes and are especially vulnerable to decomposition that is induced by the loss of ligands.^{100,101} Recently, Lin *et al.* and co-workers introduced CoCl₂ into bipyridine-or phenanthroline-based UiO-MOFs via PSM. Subsequently, NaB(Et)₃H was used to reduce the metal center from Co(II) to Co(0), yielding site-isolated [(N,N)-[Co(THF)₂] metal complexes which proved to be a powerful catalyst for hydrogenation. In the homogenous phase, the reaction lead to ligand dissociation of the Co(0) complex and ultimately to nanoparticle formation, highlighting the role of site isolation in stabilizing the active catalyst.¹⁰² It is worth mentioning, that structural insight into the active Co(0) metal complex by SCXRD was not possible even though the isolation of the metal complex was clearly demonstrated by spectroscopic methods.

MOFs have uniform pores that enable the formation of size-limiting internal environments which can influence the selectivity of a chemical reaction.^{103,104} In 2019, Yuan and co-workers reported a UiO-type platform which incorporated a Zn(II) catalyst for intramolecular hydroamination of alkynes. The [Zn(BF₄)₂] moiety tethered to the bipyridine N,N-chelation sites of the host framework carried out a cycloisomerization of 2-(phenylethynyl)aniline. In the homogenous counterpart, the reaction yields the hydration of the alkyne. This result was attributed to the unique internal environment that the MOF pore provides which yields the formation of different products.¹⁰⁵ This is a remarkable example of how the microenvironment of MOFs can influence the reaction mechanism of the allocated metal complex, yielding products that are non-feasible in homogenous systems.

The modular building block approach to MOF synthesis allows the organic linker to be precisely tuned in order to modulate the chemical, electronic properties of the supported metal complex as well as the physical properties (pore size/shape) of the supporting framework; thereby harnessing a key element of homogeneous catalysts in a heterogeneous environment. In 2016, Huang *et al.* reported the impact of the organic linker on the catalytic properties of an isolated metal complex.¹⁰⁶ A series of UiO-type MOFs have been reported using mixed-linkers biphenyl- and bipyridine-dicarboxylic acid as organic linkers (m-bpy-MOF-PdCl₂, m-6,6'-Me₂bpy-MOF-PdCl₂, m-4,4'- Me₂bpy-MOF-PdCl₂) to load a Pd(II) chloride precatalyst, which is active for Suzuki-Miyaura cross-coupling reactions (Figure 1.12). The mixed-ligand method is used to facilitate the separation between the active palladium centers thereby preventing deactivation of the catalyst, while also ensuring the MOF pore does not

become blocked with chelated Pd sites.¹⁰⁷ Under optimal metal loading conditions, the reaction between iodo or bromobenzene and phenylboronic acid occurred in excellent yields, with the m-6,6'-Me₂bpy-MOF-PdCl₂ catalyst displaying the highest activity. This enhancement was attributed to the stereoelectronic properties of the substituents on the organic linker, highlighting the importance of linker design for immobilization of homogeneous catalysts in MOFs.

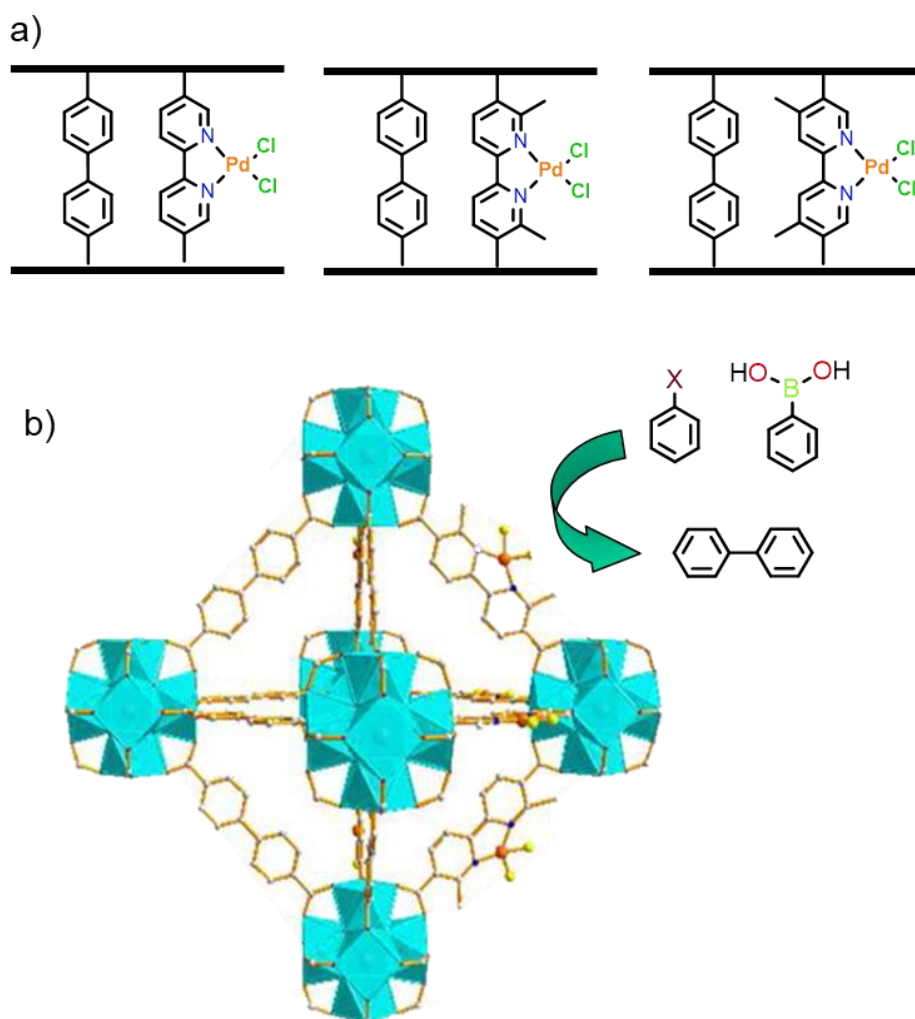


Figure 1.12. a) Schematic structures of m-MOF-PdCl₂ precatalysts. b) Ideal structure of m-6,6'-Me₂bpy-MOF-PdCl₂ for the Suzuki–Miyaura cross-coupling reaction. Figure adapted from reference 106.

Besides the UiO-topology Zr-based MOFs, porphyrinic MOFs are also capable of hosting catalytically active metals.^{108,109} In 2018, Fang *et al.* reported the confinement of a Pt(0) atom within the free chelating groups of a porphyrinic Al-MOF. This catalyst exhibited superb photocatalytic efficiency in hydrogen production from water with an improved TOF of 35 h⁻¹, an improvement of 30 times compared with platinum nanoparticles under the same conditions. Spectroscopy and Density Functional Theory (DFT) analysis showed that the introduction of Pt(0) moieties into the MOF opens an efficient electron transfer channel and improves the hydrogen binding energy, leading to enhanced activity in the production of hydrogen.¹¹⁰ This study further demonstrates the advantages of introducing isolated metal atoms in MOF systems.

Gas-phase reactions and catalysis with MOFs

Most of the investigations in heterogeneous catalysis using MOFs have focused on reactions for the synthesis of fine chemicals.^{111–113} Generally, this chemistry is carried out in solution and therefore does not take full advantage of the MOF's intrinsic characteristics such as high surface area, crystallinity, and permanent porosity. Thus, the judicious choice of chemistry and reaction conditions can showcase the unique properties of MOFs. Gas-phase reactions are an excellent example of chemistry in which MOF characteristics can be exploited towards fully realizing their potential in commercial applications.^{114,115}

Due to its relevance in industry, one of the gas phase reactions often investigated using MOF catalysts is hydrogenation.¹¹⁶ Recently, Farha and co-workers reported the use of Zr- and Hf-based-MOFs to support an active nickel catalyst for ethylene hydrogenation. The Hf-based-MOF offered superior activity in comparison with the isostructural Zr analogue because the incorporated Ni is anchored to an oxygen atom available on the MOF node. Spectroscopic characterization and computational insights showed the nickel center was more active when bound to the bridging oxygen site of the Hf-based-MOF due to a stronger interaction between the Ni center and ethylene. It is also worth mentioning that when the nickel is coordinated by a bidentate site on the node, the catalyst shows a higher activity than when nickel is bound to the monodentate sites.¹¹⁷ The Zr-based-MOF metalated with nickel has also been used for gas

phase ethylene oligomerization, with a turnover frequency (TOF) of 0.3 s^{-1} . Over the course of 10 hours on stream, catalyst deactivation occurred, due to the formation of polymeric products that blocked the MOF pores.¹¹⁸ A similar approach has been employed to incorporate Rh(I)¹¹⁹ and Ir(I) species^{120,121} into MOFs for gas phase hydrogenation and dimerization. Impressively, mononuclear Rh(I) and Ir(I) bis(ethylene) complexes have been anchored to the nodes of Zr- and Mg-based MOFs, respectively, with both Ir and Rh sites displaying catalytic activity under relevant $\text{C}_2\text{H}_4/\text{H}_2$ flow conditions for ethylene hydrogenation and dimerization.

Another approach to introducing active metal catalysts into MOFs for gas phase catalysis was explored by Pardo *et al.* in which an iron(III) complex was introduced by means of cation exchange, and the hosted species was characterized by SCXRD. Interestingly, the resulting metal complex was active for the gas-phase hydrogenation of acetylene.¹²² A similar strategy was applied by Weller *et al.* to incorporate Crabtree's catalyst, $[\text{Ir}(\text{cod})(\text{PCy}_3)(\text{py})]^+$ into of MIL-101(Cr) via ion-exchange. In solution, the Crabtree's Ir catalyst can be deactivated during the hydrogenation of olefinic alcohols through the formation of catalytically inactive polymetallic hydride clusters. The cationic Ir(I) complex supported within the MOF surpasses the homogenous equivalent in activity and selectivity of hydrogenation over isomerization. This enhancement is attributed to the well-defined hydrophilic architecture of the MOF pores and electrostatic interactions between the catalyst and the MOF backbone that provides enhanced stability to the catalyst.¹²³ The ion-exchange methodology proved to be an excellent alternative of introducing well-defined catalytically active metals to perform gas-phase reactions.

Olefin isomerization is a much less studied reaction but with appreciable industrial value in the production and refining of hydrocarbon fuels. In industry these reactions are carried out at high temperatures using heterogenous catalysts.^{124,125} Homogenous catalyst are well-known to perform isomerization with different transition metals at lower temperature.¹²⁶ However, the exorbitant costs of the product separation make this process unviable for industrial applications.¹²⁷ Recently, Noterstein and co-workers reported a Zr-based MOF (NU-1000) with the ability to perform 1-butene isomerization employing the Zr-node as the catalytic site.¹²⁸ However, the system still requires high temperatures for the reaction indicating lower activity of the zirconium node compared to conventional homogeneous

catalysts. 1-Butene isomerization was examined for Fe- and Cr-based MOFs (MIL-100 and -101) under optimal temperatures but at comparatively high-pressures. Furthermore, MIL-101 (Cr) can be recycled at least four times maintaining the conversion with a high-catalytic activity.¹²⁹ In 2019, Somorjai *et al.* studied the oligomerization and isomerization of light olefins (C3-C6) on a sulfated metal–organic framework-808 (S-MOF-808) which displays strong Brønsted-superacidic character. The strongest Brønsted acid site is shown to contain a specific arrangement of adsorbed water and sulfate moieties on the zirconium clusters. Oligomerization and isomerization were explored at 80 to 110 °C and ambient pressure with poor selectivity and activity. Interestingly, the material deactivates at temperatures over 100 °C due to the loss of adsorbed water molecules.¹³⁰ These are remarkable examples that show the potential of MOFs in gas phase catalysis and how to exploit their fascinating and novel properties to develop attractive reactions for industry.

Metal-Organic Frameworks: X-ray crystallographic insights into catalysis

Porous materials such as MOFs offer excellent opportunities as a platform to study the coordination environment of host species by integrating structurally characterized transition metal complexes into their framework architectures. A seminal example of heterogenizing well-defined metal complexes within MOFs was reported by Humphrey and co-workers. Two novel MOFs were synthesized, featuring unique monodentate free phosphine and arsine donor sites accessible *via* porous channels. The high crystallinity of these materials was maintained after PSM allowing structural characterization of the moieties by X-ray crystallography. In the arsine example, metalation of the material with AuCl(Me₂S) revealed the formation of As(AuCl).¹³¹ Surprisingly, the Au-Au distance (2.76 Å) within the MOF is very short compared with molecular complexes in which the Au-Au distance is typically between 2.84 and 3.43 Å. This short distance is promoted by the rigidity of the MOF host with a distance between adjacent donor sites of 4.8 Å, forcing the metal complexes to form with an unusually short contact distance. The MOF which features monodentate phosphine donors also possess a very short distance between the donor sites (7.22 Å), thereby effectively generating a P,P chelation site. Metalation with [AuCl(Me₂S)] or [CuBr(Me₂S)] results in the corresponding

[P(AuCl)] and [P,P(Cu₂Br₂)] chelated dimers.⁹⁵ Finally, the catalytic activity of the allocated species was investigated for the hydroaddition of 4-pentyn-1-ol revealing higher activity than their molecular counterparts. The remarkable examples reported by Humphrey *et al.* expand our understanding of post-synthetic metalation in MOFs and the role of crystallography in revealing unusual complexes that result from the precise structural metrics of the host framework.

As mentioned above, MOFs can incorporate well-defined transition metal complexes by PSM, transforming the framework into a heterogeneous catalyst. Furthermore, the host metals in MOFs have the same local environments and are isolated by a specific distance from each other (i.e., long range order). The well-defined architecture of MOFs and the isolation that the framework provides to the guest metal complex allows the elucidation of the coordination environment by SCXRD. Despite their popularity as platforms for heterogeneous catalyst, few examples of metalated UiO-type MOFs have been published in which the included metal center has been structurally characterized. This has been attributed to the challenge of growing larger crystals for SCXRD and the higher symmetry of UiO family which leads to crystallographic disorder of the active metals. Recently, a Mn(II) based MOF, **MnMOF-1**, which was synthesized at the University of Adelaide, has proven to be an exceptional platform for showcasing these properties. MnMOF-1 is formed by the reaction between L (bis(4-(4-carboxyphenyl)-1 H-3,5-dimethylpyrazolyl)methane) and MnCl₂ to form a unique 3D structure, based on Mn(II) trimer nodes. Notably, the MOF structure has vacant N,N'-chelation sites accessible to guests through 13 Å channels that penetrate the material. In a suitable solvent, the chelation sites available within the material can be postsynthetically metalated with transition metal complexes and studied by X-ray crystallography. One of the first examples of postsynthetic metalation of this material was carried out with CoCl₂·6H₂O in methanol at 65 °C which resulted in a change in the color of the crystals from colorless to pink. SCXRD revealed the formation of the octahedral complex **MnMOF-1**·[Co(H₂O)₄Cl₂]. Remarkably, under solvent exchange from methanol to acetonitrile, the crystals underwent a SCSC transformation with a further color change from pink to blue, and this color change can be rationalized by a transformation of the Co(II) coordination environment from octahedral to tetrahedral. This was subsequently confirmed via SCXRD which revealed formation of the tetrahedral complex **MnMOF-1**·[CoCl₂].¹³² This unique characteristic, the ability to study the

coordination environment of the host metal complex by SCXRD, differentiates **MnMOF-1** from other porous materials and indeed most MOFs. Furthermore, the permanent porosity, stability, ability to host well-defined metal complexes and high crystallinity offers key advantages over molecular crystals as hosts for reactive metal complexes.

The investigation of coordination and organometallic chemistry using **MnMOF-1** has been expanded to an important commercial reaction, the Monsanto process.¹³³ This reaction utilizes a homogenous rhodium(I) carbonyl catalyst which undergoes several organometallic reactions during the process including oxidative addition of methyl iodide, migratory insertion to generate an acetyl functionality and finally reductive elimination to yield acetyl iodide. To investigate this process within **MnMOF-1**, the material was post-synthetically metalated with an organorhodium compound $[\text{Rh}(\text{CO})_2\text{Cl}]_2$ resulting in **MnMOF-1**· $[\text{Rh}(\text{CO})_2][\text{Rh}(\text{CO})_2\text{Cl}_2]$. SCXRD revealed that the coordinated Rh(I) cation is charge balanced by a $[\text{Rh}(\text{CO})_2\text{Cl}_2]^-$ counter-ion generated during the metalation. The reaction of **MnMOF-1**· $[\text{Rh}(\text{CO})_2][\text{Rh}(\text{CO})_2\text{Cl}_2]$ with MeI in acetonitrile yields a SCSC transformation with a visible color change from yellow to red. SCXRD revealed the formation of **MnMOF-1**· $[\text{Rh}(\text{CO})(\text{CH}_3\text{CN})_2](\text{COMe})\text{I}] \cdot \text{I}$. Fascinatingly, the equivalent reaction with MeBr produces a double oxidative addition of the metal complex giving **MnMOF-1**· $[\text{Rh}(\text{CH}_3\text{CO})\text{Br}(\text{MeCN})_2] \cdot \text{Br}$, representing the complete consumption of the carbonyl ligands. This remarkable discrepancy in the course of the reaction, as revealed by the crystal structures; is attributed to the steric demands of the halide ligands. The elucidation of the coordination environment allowed the reactivity of the well-defined Rh complex allocated in the MOF to be understood. Under catalytic conditions in the gas phase, **MnMOF-1**· $[\text{Rh}(\text{CH}_3\text{CO})\text{Br}(\text{MeCN})_2] \cdot \text{Br}$ produced acetyl bromide at a very low rate, likely because the oxidative addition of MeBr in the catalytic cycle is the slower step. Even though the oxidative addition of MeI is faster than that of MeBr, the bulkiness of the iodide ligand generated during oxidative addition stops the reaction from proceeding through a full cycle and therefore, the catalytic activity is negligible using MeI.¹³⁴ This remarkable work is one of the first examples of a well-defined organometallic complex supported in a MOF being used for gas-phase reactions. The platform allows the elucidation of the steps in the catalytic cycle, and furthermore, to understand the observed and the distinct reactivity in of the methyl halides in the gas-phase.

Exploiting the potential of site isolation that **MnMOF-1** offers, combined with the unique ability to structurally characterize the coordination environment of supported metals, Huxley et al. reported a work in which the material was postsynthetically modified with a Mn(I) azide complex that is poised to carry out site-selective “click” reactions as shown in Figure 1.13. Throughout this process SCSC transformations enabled elucidation of the structural changes at the metal complex. Selectivity within the MnMOF-1 was shown through reactions with terminal dialkynes with different length spacers, with a selective reaction occurring on one end of the dialkyne when the distance between the azide moieties was larger than the length of the dialkyne chain.¹³⁵

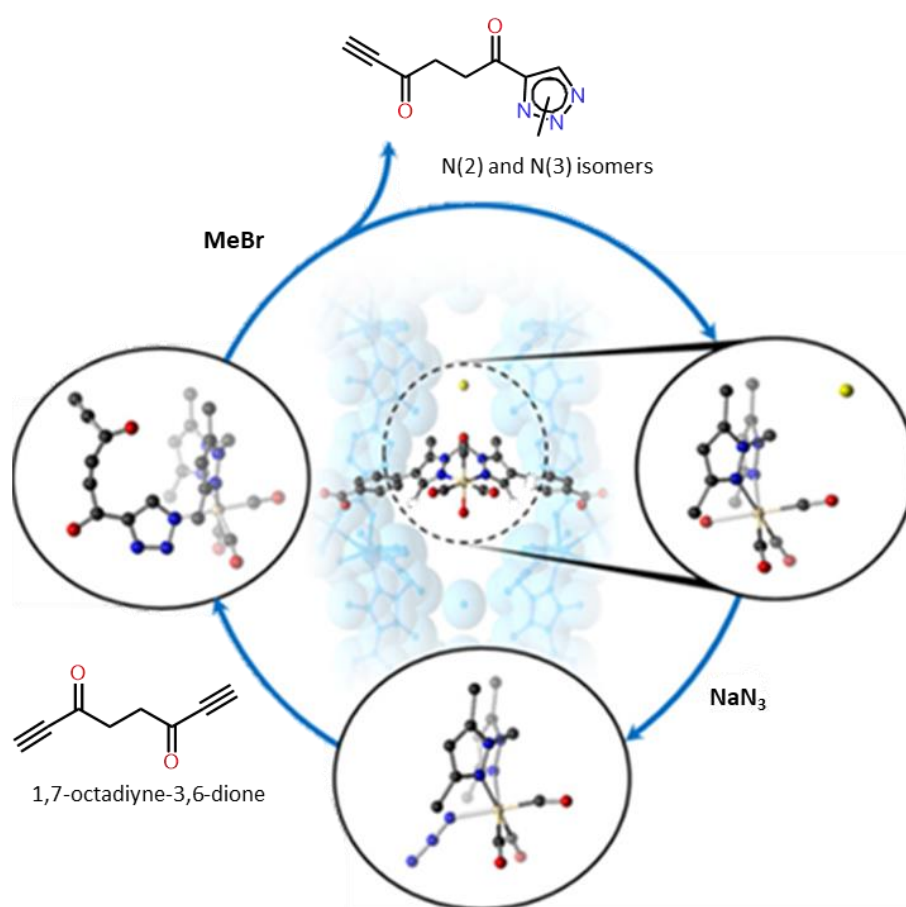


Figure 1.13. “Click” chemistry cycle followed by X-ray crystallography using a Mn-based MOF. Figure adapted from reference 135.

In related work, the allocated Mn(I) carbonyl bromide complex (which is a precursor to the azide above) was converted from an ion pair to a charge-neutral complex via coordination of

the charge-balancing halide ligand. This transformation occurred in a SCSC process by washing the MOF crystals (originally in polar EtOH) with nonpolar solvents (toluene, THF). The facile interconversion of MOF-tethered Mn(I) complexes, simply via solvent exchange, allows for the potential control of ion exchange, which can provide access to new metal complexes.¹³⁶

Contextual Statement

This thesis presents the synthesis and characterization of different transition metal complexes allocated within a Mn-based MOF. As mentioned above, a salient feature of the MOF is high crystallinity, which allows the coordination environment of the host metal to be studied via X-ray crystallography. An enhanced understanding of these complexes provides essential insights into how to develop catalysts with improved performance and stability, for a potential industrial applications.

In accordance with these objectives, Chapter 2 investigates the flexibility of Mn-based MOF, Mn_3L_2L' (where L = bis-(4-carboxyphenyl-3,5-dimethylpyrazolyl)methane) (MnMOF-1) which features a vacant N,N'-chelation site arising from a partially non-coordinated L moiety, designated L'. These spatially isolated metal-binding sites undergo quantitative metalation and subsequent modifications with retention of single crystallinity. Although metalation chemistry within MnMOF-1 has been extensively studied, this Chapter provides insight into the underlying flexibility of the framework, demonstrating how this can be controlled by judicious choice of solvent and plays an important role in the ability of the framework to both undergo metalation and retain chelated metal centres during subsequent chemistry.

In Chapter 3 and 4, the preparation and catalytic activity of reactive cationic rhodium(I) and iridium(I) bis-ethylene complexes allocated in MnMOF-1 is reported. These species were prepared via PSM under an ethylene atmosphere, a new strategy that allows MnMOF-1 to be metalated with highly reactive complexes featuring labile (ethylene) ligands. Subsequently, facile anion exchange under ethylene was employed to produce BF_4^- and Cl^- derivatives. Exploiting the crystallinity of the host framework, the immobilised Rh(I) and Ir(I) centres were structurally characterized using X-ray crystallography. To explore the reactivity of all the Rh and Ir species, the hydrogenation of ethylene was investigated using gas phase NMR spectroscopy. Intriguingly, the charge-balancing anions displayed markedly distinct activity, indicating that the anions residing in the MOF pore perform a role in the catalytic cycle.

Furthermore, in Chapter 3 the activity of mononuclear Rh(I) complexes supported within the MOF framework was investigated in gas phase 1-butene isomerisation. Under one atmosphere of butene at 46°C, the Rh(I) derivative with a weakly-coordinating BF_4^- anion

rapidly catalyses the conversion of 1-butene to 2-butene with a TOF of ca. 2000 hr⁻¹. Notably, the chloride derivative displays negligible activity in comparison, due the stronger interaction between the coordinating anion and the Rh centre which impacts the catalytic activity, as demonstrated by X-ray Photoelectron Spectroscopy (XPS) and DFT calculations. This work demonstrates the capacity of MnMOF-1 to act as a platform for gas phase catalysis using well defined, site-isolated transition metal complexes. The techniques, particularly metalation and sample handling under specialised gases, provides a new avenue to accessing highly reactive complexes in MnMOF-1.

In Chapter 5, a new methodology was developed to access novel, labile Cu(I) complexes which are otherwise difficult to characterize. Building on the strategy developed in Chapters 3 and 4, labile Cu(I) complexes were prepared by *in situ* anion metathesis of MnMOF-1·[CuCl] in the presence of specialist gases which act as labile ligands. In accordance with the porous nature of the host framework, the weakly bound 'place-holder' ligands readily undergo substitution with a broad repertoire of small guest molecules and weakly coordinating anions. The highly crystalline and robust host framework allows these transformations to be mapped via X-ray crystallography, providing exquisite insight into the exchange processes of site-isolated Cu(I) moieties within MnMOF-1, pertinent to Cu-centered catalysis.

Overall, this thesis illustrates the important role of MOFs as potential heterogenous catalysts and platform materials for elucidating the fundamental coordination chemistry involved in heterogeneous catalysis. The homogenous counterparts of such catalysts are well-defined systems which are considerably easier to study using common spectroscopic techniques. MOFs offer excellent opportunity to capitalize on this body of knowledge by integrating structurally characterized organometallic species into their framework architectures and exploring the potential of these unique systems for application to commercially attractive processes. Hitherto, MOFs have been primarily employed as structural supports for organometallic complexes catalysts during solution phase catalysis. The gas phase catalysis carried out in this thesis using well defined catalysts immobilised in MnMOF-1, are an important step towards isolating highly reactive metal centres and harnessing their potential as heterogeneous catalysts for industrially relevant gas-phase reactions. This takes full advantage of the novel properties of permanently porous, highly crystalline MOFs.

References

- 1 *Catalysis*, 2008, I–XIII.
- 2 C. T. Campbell, *ACS Catal.*, 2017, **7**, 2770–2779.
- 3 J. A. Moulijn, P. W. N. M. van Leeuwen and R. A. B. T.-S. in S. S. and C. van Santen, Eds., in *Catalysis*, Elsevier, 1993, vol. 79, pp. 3–21.
- 4 S. Li and J.-A. Ma, *Bridg. Heterog. Homog. Catal.*, 2014, 425–468.
- 5 J. Brightling, *Johnson Matthey Technol. Rev.*, 2018, **62**, 32–47.
- 6 A. Dhakshinamoorthy, A. M. Asiri and H. García, *Trends Chem.*, 2020, **2**, 454–466.
- 7 V. P. Ananikov, *Mechanisms and Catalysis Related Titles Modeling and Simulation of Heterogeneous Catalytic Homogeneous Catalysis with Metal Complexes - Kinetic Bridging Heterogeneous and NMR in Organometallic.*
- 8 A. J. Cowan and M. W. George, *Coord. Chem. Rev.*, 2008, **252**, 2504–2511.
- 9 B. K. McNamara, J. S. Yeston, R. G. Bergman and C. B. Moore, *J. Am. Chem. Soc.*, 1999, **121**, 6437–6443.
- 10 S. Geftakis and G. E. Ball, *J. Am. Chem. Soc.*, 1998, **120**, 9953–9954.
- 11 S. C. Chmely and T. P. Hanusa, *Eur. J. Inorg. Chem.*, 2010, 1321–1337.
- 12 C. Schöttle, E. Guan, A. Okrut, N. A. Grosso-Giordano, A. Palermo, A. Solovyov, B. C. Gates and A. Katz, *J. Am. Chem. Soc.*, 2019, **141**, 4010–4015.
- 13 C. H. Christensen and J. K. Nørskov, *J. Chem. Phys.*, 2008, **128**, 182503.
- 14 R. J. Young, M. T. Huxley, E. Pardo, N. R. Champness, C. J. Sumbly and C. J. Doonan, *Chem. Sci.*, 2020, **11**, 4031–4050.
- 15 S. D. Pike and A. S. Weller, *Philos. Trans. R. Soc. A Math. Phys. Eng. Sci.*, 2015, **373**, 20140187.
- 16 T. Drake, P. Ji and W. Lin, *Acc. Chem. Res.*, 2018, **51**, 2129–2138.

- 17 M. Hoshino, A. Khutia, H. Xing, Y. Inokuma and M. Fujita, *IUCrJ*, 2016, **3**, 139–151.
- 18 A. Das, G. P. Van Trieste and D. C. Powers, *Comments Inorg. Chem.*, 2020, **40**, 116–158.
- 19 J. A. Gladysz, R. B. Bedford, M. Fujita, F. P. Gabbaï, K. I. Goldberg, P. L. Holland, J. L. Kiplinger, M. J. Krische, J. Louie, C. C. Lu, J. R. Norton, M. A. Petrukhina, T. Ren, S. S. Stahl, T. D. Tilley, C. E. Webster, M. C. White and G. T. Whiteker, *Organometallics*, 2014, **33**, 1505–1527.
- 20 X. Yang, C. L. Stern and T. J. Marks, *J. Am. Chem. Soc.*, 1991, **113**, 3623–3625.
- 21 P. F. Kuijpers, J. I. van der Vlugt, S. Schneider and B. de Bruin, *Chem. – A Eur. J.*, 2017, **23**, 13819–13829.
- 22 K. M. Carsch, I. M. DiMucci, D. A. Iovan, A. Li, S.-L. Zheng, C. J. Titus, S. J. Lee, K. D. Irwin, D. Nordlund, K. M. Lancaster and T. A. Betley, *Science (80-.)*, 2019, **365**, 1138–1143.
- 23 J. G. de Vries and S. D. Jackson, *Catal. Sci. Technol.*, 2012, **2**, 2009.
- 24 X. Cui, W. Li, P. Ryabchuk, K. Junge and M. Beller, *Nat. Catal.*, 2018, **1**, 385–397.
- 25 M. J. Hülsey, C. W. Lim and N. Yan, *Chem. Sci.*, 2020, **11**, 1456–1468.
- 26 J. C. B. T.-M. O. in H. C. Védrine, Ed., in *Metal Oxides*, Elsevier, 2018, pp. 401–549.
- 27 A. Bavykina, N. Kolobov, I. S. Khan, J. A. Bau, A. Ramirez and J. Gascon, *Chem. Rev.*, 2020, **120**, 8468–8535.
- 28 G. G. Hlatky, *Chem. Rev.*, 2000, **100**, 1347–1376.
- 29 J. M. Thomas, R. Raja and D. W. Lewis, *Angew. Chemie Int. Ed.*, 2005, **44**, 6456–6482.
- 30 M. I. Burguete, J. M. Fraile, J. I. García, E. García-Verdugo, S. V Luis and J. A. Mayoral, *Org. Lett.*, 2000, **2**, 3905–3908.
- 31 S. D. Pike, A. L. Thompson, A. G. Algarra, D. C. Apperley, S. A. Macgregor and A. S. Weller, *Science (80-.)*, 2012, **337**, 1648–1651.
- 32 T. Kawamichi, T. Haneda, M. Kawano and M. Fujita, *Nature*, 2009, **461**, 633–635.
- 33 L. Vaska, *J. Am. Chem. Soc.*, 1966, **88**, 5325–5327.

- 34 A. R. Siedle and R. A. Newmark, *Organometallics*, 1989, **8**, 1442–1450.
- 35 L. Mond, C. Langer and F. Quincke, *J. Chem. Soc. Trans.*, 1890, **57**, 749–753.
- 36 F. Porta, S. Tollari, C. Bianchi and S. Recchia, *Inorganica Chim. Acta*, 1996, **249**, 79–83.
- 37 C. Bianchini, F. Zanobini, S. Aime, R. Gobetto, R. Psaro and L. Sordelli, *Organometallics*, 1993, **12**, 4757–4763.
- 38 I. R. Laskar, D. Das, G. Mostafa, T.-H. Lu, T.-C. Keng, J.-C. Wang, A. Ghosh and N. R. Chaudhuri, *New J. Chem.*, 2001, **25**, 764–768.
- 39 I. Grenthe and E. Nordin, *Inorg. Chem.*, 1979, **18**, 1869–1874.
- 40 C. Bianchini, M. Peruzzini and F. Zanobini, *Organometallics*, 1991, **10**, 3415–3417.
- 41 S. S. Stahl, *J. Am. Chem. Soc.*, 2010, **132**, 8524–8525.
- 42 A. Boudier, P.-A. R. Breuil, L. Magna, H. Olivier-Bourbigou and P. Braunstein, *Chem. Commun.*, 2014, **50**, 1398–1407.
- 43 O. L. Sydora, *Organometallics*, 2019, **38**, 997–1010.
- 44 O. Catalysts and O. Polymerization, *Organometallic Catalysts and Olefin Polymerization*, 2001.
- 45 Y. Gao, T. J. Emge, K. Krogh-Jespersen and A. S. Goldman, *J. Am. Chem. Soc.*, 2018, **140**, 2260–2264.
- 46 C. Bianchini, M. Graziani, J. Kaspar, A. Meli and F. Vizza, *Organometallics*, 1994, **13**, 1165–1173.
- 47 C. Bianchini, P. Frediani, M. Graziani, J. Kaspar, A. Meli, M. Peruzzini and F. Vizza, *Organometallics*, 1993, **12**, 2886–2887.
- 48 N. J. Coville and L. Cheng, *J. Organomet. Chem.*, 1998, **571**, 149–169.
- 49 T. Yang, M. Kurmoo and M.-H. Zeng, *J. Indian Inst. Sci.*, 2017, **97**, 299–309.
- 50 K. Rissanen, *Chem. Soc. Rev.*, 2017, **46**, 2638–2648.
- 51 Z. Huang, P. S. White and M. Brookhart, *Nature*, 2010, **465**, 598–601.

- 52 T. M. Boyd, B. E. Tegner, G. J. Tizzard, A. J. Martínez-Martínez, S. E. Neale, M. A. Hayward, S. J. Coles, S. A. Macgregor and A. S. Weller, *Angew. Chemie Int. Ed.*, 2020, **59**, 6177–6181.
- 53 F. M. Chadwick, A. I. McKay, A. J. Martinez-Martinez, N. H. Rees, T. Krämer, S. A. Macgregor and A. S. Weller, *Chem. Sci.*, 2017, **8**, 6014–6029.
- 54 A. J. Martínez-Martínez, C. G. Royle, S. K. Furfari, K. Suriye and A. S. Weller, *ACS Catal.*, 2020, **10**, 1984–1992.
- 55 O. V Zenkina, E. C. Keske, R. Wang and C. M. Crudden, *Angew. Chemie Int. Ed.*, 2011, **50**, 8100–8104.
- 56 R. J. Farrauto, eds. J. A. Kent, T. V Bommaraju and S. D. Barnicki, Springer International Publishing, Cham, 2017, pp. 1995–2035.
- 57 B. F. Hoskins and R. Robson, *J. Am. Chem. Soc.*, 1989, **111**, 5962–5964.
- 58 O. M. Yaghi, H. Li, C. Davis, D. Richardson and T. L. Groy, *Acc. Chem. Res.*, 1998, **31**, 474–484.
- 59 S. R. Batten, N. R. Champness, X.-M. Chen, J. Garcia-Martinez, S. Kitagawa, L. Öhrström, M. O’Keeffe, M. Paik Suh and J. Reedijk, *Pure Appl. Chem.*, **85**, 1715–1724.
- 60 *Chemistry of Zeolites and Related Porous Materials: Synthesis and Structure*, 2007, I–XIV.
- 61 H. Marsh and F. Rodríguez-Reinoso, eds. H. Marsh and F. B. T.-A. C. Rodríguez-Reinoso, Elsevier Science Ltd, Oxford, 2006, pp. 13–86.
- 62 H. Li, K. Wang, Y. Sun, C. T. Lollar, J. Li and H.-C. Zhou, *Mater. Today*, 2018, **21**, 108–121.
- 63 J.-R. Li, R. Kuppler and H.-C. Zhou, *Chem. Soc. Rev.*, 2009, **38**, 1477–1504.
- 64 Y. Li and R. T. Yang, *Langmuir*, 2007, **23**, 12937–12944.
- 65 H.-Y. Li, S.-N. Zhao, S.-Q. Zang and J. Li, *Chem. Soc. Rev.*, 2020, **49**, 6364–6401.
- 66 C. Zhu, R. E. Gerald, Y. Chen and J. Huang, *Sensors Actuators B Chem.*, 2020, **321**, 128608.

- 67 Y. A. Mezenov, A. A. Krasilin, V. P. Dzyuba, A. Nominé and V. A. Milichko, *Adv. Sci.*, 2019, **6**, 1900506.
- 68 S. Mendiratta, M. Usman and K.-L. Lu, *Coord. Chem. Rev.*, 2018, **360**, 77–91.
- 69 M. Ranocchiari and J. A. van Bokhoven, *Phys. Chem. Chem. Phys.*, 2011, **13**, 6388–6396.
- 70 D. Li, H.-Q. Xu, L. Jiao and H.-L. Jiang, *EnergyChem*, 2019, **1**, 100005.
- 71 C. Doonan, R. Riccò, K. Liang, D. Bradshaw and P. Falcaro, *Acc. Chem. Res.*, 2017, **50**, 1423–1432.
- 72 M. de J. Velásquez-Hernández, M. Linares-Moreau, E. Astria, F. Carraro, M. Z. Alyami, N. M. Khashab, C. J. Sumby, C. J. Doonan and P. Falcaro, *Coord. Chem. Rev.*, 2020, 213651.
- 73 M. Fujita, Y. J. Kwon, S. Washizu and K. Ogura, *J. Am. Chem. Soc.*, 1994, **116**, 1151–1152.
- 74 D. Yang, M. Babucci, W. H. Casey and B. C. Gates, *ACS Cent. Sci.*, 2020, **6**, 1523–1533.
- 75 P. Valvekens, F. Vermoortele and D. De Vos, *Catal. Sci. Technol.*, 2013, **3**, 1435–1445.
- 76 B. Li, J.-G. Ma and P. Cheng, *Small*, 2019, **15**, 1804849.
- 77 S. Wang, C. M. McGuirk, A. d’Aquino, J. A. Mason and C. A. Mirkin, *Adv. Mater.*, 2018, **30**, 1800202.
- 78 Y.-S. Wei, M. Zhang, R. Zou and Q. Xu, *Chem. Rev.*, 2020, **120**, 12089–12174.
- 79 J. D. Evans, C. J. Sumby and C. J. Doonan, *Chem. Soc. Rev.*, 2014, **43**, 5933–5951.
- 80 M. Kalaj and S. M. Cohen, *ACS Cent. Sci.*, 2020, **6**, 1046–1057.
- 81 A. M. Hamisu, A. Ariffin and A. C. Wibowo, *Inorganica Chim. Acta*, 2020, **511**, 119801.
- 82 M. Lalonde, W. Bury, O. Karagiari, Z. Brown, J. T. Hupp and O. K. Farha, *J. Mater. Chem. A*, 2013, **1**, 5453–5468.
- 83 C. K. Brozek and M. Dincă, *Chem. Soc. Rev.*, 2014, **43**, 5456–5467.
- 84 C. K. Brozek and M. Dincă, *Chem. Sci.*, 2012, **3**, 2110–2113.
- 85 S. Biswas, M. Grzywa, H. P. Nayek, S. Dehnen, I. Senkovska, S. Kaskel and D. Volkmer,

- Dalt. Trans.*, 2009, 6487–6495.
- 86 E. D. Metzger, C. K. Brozek, R. J. Comito and M. Dincă, *ACS Cent. Sci.*, 2016, **2**, 148–153.
- 87 K. Manna, T. Zhang, F. X. Greene and W. Lin, *J. Am. Chem. Soc.*, 2015, **137**, 2665–2673.
- 88 K. Manna, T. Zhang and W. Lin, *J. Am. Chem. Soc.*, 2014, **136**, 6566–6569.
- 89 H. Fei, M. D. Sampson, Y. Lee, C. P. Kubiak and S. M. Cohen, *Inorg. Chem.*, 2015, **54**, 6821–6828.
- 90 X. Yu and S. M. Cohen, *Chem. Commun.*, 2015, **51**, 9880–9883.
- 91 Z. Huang, D. Liu, J. Camacho-Bunquin, G. Zhang, D. Yang, J. M. López-Encarnación, Y. Xu, M. S. Ferrandon, J. Niklas, O. G. Poluektov, J. Jellinek, A. Lei, E. E. Bunel and M. Delferro, *Organometallics*, 2017, **36**, 3921–3930.
- 92 K. Manna, T. Zhang, M. Carboni, C. W. Abney and W. Lin, *J. Am. Chem. Soc.*, 2014, **136**, 13182–13185.
- 93 J. M. Falkowski, T. Sawano, T. Zhang, G. Tsun, Y. Chen, J. V Lockard and W. Lin, *J. Am. Chem. Soc.*, 2014, **136**, 5213–5216.
- 94 X. Zhang, Y. Jiang and H. Fei, *Chem. Commun.*, 2019, **55**, 11928–11931.
- 95 S. G. Dunning, G. Nandra, A. D. Conn, W. Chai, R. E. Sikma, J. S. Lee, P. Kunal, J. E. Reynolds III, J.-S. Chang, A. Steiner, G. Henkelman and S. M. Humphrey, *Angew. Chemie Int. Ed.*, 2018, **57**, 9295–9299.
- 96 M. I. Gonzalez, J. Oktawiec and J. R. Long, *Faraday Discuss.*, 2017, **201**, 351–367.
- 97 M. I. Gonzalez, E. D. Bloch, J. A. Mason, S. J. Teat and J. R. Long, *Inorg. Chem.*, 2015, **54**, 2995–3005.
- 98 M. I. Gonzalez, A. B. Turkiewicz, L. E. Darago, J. Oktawiec, K. Bustillo, F. Grandjean, G. J. Long and J. R. Long, *Nature*, 2020, **577**, 64–68.
- 99 J. M. Becker, J. Barker, G. J. Clarkson, R. van Gorkum, G. K. Johal, R. I. Walton and P. Scott, *Dalt. Trans.*, 2010, **39**, 2309–2326.
- 100 J. Hicks, ed. J. Hicks, Springer Singapore, Singapore, 2017, pp. 131–159.

- 101 C. L. B. Macdonald, B. D. Ellis and A. Swidan, *Encycl. Inorg. Bioinorg. Chem.*, 2012.
- 102 T. Zhang, K. Manna and W. Lin, *J. Am. Chem. Soc.*, 2016, **138**, 3241–3249.
- 103 M. Zille, A. Stolle, A. Wild and U. S. Schubert, *RSC Adv.*, 2014, **4**, 13126–13133.
- 104 A. K. Cook and C. Copéret, *Organometallics*, 2018, **37**, 1342–1345.
- 105 B. Li, Z. Ju, M. Zhou, K. Su and D. Yuan, *Angew. Chemie Int. Ed.*, 2019, **58**, 7687–7691.
- 106 X. Li, R. Van Zeeland, R. V Maligal-Ganesh, Y. Pei, G. Power, L. Stanley and W. Huang, *ACS Catal.*, 2016, **6**, 6324–6328.
- 107 Y. Sun, Q. Du, F. Wang, P. Dramou and H. He, *New J. Chem.*, , DOI:10.1039/D0NJ05029F.
- 108 W.-Y. Gao, M. Chrzanowski and S. Ma, *Chem. Soc. Rev.*, 2014, **43**, 5841–5866.
- 109 X. Zhang, M. C. Wasson, M. Shayan, E. K. Berdichevsky, J. Ricardo-Noordberg, Z. Singh, E. K. Papazyan, A. J. Castro, P. Marino, Z. Ajoyan, Z. Chen, T. Islamoglu, A. J. Howarth, Y. Liu, M. B. Majewski, M. J. Katz, J. E. Mondloch and O. K. Farha, *Coord. Chem. Rev.*, 2020, 213615.
- 110 X. Fang, Q. Shang, Y. Wang, L. Jiao, T. Yao, Y. Li, Q. Zhang, Y. Luo and H.-L. Jiang, *Adv. Mater.*, 2018, **30**, 1705112.
- 111 C. Wang, M. Zheng and W. Lin, *J. Phys. Chem. Lett.*, 2011, **2**, 1701–1709.
- 112 D. Brühwiler, *Nanoscale*, 2010, **2**, 887–892.
- 113 D. E. De Vos, M. Dams, B. F. Sels and P. A. Jacobs, *Chem. Rev.*, 2002, **102**, 3615–3640.
- 114 V. Pascanu, G. González Miera, A. K. Inge and B. Martín-Matute, *J. Am. Chem. Soc.*, 2019, **141**, 7223–7234.
- 115 C. Wang, B. An and W. Lin, *ACS Catal.*, 2019, **9**, 130–146.
- 116 Z. Chen, J. Chen and Y. Li, *Chinese J. Catal.*, 2017, **38**, 1108–1126.
- 117 X. Wang, X. Zhang, R. Pandharkar, J. Lyu, D. Ray, Y. Yang, S. Kato, J. Liu, M. C. Wasson, T. Islamoglu, Z. Li, J. T. Hupp, C. J. Cramer, L. Gagliardi and O. K. Farha, *ACS Catal.*, 2020, **10**, 8995–9005.

- 118 Z. Li, N. M. Schweitzer, A. B. League, V. Bernales, A. W. Peters, A. B. Getsoian, T. C. Wang, J. T. Miller, A. Vjunov, J. L. Fulton, J. A. Lercher, C. J. Cramer, L. Gagliardi, J. T. Hupp and O. K. Farha, *J. Am. Chem. Soc.*, 2016, **138**, 1977–1982.
- 119 V. Bernales, D. Yang, J. Yu, G. Gümüşlu, C. J. Cramer, B. C. Gates and L. Gagliardi, *ACS Appl. Mater. Interfaces*, 2017, **9**, 33511–33520.
- 120 D. Yang, M. R. Momeni, H. Demir, D. R. Pahls, M. Rimoldi, T. C. Wang, O. K. Farha, J. T. Hupp, C. J. Cramer, B. C. Gates and L. Gagliardi, *Faraday Discuss.*, 2017, **201**, 195–206.
- 121 D. Yang, S. O. Odoh, T. C. Wang, O. K. Farha, J. T. Hupp, C. J. Cramer, L. Gagliardi and B. C. Gates, *J. Am. Chem. Soc.*, 2015, **137**, 7391–7396.
- 122 M. Tejada-Serrano, M. Mon, B. Ross, F. Gonell, J. Ferrando-Soria, A. Corma, A. Leyva-Pérez, D. Armentano and E. Pardo, *J. Am. Chem. Soc.*, 2018, **140**, 8827–8832.
- 123 A. Grigoropoulos, A. I. McKay, A. P. Katsoulidis, R. P. Davies, A. Haynes, L. Brammer, J. Xiao, A. S. Weller and M. J. Rosseinsky, *Angew. Chemie - Int. Ed.*, 2018, **57**, 4532–4537.
- 124 G. C. Bond, *Metal-catalysed reactions of hydrocarbons*, 2006, vol. 2006.
- 125 K. Tanabe and W. F. Hölderich, *Appl. Catal. A Gen.*, 1999, **181**, 399–434.
- 126 H. Kanai, S. B. Choe and K. J. Klabunde, *J. Am. Chem. Soc.*, 1986, **108**, 2019–2023.
- 127 M. Orchin, eds. D. D. Eley, H. Pines and P. B. B. T.-A. in C. Weisz, Academic Press, 1966, vol. 16, pp. 1–47.
- 128 K. E. Hicks, A. S. Rosen, Z. H. Syed, R. Q. Snurr, O. K. Farha and J. M. Notestein, *ACS Catal.*, 2020, **10**, 14959–14970.
- 129 D. Sheng, Y. Zhang, Q. Song, G. Xu, D. Peng, H. Hou, R. Xie, D. Shan and P. Liu, *Organometallics*, 2020, **39**, 51–57.
- 130 P. Liu, E. Redekop, X. Gao, W. C. Liu, U. Olsbye and G. A. Somorjai, *J. Am. Chem. Soc.*, 2019, **141**, 11557–11564.
- 131 R. E. Sikma, P. Kunal, S. G. Dunning, J. E. Reynolds, J. S. Lee, J.-S. Chang and S. M. Humphrey, *J. Am. Chem. Soc.*, 2018, **140**, 9806–9809.

- 132 W. M. Bloch, A. Burgun, C. J. Coghlan, R. Lee, M. L. Coote, C. J. Doonan and C. J. Sumbly, *Nat. Chem.*, 2014, **6**, 906–912.
- 133 P. W. N. M. van Leeuwen, *Homog. Catal.*, 2004, 109–124.
- 134 A. Burgun, C. J. Coghlan, D. M. Huang, W. Chen, S. Horike, S. Kitagawa, J. F. Alvino, G. F. Metha, C. J. Sumbly and C. J. Doonan, *Angew. Chemie - Int. Ed.*, 2017, **56**, 8412–8416.
- 135 M. T. Huxley, A. Burgun, H. Ghodrati, C. J. Coghlan, A. Lemieux, N. R. Champness, D. M. Huang, C. J. Doonan and C. J. Sumbly, *J. Am. Chem. Soc.*, 2018, **140**, 6416–6425.
- 136 M. T. Huxley, R. J. Young, W. M. Bloch, N. R. Champness, C. J. Sumbly and C. J. Doonan, *Organometallics*, 2019, **38**, 3412–3418.

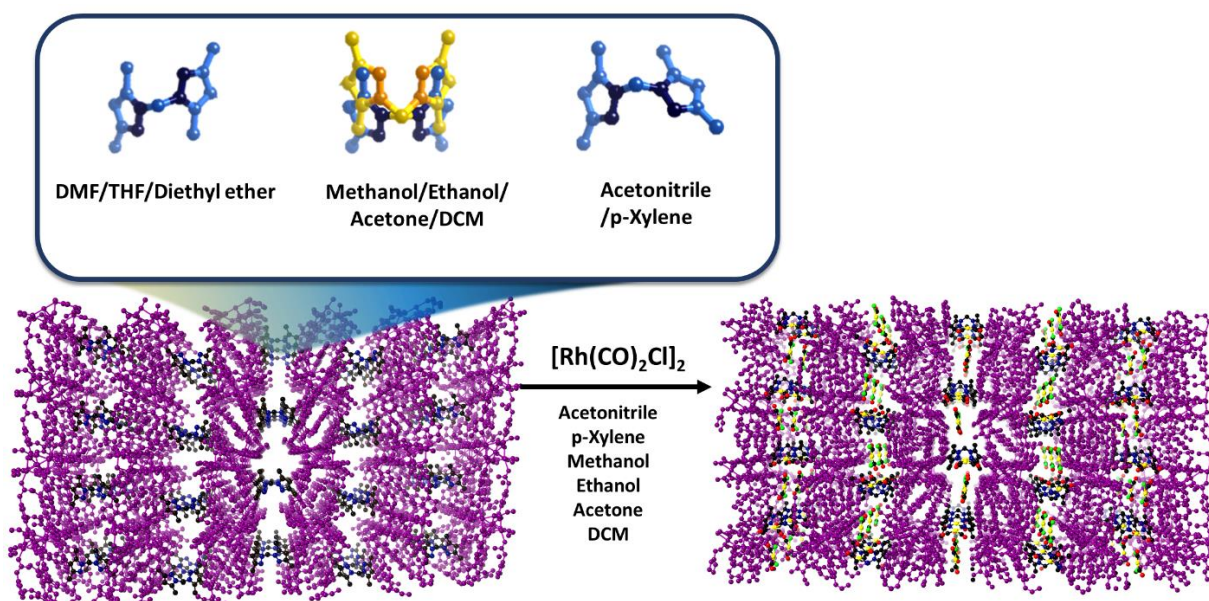
Chapter 2. MOF Matrix Isolation: Cooperative Conformational Mobility Enables Reliable Single Crystal Transformations

Ricardo A. Peralta,^a Michael T. Huxley,^a Rosemary J. Young,^a Oliver M Linder-Patton,^a Jack D. Evans,^b Christian J. Doonan^a and Christopher J. Sumby^{*a}

^a Department of Chemistry and Centre for Advanced Nanomaterials, The University of Adelaide, Adelaide, Australia

^b Department of Inorganic Chemistry, Technische Universität Dresden, Bergstraße 66, 01062 Dresden, Germany


Peralta, R. A., Huxley, M. T., Young, R. J., Linder-Patton, O. M., Evans, J. D., Doonan C. J., Sumby, C. J., MOF Matrix Isolation: Cooperative Conformational Mobility Enables Reliable Single Crystal Transformations, *Faraday Discuss.*, DOI:10.1039/D0FD00012D.



Statement of Authorship

Title of Paper	MOF Matrix Isolation: Cooperative Conformational Mobility Enables Reliable Single Crystal Transformations
Publication Status	<input checked="" type="checkbox"/> Published <input type="checkbox"/> Accepted for Publication <input type="checkbox"/> Submitted for Publication <input type="checkbox"/> Unpublished and Unsubmitted work written in manuscript style
Publication Details	Peralta, R. A., Huxley, M. T., Young, R. J., Linder-Patton, O. M., Evans, J. D., Doonan C. J., Sumbly, C. J., MOF Matrix Isolation: Cooperative Conformational Mobility Enables Reliable Single Crystal Transformations, Faraday Discuss., DOI:10.1039/D0FD00012D.


Principal Author


Name of Principal Author (Candidate)	Ricardo A. Peralta
Contribution to the Paper	Design, development, and subsequent characterization of the samples for this project. Analysis and interpretation of the crystal structures. Preparation of the manuscript.
Overall percentage (%)	70%
Certification:	This paper reports on original research I conducted during the period of my Higher Degree by Research candidature and is not subject to any obligations or contractual agreements with a third party that would constrain its inclusion in this thesis. I am the primary author of this paper.
Signature	 Date 23/2/21

Co-Author Contributions

By signing the Statement of Authorship, each author certifies that:

- i. the candidate's stated contribution to the publication is accurate (as detailed above);
- ii. permission is granted for the candidate to include the publication in the thesis; and
- iii. the sum of all co-author contributions is equal to 100% less the candidate's stated contribution.

Name of Co-Author	Michael T. Huxley
Contribution to the Paper	Assisted with the conception of the project, sample preparation, collection of X-Ray crystallography data and drafting the manuscript.
Signature	 Date 19/03/2021

Name of Co-Author	Rosemary J. Young
Contribution to the Paper	Assisted with sample preparation and collection of X-Ray crystallography data.
Signature	 Date

Chapter 2

Name of Co-Author	Oliver M Linder-Patton		
Contribution to the Paper	Assisted with sample data interpretation and preparation.		
Signature		Date	18/3/21

Name of Co-Author	Jack D. Evans		
Contribution to the Paper	Performed computational work and assisted with the preparation of the manuscript.		
Signature		Date	

Name of Co-Author	Christian J. Doonan		
Contribution to the Paper	Assisted with the conception of the project, analysis of data and preparation of the manuscript.		
Signature		Date	17/3/21

Name of Co-Author	Christopher J. Sumbly		
Contribution to the Paper	Assisted with the conception of the project, analysis of data and preparation of the manuscript.		
Signature		Date	17/3/21

Statement of Authorship

Title of Paper	MOF Matrix Isolation: Cooperative Conformational Mobility Enables Reliable Single Crystal Transformations
Publication Status	<input checked="" type="checkbox"/> Published <input type="checkbox"/> Accepted for Publication <input type="checkbox"/> Submitted for Publication <input type="checkbox"/> Unpublished and Unsubmitted work written in manuscript style
Publication Details	Peralta, R. A., Huxley, M. T., Young, R. J., Linder-Patton, O. M., Evans, J. D., Doonan C. J., Sumby, C. J., MOF Matrix Isolation: Cooperative Conformational Mobility Enables Reliable Single Crystal Transformations, Faraday Discuss., DOI:10.1039/D0FD00012D.


Principal Author

Name of Principal Author (Candidate)	Ricardo A. Peralta
Contribution to the Paper	Design, development, and subsequent characterization of the samples for this project. Analysis and interpretation of the crystal structures. Preparation of the manuscript.
Overall percentage (%)	70%
Certification:	This paper reports on original research I conducted during the period of my Higher Degree by Research candidature and is not subject to any obligations or contractual agreements with a third party that would constrain its inclusion in this thesis. I am the primary author of this paper.
Signature	Date 23/2/21

Co-Author Contributions

By signing the Statement of Authorship, each author certifies that:

- i. the candidate's stated contribution to the publication is accurate (as detailed above);
- ii. permission is granted for the candidate to include the publication in the thesis; and
- iii. the sum of all co-author contributions is equal to 100% less the candidate's stated contribution.

Name of Co-Author	Rosemary J. Young
Contribution to the Paper	Assisted with sample preparation and collection of X-Ray crystallography data.
<input checked="" type="checkbox"/> Recoverable Signature 	Date 11/03/21
Signature Signed by: Rosemary Young	Date 11/03/21

Name of Co-Author	Jack D. Evans
Contribution to the Paper	Performed computational work and assisted with the preparation of the manuscript.

Statement of Authorship

Title of Paper	MOF Matrix Isolation: Cooperative Conformational Mobility Enables Reliable Single Crystal Transformations
Publication Status	<input checked="" type="checkbox"/> Published <input type="checkbox"/> Accepted for Publication <input type="checkbox"/> Submitted for Publication <input type="checkbox"/> Unpublished and Unsubmitted work written in manuscript style
Publication Details	Peralta, R. A., Huxley, M. T., Young, R. J., Linder-Patton, O. M., Evans, J. D., Doonan C. J., Sumbly, C. J., MOF Matrix Isolation: Cooperative Conformational Mobility Enables Reliable Single Crystal Transformations, Faraday Discuss., DOI:10.1039/D0FD00012D.

Principal Author

Name of Principal Author (Candidate)	Ricardo A. Peralta		
Contribution to the Paper	Design, development, and subsequent characterization of the samples for this project. Analysis and interpretation of the crystal structures. Preparation of the manuscript.		
Overall percentage (%)	70%		
Certification:	This paper reports on original research I conducted during the period of my Higher Degree by Research candidature and is not subject to any obligations or contractual agreements with a third party that would constrain its inclusion in this thesis. I am the primary author of this paper.		
Signature		Date	23/2/21

Co-Author Contributions

By signing the Statement of Authorship, each author certifies that:

- i. the candidate's stated contribution to the publication is accurate (as detailed above);
- ii. permission is granted for the candidate to include the publication in the thesis; and
- iii. the sum of all co-author contributions is equal to 100% less the candidate's stated contribution.

Name of Co-Author	Rosemary J. Young		
Contribution to the Paper	Assisted with sample preparation and collection of X-Ray crystallography data.		
Signature		Date	

Name of Co-Author	Jack D. Evans		
Contribution to the Paper	Performed computational work and assisted with the preparation of the manuscript.		
Signature		Date	10/03/2021

2.1 Abstract

Obtaining structural information for highly reactive metal-based species can provide valuable insight into important chemical transformations or catalytic processes. Trapping these metal-based species within the cavities of porous crystalline hosts, such as metal–organic frameworks (MOFs), can stabilize them, allowing detailed structural elucidation by single crystal X-ray diffraction. Previously, we have used a bespoke flexible MOF, $[Mn_3L_2L']$ (MnMOF-1, where L = bis-(4-carboxyphenyl-3,5-dimethylpyrazolyl)methane and L = L', but L' has a vacant *N,N'*-chelation site), which has a chelating site capable of post-synthetically binding metal ions, to study organometallic transformations and fundamental isomerization processes. This manuscript will report the underlying conformational flexibility of the framework, demonstrate the solvent dependency of post-synthetic metalation, and show that the structural flexibility of the linker site and framework are critical to controlling and achieving high levels of metal loading (and therefore site occupancy) during chemical transformations. From these results, a set of design principles for linker-based “matrix isolation” and structure determination in MOFs are derived.

2.2 Introduction

Extracting structural information about reactive metal-based species can provide fundamental insight into small molecule activation processes relevant to homogeneous catalysts¹ or gas separations.^{2,3} However, the species responsible are often coordinatively unsaturated and thereby present challenging characterization targets due to their reactivity and transient lifetimes. Nevertheless, trapping reactive species within the cavities of host supramolecules or frameworks can stabilize them, allowing “matrix isolation” and detailed structural elucidation. Molecular capsules,⁴ supramolecular assemblies^{5,6} and, more recently, metal–organic frameworks (MOFs)^{1,2,7–10} have been used to trap reactive species and facilitate their structure determination. For MOFs, their building block synthetic approach using chemically mutable links, coupled with a high degree of crystallinity, and excellent chemical and thermal stability,¹¹ allows them to trap and isolate metal-centered reactive species.

Examples of MOFs being used to isolate and structurally characterize reactive species include elucidating the structure or dynamics of organic or organometallic species trapped within the pore network of so-called crystalline sponge materials,^{12,13} structurally characterizing

coordinatively unsaturated metal nanoclusters within MOF pores,¹⁴ trapping reactive entities at metal nodes¹⁵ and examining photochemical conversions of metal carbonyl complexes.¹⁶ We have similarly studied the organometallic transformations of a Rh(I) dicarbonyl complex,^{17,18} demonstrated a structural basis for site selective “click” chemistry reactions which take place within the pores of a MOF,¹⁹ and examined fundamental isomerization processes,²⁰ all occurring at post-synthetically added metal sites in a bespoke, flexible Mn-based MOF structure.

With the emergence of a handful of MOF materials that facilitate matrix isolation and single-crystal X-ray diffraction (SCXRD) of reactive metal species at metal linkers,¹⁷⁻²⁴ we can start to identify the structural features that facilitate this behavior. Some of the important aspects appear to include: an overall flexibility of the MOF structure with a number of well-defined structural conformations; chemically robust yet locally adaptable metal binding; relatively low symmetry structures; near quantitative metalation; a high degree of initial crystallinity, and retention of crystallinity throughout a range of post-synthetic chemical transformations to generate the moiety of interest. Furnishing a greater understanding of these design principles may guide the development of new MOFs which can expand this approach to additional reactive species.

This contribution will examine the conformational mobility of the flexible MOF, [Mn₃L₂L'] (**MnMOF-1**, where L = bis-(4-carboxyphenyl-3,5-dimethylpyrazolyl)methane and L = L', but L' has a vacant *N,N'*-chelation site). This material has been used to isolate and study reactive metal complexes *via* SCXRD,¹⁷⁻²⁰ a property we attribute to a large number of accessible structural minima on its conformational energy landscape. **MnMOF-1** has a relatively low symmetry structure, containing spatially isolated metal-binding sites that undergo quantitative post-synthetic metalation (PSMet)²⁵ and subsequent modifications (PSM)²⁶ with retention of single crystallinity. Herein, we report the underlying cooperative flexibility of the framework that is important for PSMet, and suggest that the conformational mobility of the linker site, and the overall framework, are critical to retaining high levels of metal loading and structural order during chemical transformations. These features govern the ability to achieve sequential “snapshots” of the structure *via* SCXRD. To provide some context, these observations for **MnMOF-1** will be contrasted with other materials, specifically the comparatively rigid Zr-based MOF, **UiO-67-bpy** (where bpy = 2,2'-bipyridine-5,5'-

dicarboxylate),^{21–23} to further support the MOF design criteria needed for linker-based matrix isolation and structure determination.

2.3 Results and discussion

2.3.1 MnMOF-1 structure type

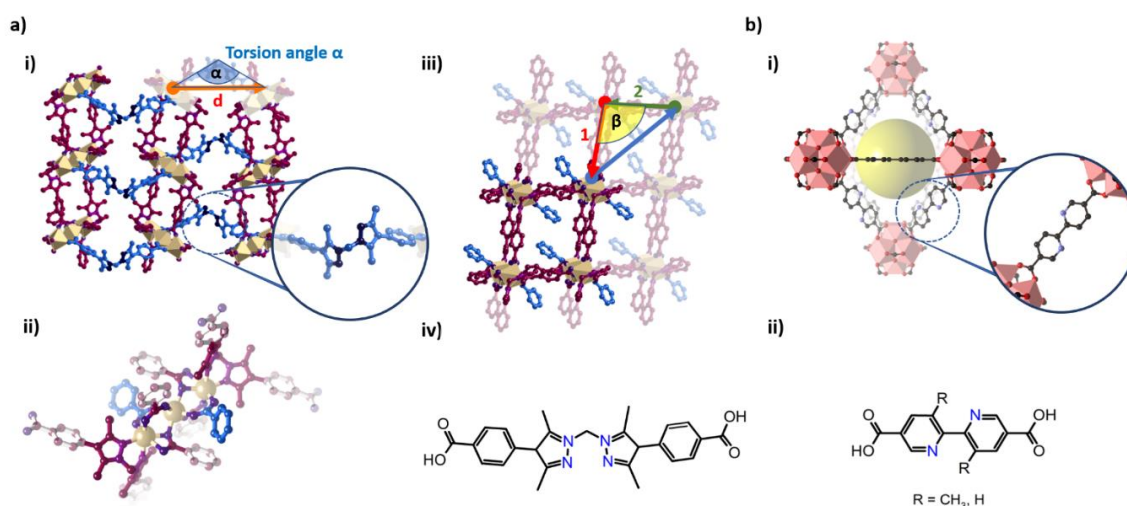


Figure 2.1. (a) (i) The structure of **MnMOF-1-DMF/as** viewed along the a -axis, displaying the open pore structure with pillaring ligands (blue) featuring free N,N -chelation sites. The Mn_3 nodes and fully coordinated linkers (ii) form 2D sheets which lie in the ac plane for **MnMOF-1-DMF/as** (iii). Panel (iv) shows the organic ligand from which **MnMOF-1** is synthesized. (b) (i) The structure of **UiO-67-bpy** features Zr_6O_8 nodes which are bridged by 2,2'-bipyridine-5,5'-dicarboxylate ligands (ii) to form interconnected octahedral cages (and tetrahedral cages – not shown) in which the N,N -chelating site is accessible for PSMet. The annotations to the Figure show the distances and angles used to compare the **MnMOF-1** structures given in Table 2.

The structure of the as-synthesized form of **MnMOF-1** has been previously described¹⁷ but salient features are recorded here to orient the reader (this structure is DMF solvated, Figure 2.1). **MnMOF-1-DMF/as** (as = as-synthesized) has the formula $[Mn_3L_2L']$ and is composed of linear Mn_3 clusters, wherein the three Mn^{2+} centers are bridged by a total of six carboxylate groups from six different ligand molecules (Figure 2.1(a-ii)). The central octahedral Mn^{2+} atom has an octahedral ligand environment bound solely by the carboxylate groups, while the terminal six-coordinate centers are bound by four carboxylate oxygen atoms and are terminated by a chelating bispyrazole moiety. Considering the overall structure, two linkers

Chapter 2

bridge adjacent trinuclear Mn clusters in the crystallographic *ac*-plane (in all monoclinic forms except the desolvated structure) to form a distorted square grid (Figure 2.1(a-iii)). The final linker of **MnMOF-1**, bound through its carboxylate groups only, pillars these layers at each Mn₃ cluster to form a three-dimensional framework. The structure of the desolvated material, **MnMOF-1-des**, which is still porous to N₂, contracts considerably through twisting and bending about the methylene hinge of the pillaring ligand and distortion of the square grid (Tables 2.1 and 2.2).¹⁷

Table 2.1. Space group, unit cell parameters and orientation of the distorted square grid in the various solvates of **MnMOF-1**.

Solvate	Space group	a (Å)	b (Å)	c (Å)	α (°)	β (°)	γ (°)	Volume (Å ³)	Orientation of square grid	Reference
DMF (as synthesized)	<i>P2₁/c</i>	12.289(3)	32.302(7)	25.974(5)	90	93.57(3)	90	10291(4)	<i>ac</i>	12
desolvated	<i>C2/c</i>	16.9293(10)	18.4694(7)	28.346(2)	90	100.629(6)	90	8711.0(9)	<i>ab</i>	12
CH₃CN	<i>P-1</i>	12.281(3)	12.919(3)	30.425(6)	94.65(3)	93.93(3)	92.40(3)	4794.5(19)	<i>ab</i>	22
MeOH	<i>P2₁/m</i>	12.323(3)	32.145(6)	12.931(3)	90	93.58(3)	90	5112.3(18)	<i>ac</i>	This work
EtOH	<i>P2₁/m</i>	12.274(3)	32.826(7)	12.930(3)	90	95.51(3)	90	5185.5(18)	<i>ac</i>	This work
acetone	<i>P2₁/m</i>	12.307(3)	31.637(6)	13.006(3)	90	92.10(3)	90	5060.6(18)	<i>ac</i>	This work
DCM	<i>P2₁/m</i>	12.313(3)	31.877(6)	12.954(3)	90	92.93(3)	90	5077.8(18)	<i>ac</i>	This work
THF	<i>P-1</i>	12.457(3)	13.242(3)	33.037(7)	86.69(3)	86.08(3)	85.22(3)	5411(2)	<i>ab</i>	This work
DEE	<i>P-1</i>	12.364(3)	12.947(3)	30.366(6)	99.40(3)	97.35(3)	91.57(3)	4750.4(17)	<i>ab</i>	This work
<i>p</i>-xylene	<i>P-1</i>	12.276(3)	12.869(3)	31.586(6)	93.98(3)	97.43(3)	92.02(3)	4931.1(18)	<i>ab</i>	This work

Table 2.2. Structural parameters for the various solvates of **MnMOF-1**.

Solvate	ε	d (pillar COO-COO distance, Å)	α (pillar COO-CH ₂ -COO angle, °)	Mn-Mn distance 1 (Å)	Mn-Mn distance 2 (Å)	Mn-Mn diagonal (Å)	β (obtuse angle, °)	Pyrazole ring torsion angle (°)	Volume per repeat unit ^a
DMF (as synthesized)	38.25	14.66	105.1	12.99	12.28	18.26	109.7	157.2	118%
desolvated	-	13.83	97.7	12.53	12.53	18.47	95.5	155.6	-
CH₃CN	37.5	14.04	99.0	12.92	12.29	18.19	98.3	13.6	110%
MeOH	32.7	14.81	106.4	12.93	12.32	17.29	107.7	-	117%
EtOH	24.5	15.18	110.4	12.93	12.27	16.95	111.0	-	119%
acetone	21.01	14.51	103.4	13.01	12.31	18.23	105.5	-	116%
DCM	9.08	14.61	104.6	12.95	12.31	18.32	106.6	-	116%
THF	7.52	15.08	108.3	13.24	12.45	18.92	109.3	168.8	124%
DEE	4.27	14.07	100.5	12.94	12.36	17.65	100.0	171.5	109%
<i>p</i>-xylene	2.27	14.70	106.5	12.87	12.28	18.10	98.5	26.0	113%

^a These values are calculated as a percentage of the desolvated structure, which we believe to be fully contracted. For **MnMOF-1-des** the repeat unit volume is 2177.8 Å³ (which is calculated by dividing the volume by Z).

The salient feature of **MnMOF-1** that allows post-synthetic metalation (PSMet) is the free bispyrazole moiety of the pillaring link. In the as-synthesized form of **MnMOF-1-DMF/as**, this bispyrazole moiety adopts an *anti* conformation with the plane of the pyrazole groups twisted by 157.2° (the torsion angle between the N–N bonds of the pyrazole rings, Table 2.2).

Metalation of **MnMOF-1-DMF/as** does not favorably occur in DMF,²⁷ which is presumably partly attributable to the *anti* arrangement of the pyrazole donors.¹⁷ However, as we have shown, PSMet of **MnMOF-1** is facile for most transition metals when those reactions are conducted in solvents such as acetonitrile (CH₃CN), ethanol (EtOH) and methanol (MeOH).^{18-20,27-29}

2.3.2 Solvatomorphs of MnMOF-1

The structure of **MnMOF-1** solvated with CH₃CN (**MnMOF-1-CH₃CN**) has been disclosed²⁷ but not previously discussed, and clearly explains why PSMet is facile in this solvent. The two pyrazole rings are in a *syn* conformation, with the torsion angle between the N–N bonds of the pyrazole rings being 13.6°, placing them in an ideal arrangement to coordinate to an incoming metal species. This change does not occur in isolation, with the pillaring link bending to bring the layers closer together (Table 2.2). Additional changes occur to the square grid, which becomes less laterally skewed. Coincidentally, some of these distortions are quite similar to those observed for the desolvated structure, as is the overall contraction of the MOF (Table 2.2).

Methanol and ethanol are also good solvents in which to effect PSMet.^{19,29} Direct solvent exchange of **MnMOF-1-DMF/as** with either methanol or ethanol provides a facile conversion to new solvatomorphs, with both new conformations of **MnMOF-1** crystallizing in the monoclinic space group $P2_1/n$ (Figure 2.2). Close inspection of the structures reveals that subtle increases in the separation of the square grids have occurred (Table 2.2), denoted by changes in the pillar link distance and angle. There are also further distortions of the square grid itself but the structures are not vastly different to the as-synthesized form. These changes result in the pillaring link being disordered in both structures and thus the conformation (*syn* or *anti*) cannot be determined. However, given that facile metalation occurs in these solvents we postulate that this might be the disordered *syn* conformation, although we cannot rule out that the more open MOF structure (albeit similar to **MnMOF-1-DMF/as**) allows interconversion of the *anti* and *syn* forms.

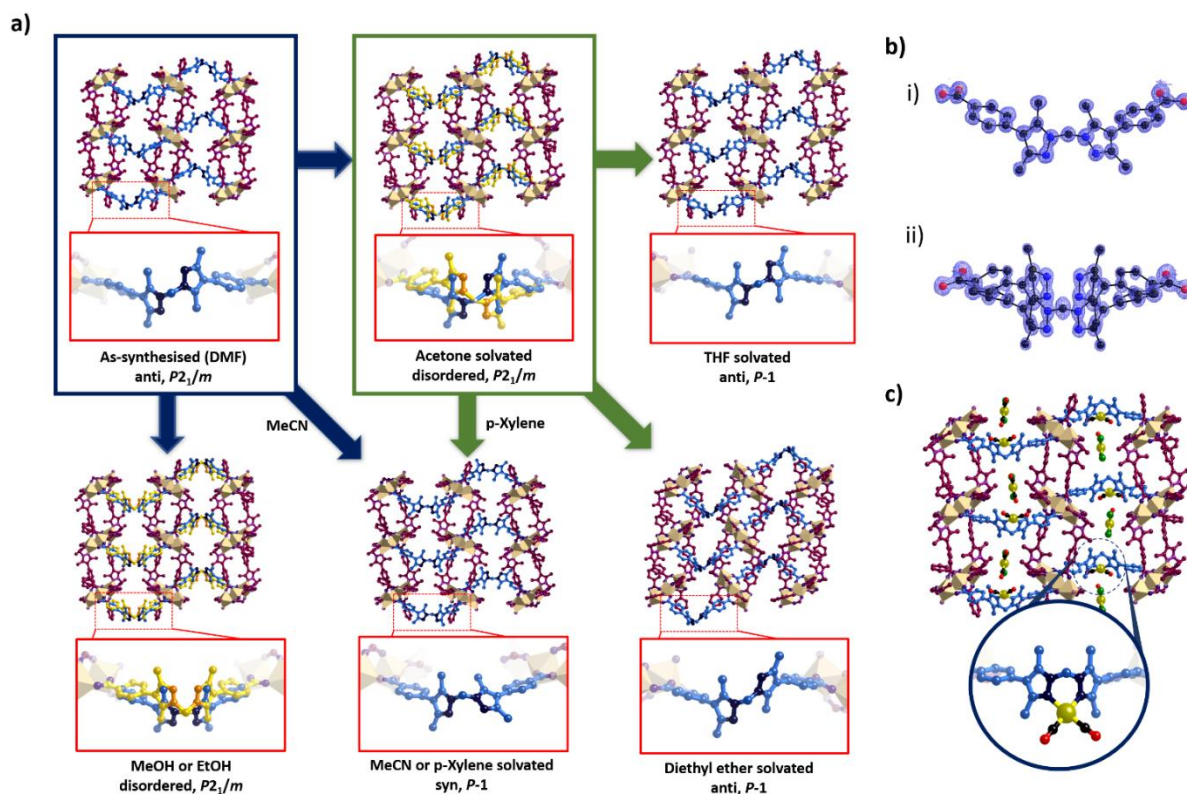


Figure 2.2. (a) Representative examples of the effects of solvation on the conformation of the free pyrazole sites in **MnMOF-1**, including ordered ‘*anti*’ (DMF, THF, diethyl ether), ordered ‘*syn*’ (MeCN, *p*-xylene) and disordered structures (MeOH, EtOH, acetone). (b) Electron density maps support the structures presented in (a), and representative electron density maps are displayed for acetone (i) and *p*-xylene (ii). Post-synthetic metalation of the free pyrazole site with $[\text{Rh}(\text{CO})_2\text{Cl}]_2$ is possible when the metalation reaction is performed in acetonitrile or *p*-xylene, yielding the metalated MOF **MnMOF-1**· $[\text{Rh}(\text{CO})_2][\text{Rh}(\text{CO})_2\text{Cl}_2]$ as confirmed *via* SCXRD (c) (the product formed in *p*-xylene is shown but it is simply a solvatomorph of **MnMOF-1**· $[\text{Rh}(\text{CO})_2][\text{Rh}(\text{CO})_2\text{Cl}_2]$ formed in acetonitrile).¹⁷

While the three solvents (CH_3CN , MeOH and EtOH; dielectric constants, ϵ 37.5, 32.7 and 24.5, respectively) allow post-synthetic metalation with a wide selection of metal complexes, we wanted to be able to undertake chemistry in less polar solvents and in solvents that can be rigorously dried. However, direct solvent exchange of **MnMOF-1-DMF/as** with tetrahydrofuran (THF, $\epsilon = 7.52$), diethyl ether (DEE, $\epsilon = 4.27$), dichloromethane (DCM, $\epsilon = 9.08$), the individual xylene isomers (*ortho*, $\epsilon = 2.57$; *meta*, $\epsilon = 2.37$; and *para*, $\epsilon = 2.27$), and toluene (Tol, $\epsilon = 2.38$) led to loss of single crystallinity. Given the noticeably different dielectric constants for these solvents and DMF ($\epsilon = 38.25$), this prompted us to investigate other solvents. Specifically, we sought a solvent with a dielectric constant midway between the two extremes, which would perhaps provide access to an intermediate **MnMOF-1** structure that

could be then converted to the desired solvates without loss of crystallinity. This type of approach has been used for activation of MOFs³⁰ and porous organic cages.³¹ Acetone ($\epsilon = 21.01$) is miscible with all the solvents considered and thus seemed an ideal choice. Pleasingly, exchanging **MnMOF-1-DMF/as** with acetone to form the intermediate **MnMOF-1-ace** (ace = acetone), followed by exposure to THF, DEE, DCM, and *p*-xylene gave access to new solvatomorphs *via* single crystal-to-single crystal (SC–SC) transformations. Complete exchange of the solvates was confirmed by conducting ¹H NMR spectroscopy on digested samples of the MOF. Curiously, this route was not effective for toluene and *m*-xylene (*o*-xylene retained crystallinity but we could not collect satisfactory structural data).

To understand how the stepwise nature of these transformations might facilitate retention of crystallinity, we collected SCXRD structures for **MnMOF-1** solvated with acetone and THF, DEE, DCM, and *p*-xylene. The structure of **MnMOF-1-ace** is not dissimilar to the as-synthesized structure and the alcohol solvated forms (Tables 2.1 and 2.2). In particular the volume of the repeat unit of the structure almost matches these other forms, and the relevant structural parameters (unit cell axes and angles, layer structure and pillaring ligand geometry) are similar. Again, the bispyrazole chelating unit is disordered but it is interesting to note that PSMet is facile in this solvent (see below); this suggests that the *syn* conformation might be present. Intriguingly, despite being unable to be prepared directly from **MnMOF-1-DMF/as**, **MnMOF-1-DCM** is isomorphous with **MnMOF-1-ace** (Tables 2.1 and 2.2). Given the lack of structural differences, this suggests that local solvate–framework interactions might be responsible for the loss in crystallinity here, rather than changes in the overall structure.

Considering the other solvates, **MnMOF-1-THF** crystallizes in the triclinic space group $P\bar{1}$ with a notably expanded volume with respect to all other structures. This is driven by layer–layer expansion as evidenced by the parameters for the pillaring ligand and the *c*-axis length (compared directly with **MnMOF-1-CH₃CN** or the *b*-axis for the DMF, MeOH, EtOH and acetone solvates). Intriguingly, despite being observed in a solvent with a similar polarity to THF, the structure of **MnMOF-1-DEE** is almost identical to the structure of **MnMOF-1-CH₃CN**, albeit possessing an *anti* arrangement of the pyrazole donors. Finally, we determined the structure of **MnMOF-1-*p*-xylene**. Notably, **MnMOF-1-*p*-xylene** has a *syn* arrangement of the pyrazole donors, like **MnMOF-1-CH₃CN**, which bodes well for post-synthetic metalation. Given this similarity, **MnMOF-1-*p*-xylene** and **MnMOF-1-CH₃CN** possess quite similar structures,

although the separations between the square grids are different; the layers in **MnMOF-1-CH₃CN** are moderately closer together.

2.3.3 Post-synthetic metalation of **MnMOF-1** with [Rh(CO)₂Cl]₂

As noted, our exploration of the various solvatomorphs of **MnMOF-1** was motivated by the need to expand the solvents available for metalation. Prior to this work, all metalations of **MnMOF-1** were conducted in relatively polar solvents, acetonitrile, methanol and ethanol. With the new solvatomorphs of **MnMOF-1** in hand, the acetone, THF, DCM, diethyl ether and *p*-xylene solvates, we assessed their ability to undergo PSMet. We had previously shown that treatment of **MnMOF-1-CH₃CN** with the Rh dimer [Rh(CO)₂Cl]₂ quantitatively gives **MnMOF-1**·[Rh(CO)₂][RhCl₂(CO)₂], which possesses a square planar Rh(I)(CO)₂ moiety complexed to the bispyrazole site in the MOF and a [RhCl₂(CO)₂] anion in the MOF pore.¹⁷ Given the well-ordered nature of the structure and the useful spectroscopic handle provided by the CO ligands, we investigated the same post-synthetic metalation in other solvents.

MnMOF-1-*p*-xylene, **MnMOF-1-ace**, **MnMOF-1-DCM**, **MnMOF-1-THF** and **MnMOF-1-DEE** were subjected to metalation with [Rh(CO)₂Cl]₂. The first three solvents gave rise to pale yellow MOF crystals, and furthermore IR spectroscopy revealed the distinctive CO stretches¹⁷ that support the formation of **MnMOF-1**·[Rh(CO)₂][Rh(CO)₂Cl₂] (see Figure 7.1.2). However, when metalation was performed with **MnMOF-1-THF** and **MnMOF-1-DEE** solvates, no CO stretches were observed in the IR spectra and the samples did not adopt the pale yellow color of the Rh(I) species; this clearly indicated that metalation does not occur in THF or diethyl ether, likely due to the *anti* conformation of the pyrazole sites. These results were corroborated using energy dispersive X-ray (EDX) data which confirmed the presence of Rh in a 2 : 3 Rh : Mn ratio for samples metalated in *p*-xylene, acetone and DCM, while no appreciable Rh signal was observed for samples metalated in THF or diethyl ether (Table 7.1.6). We hypothesize that the metalation was unsuccessful in THF and diethyl ether because of the *anti* arrangement of the free pyrazole sites within the MOF.

SCXRD was undertaken to determine the structure of **MnMOF-1**·[Rh(CO)₂][RhCl₂(CO)₂] formed in *p*-xylene. This showed the expected square planar arrangement of the Rh(I)(CO)₂ moiety coordinated to the pyrazole units (Rh–N bond lengths 2.060(7) and 2.094(7);

Rh–C 1.860(13) and 1.906(12) Å). One Cl atom of the [RhCl₂(CO)₂] anion (Rh–Cl bond lengths 2.358(3) and 2.321(3); Rh–C 1.753(16) and 1.827(16) Å) is located 3.73 Å from the vacant axial site of the coordinated Rh center, and the anion also interacts with the MOF *via* weak C–H···Cl hydrogen bonds. Despite the pre-metalation ordering of the *p*-xylene structure into the *syn* conformer, it is worth noting that during metalation the pyrazole donors undergo a further twisting motion relative to the MOF backbone, which is clearly visible when the *syn* and metalated structures are compared (Fig. 2). Prior to metalation, in the *syn* structure, the pyrazole sites are slightly splayed out with a separation (N–N) of 2.93 Å. In order to chelate the incoming metal center, the ligand pivots about the methylene hinge, drawing the N-donor sites inwards (N–N separation of 2.80 Å). This is also associated with an inversion of the bispyrazole moiety, as observed when the relative arrangements of the pyrazole sites in the ‘*syn*’ and metalated structures are compared (Figure 2.2). Like the non-metallated **MnMOF-1-*p*-xylene** structure, well-ordered *p*-xylene solvate molecules are also located in the pores. With the exception of the solvent ordering, these structural parameters are very similar to **MnMOF-1**·[Rh(CO)₂][RhCl₂(CO)₂] formed in acetonitrile.¹⁷

2.3.4 Structure analysis

Overall, **MnMOF-1** appears to have a conformational landscape punctuated with a number of distinct structural minima. Disregarding the conformation of the pyrazole donors (these are definitely in the *syn* arrangement for the acetonitrile and *p*-xylene solvates), there are five main structure types: namely (1) the as-synthesized form (*P*₂₁/*c* and the *P*₂₁/*m* solvatomorphs); (2) the *syn* conformers (*P*₁[–], acetonitrile and *p*-xylene solvates); (3) **MnMOF-1-THF** (*P*₁[–], expanded, *anti*); (4) **MnMOF-1-DEE** (*P*₁[–], contracted, *anti*); and (5) the desolvated form (*C*₂/*c*, *anti*). This complex structural behavior has been observed for other flexible MOFs, including recent reports on amino acid-derived MOFs,^{32,33} which convert between a number of conformers in a facile manner. Within form (1) there seems to be little preference for a *syn/anti* conformation of the pyrazole groups, but metalation experiments do suggest that *syn* is favored or accessible in methanol, ethanol, acetone and dichloromethane. Similarly, for the *P*₁[–] structures (types (2–4)) there is much greater variation in the structure yet no particular pattern in terms of the conformation of the pyrazole groups;

both *syn* and *anti* arrangements are observed. Again however, outcomes of the PSMet do suggest that the *syn* or *anti* arrangements of the pyrazole rings are fixed.

Surveying the literature, two MOFs appear to be able to reliably undergo quantitative metalation in a SC–SC manner and allow SCXRD to be used to characterize the ligand tethered metal center: these are **MnMOF-1**,^{17–20,27–29} and **UiO-67-bpy**,^{21–23} although the former does this in a wider number of instances. As far as we are aware, there is only one instance for **UiO-67-bpy** where sequential SC–SC transformations of a metalated structure can allow SCXRD.²³ Given the high degree of conformational freedom observed for the pyrazole linker (Me₄bcppm) in the **MnMOF-1** solvatomorphs, we set out to probe this further by computational studies. To provide a suitable comparison, we compared the flexibility of the **MnMOF-1** link to a methyl substituted version of 2,2'-bipyridine, namely 6,6'-dimethyl-2,2'-bipyridine-5,5'-dicarboxylic acid (Me₂bpy).³⁴ For simplicity, the ligands were considered as their corresponding acids (and not part of the MOF structure), and their different conformers were investigated using the semiempirical tight-binding based quantum chemistry method GFN2-xTB.³⁵ The conformational space of these ligands was first explored by employing the conformer–rotamer ensemble sampling tool (CREST).³⁶ This methodology uses extensive meta-dynamics sampling, genetic z-matrix crossing and geometry optimizations, designed to efficiently identify low lying and unique conformers. The conformer analysis identifies, as expected, that both ligands have two distinct conformations with respect to the *syn* or *anti* configuration of the chelating nitrogen atoms (Figure 2.3a); the unsubstituted 2,2'-bipyridine-5,5'-dicarboxylate is known to favor the *anti* conformation due to the release of steric clash between the H3 protons. Interestingly, the relative energies between these conformers for the different ligands are about the same but there are more unique conformations of the *syn*-like arrangement for Me₄bcppm (in **MnMOF-1**). This might point to **MnMOF-1** being able to bind a greater diversity of metal ions (atomic radii, bond lengths and coordination numbers) than **UiO-67-bpy** materials.

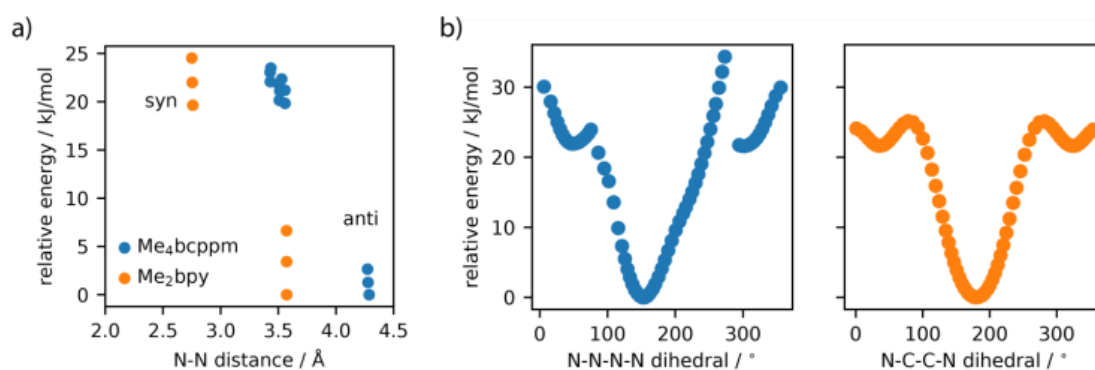


Figure 2.3. Relative energies of the conformers identified by CREST for Me₄bcppm (from **MnMOF-1**) and Me₂bpy (the link in **UiO-67-Me₂bpy**) displayed with respect to the N–N distance (a). The potential energy landscapes for Me₄bcppm and Me₂bpy generated by scanning the N–N–N–N dihedral for Me₄bcppm and the N–C–C–N dihedral for Me₂bpy (b).

To provide insight into the conversion between these conformers, we further investigated the potential energy landscape by constrained structural optimizations, scanning the N–N–N–N dihedral for Me₄bcppm and the N–C–C–N dihedral for Me₂bpy (Figure 2.3b). For **MnMOF-1** and **UiO-67**, the energy barrier for the ligand *anti* → *syn* conversion is approximately 25 kJ mol⁻¹; however, because of the methylene hinge and the bent structure of Me₄bcppm, this only occurs for one direction of rotation. For Me₄bcppm, rotation in the other direction has a barrier greater than 34 kJ mol⁻¹. In the case of Me₂bpy, the barrier and the higher energy of the *syn* conformation represent the loss of conjugation between the orthogonal pyridine groups and the steric hindrance that arises between H3 protons in the *syn* conformer, respectively. For Me₄bcppm, passage of the 3- or 5-methyl substituent past the pyrazole N donor is presumably a barrier to conversion between the two conformers.

These calculations provide insight into PSMet and structure determination in both materials. There is clearly a barrier to converting the conformers from *anti* to *syn* in both cases, which is required for PSMet. For **MnMOF-1**, it has been shown that this conversion can be achieved by manipulating the solvent such that metalation can occur without this barrier. However, for **UiO-67-bpy** derivatives, the favorable C–H⋯N interactions in the *anti* conformation and the stabilization achieved by conjugation likely limit access to the *syn* conformation until metalation occurs (although there is only one non-metalated structure of **UiO-67-bpy** reported).²¹ Additionally, the lack of flexibility afforded by the bpy ligands disfavors changes to the overall structure of the framework, and there is likely a larger energy barrier to long range structural change for **UiO-67** than for **MnMOF-1** (outside of simple ligand

rotation). However, in the present work we have not considered constraints, or stabilizing effects, imposed by the framework structures of **UiO-67-bpy** and **MnMOF-1**.

Another point of distinction between the two systems is the symmetry. **UiO-67-bpy** crystallizes in the F-centered cubic space group $Fm\bar{3}m$ which lowers to a primitive setting ($Pa\bar{3}$) upon metalation.²¹ While the symmetry of the structure is lowered upon metalation, these higher symmetry space groups provide more opportunity for disorder of the site (more ligands per node at crystallographically related locations), even before the co-ligands are placed about the metal center. In comparison, the lower symmetry of **MnMOF-1** provides a crystallographically distinct site in the framework for metalation, which does not suffer from disorder to the extent observed for **UiO-67-bpy**.

Thus, as noted at the outset, some of the important structural features that provide for facile matrix isolation and SC–SC transformations include: the overall flexibility of the MOF structure, chemically robust yet locally adaptable metal binding and low symmetry structures. Near quantitative metalation is obviously necessary, as noted by Fujita for guests in his crystalline sponge materials.^{7–9} Indeed, some of these design principles were exemplified in the MOF reported by Li and Zhou *et al.*,²⁴ which is capable of matrix isolation and structure determination of metal clusters. The authors showed that *N,N*-chelating sites could be generated in a MOF by rotational flexibility of the monodentate triazole moieties of the linker, thereby allowing PSMet and structural characterization of the Ni clusters *via* X-ray crystallography. Thus, while the design of such MOF materials is non-trivial, consideration of structures against these criteria might allow SCXRD to be applied more widely to the structure characterization of reactive metal-based species matrix isolated in MOFs.

2.4 Conclusions

Herein we have clearly demonstrated that the high degree of conformational mobility – structural flexibility – of **MnMOF-1** underpins its ability to undergo post-synthetic metalation and subsequent chemical transformations with retention of crystallinity. This allows the material to “matrix isolate” metal-based species and provide structural insights into reactivity. **MnMOF-1** has both a level of local flexibility around the metal coordinating site and conformational flexibility in the framework itself, which allows it to adapt to and/or facilitate structural changes. Notwithstanding the *syn versus anti* arrangement of the chelating site

there are a number of contracted and open states of the MOF structure, giving a conformational landscape characterized by multiple accessible minima.

Solvents can be used to control post-synthetic metalation of **MnMOF-1** and access these conformers. While there are forms of **MnMOF-1** with pre-organized *syn* donors that can be accessed directly from the as-synthesized (DMF solvated) form, we found that stepwise solvent exchanges were necessary to access competent metal binding forms in low polarity solvents. Direct exchange of **MnMOF-1-DMF/as** with low polarity solvents (DCM, diethyl ether, THF and *p*-xylene) led to loss of single crystallinity, whereas acetone could act as an intermediate solvate. Structure determination of the various solvatomorphs identified forms pre-organized for post-synthetic metalation (with a *syn* arrangement), and treatment with $[\text{Rh}(\text{CO})_2\text{Cl}]_2$ demonstrated that only these species underwent facile post-synthetic metalation. Identification of the *anti* conformation in **MnMOF-1-THF** and **MnMOF-1-DEE** suggests an opportunity to bind one or more metals that prefer a digonal geometry per site. In summary, we hope these observations allow researchers to make more widespread use of this “matrix isolation” strategy, in particular to identify other MOFs capable of this and hence to expand this approach to other reactive metal-based species.

2.5 Experimental

2.5.1 General experimental

Unless otherwise stated, all chemicals were obtained from commercial sources and used as received. Solvents were dried using literature procedures and degassed with Ar prior to use. Specifically, CH_3CN and DCM were distilled over CaH_2 under N_2 ; acetone was distilled over CaSO_4 under N_2 ; THF, diethyl ether and *p*-xylene were distilled from Na/benzophenone. The ligand bis-(4-carboxyphenyl-3,5-dimethylpyrazolyl) and **MnMOF-1** were synthesized as previously reported.¹⁷ $[\text{Rh}(\text{CO})_2\text{Cl}]_2$ was obtained from commercial vendors and used without purification.

Powder X-ray diffraction data were collected on a Bruker Advanced D8 diffractometer (capillary stage) using Cu $\text{K}\alpha$ radiation ($\lambda = 1.54056 \text{ \AA}$, 40 kW/40 mA, $2\theta = 2\text{--}52.94^\circ$, phi rotation = 20 rotations per min at 1 s exposure per step, with 5001 steps using 0.5 mm glass capillaries). NMR spectra were recorded on a Varian 500 MHz spectrometer at 23 °C using a 5 mm probe. **MnMOF-1** samples (*ca.* 5 mg) were digested in $\text{DCl}/d_6\text{-DMSO}$ (2 drops of $\text{DCl}/600$

$\mu\text{L } d_6\text{-DMSO}$) at room temperature prior to NMR analysis. Infrared (IR) spectra were collected on a PerkinElmer Spectrum 100 using a UATR sampling accessory, or on a PerkinElmer Spectrum Two, with the sample dispersed between two NaCl disks in Nujol. Energy-dispersive X-ray spectroscopy (EDX) was performed on a Philips XL30 field emission scanning electron microscope.

2.5.2 Solvent exchange of MnMOF-1

Single crystals of **MnMOF-1** were washed in DMF (5×3 ml) and transferred to a 4 ml glass vial. The DMF was replaced by acetone (5×3 ml), allowing the crystals to soak in the new solvent for 10 minutes between each exchange. The same process was performed for exchanges from DMF to MeCN, MeOH and EtOH. Solvent exchange from acetone to THF, DCM, DEE and *p*-xylene was performed similarly. **MnMOF-1** crystals in acetone were washed with 3 ml of fresh solvent (DCM, diethyl ether, THF or *p*-xylene) at intervals of 10 minutes a total of 5 times.

2.5.3 Post-synthetic metalation of MnMOF-1 with $[\text{Rh}(\text{CO})_2\text{Cl}]_2$

2.5.3.1 From **MnMOF-1-THF**

An excess of $[\text{Rh}(\text{CO})_2\text{Cl}]_2$ was added to a 4 ml vial containing **MnMOF-1** crystals (30 mg) in THF (3 ml) under an Ar atmosphere. The vial was sealed under Ar and allowed to stand at room temperature overnight. The resulting yellow solution was replaced with fresh THF (5×3 ml) under Ar. The isolated crystals were pale yellow/colorless, suggesting that only non-metalated MOF was isolated. IR ν_{max} (cm^{-1} , Nujol): 1613 (m, CO), 1552 (m, C=C), 1509 (m, C=C), 1409 (s), 1305 (s).

2.5.3.2 From **MnMOF-1-DEE**

An excess of $[\text{Rh}(\text{CO})_2\text{Cl}]_2$ was added to a 4 ml vial containing **MnMOF-1** crystals (30 mg) in diethyl ether (3 ml) under an Ar atmosphere. The vial was sealed under Ar and allowed to

stand at room temperature overnight. The resulting yellow solution was replaced with fresh diethyl ether (5 × 3 ml) under Ar. The crystals were pale yellow/colorless, suggesting that only non-metalated MOF was isolated. IR ν_{\max} (cm⁻¹, Nujol): 1611 (m, CO), 1555 (m, C=C), 1512 (m, C=C), 1409 (s), 1304 (s).

2.5.3.3 From **MnMOF-1-ace**

An excess of [Rh(CO)₂Cl]₂ was added to a 4 ml vial containing **MnMOF-1** crystals (30 mg) in acetone (3 ml) under an Ar atmosphere. The vial was sealed under Ar and allowed to stand at room temperature overnight. The resulting yellow solution was replaced with fresh acetone (5 × 3 ml) under Ar, yielding **MnMOF-1**·[Rh(CO)₂][Rh(CO)₂Cl₂] as pale yellow crystals. IR ν_{\max} (cm⁻¹, Nujol): 2103 (m, CO), 2074 (m, CO), 2046 (m, CO), 2036 (m, CO), 1999 (m, CO), 1713 (s, CO), 1611 (m, CO), 1555 (m, C=C), 1512 (m, C=C), 1409 (s), 1304 (s).

2.5.3.4 From **MnMOF-1-DCM**

An excess of [Rh(CO)₂Cl]₂ was added to a 4 ml vial containing **MnMOF-1** crystals (30 mg) in dichloromethane (3 ml) under an Ar atmosphere. The vial was sealed under Ar and allowed to stand at room temperature overnight. The resulting yellow solution was replaced with fresh dichloromethane (5 × 3 ml) under Ar, yielding **MnMOF-1**·[Rh(CO)₂][Rh(CO)₂Cl₂] as pale yellow crystals. IR ν_{\max} (cm⁻¹, Nujol): 2101 (m, CO), 2074 (m, CO), 2044 (m, CO), 2033 (m, CO), 1996 (m, CO), 1613 (m, CO), 1556 (m, C=C), 1512 (m, C=C), 1416 (s), 1304 (s).

2.5.3.5 From **MnMOF-1-p-xylene**

An excess of [Rh(CO)₂Cl]₂ was added to a 4 ml vial containing **MnMOF-1** crystals (30 mg) in *p*-xylene (3 ml) under an Ar atmosphere. The vial was sealed under Ar and allowed to stand at room temperature overnight. The resulting yellow solution was replaced with fresh *p*-xylene (5 × 3 ml) under Ar, yielding **MnMOF-1**·[Rh(CO)₂][Rh(CO)₂Cl₂] as pale yellow crystals. IR ν_{\max} (cm⁻¹, Nujol): 2105 (m, CO), 2076 (m, CO), 2045 (m, CO), 2033 (m, CO), 2000 (m, CO), 1610 (m, CO), 1556 (m, C=C), 1516 (m, C=C), 1407 (s), 1303 (s).

2.5.4 Single crystal X-ray diffraction (SCXRD)

Single crystals were mounted in Paratone-N oil or in Fomblin oil on a MiTeGen MicroMount. Single crystal data for the samples were collected at 100 K on the MX1 or MX2 beamline at the Australian Synchrotron using the Blue-ice software interface.³⁷³⁸ Absorption corrections were applied using empirical methods, the structures were solved by direct methods using SHELXS or SHELXT^{39,40} and refined by full-matrix least squares on F^2 by SHELXL,⁴¹ interfaced through the programs X-Seed⁴² or Olex.⁴³ In general, all non-hydrogen atoms were refined anisotropically and hydrogen atoms were included as invariants at geometrically estimated positions, unless specified otherwise in the additional details in the Chapter 7.1. X-ray experimental data is given in Table 7.1.4. Figures were produced using the program CrystalMaker. CIF data have been deposited with the Cambridge Crystallographic Data Centre, CCDC reference numbers CCDC 1977797–1977804 (**MnMOF-1-MeOH**, 1977797; **MnMOF-1-*p*-xylene**, 1977798; **MnMOF-1-DEE**,_1977799; **MnMOF-1-EtOH**,_1977800; **MnMOF-1-[Rh(CO)₂][RhCl₂(CO)₂](*p*-xylene)**,_1977801; **MnMOF-1-DCM**,_1977802; **MnMOF-1-ace**, 1977803; **MnMOF-1-THF**, 1977804).

2.5.5 Computational methods

The conformational landscapes of the ligands, as neutral acids, which comprise **MnMOF-1** (Me₄bcppm) and **UiO-67-bpy** (Me₂bpy) were investigated using the semiempirical tight-binding based quantum chemistry method GFN2-xTB. The CREST methodology was initially employed to explore the stable conformers. Constrained structural optimizations were subsequently used to examine the potential energy surfaces of the specific dihedral angles responsible for the *anti* and *syn* conformations. Representative data files for the simulations described here are available online in the data repository at <https://github.com/jackevansadl/supp-data>.

2.6 Associate content

Supporting information: IR spectroscopic data, powder X-ray diffraction data and details of the SCXRD and tables of crystallography data collection and refinement parameters, crystallographic information files (cifs).

2.7 Acknowledgements

C. J. S. and C. J. D. gratefully acknowledge the Australian Research Council for funding (DP160103234 and DP190101402). Aspects of this research were undertaken on the MX1 and MX2 beamlines at the Australian Synchrotron, Victoria, Australia. J. D. E. acknowledges the support of the Alexander von Humboldt Foundation and HPC platforms provided by a GENCI grant (A0070807069) and the Center for Information Services and High Performance Computing (ZIH) at TU Dresden.

2.8 References

- 1 V. Pascanu, G. González Miera, A. K. Inge and B. Martín-Matute, *J. Am. Chem. Soc.*, 2019, **141**, 7223–7234.
- 2 E. J. Carrington, I. J. Vitorica-Yrezabal and L. Brammer, *Acta Crystallogr. Sect. B*, 2014, **70**, 404–422.
- 3 T. L. Easun, F. Moreau, Y. Yan, S. Yang and M. Schröder, *Chem. Soc. Rev.*, 2017, **46**, 239–274.
- 4 D. J. Cram and J. M. Cram, *Acc. Chem. Res.*, 1978, **11**, 8–14.
- 5 Y. Inokuma, M. Kawano and M. Fujita, *Nat. Chem.*, 2011, **3**, 349–358.
- 6 F. J. Rizzuto, L. K. S. von Krbek and J. R. Nitschke, *Nat. Rev. Chem.*, 2019, **3**, 204–222.
- 7 M. Hoshino, A. Khutia, H. Xing, Y. Inokuma and M. Fujita, *IUCrJ*, 2016, **3**, 139–151.
- 8 W. J. Gee, *Dalt. Trans.*, 2017, **46**, 15979–15986.
- 9 Q. Du, J. Peng, P. Wu and H. He, *TrAC Trends Anal. Chem.*, 2018, **102**, 290–310.

- 10 W. M. Bloch, N. R. Champness and C. J. Doonan, *Angew. Chemie Int. Ed.*, 2015, **54**, 12860–12867.
- 11 H. Furukawa, K. E. Cordova, M. O’Keeffe and O. M. Yaghi, *Science*, 2013., **341**, 1230444, DOI:10.1126/science.1230444.
- 12 G. Brunet, D. A. Safin, K. Robeyns, G. A. Facey, I. Korobkov, Y. Filinchuk and M. Murugesu, *Chem. Commun.*, 2017, **53**, 5645–5648.
- 13 E. V Vinogradova, P. Müller and S. L. Buchwald, *Angew. Chemie Int. Ed.*, 2014, **53**, 3125–3128.
- 14 F. R. Fortea-Pérez, M. Mon, J. Ferrando-Soria, M. Boronat, A. Leyva-Pérez, A. Corma, J. M. Herrera, D. Osadchii, J. Gascon, D. Armentano and E. Pardo, *Nat. Mater.*, 2017, **16**, 760–766.
- 15 E. D. Bloch, L. J. Murray, W. L. Queen, S. Chavan, S. N. Maximoff, J. P. Bigi, R. Krishna, V. K. Peterson, F. Grandjean, G. J. Long, B. Smit, S. Bordiga, C. M. Brown and J. R. Long, *J. Am. Chem. Soc.*, 2011, **133**, 14814–14822.
- 16 A. J. Blake, N. R. Champness, T. L. Easun, D. R. Allan, H. Nowell, M. W. George, J. Jia and X.-Z. Sun, *Nat. Chem.*, 2010, **2**, 688–694.
- 17 W. M. Bloch, A. Burgun, C. J. Coghlan, R. Lee, M. L. Coote, C. J. Doonan and C. J. Sumbly, *Nat. Chem.*, 2014, **6**, 906–912.
- 18 A. Burgun, C. J. Coghlan, D. M. Huang, W. Chen, S. Horike, S. Kitagawa, J. F. Alvino, G. F. Metha, C. J. Sumbly and C. J. Doonan, *Angew. Chemie - Int. Ed.*, 2017, **56**, 8412–8416.
- 19 M. T. Huxley, A. Burgun, H. Ghodrati, C. J. Coghlan, A. Lemieux, N. R. Champness, D. M. Huang, C. J. Doonan and C. J. Sumbly, *J. Am. Chem. Soc.*, 2018, **140**, 6416–6425.
- 20 M. T. Huxley, R. J. Young, W. M. Bloch, N. R. Champness, C. J. Sumbly and C. J. Doonan, *Organometallics*, 2019, **38**, 3412–3418.
- 21 M. I. Gonzalez, E. D. Bloch, J. A. Mason, S. J. Teat and J. R. Long, *Inorg. Chem.*, 2015, **54**, 2995–3005.
- 22 M. I. Gonzalez, J. Oktawiec and J. R. Long, *Faraday Discuss.*, 2017, **201**, 351–367.

- 23 M. I. Gonzalez, A. B. Turkiewicz, L. E. Darago, J. Oktawiec, K. Bustillo, F. Grandjean, G. J. Long and J. R. Long, *Nature*, 2020, **577**, 64–68.
- 24 X.-N. Wang, P. Zhang, A. Kirchon, J.-L. Li, W.-M. Chen, Y.-M. Zhao, B. Li and H.-C. Zhou, *J. Am. Chem. Soc.*, 2019, **141**, 13654–13663.
- 25 J. D. Evans, C. J. Sumby and C. J. Doonan, *Chem. Soc. Rev.*, 2014, **43**, 5933–5951.
- 26 S. M. Cohen, *Chem. Rev.*, 2012, **112**, 970–1000.
- 27 W. M. Bloch, A. Burgun, C. J. Doonan and C. J. Sumby, *Chem. Commun.*, 2015, **51**, 5486–5489.
- 28 M. Huxley, C. J. Coghlan, A. Burgun, A. Tarzia, K. Sumida, C. J. Sumby and C. J. Doonan, *Dalt. Trans.*, 2016, **45**, 4431–4438.
- 29 M. T. Huxley, C. J. Coghlan, W. M. Bloch, A. Burgun, C. J. Doonan and C. J. Sumby, *Philos. Trans. R. Soc. A Math. Phys. Eng. Sci.*, 2017, **375**, 20160028.
- 30 J. Bae, J. S. Choi, S. Hwang, W. S. Yun, D. Song, J. Lee and N. C. Jeong, *ACS Appl. Mater. Interfaces*, 2017, **9**, 24743–24752.
- 31 G. Zhang, O. Presly, F. White, I. M. Oppel and M. Mastalerz, *Angew. Chemie Int. Ed.*, 2014, **53**, 1516–1520.
- 32 A. P. Katsoulidis, D. Antypov, G. F. S. Whitehead, E. J. Carrington, D. J. Adams, N. G. Berry, G. R. Darling, M. S. Dyer and M. J. Rosseinsky, *Nature*, 2019, **565**, 213–217.
- 33 C. Martí-Gastaldo, D. Antypov, J. E. Warren, M. E. Briggs, P. A. Chater, P. V Wiper, G. J. Miller, Y. Z. Khimyak, G. R. Darling, N. G. Berry and M. J. Rosseinsky, *Nat. Chem.*, 2014, **6**, 343–351.
- 34 X. Li, R. Van Zeeland, R. V Maligal-Ganesh, Y. Pei, G. Power, L. Stanley and W. Huang, *ACS Catal.*, 2016, **6**, 6324–6328.
- 35 C. Bannwarth, S. Ehlert and S. Grimme, *J. Chem. Theory Comput.*, 2019, **15**, 1652–1671.
- 36 S. Grimme, *J. Chem. Theory Comput.*, 2019, **15**, 2847–2862.
- 37 T. M. McPhillips, S. E. McPhillips, H.-J. Chiu, A. E. Cohen, A. M. Deacon, P. J. Ellis, E.

- Garman, A. Gonzalez, N. K. Sauter, R. P. Phizackerley, S. M. Soltis and P. Kuhn, *J. Synchrotron Radiat.*, 2002, **9**, 401–406.
- 38 N. P. Cowieson, D. Aragao, M. Clift, D. J. Ericsson, C. Gee, S. J. Harrop, N. Mudie, S. Panjikar, J. R. Price, A. Riboldi-Tunncliffe, R. Williamson and T. Caradoc-Davies, *J. Synchrotron Radiat.*, 2015, **22**, 187–190.
- 39 G. M. Sheldrick, *Acta Crystallogr. Sect. A*, 2008, **64**, 112–122.
- 40 G. M. Sheldrick, *Acta Crystallogr. Sect. A*, 2015, **71**, 3–8.
- 41 G. M. Sheldrick, *Acta Crystallogr. Sect. C*, 2015, **71**, 3–8.
- 42 L. J. Barbour, *J. Supramol. Chem.*, 2001, **1**, 189–191.
- 43 O. V Dolomanov, L. J. Bourhis, R. J. Gildea, J. A. K. Howard and H. Puschmann, *J. Appl. Crystallogr.*, 2009, **42**, 339–341.

Chapter 3. Highly Active Gas Phase Organometallic Catalysis Supported Within Metal-organic Framework Pores

Ricardo A. Peralta^a, Michael T. Huxley^a, Jack D. Evans^b, Haijie Cao^c, Maoxia He^d,
Xiu Song Zhao^{c,e}, Stefano Agnoli^f, Christopher J. Sumbly^{a*} and Christian J.
Doonan^{a*}

^a Centre for Advanced Nanomaterials and Department of Chemistry, The University of Adelaide, North Terrace, Adelaide, SA 5000, Australia

^b Department of Inorganic Chemistry, Technische Universität Dresden, Bergstraße 66, 01062 Dresden, Germany

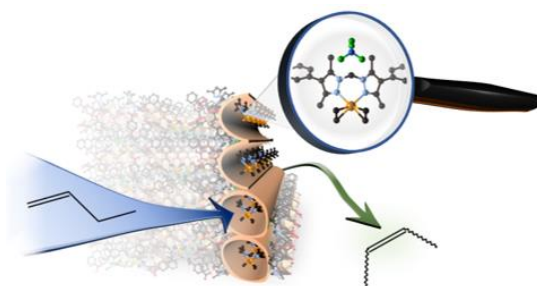
^c Institute of Materials for Energy and Environment, College of Materials Science and Engineering, Qingdao University, Qingdao, 266071, PR China

^d Environment Research Institute, Shandong University, Qingdao, 266237, PR China

^e School of Chemical Engineering, The University of Queensland, St Lucia, Brisbane, 4072, Australia

^f Dipartimento di Scienze Chimiche, Università di Padova, Via Marzolo 1, 35131 Padova, Italy

Peralta, R. A., Huxley, M. T., Evans, J. D., Fallon, T., Cao, H., He, M., Zhao, X. S., Agnoli, S., Sumbly C. J., Doonan, C. J., Highly Active Gas Phase Organometallic Catalysis Supported Within Metal-organic Framework Pores, *J. Am. Chem. Soc.*, 2020, 142, 13533–13543.



Statement of Authorship

Title of Paper	Highly Active Gas Phase Organometallic Catalysis Supported Within Metal-organic Framework Pores
Publication Status	<input checked="" type="checkbox"/> Published <input type="checkbox"/> Accepted for Publication <input type="checkbox"/> Submitted for Publication <input type="checkbox"/> Unpublished and Unsubmitted work written in manuscript style
Publication Details	Peralta, R. A., Huxley, M. T., Evans, J. D., Fallon, T., Cao, H., He, M., Zhao, X. S., Agnoli, S., Sumbly C. J., Doonan, C. J., Highly Active Gas Phase Organometallic Catalysis Supported Within Metal-organic Framework Pores, J. Am. Chem. Soc., 2020,

Principal Author

Name of Principal Author (Candidate)	Ricardo A. Peralta
Contribution to the Paper	Design and development of the project. Preparation of samples and collection of data. Analysis and interpretation of gas-phase NMR and X-Ray crystallography data. Preparation and drafting of the manuscript.
Overall percentage (%)	70%
Certification:	This paper reports on original research I conducted during the period of my Higher Degree by Research candidature and is not subject to any obligations or contractual agreements with a third party that would constrain its inclusion in this thesis. I am the primary author of this paper.
Signature	Date 23/2/21

Co-Author Contributions

By signing the Statement of Authorship, each author certifies that:

- i. the candidate's stated contribution to the publication is accurate (as detailed above);
- ii. permission is granted for the candidate to include the publication in the thesis; and
- iii. the sum of all co-author contributions is equal to 100% less the candidate's stated contribution.

Name of Co-Author	Michael T. Huxley
Contribution to the Paper	Assisted with the conception of the project, interpretation of the data, sample preparation, collection of X-Ray crystallography data and drafting the manuscript.
Signature	Date 19/03/2021

Name of Co-Author	Jack D. Evans
Contribution to the Paper	Performed computational work and assisted with the preparation of the manuscript.
Signature	Date

Name of Co-Author	Haijie Cao		
Contribution to the Paper	Performed computational work		
Signature		Date	

Name of Co-Author	Maoxia He		
Contribution to the Paper	Assisted with the computational work. CONTACTED BUT HAS NOT RESPONDED.		
Signature		Date	19/03/2021

Name of Co-Author	Xiu Song Zhao		
Contribution to the Paper	Assisted with the computational work.		
Signature		Date	

Name of Co-Author	Stefano Agnoli		
Contribution to the Paper	Performed XPS experiments.		
Signature		Date	

Name of Co-Author	Christopher J. Sumbly		
Contribution to the Paper	Assisted with the conception of the project, analysis of data and preparation of the manuscript.		
Signature		Date	17/03/2021

Name of Co-Author	Christian J. Doonan		
Contribution to the Paper	Assisted with the conception of the project, analysis of data and preparation of the manuscript.		
Signature		Date	17/03/21

Statement of Authorship

Title of Paper	Highly Active Gas Phase Organometallic Catalysis Supported Within Metal-organic Framework Pores
Publication Status	<input checked="" type="checkbox"/> Published <input type="checkbox"/> Accepted for Publication <input type="checkbox"/> Submitted for Publication <input type="checkbox"/> Unpublished and Unsubmitted work written in manuscript style
Publication Details	Peralta, R. A., Huxley, M. T., Evans, J. D., Fallon, T., Cao, H., He, M., Zhao, X. S., Agnoli, S., Sumbly C. J., Doonan, C. J., Highly Active Gas Phase Organometallic Catalysis Supported Within Metal-organic Framework Pores, J. Am. Chem. Soc., 2020,

Principal Author

Name of Principal Author (Candidate)	Ricardo A. Peralta
Contribution to the Paper	Design and development of the project. Preparation of samples and collection of data. Analysis and interpretation of gas-phase NMR and X-Ray crystallography data. Preparation and drafting of the manuscript.
Overall percentage (%)	70%
Certification:	This paper reports on original research I conducted during the period of my Higher Degree by Research candidature and is not subject to any obligations or contractual agreements with a third party that would constrain its inclusion in this thesis. I am the primary author of this paper.
Signature	Date 23/2/21

Co-Author Contributions

By signing the Statement of Authorship, each author certifies that:

- i. the candidate's stated contribution to the publication is accurate (as detailed above);
- ii. permission is granted for the candidate to include the publication in the thesis; and
- iii. the sum of all co-author contributions is equal to 100% less the candidate's stated contribution.


Name of Co-Author	Michael T. Huxley
Contribution to the Paper	Assisted with the conception of the project, interpretation of the data, sample preparation, collection of X-Ray crystallography data and drafting the manuscript.
Signature	Date

Name of Co-Author	Jack D. Evans
Contribution to the Paper	Performed computational work and assisted with the preparation of the manuscript.
Signature	Date 10/03/2021

Name of Co-Author	Haijie Cao		
Contribution to the Paper	Performed computational work		
Signature		Date	16 March 2021

Name of Co-Author	Maoxia He		
Contribution to the Paper	Assisted with the computational work.		
Signature		Date	

Name of Co-Author	Xiu Song Zhao		
Contribution to the Paper	Assisted with the computational work.		
Signature		Date	16 March 2021

Name of Co-Author	Stefano Agnoli		
Contribution to the Paper	Performed XPS experiments.		
Signature		Date	16 March 2021

Name of Co-Author	Christopher J. Sumbly		
Contribution to the Paper	Assisted with the conception of the project, analysis of data and preparation of the manuscript.		
Signature		Date	

Name of Co-Author	Christian J. Doonan		
Contribution to the Paper	Assisted with the conception of the project, analysis of data and preparation of the manuscript.		
Signature		Date	

3.1 Abstract

Metal-organic Frameworks (MOFs) can act as a platform for the heterogenization of molecular catalysts, providing improved stability, allowing easy catalyst recovery and a route towards structural elucidation of the active catalyst. We have developed a MOF, **1**, possessing vacant *N,N*-chelating sites which are accessible via the porous channels that penetrate the structure. In the present work, cationic rhodium(I) norbornadiene (NBD) and bis(ethylene) (ETH) complexes paired with both non-coordinating and coordinating anions have been incorporated into the *N,N*-chelation sites of **1** via post-synthetic metalation and facile anion exchange. Exploiting the crystallinity of the host framework, the immobilized Rh(I) complexes were structurally characterized using X-ray crystallography. The ethylene hydrogenation catalysis by **1**·[Rh(NBD)]X and **1**·[Rh(ETH)₂]X (X = Cl and BF₄) was studied in the gas phase (2 bar, 46°C) to reveal that **1**·[Rh(ETH)₂](BF₄) was the most active catalyst (TOF = 64 hr⁻¹); the NBD starting materials and the chloride salt were notably less active. Based on these observations, the activity of the Rh(I) bis(ethylene) complexes, **1**·[Rh(ETH)₂]BF₄ and **1**·[Rh(ETH)₂]Cl, in butene isomerization was also studied using gas-phase NMR spectroscopy. Under one bar of butene at 46°C, **1**·[Rh(ETH)₂]BF₄ rapidly catalyses the conversion of 1-butene to 2-butene with a TOF averaging 2000 hr⁻¹ over five cycles. Notably, the chloride derivative, **1**·[Rh(ETH)₂]Cl displays negligible activity in comparison. XPS analysis of the post-catalysis sample, supported by DFT calculations, suggest that the catalytic activity is inhibited by the strong interactions between a Rh(III) allyl hydride intermediate and the chloride anion.

3.2 Introduction

Metal-organic Frameworks (MOFs) are a class of network solids comprised of metal nodes interconnected by chemically and structurally mutable organic links.¹⁻³ A salient feature of MOF chemistry is that their robust porosity, stability and chemical functionality can be controlled via the considered selection of the organic and inorganic building blocks.³ These design principles, termed 'reticular chemistry', have led to the synthesis of materials tailored towards applications including gas separation,⁴⁻⁷ sensing,⁸⁻⁹ biotechnology¹⁰⁻¹² and catalysis.^{1-3, 13-17} With respect to catalysis, MOF synthesis offers a straight-forward approach to incorporating homogeneous systems within a heterogeneous environment.^{12, 18} This can be

achieved via incorporating pre-synthesized homogeneous species into the MOF network or post-synthesis metalation of suitably functionalized organic links. A recent, representative, example of the former is the heterogenization of the molecular iridium complex, $[\text{Ir}(\text{bipy})\text{Cl}_3(\text{THF})]$, for CO_2 hydrogenation.¹⁹ The same research group have also shown that post-synthesis metalation can be successfully applied to stabilize coordinatively unsaturated Ir species for methane activation.²⁰ In general, these strategies have been widely employed for the synthesis of MOF catalysts or for exploring chemical reactions within their pore networks.²¹⁻²⁵

Incorporating molecular catalysts into a porous MOF architecture facilitates the exploration of their gas phase reactivity. However, although MOF chemistry offers unprecedented opportunities for transposing homogeneous organometallic catalysts to a porous heterogeneous environment, examples of single-site, gas phase, organometallic chemistry in MOFs are rare.²⁶ This observation is intriguing as related work on solid-state organometallic complexes has shown that a solvent free environment allows for highly reactive species to be examined.²⁷⁻³³ For example, Weller and co-workers have applied this strategy to elucidate the structure of an elusive transition-metal σ -alkane complex and develop solid-state catalysts that operate in the gas phase.^{30, 34} Though experiments performed on well-defined, single molecules in the solid-state have provided insight into bond activation and catalytic processes, MOFs offer a clear advantage for exploring solid/gas chemistry. Namely, their 'node' and 'linker' modular synthesis gives rise to, robust, porous networks of predetermined structure metrics. Thus, a reactive metal complexes can be site-isolated within a porous network of predetermined porosity. In contrast, the arrangement of molecules in a crystal are determined by supramolecular crystal packing forces and are yet to be controlled or predicted with precision. Moreover, the structures are typically sensitive to solvent removal under reduced pressure or temperature, i.e. they lack permanent porosity.

We have recently shown that a manganese-based MOF, **1** ($[\text{Mn}_3(\text{L})_2\text{L}']$, where L = bis(4-carboxyphenyl-3,5-dimethyl-pyrazol-1-yl)methane), is a promising system for examining chemical reactions confined within pore networks.³⁵⁻³⁹ A key feature of **1** is the modulated flexibility of the organic linker⁴⁰ which can accommodate structural perturbations associated with post-synthesis metalation and subsequent chemical reactions at the metal site with retention of crystallinity.³⁵⁻³⁹ As a result, single crystal X-ray diffraction (SCXRD) can be

employed to precisely study chemistry within the MOF. Importantly, such atomic level insight is crucial to develop our knowledge of how nanoporous environments can modify chemical reactivity. To this end we sought to incorporate well-defined Rh(I) olefin species into **1** due to their potential to carry out solid/gas reactions of commercial interest. Organometallic Rh(I) complexes bearing olefin ligands have been previously isolated on solid supports including alumina,⁴¹ zeolites⁴²⁻⁴⁶ and MOFs.⁴⁷ However, their precise structural characterization by SCXRD was not possible because these species lacked long range order. Here we report the synthesis, characterization and reactivity of a series of [Rh(olefin)]⁺ species bound to the pyrazole groups of **1**. We show that **1**·[Rh(ETH)₂](BF₄) is a highly active (average TOF^{90%} ca. 2000 h⁻¹ over five cycles) and recyclable catalyst for the low temperature gas phase isomerization of 1-butene to 2-butene, a reaction of interest in alkane upgrading processes; notably however, the Cl salt is essentially inactive. This work exemplifies how a well-defined organometallic complex can be incorporated and stabilized within a MOF and carry out efficient, cycled catalysis in the gas phase. The exceptional catalytic performance of this system highlights that MOFs are an excellent platform material for the design of bone fide single atom catalysis in the solid-state.

3.3 Results and discussion

Post-synthetic metalation (PSM) is known to be an effective strategy for incorporating metal complexes into the pore networks of MOFs.^{18, 48-49} We have previously reported that the *N,N*-chelation site of as-synthesized **1** is metal free and thus poised for PSM via the open channels of the structure.^{35, 37-40, 50} A remarkable feature of **1** is that PSM can be employed to bind transition metal complexes in solution with retention of crystallinity. Indeed, **1** can retain crystallinity after consecutive reactions at the tethered metal site, thus enabling structural elucidation of metalation products via SCXRD.^{37, 39}

MOFs are known to be thermally stable over 773 K;⁵¹⁻⁵⁶ however, exposure to such conditions often results in structure degradation and loss of porosity. Furthermore, a number of common solvents are known to play a role framework decomposition,⁵⁷ and structural transformations.⁵⁸⁻⁵⁹ Thus, we sought to design a MOF-based catalyst for application in reactions that operate in the gas phase at temperatures mild enough to allow for the intrinsic

properties of the network to be retained, i.e. porosity and crystallinity. Light hydrocarbon processing is of significant commercial interest and there a number of organometallic moieties that carry out alkene hydrogenation and isomerization under mild conditions.⁶⁰⁻⁶² These include a number of molecular Rh(I) species,^{30, 63} however crystallographically well-defined solid-state systems are uncommon. We hypothesized that MOFs are excellent platform materials for transposing such homogeneous organometallic chemistry into the solid-state. By applying the well-established principles of reticular chemistry and PSM, single-site, organometallic catalysts poised to carry-out industrially favored solid/gas hydrocarbon processing could be realized. Accordingly, we synthesized several forms of MOF **1** furnished with organometallic Rh(I) olefin complexes and examined their catalytic reactivity towards the hydrogenation and isomerization of alkenes.

Reaction between **1** and $[\text{Rh}(\text{ETH})_2\text{Cl}]_2$ or $[\text{Rh}(\text{NBD})\text{Cl}]_2$ yields the corresponding cationic complexes $\mathbf{1}\cdot[\text{Rh}(\text{NBD})][\text{Rh}(\text{NBD})\text{Cl}_2]$ ($\mathbf{1}\cdot\text{NBD}$, $\text{NBD} = \text{norbornadiene}$) and $\mathbf{1}\cdot[\text{Rh}(\text{ETH})_2][\text{Rh}(\text{ETH})_2\text{Cl}_2]$ ($\mathbf{1}\cdot\text{ETH}$) quantitatively as pale yellow crystals. Due to the sensitivity of $[\text{Rh}(\text{ETH})_2\text{Cl}_2]$ towards ligand displacement and subsequent decomposition in solution, we conducted the reaction between **1** and the Rh(I) precursor at 40°C in ethanol (EtOH) under an atmosphere of ethylene in a sealed glass pressure tube (Figure 3.1). These conditions afforded $\mathbf{1}\cdot[\text{Rh}(\text{ETH})_2][\text{Rh}(\text{ETH})_2\text{Cl}_2]$ as yellow crystals. It is worth noting that reaction in acetonitrile (MeCN) resulted in loss of the ethylene ligands and formation of the corresponding bis-acetonitrile complex, $\mathbf{1}\cdot[\text{Rh}(\text{MeCN})_2]\text{Cl}$ (structurally characterized following anion exchange with NaCl in MeCN) (Figure 7.2.5.3.7).

In each case, quantitative metalation was determined by Energy Dispersive X-ray (EDX) analysis, which revealed the expected 3:2 Mn:Rh ratio (Sl. 1.0). Subsequent to PSM the MOF crystals retain their crystallinity, allowing the coordination sphere of the Rh(I) complexes to be elucidated using SCXRD; additionally, bulk sample crystallinity was confirmed by powder X-ray diffraction (PXRD) analysis, see Figure 7.2.4.1 and 7.2.4.4. The structure data of $\mathbf{1}\cdot[\text{Rh}(\text{NBD})][\text{Rh}(\text{NBD})\text{Cl}_2]$ revealed the expected square planar coordination geometry for a d^8 Rh(I) moiety.

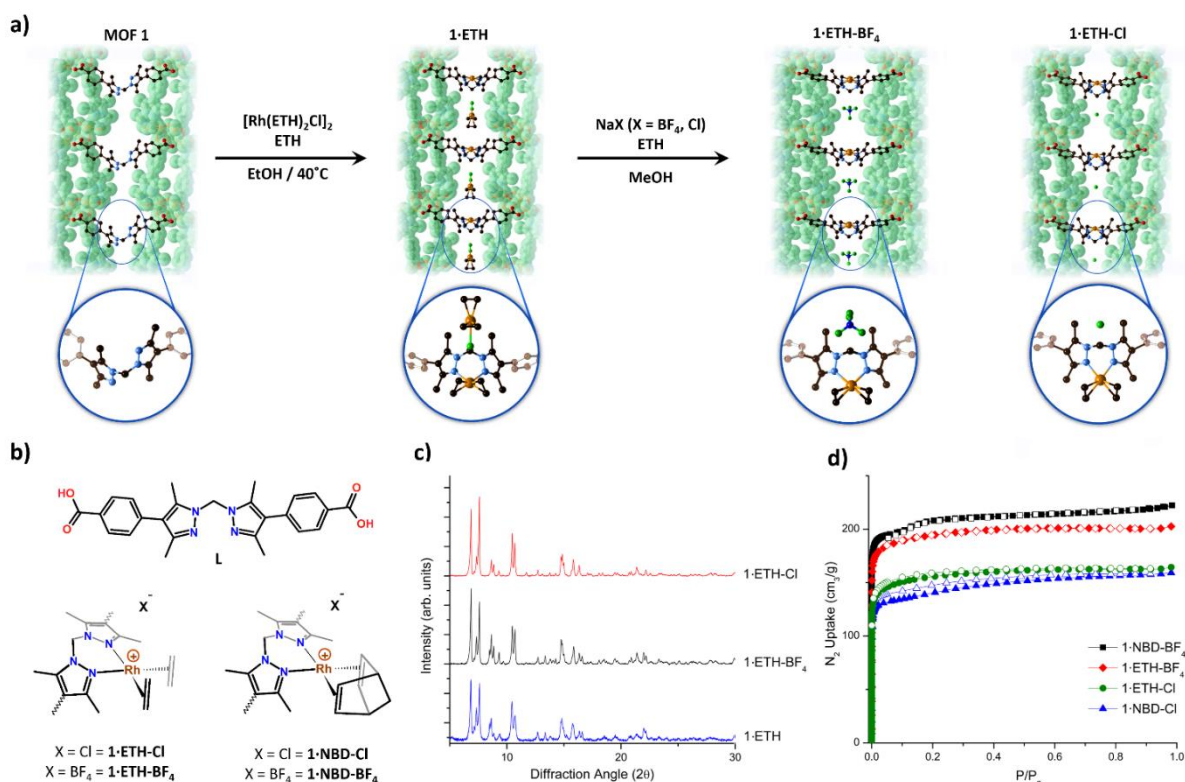


Figure 3.1. a) The metalation of **1** with [Rh(ETH)₂Cl]₂ proceeds to form the corresponding 1·[Rh(ETH)₂][Rh(ETH)₂Cl₂] complex and anion exchange with NaBF₄ or NaCl yields the corresponding BF₄ or Cl complexes respectively. The charge balancing anions ([Rh(ETH)₂Cl₂]⁻, BF₄⁻, Cl⁻) all occupy the same position in the MOF pore adjacent the coordinated Rh centre stabilized by a series of weak C-H-anion hydrogen bonds with the MOF. For clarity, the MOF is presented as a green van der Waals surface while the bridging ligand and chelated metal complex are presented in a ball and stick format (C, black; N, pale blue; Cl, green; Rh, orange; B, blue; F, green). b) Representations of the MOF ligand (L) and the chelated Rh sites described herein. c) PXRD plots of 1·ETH, 1·ETH-Cl and 1·ETH-BF₄ indicating retention of crystallinity and d) N₂ isotherms collected at 77 K for each Rh(I) metalated sample.

Specifically, the NBD ligand chelates the Rh center, both of which lie on a mirror plane, with Rh–C bond lengths of 2.167(13)/2.094(8) Å that are comparable to those observed in analogous molecular materials.^{64–66} The complexes are charge balanced by a [Rh(NBD)Cl₂]⁻ anion which occupies a pocket in the MOF pore adjacent to the *N,N*-chelated Rh(I) cation. In the case of 1·[Rh(ETH)₂][Rh(ETH)₂Cl₂], refinement of the structural model confirmed the presence of the *N,N*-chelated [Rh(ETH)₂]⁺ cation and an accompanying [Rh(ETH)₂Cl₂]⁻ anion. The Rh–C bond lengths are 2.13(2) and 2.05(3) Å, which again is in agreement with equivalent interactions in other Rh(I) ethylene complexes.^{67–68} It is worth mentioning that this is a rare

example of a Rh(I) bis-ethylene complex supported by an N-donor ligand system,⁶⁷⁻⁶⁸ highlighting that the MOF can act as a matrix for the isolation of kinetically unstable transition metal complexes.^{39, 69} We also note that the $[\text{Rh}(\text{ETH})_2\text{Cl}_2]$ anion is uncommon and has only been reported recently (Rh-C bond lengths of 1.985(18) and 2.215(16) Å).⁷⁰

Prior to examining the catalytic performance of metalated forms of **1** it is essential that the $[\text{Rh}(\text{olefin})\text{Cl}_2]$ anions are removed as they provide extraneous reactive sites. Facile and quantitative anion exchange of $[\text{Rh}(\text{olefin})\text{Cl}_2]$ with NaBF_4 or NaCl was achieved by soaking single crystals of $\mathbf{1}\cdot[\text{Rh}(\text{NBD})][\text{Rh}(\text{NBD})\text{Cl}_2]$ or $\mathbf{1}\cdot[\text{Rh}(\text{ETH})_2][\text{Rh}(\text{ETH})_2\text{Cl}_2]$ in methanol solutions of NaBF_4 or NaCl (Figure 3.1a for the ethylene complexes). However, for the more sensitive bis(ethylene) species, $\mathbf{1}\cdot[\text{Rh}(\text{ETH})_2][\text{Rh}(\text{ETH})_2\text{Cl}_2]$, the anion exchange process was performed under an ethylene atmosphere to prevent decomposition of the complex. Samples of the four Rh(I) functionalized species, $\mathbf{1}\cdot[\text{Rh}(\text{NBD})](\text{BF}_4)$ (**1**·NBD-BF₄), $\mathbf{1}\cdot[\text{Rh}(\text{NBD})]\text{Cl}$ (**1**·NBD-Cl), $\mathbf{1}\cdot[\text{Rh}(\text{ETH})_2](\text{BF}_4)$ (**1**·ETH-BF₄) and $\mathbf{1}\cdot[\text{Rh}(\text{ETH})_2]\text{Cl}$ (**1**·ETH-Cl), were examined via EDX analysis (SI 7.2.1) to confirm quantitative exchange of the $[\text{Rh}(\text{olefin})\text{Cl}_2]$ anion for Cl or BF₄. Following the two-step PSM and anion exchange process the MOF crystals retain their crystallinity, as confirmed via PXRD analysis (Figure 3.1 and Chapter 7, Figures 7.2.4.1 and 7.2.4.4). We then employed SCXRD to elucidate the coordination environment of the resulting Rh(I) species. **1**·NBD-BF₄ and **1**·NBD-Cl were solved in the monoclinic space group $P2_1/c$, with the diene ligand retaining a canted binding motif with Rh-C bond lengths for the alkene groups of 2.111(4)/2.135(4) and 2.141(4)/2.124(5) Å, and 2.159(12)/2.110(15) and 2.189(12)/2.100(10) Å for the BF₄ and Cl salts respectively (Figure 3.2a, these structures lack the mirror symmetry of the precursor which contains the $[\text{Rh}(\text{NBD})\text{Cl}_2]$ anion). The canting of the NBD ligands avoids steric encumbrance from the methyl groups of the MOF linker. For both **1**·NBD-BF₄ and **1**·NBD-Cl, the BF₄ and Cl anions, respectively, reside in a pocket within the MOF pore previously occupied by the $[\text{Rh}(\text{L})\text{Cl}_2]^-$. We note that this pocket is commonly occupied by anions³⁶⁻³⁷ due to the presence of multiple weak C-H...anion interactions. The anion exchanged samples **1**·ETH-BF₄ and **1**·ETH-Cl crystallized in the monoclinic space group $P2_1/m$. Rh-ethylene bond lengths refined to 2.26(3)/2.10(3) Å and 2.18(2)/2.072(10) Å, respectively for the Cl and BF₄ salts, and the Cl and BF₄ anions are located within the same pocket as the NBD analogues. To the best of our knowledge, the only other examples in which a $\text{M}(\text{ethylene})_2$ (M = Rh, Ir) moiety has been

incorporated within a MOF feature dispersed complexes bound to the nodes of Zr(IV) based frameworks and these sites were not able to be characterized by SCXRD.^{43, 71-72}

The bulk crystallinity and permanent porosity of the Rh(I) olefin species were assessed by performing PXRD measurements and gas adsorption isotherms, respectively. Samples of **1**·NBD-BF₄ and **1**·NBD-Cl were solvent exchanged with acetone and then heated at 80°C for 20 hr. PXRD analysis of samples following removal of pore solvent confirmed that crystallinity was retained (Figure 7.2.4.5-7.2.4.6). 77K N₂ gas adsorption isotherms were performed on **1**·NBD-BF₄ and **1**·NBD-Cl (Figure 3.1) and BET analysis was applied to the data. Surface areas of 808 and 539 m²/g were obtained for **1**·NBD-BF₄ and **1**·NBD-Cl respectively, albeit lower than expected for the Cl salt. These values are; however, in broad agreement with surface areas observed for other metalated derivatives of **1**.³⁵ Crystalline samples of **1**·ETH-BF₄ and **1**·ETH-Cl were washed with pentane and placed under vacuum for 2 hrs. 77K N₂ isotherms were collected and BET analysis of the data yielded surface areas of 732 and 562 m²/g for **1**·ETH-BF₄ and **1**·ETH-Cl respectively (Figure 3.1). The composition of the samples used for these adsorption analyses was examined via gas phase NMR spectroscopy. For samples of **1**·ETH-BF₄ and **1**·ETH-Cl exposure to CO/Me (1:1, 2 bar) displaced the coordinated ethylene, which was measured by integration against the methane signal in the gas phase, and demonstrated retention of approximately two ethylene ligands within the coordination sphere of the Rh for both samples (Chapter 7.7.3). PXRD analysis also confirmed that both materials retain crystallinity (Figure 7.2.4.2-7.2.4.3).

The similar differential between the surface areas of the BF₄ and Cl samples for both sets of Rh(I)-metalated MOFs prompted us to further consider the structures. Geometric surface areas were calculated for all species (taking into account the various disorder models, (see Table 7.9) and in both cases the Cl salt has a lower surface area than the BF₄ sample; approximately 15% lower for the NBD and 7% lower for the bis(ethylene) forms. Calculated pore volumes reflect these trends also (Table 7.9).

3.3.1 Gas phase alkene hydrogenation

We examined the reaction between activated samples of **1**·ETH-BF₄, **1**·ETH-Cl, **1**·NBD-Cl and **1**·NBD-BF₄ and H₂ in the gas phase. The yellow crystals of **1**·ETH-BF₄ and **1**·ETH-Cl turn black

instantaneously whilst **1**·NBD-BF₄ and **1**·NBD-Cl become black after 1 and 6 hrs, respectively. Despite this, the MOF crystals remained in excellent condition, allowing SCXRD data to establish that Rh was no longer coordinated to the *N,N*-chelating site of the MOF. Transmission Electron Microscopy (TEM) and Selected Angle Diffraction (SAD) analysis confirmed that in the presence of H₂ the Rh cations had undergone reduction to Rh(0) nanoparticles with an average diameter of 7 nm (**1**-NP) (See Chapter S7.2 and S7.3 for details). The 7 nm diameter of the Rh nanoparticles appears to be dictated by the pore size of the MOF structure (*ca.* 1 nm pore diameter), as observed for other systems where only a low density of the metal source is provided.⁷³ Despite varying the reaction temperature, H₂ pressure or performing the hydrogenation reaction in solution, nanoparticle formation could not be averted. These data suggest that the *N,N*-chelated Rh(I) center is unstable towards H₂ once the alkene is hydrogenated.

We hypothesized that the presence of excess alkene would prevent nanoparticle formation by stabilizing the Rh(I) sites to H₂ reduction, thereby facilitating gas-phase alkene hydrogenation. Thus, we examined the catalytic hydrogenation of ethylene by **1**·NBD-BF₄, **1**·NBD-Cl, **1**·ETH-BF₄ and **1**·ETH-Cl under conditions of excess alkene (Figure 3.2). Reactions were conducted in gas-tight NMR tubes and the headspace of the tube was monitored via ¹H NMR spectroscopy. Each sample (~2-3 mg of known mass) was exposed to a mixture of ethylene (1.2 bar, 140 μmol) and H₂ (0.8 bar, 95 μmol), giving a Rh loading of ~2 mol% based on H₂ content. **1**·ETH-BF₄ showed rapid ethylene hydrogenation at 46 °C, consuming the available hydrogen within 25 minutes (Figure 3.2, TOF^{90%} of 64 h⁻¹). Under these conditions, the catalytic activity is limited by the excess of ethylene, and improved activity can be achieved by using a greater portion of H₂ in the reaction mixture; however, those conditions lead to nanoparticle formation (*vide supra*). Catalyst cycling was investigated by placing the NMR tube under vacuum for 3 minutes before dosing with fresh H₂/ethylene. **1**·ETH-BF₄ maintained activity over 5 cycles (TOF 44 h⁻¹ on the fifth cycle), the crystals remained yellow, and PXRD analysis confirmed that the MOF had retained crystallinity and overall structure during the catalytic cycles.

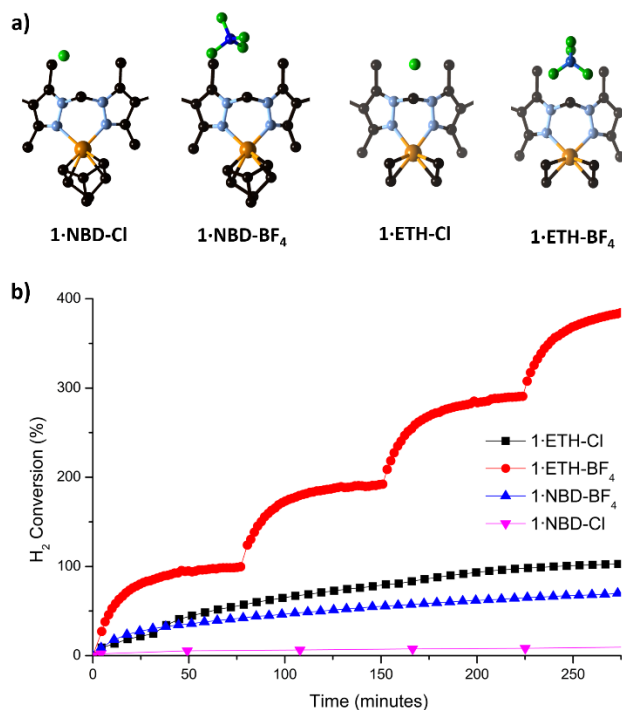


Figure 3.2. a) X-ray crystal structures of the Rh(I) site in **1·NBD-Cl**, **1·NBD-BF₄**, **1·ETH-Cl** and **1·ETH-BF₄**. b) Hydrogenation of ethylene catalyzed by the family of **1·[Rh(olefin)₂]** complexes. **1·ETH-BF₄** is the most active catalyst (plot truncated), while the NBD compounds show much lower activity.

Intriguingly, the chloride derivative, **1·ETH-Cl** displayed markedly lower activity (Figure 3.2) than its BF₄-counterpart, suggesting that the stronger coordinating anion significantly impacts the activity of the Rh center. Indeed, XPS analysis of **1·ETH-Cl** post hydrogenation shows that chlorine anions (Cl 2p peak maximum centered at 199 eV) are likely bonded to the Rh site (See Chapter 7.2.10, Figure 7.2.10.1). Furthermore, the IR spectrum of the catalyst post hydrogenation possesses weak bands centered at 2026 and 1934 cm⁻¹ that may be attributed to a Rh(III)-hydride moiety (Figure 7.2.8.2).⁷⁴⁻⁷⁵ Collectively, these data support the presence of a chloride in the coordination sphere of a Rh(III) species that deactivates the catalyst, whereas the weakly coordinating BF₄ does not bind to the Rh and thus facilitates catalysis.

The diene samples, **1·NBD-BF₄** and **1·NBD-Cl** displayed significantly lower activity for ethylene hydrogenation than **1·ETH-X**, failing to reach complete conversion of H₂ after 9 hrs. This can be attributed to the slow kinetics of NBD hydrogenation required to generate the active Rh(I) catalyst.⁷⁶ Additionally, hydrogenation of the NBD samples follows the same anion dependency as their ethylene counterparts: the chloride anion significantly reduces the

catalytic activity of the Rh(I) complex. Similar behavior has been reported for homogeneous olefin hydrogenation using Ir(I) catalysts, which display negligible activity in the presence of halide anions.⁷⁷

Finally, we investigated the activity of activated **1**·NP towards ethylene hydrogenation. In line with its retention of porosity (Figure 7.2.6.1), **1**·NP displayed good ethylene hydrogenation activity in the first cycle ($\text{TOF}^{90\%} = 32 \text{ h}^{-1}$), but this activity was considerably diminished in the second cycle ($\text{TOF}^{90\%} = 9 \text{ h}^{-1}$) highlighting the importance of retaining the active single atom Rh(I) center. (Figure 7.2.7.1.1)

3.3.2 Gas phase alkene isomerization

Rh(I) ethylene complexes are known to catalyze the isomerization of 1-butene to 2-butene, which is a valuable precursor in the synthesis of 2,3-butanediol used as a cross-linking agent in rubber manufacturing.⁷⁸ Single crystals of organometallic Rh(I) species are known to successfully isomerize 1-butene in the solid-state (room temperature, 1 bar). However, the porosity of these structures is serendipitous and realized via weak, intrinsically fragile, crystal packing forces. We postulated that the permanent porosity of **1**·ETH would provide an ideal platform for gas-phase butene isomerization (Chapter 7.11.1), owing to the accessibility of the Rh centers and permanent porosity of **1**. Moreover, we anticipated that **1**·ETH-BF₄ and **1**·ETH-Cl would display disparate activity based on the presence of non- or weakly coordinating BF₄ and coordinating Cl⁻ anions respectively, as observed under hydrogenation conditions.

Samples of **1**·ETH-BF₄ and **1**·ETH-Cl were activated in NMR tubes using the same protocol described above. 1-Butene (1 bar, 86 μmol) was subsequently added to the tube, which was sealed, and the conversion of 1-butene to 2-butene was monitored via gas-phase NMR spectroscopy (46 °C). **1**·ETH-BF₄ rapidly catalyzes the conversion, reaching the thermodynamic limit (98%) within 9 minutes with a $\text{TOF}^{90\%}$ of ca. $1845 \pm 275 \text{ h}^{-1}$ (Figure 3.3). Over the course of five successive cycles, the activity is retained (average $\text{TOF}^{90\%}$ of ca. 2000 h^{-1}), demonstrating that the host framework is capable of maintaining site-isolation and activity of the Rh centers.

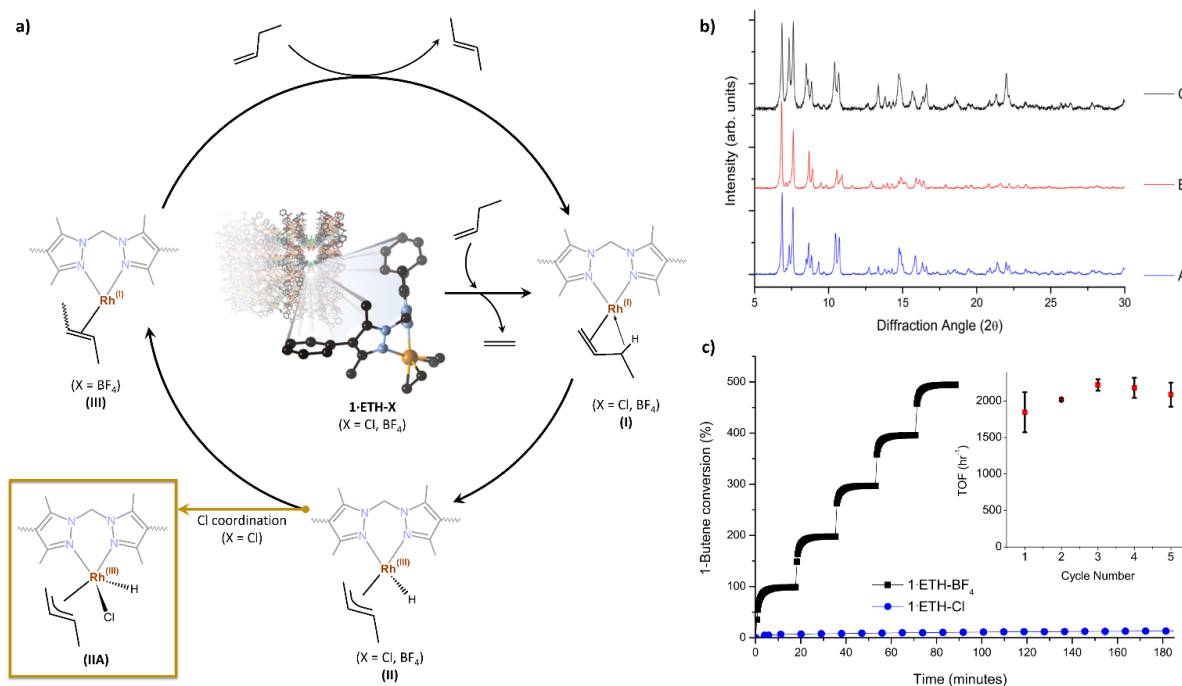


Figure 3.3. a) The proposed mechanism for 1-butene isomerization catalyzed by 1·ETH-BF₄ with (inset) the proposed inactive Rh(III) intermediate formed upon reaction of 1·ETH-Cl with 1-butene. b) PXRD data for 1·ETH-BF₄ initial (A), activated (B) and after butene isomerization catalysis (C). c) Butene isomerization catalyzed by 1·ETH-BF₄ over five successive cycles (black curve), whereas the analogous chloride complex 1·ETH-Cl displays negligible activity in comparison (blue curve). The inset shows butene isomerization TOF^{95%} for 1·ETH-BF₄ over five consecutive cycles.

As predicted, the chloride analogue **1·ETH-Cl** displays negligible activity in butene isomerization at 46 °C; reaching 5% conversion in the initial minutes of the reaction but achieving only 19% conversion over the ensuing 9 hours (Figure 3.3). As the sample remains porous (Figure 7.2.6.2), such rapid inactivation points to the involvement of the chloride anion in the formation of a catalytically incompetent species during the initial stages of catalysis (within the first ~2 cycles considering the initial 5% conversion). The mechanism of butene isomerization is proposed to proceed via a C-H activation of the CH₂ functionality adjacent to the alkene, forming an Rh(III) allyl hydride which undergoes reductive elimination to yield 2-butene (Figure 3.3).³⁰ We hypothesized that the formation of a Rh(III) allyl hydride intermediate would provide an opportunity for the adjacent chloride anion to bind, generating a stable Rh(III) complex and thereby inhibiting catalytic activity.

To examine anion interference, DFT calculations were employed to explore the energy landscape of the proposed butene isomerization mechanism, using a representative molecular analogue of the MOF bound Rh site (Chapter 7.11). Starting at the 1-butene bound cation I (4.95 kJ mol^{-1}), oxidative cleavage of the C–H bond proceeds with a barrier of 36.6 kJ mol^{-1} to give allyl-cation II (12.2 kJ mol^{-1}). The subsequent C-H activation has a barrier of 14.7 kJ mol^{-1} to produce the 2-butene bound cation III (0.00 kJ mol^{-1}). This modest overall barrier of 36.6 kJ mol^{-1} is consistent with analogous chemistry.³⁰ The key steps (giving species II and III) for this reaction were further investigated in the presence of BF_4 and Cl counter anions. These simulations confirm that chloride (Figure 3.3, inset) significantly stabilizes the Rh(III) allyl complex by more than 80 kJ mol^{-1} (relative to the butene bound complexes). In contrast the BF_4 anion only stabilizes the Rh site by approximately 30 kJ mol^{-1} , relative to the two butene complexes. These data support the experimental results that show the chloride complex is catalytically incompetent. Further, we performed XPS and IR analysis on **1**·ETH-Cl after exposure to 1-butene to experimentally probe the putative chloride bound species. The XPS data provides evidence of Cl anions bound to the Rh site in a 1:1 ratio (Figure 7.2.10.1) whilst the IR shows the presence of two weak bands at 2000 and 2036 cm^{-1} that can be attributed to $\nu(\text{Rh-H stretch})$ of the **1**· $[\text{Rh}(\text{C}_4\text{H}_7)](\text{H})(\text{Cl})$ species (Figure 7.2.8.1).⁷⁴⁻⁷⁵ In contrast, no such stretch was observed in the case of the BF_4 analogue. In summary, DFT, XPS and IR spectroscopy collectively support that chloride coordination to the Rh(III) allyl hydride intermediate occurs in **1**·ETH-Cl and is responsible for the comparatively poor catalytic performance.

We sought to determine whether the catalysis occurs within the pore network or primarily at the surface of the MOF crystals. To this end we finely crushed single crystals of **1**·ETH- BF_4 were prepared by placing a sample of **1**·ETH- BF_4 (pentane solvated) in a glass pressure tube under an ethylene atmosphere and stirring rapidly with a magnetic stirrer to crush the crystals. If catalysis is primarily surface-based one would expect that activity would increase due to increased surface area;³⁰ however, if catalysis occurred within the MOF pores (in addition to the surface) and mechanical stress led to partial collapse of the framework structure we would anticipate activity would diminish. Accordingly, we performed a butene isomerization experiment on a sample of finely crushed crystals. Catalytic activity was notably reduced by ca. one order of magnitude ($\text{TOF}^{90\%} 219 \text{ hr}^{-1}$). We then collected a 77K N_2 isotherm to ascertain

if the pore structure had been compromised by crushing. Close inspection of the data showed a significantly reduced uptake of N₂, with a BET surface area of 247 m²g⁻¹ (Figure 7.2.6.3, compared with 732 m²/g prior to crushing) confirmed that the pore access was restricted in this sample. These results suggest that the robust, open, porous structure of the MOF scaffold is integral to the gas phase catalytic activity of the material as it allows access of the substrate to all of the Rh active sites. To ascertain that all the 1·ETH-BF₄ catalytic sites are accessible in a pristine sample we examined the diffusion of 1-butene within the MOF pore network using classical molecular dynamics simulations. Close inspection of the computational results showed that diffusion of 1-butene is unrestricted in 1·ETH-BF₄, thus underscoring the importance of the open network for reactive site accessibility. The diffusion of the 2-butene product is somewhat restricted and would occur more slowly, possibly indicating that the diffusion of the product out of the MOF structure is a limiting factor in the gas phase catalytic activity.

3.4 Conclusion

Here we showed that the intrinsic properties of MOF materials, high crystallinity and robust porosity, coupled with reticular synthesis principles facilitate the design of solid-state single-site organometallic catalysts for commercially relevant gas phase reactions. Indeed, 1·ETH-BF₄ is a highly efficient catalyst for the isomerization of 1-butene (average TOF^{90%} ca. 2000 hr⁻¹). Additionally, due to the rigid MOF architecture, the catalyst can be cycled without a measurable loss of activity. Although some homogeneous catalysts show higher TOFs,⁷⁹⁻⁸¹ up to (8600 hr⁻¹), they are prone to decomposition.⁷⁹ While known examples of nanoparticle-based heterogeneous catalysts show comparable activity, these operate at higher temperatures. Thus, due to the MOF scaffold, gas phase catalysis by reactive organometallic entities can be conducted under mild conditions without decomposition. Furthermore, the reticular design principles inherent to MOF chemistry can allow for outer-sphere interactions to be tailored⁸² which could have a marked influence on the chemo-, stereo-, and regioselectivity of chemical transformations.

3.5 Experimental

3.5.1 General Experimental Considerations

Single crystals of MOF **1** were prepared as previously reported.³⁵ The chemicals ethylene, 1-butene, $[\text{Rh}(\text{NBD})_2\text{Cl}]_2$, $[\text{Rh}(\text{ETH})_2\text{Cl}]_2$ were purchased from commercial vendors and used as received. Samples were handled under standard Schlenk techniques unless otherwise stated. Solvents were dried using literature procedures and degassed with Ar prior to use. Specifically, MeCN was dried from CaH_2 under nitrogen; EtOH and methanol (MeOH) were dried by refluxing them over Mg under N_2 ; acetone was dried from CaSO_4 under nitrogen; and pentane was dried over Na/benzophenone. NaBF_4 and NaCl used for anion exchange were stored in a 120°C drying oven.

Powder X-ray diffraction (PXRD) data were collected on a Bruker Advanced D8 diffractometer (capillary stage) using Cu $K\alpha$ radiation ($\lambda = 1.5456 \text{ \AA}$, 40 kW/ 40mA, $2\theta = 2 - 52.94^\circ$, phi rotation = 20 rotation/min, at 1 sec exposure per step with 5001 steps and using 0.5 mm glass capillaries). Solution NMR spectra were recorded on Varian 500 or 600 MHz instruments at 23°C using a 5 mm probe. Gas phase NMR spectra were collected on a Varian Gemini 600MHz NMR spectrometer as described below. Infrared (IR) spectra were collected on a Perkin-Elmer Spectrum Two, with the sample distributed between two NaCl disks in Nujol. High-resolution transmission electron microscopy (HRTEM) images and diffraction pattern were acquired using an uncorrected FEI Titan Themis 80-200. Energy dispersive X-ray spectroscopy (EDX) was performed on a Philips XL30 field emission scanning electron microscope. Gas adsorption isotherm measurements were performed on an ASAP 2020 Surface Area and Pore Size Analyser. Activation of samples was carried out as described.

3.5.2 Preparation of $1 \cdot [\text{Rh}(\text{NBD})][\text{Rh}(\text{NBD})\text{Cl}_2]$ ($1 \cdot \text{NBD}$)

Single crystals of **1** (~24 mg) were placed in a 4 ml glass vial and washed with freshly distilled acetonitrile under Ar flow a total of 5 times (the solution was degassed with Ar after each exchange and the sample was allowed to soak for 1 hr between washings). Under Ar flow,

[Rh(NBD)Cl]₂ (30 mg) was added and the vial was sealed under Ar and heated at 65 °C for 16 hrs. The resulting yellow crystals were washed with freshly distilled acetonitrile five times under Ar flow to give **1**·NBD as yellow crystals. IR ν_{max} (nujol, cm⁻¹): 1612 (s, C=C), 1556 (m, C=C), 1458 (m, C=C) 1408, 1376.

3.5.3 Anion Exchange Protocols for **1**·NBD-BF₄ and **1**·NBD-Cl

Single crystals of **1**·NBD (~24 mg) were placed in a 4 ml glass vial and washed with freshly distilled methanol under Ar flow a total of 5 times (the solution was degassed with Ar after each exchange and the sample was allowed to soak for 1 hr between washings). Dry NaBF₄ or NaCl (~300 mg) was added to a small glass ampule which was subsequently submerged in the 4 ml vial containing the MOF sample. The solution was degassed with Ar, the vial was sealed and allowed to stand at room temperature (RT) for 48 hrs (BF₄) and 7 days (Cl). Under Ar flow, the ampule containing undissolved salt was removed and the yellow MOF crystals were washed with freshly distilled methanol five times under Ar flow.

1·NBD-BF₄: IR ν_{max} (nujol, cm⁻¹): 1614 (s, C=C), 1556 (m, C=C), 1452 (m, C=C) 1405, 1376.

1·NBD-Cl: IR ν_{max} (nujol, cm⁻¹): 1611 (s, C=C), 1556 (m, C=C), 1457 (m, C=C) 1409, 1377.

3.5.4 Preparation of **1**·[Rh(CH₂CH₂)₂][Rh(CH₂CH₂)₂Cl₂] (**1**·ETH)

Single crystals of **1** (~24 mg) were placed in a 20 ml glass pressure vessel fitted with a pressure gauge and Swagelok tap assembly (See Chapter 7.9 for details). The crystals were washed with freshly distilled ethanol (5 x 5 ml) under Ar flow a total of 5 times (the solution was degassed with Ar after each exchange and the sample was allowed to soak for 1 hr between washings). The solution was degassed with ethylene, excess [Rh(ETH)₂Cl]₂ (30 mg) was added and the pressure tube was sealed under ethylene (~1.2 bar) and heated at 40 °C for 24 hr. The resulting yellow crystals were washed with freshly distilled, ethylene degassed ethanol (5 x 5 ml) to remove dissolved Rh precursor. Insoluble Rh by-products were removed by washing the MOF crystals with dry, ethylene degassed acetone (5 x 5 ml) under ethylene flow to give **1**·ETH as yellow crystals. IR ν_{max} (nujol, cm⁻¹): 1610 (s, C=C), 1555 (m, C=C), 1458 (m, C=C) 1376, 1306.

3.5.5 Anion Exchange Protocols for 1·ETH-BF₄ and 1·ETH-Cl

Single crystals of **1**·ETH (~24 mg) were placed in a 20 ml glass pressure vessel fitted with a pressure gauge and tap assembly (see Chapter 7.9 for details) and washed with freshly distilled, ethanol and methanol degassed (5 ml) under ethylene flow a total of 5 times (the solution was degassed with ethylene after each exchange and the sample was allowed to soak for 1 hr between washings). Excess oven dried NaBF₄ or NaCl was added to a small glass ampule which was subsequently submerged in the glass pressure tube containing the MOF sample. The solution was degassed with ethylene, the pressure tube was sealed and allowed to stand at RT for 24 hrs (BF₄) or 6 days (Cl). Under ethylene flow, the ampule containing undissolved salt was removed and the yellow MOF crystals were washed with freshly distilled, ethylene degassed methanol (5 ml) five times under ethylene flow.

1·ETH-BF₄: IR ν_{\max} (nujol, cm⁻¹): 1611 (s, C=C), 1553 (m, C=C), 1455 (m, C=C) 1374, 1305.

1·ETH-Cl: IR ν_{\max} (nujol, cm⁻¹): 1612 (s, C=C), 1554 (m, C=C), 1457 (m, C=C) 1377, 1307.

3.5.6 Preparation of 1·[Rh(MeCN)₂]Cl

Single crystals of **1** (~24mg) were placed in an 8 ml glass vial. The crystals were washed with freshly distilled acetonitrile (5 x 5 ml) under Ar flow a total of 5 times (the solution was degassed with Ar after each exchange and the sample was allowed to soak for 1 hr between washings). Excess [Rh(ETH)₂Cl]₂ (30 mg) was added and the vial was sealed under an Ar atmosphere and allowed to stand at RT for 72 hrs. The resulting yellow crystals were washed with freshly distilled, argon degassed acetonitrile (5 x 5 ml) to remove dissolved Rh precursor. The resulting crystals were washed again with freshly distilled acetonitrile (5 x 5 ml) under argon. A small glass vessel containing dry NaCl was submerged in the acetonitrile such that the NaCl could dissolve and access the MOF crystals. After 7 days, the undissolved NaCl was removed and the MOF crystals were washed with freshly distilled acetonitrile under argon (5 x 5 ml) to give **1**·[Rh(MeCN)₂]Cl as yellow crystals. An X-ray crystal structure was collected on a single crystal following solvent exchange with distilled THF. IR ν_{\max} (nujol, cm⁻¹): 2315 (w, Rh-

$\text{N}\equiv\text{CCH}_3$), 2293 (w, free $\text{CH}_3\text{C}\equiv\text{N}$), 2251 (w, free $\text{CH}_3\text{C}\equiv\text{N}$), 1612 (s, $\text{C}=\text{O}$), 1555 (m, $\text{C}=\text{C}$), 1458 (m, $\text{C}=\text{C}$) 1407, 1376.

3.5.7 Gas Phase Hydrogenation

1·NBD-X or 1·NP crystals (~2 mg) were washed with freshly distilled acetone (5 x 5ml) under argon degas, allowing the crystals to soak for 1 hr between exchanges. The sample was pipetted under argon flow into a pre-weighed NORELL high-pressure NMR tube fitted with a Young's tap. The excess of acetone was removed and the NMR tube placed under vacuum and heated in an oil bath at 85 °C for 20 hr. The NMR tube was cooled to room temperature under vacuum and dosed with ethylene (1.2 bar, 140 μmol) followed by hydrogen (0.8 bar, 95 μmol). The NMR tube was sealed and placed in a Varian Gemini 600MHz NMR spectrometer pre-heated to 46 °C.

1·ETH- BF_4 and 1·ETH-Cl (~2 mg) were washed with recently distilled acetone (previously degassed with ethylene) five times under ethylene, allowing the crystals to soak for 1 hr between exchanges. Consequently, the crystals were washed with distilled pentane (previously degassed with ethylene) five times under ethylene, soaked for 1 hr between each exchange. The sample was pipetted into a pre-weighed NORELL high-pressure NMR tube fitted with a Young's tap under ethylene flow. The excess pentane was removed before the NMR tube was placed under vacuum for 2 hrs. The NMR tube then was dosed with ethylene (1.2 bar, 140 μmol) followed by hydrogen (0.8 bar, 95 μmol). The NMR tube was sealed and placed in a Varian Gemini 600MHz NMR spectrometer pre-heated to 46 °C.

3.5.7.1 Data Collection and Processing Details

Gas phase chemical shifts are referenced relative to reported data.³⁴ Before the collection the NMR was locked with a benzene (C_6D_6) charged NMR tube at 46 °C, which was then replaced with the pre-loaded high-pressure NMR tube. A T1 delay 25 s was used. The extent of conversion was calculated by the comparison of the reduction/disappearance in the integral

of the alkene CH₂ resonance of ethylene (5.31 ppm) and hydrogen (4.57 ppm), and the appearance of the two CH₃ alkyl resonance of ethane (0.88 ppm).

3.5.8 Gas Phase Alkene Isomerization

Samples of Rh(I) bis(ethylene) metalated **1** (~2mg) were washed as previously stated for the gas phase hydrogenation experiments. The crystals were loaded into a high-pressure NMR tube fitted with a Teflon stopcock and activated for 2hr under vacuum at RT. Following activation, the NMR tube was dosed with ethylene (1 bar) for 5 minutes and subsequently evacuated for 3 minutes. 1-Butene was added (1 bar, 86 μmol) and placed in a Varian Gemini 600MHz NMR spectrometer pre-heated to 46 °C.

A crushed sample of **1**·ETH-BF₄ was prepared by transferring a sample of **1**·ETH-BF₄ (~30mg) in pentane to a glass high pressure tube (See Chapter 7.2.9 for tube details) charged with ethylene and a magnetic stir-bar. The vessel was placed above a magnetic stirrer for 30 minutes, thereby generating a crushed sample of **1**·ETH-BF₄ which was transferred to a high-pressure NMR tube for catalytic activity analysis as described above.

3.5.8.1 Data Collection and Processing Details

Gas phase chemical shifts are referenced relative to reported data.³⁰ Before the collection the NMR was locked with a benzene (C₆D₆) charged NMR tube at 46 °C, which was then replaced with the pre-loaded high-pressure NMR tube. A T1 delay of 0.01 s with 4 scans was used to collect data for **1**·ETH-BF₄ and while a T1 delay of 25 s with 4 scans was used for **1**·ETH-Cl. The extent of conversion was calculated by the comparison of the reduction in the integral of the alkyl CH₂ resonance of 1-butene at 6.0 ppm and the appearance of the two alkene CH resonances from 2-butene at 5.25 ppm.

3.6 Molecular simulations

Surface area and probe-occupiable volume was simulated for a probe radius of 1.82 Å (equivalent to the size of N₂) using the Zeo++ program.⁸³⁻⁸⁴ A cluster model was derived for a representative Rh complex, where the framework was cleaved at the pyrazole C4 position and capped with methyl functionality. Geometry optimizations of the butene and allyl containing complexes used the BP86 density functional⁸⁵⁻⁸⁶ and employed by the ORCA software package.⁸⁷⁻⁸⁸ Coulomb with the chain of spheres exchange algorithms (RIJCOSX)⁸⁹ were employed for the efficiency of calculations and the segmented all-electron def2-TZVP(-f) basis set and def2-TZVP/J auxiliary basis set for all atoms were used.⁹⁰⁻⁹¹ This also included the def2 effective core potentials for rhodium. Tight SCF convergence criteria and a fine DFT integration grid (Grid6) were implemented to obtain reliable accuracy and dispersion corrections (D3-BJ) was applied.⁹²

Frequency calculations were performed analytically, and each intermediate was identified as a stationary point (minimum structure) as characterized by the absence of imaginary frequencies. This analysis further provided the necessary correction to the Gibbs free energy to give the free energy of each structure at 298 K. The energetic barriers between these characterized intermediates (I, II, III), were approximated using climbing image nudged elastic band (CI-NEB) approach with 6 images.⁹³

Molecular dynamics simulations were performed on a fixed structure of a 2×1×2 supercell of 1·[Rh(ETH)₂](BF₄) using the RASPA software package.⁹⁴ Butene molecules were treated using the TraPPE potential⁹⁵ and framework dispersion interactions were treated using universal force field parameters.⁹⁶ Dynamics were simulated with the NVT ensemble at 300 K for 20 molecules of butene employing 1 fs timestep and 1000 ps equilibration, the butene mean-squared displacement was recorded for a subsequent 5000 ps.

Representative input files for molecular simulations are available online in the data repository <https://github.com/jackevansadl/supp-data>.

3.7 Associated content

Supporting information: characterization data for the MOF samples, IR spectroscopic data, additional gas phase NMR spectroscopy, gas adsorption data, details of high-pressure reaction vessels powder, powder X-ray diffraction data and details of the SCXRD and tables of crystallography data collection and refinement parameters, computational results, crystallographic information files (cifs).

3.8 Acknowledgment

CJS and CJD gratefully acknowledge the Australian Research Council for funding (DP160103234 and DP190101402). XSZ acknowledge the ARC for funding (FL170100101). J. D. E. acknowledges the support of the Alexander von Humboldt foundation and HPC platforms provided by a Grand équipement national de calcul intensif (GENCI) grant (A0010807069) and the Center for Information Services and High Performance Computing (ZIH) at TU Dresden. This research was undertaken in part using the MX1 and MX2 beamlines at the Australian Synchrotron, part of ANSTO, and made use of the Australian Cancer Research Foundation (ACRF) detector. RAP gratefully acknowledges Adelaide Scholarship International. We acknowledge the contribution of Peter Apoefis in developing the high-pressure reaction vessels used in this work (Chapter 7.2.9.).

3.9 References

- (1) Kitagawa, S.; Kitaura, R.; Noro, S. Functional porous coordination polymers. *Angew. Chem., Int. Ed. Engl.* **2004**, *43*, 2334.
- (2) Furukawa, H.; Cordova, K. E.; O'Keeffe, M.; Yaghi, O. M. The chemistry and applications of metal-organic frameworks. *Science* **2013**, *341*, 974.
- (3) Yaghi, O. M.; O'Keeffe, M.; Ockwig, N. W.; Chae, H. K.; Eddaoudi, M.; Kim, J. Reticular synthesis and the design of new materials. *Nature* **2003**, *423*, 705.
- (4) Dechnik, J.; Sumbly, C. J.; Janiak, C. Enhancing Mixed-Matrix Membrane Performance with Metal–Organic Framework Additives. *Cryst. Growth Des.* **2017**, *17*, 4467.
- (5) Dechnik, J.; Gascon, J.; Doonan, C. J.; Janiak, C.; Sumbly, C. J. Mixed-Matrix Membranes. *Angew. Chem., Int. Ed. Engl.* **2017**, *56*, 9292.
- (6) Seoane, B.; Coronas, J.; Gascon, I.; Benavides, M. E.; Karvan, O.; Caro, J.; Kapteijn, F.; Gascon, J. Metal-organic framework based mixed matrix membranes: a solution for highly efficient CO₂ capture? *Chem. Soc. Rev.* **2015**, *44*, 2421.
- (7) Mason, J. A.; Veenstra, M.; Long, J. R. Evaluating metal-organic frameworks for natural gas storage. *Chem. Sci.* **2014**, *5*, 32.
- (8) Zhang, Y.; Yuan, S.; Day, G.; Wang, X.; Yang, X.; Zhou, H.-C. Luminescent sensors based on metal-organic frameworks. *Coord. Chem. Rev.* **2018**, *354*, 28.
- (9) Cui, Y.; Chen, B.; Qian, G. Lanthanide metal-organic frameworks for luminescent sensing and light-emitting applications. *Coord. Chem. Rev.* **2014**, *273*, 76.
- (10) Rogge, S. M. J.; Bavykina, A.; Hajek, J.; Garcia, H.; Olivos-Suarez, A. I.; Sepulveda-Escribano, A.; Vimont, A.; Clet, G.; Bazin, P.; Kapteijn, F.; Daturi, M.; Ramos-Fernandez, E. V.; Llabres, I. X. F. X.; Van Speybroeck, V.; Gascon, J. Metal-organic and covalent organic frameworks as single-site catalysts. *Chem. Soc. Rev.* **2017**, *46*, 3134.
- (11) Wang, C.; An, B.; Lin, W. Metal–Organic Frameworks in Solid–Gas Phase Catalysis. *ACS Catal.* **2018**, *9*, 130.
- (12) Drake, T.; Ji, P.; Lin, W. Site Isolation in Metal–Organic Frameworks Enables Novel Transition Metal Catalysis. *Acc. Chem. Res.* **2018**, *51*, 2129.
- (13) Huang, Y. B.; Liang, J.; Wang, X. S.; Cao, R. Multifunctional metal-organic framework catalysts: synergistic catalysis and tandem reactions. *Chem. Soc. Rev.* **2016**, *46*, 126.

(14) Dhakshinamoorthy, A.; Garcia, H. Cascade reactions catalyzed by metal organic frameworks. *ChemSusChem*. **2014**, *7*, 2392.

(15) Dhakshinamoorthy, A.; Asiri, A. M.; Garcia, H. Metal-Organic Framework (MOF) Compounds: Photocatalysts for Redox Reactions and Solar Fuel Production. *Angew. Chem., Int. Ed. Engl.* **2016**, *55*, 5414.

(16) Ferey, G. Hybrid porous solids: past, present, future. *Chem. Soc. Rev.* **2008**, *37*, 191.

(17) Inokuma, Y.; Yoshioka, S.; Ariyoshi, J.; Arai, T.; Hitora, Y.; Takada, K.; Matsunaga, S.; Rissanen, K.; Fujita, M. X-ray analysis on the nanogram to microgram scale using porous complexes. *Nature* **2013**, *495*, 461.

(18) Manna, K.; Zhang, T.; Lin, W. Postsynthetic metalation of bipyridyl-containing metal-organic frameworks for highly efficient catalytic organic transformations. *J. Am. Chem. Soc.* **2014**, *136*.

(19) An, B.; Zeng, L.; Jia, M.; Li, Z.; Lin, Z.; Song, Y.; Zhou, Y.; Cheng, J.; Wang, C.; Lin, W. Molecular Iridium Complexes in Metal–Organic Frameworks Catalyze CO₂ Hydrogenation via Concerted Proton and Hydride Transfer. *J. Am. Chem. Soc.* **2017**, *139*, 17747.

(20) Feng, X.; Song, Y.; Li, Z.; Kaufmann, M.; Pi, Y.; Chen, J. S.; Xu, Z.; Li, Z.; Wang, C.; Lin, W. Metal-Organic Framework Stabilizes a Low-Coordinate Iridium Complex for Catalytic Methane Borylation. *J. Am. Chem. Soc.* **2019**, *141*, 11196.

(21) Zhang, T.; Manna, K.; Lin, W. Metal-Organic Frameworks Stabilize Solution-Inaccessible Cobalt Catalysts for Highly Efficient Broad-Scope Organic Transformations. *J. Am. Chem. Soc.* **2016**, *138*, 3241.

(22) Sawano, T.; Lin, Z.; Boures, D.; An, B.; Wang, C.; Lin, W. Metal-Organic Frameworks Stabilize Mono(phosphine)-Metal Complexes for Broad-Scope Catalytic Reactions. *J. Am. Chem. Soc.* **2016**, *138*, 9783.

(23) Zhang, X.; Huang, Z.; Ferrandon, M.; Yang, D.; Robison, L.; Li, P.; Wang, T. C.; Delferro, M.; Farha, O. K. Catalytic chemoselective functionalization of methane in a metal–organic framework. *Nature Catalysis* **2018**, *1*, 356.

(24) Dunning, S. G.; Nandra, G.; Conn, A. D.; Chai, W.; Sikma, R. E.; Lee, J. S.; Kunal, P.; Reynolds, J. E., 3rd; Chang, J. S.; Steiner, A.; Henkelman, G.; Humphrey, S. M. A Metal-Organic Framework with Cooperative Phosphines That Permit Post-Synthetic Installation of Open Metal Sites. *Angew. Chem., Int. Ed. Engl.* **2018**, *57*, 9295.

(25) Manna, K.; Zhang, T.; Greene, F. X.; Lin, W. Bipyridine- and Phenanthroline-Based Metal–Organic Frameworks for Highly Efficient and Tandem Catalytic Organic Transformations via Directed C–H Activation. *J. Am. Chem. Soc.* **2015**, *137*, 2665.

(26) Beloqui Redondo, A.; Morel, F. L.; Ranocchiari, M.; van Bokhoven, J. A. Functionalized Ruthenium–Phosphine Metal–Organic Framework for Continuous Vapor-Phase Dehydrogenation of Formic Acid. *ACS Catalysis* **2015**, *5*, 7099.

(27) Boyd, T. M.; Tegner, B. E.; Tizzard, G. J.; Martinez-Martinez, A. J.; Neale, S. E.; Hayward, M. A.; Coles, S. J.; Macgregor, S. A.; Weller, A. S. A Structurally Characterized Cobalt(I) sigma-Alkane Complex. *Angew. Chem., Int. Ed. Engl.* **2020**, *59*, 6177.

(28) McKay, A. I.; Martínez-Martínez, A. J.; Griffiths, H. J.; Rees, N. H.; Waters, J. B.; Weller, A. S.; Krämer, T.; Macgregor, S. A. Controlling Structure and Reactivity in Cationic Solid-State Molecular Organometallic Systems Using Anion Templating. *Organometallics* **2018**, *37*, 3524.

(29) Martínez-Martínez, A. J.; Tegner, B. E.; McKay, A. I.; Bukvic, A. J.; Rees, N. H.; Tizzard, G. J.; Coles, S. J.; Warren, M. R.; Macgregor, S. A.; Weller, A. S. Modulation of σ -Alkane Interactions in $[\text{Rh}(\text{L}_2)(\text{alkane})]^+$ Solid-State Molecular Organometallic (SMOM) Systems by Variation of the Chelating Phosphine and Alkane: Access to η^2, η^2 - σ -Alkane Rh(I), η^1 - σ -Alkane Rh(III) Complexes, and Alkane Encapsulation. *J. Am. Chem. Soc.* **2018**, *140*, 14958.

(30) Chadwick, F. M.; McKay, A. I.; Martinez-Martinez, A. J.; Rees, N. H.; Kramer, T.; Macgregor, S. A.; Weller, A. S. Solid-state molecular organometallic chemistry. Single-crystal to single-crystal reactivity and catalysis with light hydrocarbon substrates. *Chem. Sci.* **2017**, *8*, 6014.

(31) Chadwick, F. M.; Kramer, T.; Gutmann, T.; Rees, N. H.; Thompson, A. L.; Edwards, A. J.; Buntkowsky, G.; Macgregor, S. A.; Weller, A. S. Selective C–H Activation at a Molecular Rhodium Sigma-Alkane Complex by Solid/Gas Single-Crystal to Single-Crystal H/D Exchange. *J. Am. Chem. Soc.* **2016**, *138*, 13369.

(32) Chadwick, F. M.; Rees, N. H.; Weller, A. S.; Kramer, T.; Iannuzzi, M.; Macgregor, S. A. A Rhodium-Pentane Sigma-Alkane Complex: Characterization in the Solid State by Experimental and Computational Techniques. *Angew. Chem., Int. Ed. Engl.* **2016**, *55*, 3677.

(33) Pike, S. D.; Thompson, A. L.; Algarra, A. G.; Apperley, D. C.; Macgregor, S. A.; Weller, A. S. Synthesis and Characterization of a Rhodium(I) σ -Alkane Complex in the Solid State. *Science* **2012**, *337*, 1648.

(34) Pike, S. D.; Krämer, T.; Rees, N. H.; Macgregor, S. A.; Weller, A. S. Stoichiometric and Catalytic Solid–Gas Reactivity of Rhodium Bis-phosphine Complexes. *Organometallics* **2015**, *34*, 1487.

(35) Bloch, W. M.; Burgun, A.; Coghlan, C. J.; Lee, R.; Coote, M. L.; Doonan, C. J.; Sumbly, C. J. Capturing snapshots of post-synthetic metallation chemistry in metal-organic frameworks. *Nat. Chem.* **2014**, *6*, 906.

(36) Huxley, M. T.; Young, R. J.; Bloch, W. M.; Champness, N. R.; Sumbly, C. J.; Doonan, C. J. Isomer Interconversion Studied through Single-Crystal to Single-Crystal Transformations in a Metal–Organic Framework Matrix. *Organometallics* **2019**, *38*, 3412.

(37) Huxley, M. T.; Burgun, A.; Ghodrati, H.; Coghlan, C. J.; Lemieux, A.; Champness, N. R.; Huang, D. M.; Doonan, C. J.; Sumbly, C. J. Protecting-Group-Free Site-Selective Reactions in a Metal-Organic Framework Reaction Vessel. *J. Am. Chem. Soc.* **2018**, *140*, 6416.

(38) Huxley, M. T.; Coghlan, C. J.; Bloch, W. M.; Burgun, A.; Doonan, C. J.; Sumbly, C. J. X-ray crystallographic insights into post-synthetic metalation products in a metal-organic framework. *Phil. Trans. R. Soc. A* **2017**, *375*, 20160028.

(39) Burgun, A.; Coghlan, C. J.; Huang, D. M.; Chen, W.; Horike, S.; Kitagawa, S.; Alvino, J. F.; Metha, G. F.; Sumbly, C. J.; Doonan, C. J. Mapping-Out Catalytic Processes in a Metal-Organic Framework with Single-Crystal X-ray Crystallography. *Angew. Chem., Int. Ed. Engl.* **2017**, *56*, 1.

(40) Peralta, R.; Huxley, M.; Young, R.; Linder-Patton, O. M.; Evans, J. D.; Doonan, C. J.; Sumbly, C. J. MOF Matrix Isolation: Cooperative Conformational Mobility Enables Reliable Single Crystal Transformations. *Faraday Discuss.* **2020**, DOI: 10.1039/D0FD00012D.

(41) Spek, T. G.; Scholten, J. J. F. Rh(π -C₃H₅)CO(PPh₃)₂ on γ -alumina. Synthesis, texture and infrared spectroscopy. *J. Mol. Cat.* **1977**, *3*, 81.

(42) Sánchez, F.; Iglesias, M.; Corma, A.; del Pino, C. New rhodium complexes anchored on silica and modified Y-zeolite as efficient catalysts for hydrogenation of olefins. *J. Mol. Cat.* **1991**, *70*, 369.

(43) Bernales, V.; Yang, D.; Yu, J.; Gümüşlü, G.; Cramer, C. J.; Gates, B. C.; Gagliardi, L. Molecular Rhodium Complexes Supported on the Metal-Oxide-Like Nodes of Metal Organic Frameworks and on Zeolite HY: Catalysts for Ethylene Hydrogenation and Dimerization. *ACS Appl. Mater. Interfaces* **2017**, *9*, 33511.

(44) Govindasamy, A.; Markova, V. K.; Genest, A.; Rösch, N. Ethene hydrogenation vs. dimerization over a faujasite-supported $[\text{Rh}(\text{C}_2\text{H}_4)_2]$ complex. A computational study of mechanism. *Catal. Sci. Technol.* **2017**, *7*, 102.

(45) Liang, A. J.; Craciun, R.; Chen, M.; Kelly, T. G.; Kletnieks, P. W.; Haw, J. F.; Dixon, D. A.; Gates, B. C. Zeolite-Supported Organorhodium Fragments: Essentially Molecular Surface Chemistry Elucidated with Spectroscopy and Theory. *J. Am. Chem. Soc.* **2009**, *131*, 8460.

(46) Liang, A. J.; Bhirud, V. A.; Ehresmann, J. O.; Kletnieks, P. W.; Haw, J. F.; Gates, B. C. A Site-Isolated Rhodium–Diethylene Complex Supported on Highly Dealuminated Y Zeolite: Synthesis and Characterization. *J. Phys. Chem. B* **2005**, *109*, 24236.

(47) Genna, D. T.; Pfund, L. Y.; Samblanet, D. C.; Wong-Foy, A. G.; Matzger, A. J.; Sanford, M. S. Rhodium Hydrogenation Catalysts Supported in Metal Organic Frameworks: Influence of the Framework on Catalytic Activity and Selectivity. *ACS Catalysis* **2016**, *6*, 3569.

(48) Evans, J. D.; Sumbly, C. J.; Doonan, C. J. Post-synthetic metalation of metal-organic frameworks. *Chem. Soc. Rev.* **2014**, *43*, 5933.

(49) Gonzalez, M. I.; Bloch, E. D.; Mason, J. A.; Teat, S. J.; Long, J. R. Single-crystal-to-single-crystal metalation of a metal-organic framework: a route toward structurally well-defined catalysts. *Inorg. Chem.* **2015**, *54*, 2995.

(50) Bloch, W. M.; Burgun, A.; Doonan, C. J.; Sumbly, C. J. Probing post-synthetic metallation in metal-organic frameworks: insights from X-ray crystallography. *Chem. Commun.* **2015**, *51*, 5486.

(51) Banerjee, D.; Kim, S. J.; Parise, J. B. Lithium Based Metal–Organic Framework with Exceptional Stability. *Cryst. Growth Des.* **2009**, *9*, 2500.

(52) Park, K. S.; Ni, Z.; Côté, A. P.; Choi, J. Y.; Huang, R.; Uribe-Romo, F. J.; Chae, H. K.; O’Keeffe, M.; Yaghi, O. M. Exceptional chemical and thermal stability of zeolitic imidazolate frameworks. *Proc. Natl. Acad. Sci.* **2006**, *103*, 10186.

(53) Ibarra, I. A.; Yang, S.; Lin, X.; Blake, A. J.; Rizkallah, P. J.; Nowell, H.; Allan, D. R.; Champness, N. R.; Hubberstey, P.; Schröder, M. Highly porous and robust scandium-based metal–organic frameworks for hydrogen storage. *Chem. Commun.* **2011**, *47*, 8304.

(54) Banerjee, D.; Borkowski, L. A.; Kim, S. J.; Parise, J. B. Synthesis and Structural Characterization of Lithium-Based Metal–Organic Frameworks. *Cryst. Growth Des.* **2009**, *9*, 4922.

(55) Cavka, J. H.; Jakobsen, S.; Olsbye, U.; Guillou, N.; Lamberti, C.; Bordiga, S.; Lillerud, K. P. A New Zirconium Inorganic Building Brick Forming Metal Organic Frameworks with Exceptional Stability. *J. Am. Chem. Soc.* **2008**, *130*, 13850.

(56) Colombo, V.; Galli, S.; Choi, H. J.; Han, G. D.; Maspero, A.; Palmisano, G.; Masciocchi, N.; Long, J. R. High thermal and chemical stability in pyrazolate-bridged metal–organic frameworks with exposed metal sites. *Chem. Sci.* **2011**, *2*, 1311.

(57) DeCoste, J. B.; Peterson, G. W.; Jasuja, H.; Glover, T. G.; Huang, Y.-g.; Walton, K. S. Stability and degradation mechanisms of metal–organic frameworks containing the $Zr_6O_4(OH)_4$ secondary building unit. *J. Mater. Chem. A* **2013**, *1*, 5642.

(58) Wen, L.; Cheng, P.; Lin, W. Solvent-induced single-crystal to single-crystal transformation of a 2D coordination network to a 3D metal–organic framework greatly enhances porosity and hydrogen uptake. *Chem. Commun.* **2012**, *48*, 2846.

(59) Zhang, J.-P.; Liao, P.-Q.; Zhou, H.-L.; Lin, R.-B.; Chen, X.-M. Single-crystal X-ray diffraction studies on structural transformations of porous coordination polymers. *Chem. Soc. Rev.* **2014**, *43*, 5789.

(60) Erdogan, G.; Grotjahn, D. B. Mild and Selective Deuteration and Isomerization of Alkenes by a Bifunctional Catalyst and Deuterium Oxide. *J. Am. Chem. Soc.* **2009**, *131*, 10354.

(61) Kocen, A. L.; Klimovica, K.; Brookhart, M.; Daugulis, O. Alkene Isomerization by “Sandwich” Diimine-Palladium Catalysts. *Organometallics* **2017**, *36*, 787.

(62) Huang, Z.; White, P. S.; Brookhart, M. Ligand exchanges and selective catalytic hydrogenation in molecular single crystals. *Nature* **2010**, *465*, 598.

(63) Yagupsky, M.; Wilkinson, G. Further studies on hydridocarbonyltris(triphenylphosphine)rhodium(I). Part II. Isomerisation of n-pentenes and hex-1-ene. *J. Chem. Soc. A Inorg. Phys. Theor.* **1970**, *1*, 941.

(64) Ballesteros, P.; Lopez, C.; Lopez, C.; Claramunt, R. M.; Jimenez, J. A.; Cano, M.; Heras, J. V.; Pinilla, E.; Monge, A. (2,5-Norbornadiene)rhodium(I) complexes with bis- and tris(azol-1-yl)methanes. *Organometallics* **1994**, *13*, 289.

(65) Robertson, J. J.; Kadziola, A.; Krause, R. A.; Larsen, S. Preparation and characterization of four- and five-coordinate rhodium(I) complexes. Crystal structures of chloro(2-phenylazo)pyridine)(norbornadiene)rhodium(I), (2,2'-bipyridyl)(norbornadiene)rhodium(I) chloride hydrate, and chloro(2,2'-bipyridyl)(norbornadiene)rhodium(I). *Inorg. Chem.* **1989**, *28*, 2097.

(66) Man, B. Y. W.; Bhadbhade, M.; Messerle, B. A. Rhodium(i) complexes bearing N-donor ligands: catalytic activity towards intramolecular cyclization of alkynoic acids and ligand lability. *New J. Chem.* **2011**, *35*, 1730.

(67) Brown, J. M.; Guiry, P.J.; Price, D.W.; Hursthouse, M.B.; Karalulov, S. Chirality and the metal-alkene bond; distortions in the solution and solid-state structures of η^2 -ethene rhodium bis-oxazolinylmethane complexes. *Tetrahedron Asymmetry* **1994**, *5*, 561.

(68) Budzelaar, Peter H. M.; Moonen, Nicolle N. P.; Gelder, René d.; Smits, Jan M. M.; Gal, Anton W. Rhodium and Iridium β -Diiminate Complexes – Olefin Hydrogenation Step by Step. *Eur. J. Inorg. Chem.* **2000**, *2000*, 753.

(69) Young, R. J.; Huxley, M. T.; Pardo, E.; Champness, N. R.; Sumby, C. J.; Doonan, C. J. Isolating reactive metal-based species in Metal–Organic Frameworks – viable strategies and opportunities. *Chem. Sci.* **2020**, *11*, 4031.

(70) Meißner, A.; Preetz, A.; Drexler, H.-J.; Baumann, W.; Spannenberg, A.; König, A.; Heller, D. In Situ Synthesis of Neutral Dinuclear Rhodium Diphosphine Complexes $[\{\text{Rh}(\text{diphosphine})(\mu_2\text{-X})\}_2]$: Systematic Investigations. *ChemPlusChem* **2015**, *80*, 169.

(71) Yang, D.; Odoh, S. O.; Wang, T. C.; Farha, O. K.; Hupp, J. T.; Cramer, C. J.; Gagliardi, L.; Gates, B. C. Metal–Organic Framework Nodes as Nearly Ideal Supports for Molecular Catalysts: NU-1000- and UiO-66-Supported Iridium Complexes. *J. Am. Chem. Soc.* **2015**, *137*, 7391.

(72) Yang, D.; Odoh, S. O.; Borycz, J.; Wang, T. C.; Farha, O. K.; Hupp, J. T.; Cramer, C. J.; Gagliardi, L.; Gates, B. C. Tuning Zr_6 Metal–Organic Framework (MOF) Nodes as Catalyst Supports: Site Densities and Electron-Donor Properties Influence Molecular Iridium Complexes as Ethylene Conversion Catalysts. *ACS Catalysis* **2016**, *6*, 235.

(73) Goswami, S.; Noh, H.; Redfern, L. R.; Otake, K.-i.; Kung, C.-W.; Cui, Y.; Chapman, K. W.; Farha, O. K.; Hupp, J. T. Pore-Templated Growth of Catalytically Active Gold Nanoparticles within a Metal–Organic Framework. *Chem. Mater.* **2019**, *31*, 1485.

(74) Schrock, R. R.; Osborn, J. A. Catalytic hydrogenation using cationic rhodium complexes. I. Evolution of the catalytic system and the hydrogenation of olefins. *J. Am. Chem. Soc.* **1976**, *98*, 2134.

(75) Iglesias, M.; Del Pino, C.; Corma, A.; Garcia-Blanco, S.; Martinez Carrera, S. Rhodium complexes with phosphine and diazabutadiene ligands. Their properties as hydrogenation catalysts. Molecular structure of $\text{RhCl}(\text{COD})\text{P}(\text{p-C}_6\text{H}_4\text{F})_3$. *Inorg. Chim. Acta* **1987**, *127*, 215.

(76) Preetz, A.; Drexler, H.-J.; Fischer, C.; Dai, Z.; Börner, A.; Baumann, W.; Spannenberg, A.; Thede, R.; Heller, D. Rhodium-Complex-Catalyzed Asymmetric Hydrogenation: Transformation of Precatalysts into Active Species. *Chem. Eur. J.* **2008**, *14*, 1445.

(77) Smidt, S. P.; Zimmermann, N.; Studer, M.; Pfaltz, A. Enantioselective hydrogenation of alkenes with iridium-PHOX catalysts: a kinetic study of anion effects. *Chem. Eur. J.* **2004**, *10*, 4685.

(78) Chen, J.; Wang, J.; Guo, L.; Li, L.; Yang, Q.; Zhang, Z.; Yang, Y.; Bao, Z.; Ren, Q. Adsorptive Separation of Geometric Isomers of 2-Butene on Gallate-Based Metal–Organic Frameworks. *ACS Appl. Mater. Interfaces* **2020**, *12*, 9609.

(79) Kanai, H.; Choe, S. B.; Klabunde, K. J. Isomerization of 1-butene catalyzed by (η -6-arene)NiR₂. A very active homogeneous catalyst system. *J. Am. Chem. Soc.* **1986**, *108*, 2019.

(80) Tolman, C. A. Chemistry of tetrakis(triethyl phosphite)nickel hydride, HNi[P(OEt)₃]⁴⁺. *J. Am. Chem. Soc.* **1972**, *94*, 2994.

(81) Sen, A.; Lai, T. W. Mechanism of palladium(II)-catalyzed carbon-carbon double bond isomerization in olefins. *Inorganic Chemistry* **1984**, *23*, 3257.

(82) Xiao, D. J.; Oktawiec, J.; Milner, P. J.; Long, J. R. Pore Environment Effects on Catalytic Cyclohexane Oxidation in Expanded Fe₂(dobdc) Analogues. *J. Am. Chem. Soc.* **2016**, *138*, 14371.

(83) Willems, T. F.; Rycroft, C. H.; Kazi, M.; Meza, J. C.; Haranczyk, M. Algorithms and tools for high-throughput geometry-based analysis of crystalline porous materials. *Micropor. Mesopor. Mat.* **2012**, *149*, 134.

(84) Ongari, D.; Boyd, P. G.; Barthel, S.; Witman, M.; Haranczyk, M.; Smit, B. Accurate Characterization of the Pore Volume in Microporous Crystalline Materials. *Langmuir* **2017**, *33*, 14529.

(85) Becke, A. D. Density-functional exchange-energy approximation with correct asymptotic behavior. *Phys. Rev. A* **1988**, *38*, 3098.

(86) Perdew, J. P. Density-functional approximation for the correlation energy of the inhomogeneous electron gas. *Phys. Rev. B* **1986**, *33*, 8822.

(87) Neese, F. The ORCA program system. *WIREs Comp. Mol. Sci.* **2012**, *2*, 73.

(88) Neese, F. Software update: the ORCA program system, version 4.0. *WIREs Comp. Mol. Sci.* **2018**, *8*, e1327.

(89) Neese, F.; Wennmohs, F.; Hansen, A.; Becker, U. Efficient, approximate and parallel Hartree–Fock and hybrid DFT calculations. A ‘chain-of-spheres’ algorithm for the Hartree–Fock exchange. *Chem. Phys.* **2009**, *356*, 98.

(90) Weigend, F.; Ahlrichs, R. Balanced basis sets of split valence, triple zeta valence and quadruple zeta valence quality for H to Rn: Design and assessment of accuracy. *Phys. Chem. Chem. Phys.* **2005**, *7*, 3297.

(91) Weigend, F. Accurate Coulomb-fitting basis sets for H to Rn. *Phys. Chem. Chem. Phys.* **2006**, *8*, 1057.

(92) Grimme, S.; Ehrlich, S.; Goerigk, L. Effect of the damping function in dispersion corrected density functional theory. *J. Comput. Chem.* **2011**, *32*, 1456.

(93) Henkelman, G.; Jónsson, H. Improved tangent estimate in the nudged elastic band method for finding minimum energy paths and saddle points. *J. Chem. Phys.* **2000**, *113*, 9978.

(94) Dubbeldam, D.; Calero, S.; Ellis, D. E.; Snurr, R. Q. RASPA: molecular simulation software for adsorption and diffusion in flexible nanoporous materials. *Mol Simul.* **2016**, *42*, 81.

(95) Wick, C. D.; Martin, M. G.; Siepmann, J. I. Transferable Potentials for Phase Equilibria. 4. United-Atom Description of Linear and Branched Alkenes and Alkylbenzenes. *J. Phys. Chem. B* **2000**, *104*, 8008.

(96) Rappe, A. K.; Casewit, C. J.; Colwell, K. S.; Goddard, W. A.; Skiff, W. M. UFF, a full periodic table force field for molecular mechanics and molecular dynamics simulations. *J. Am. Chem. Soc.* **1992**, *114*, 10024.

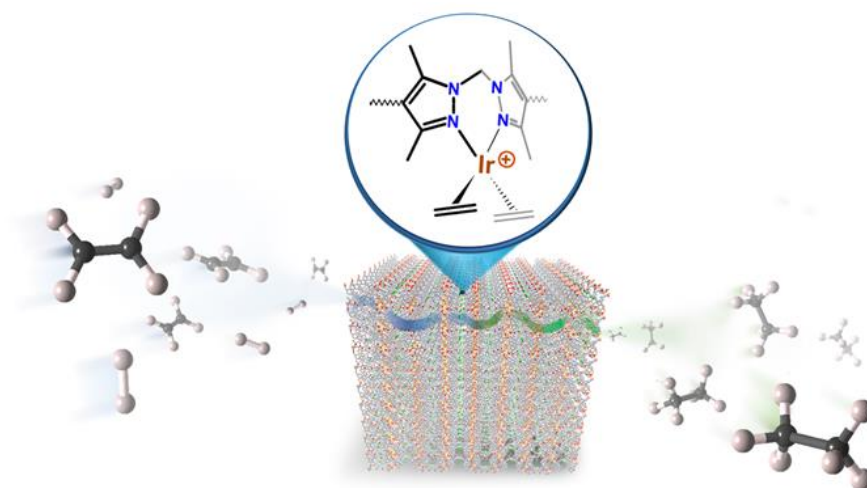
Chapter 4. A Metal-organic Framework Supported Iridium Catalyst for the Gas Phase Hydrogenation of Ethylene

Ricardo A. Peralta,^a Michael T. Huxley,^a Zhaolin Shi,^b Yue-Biao Zhang,^b Christopher J. Sumby^{*a}
and Christian J. Doonan^{*a}

^a Department of Chemistry and the Centre for Advanced Nanomaterials, The University of Adelaide, Adelaide, SA 5005, Australia.

^b School of Physical Science and Technology, ShanghaiTech University, Shanghai, 201210, China

Peralta, R. A., Huxley, M. T., Shi, Z., Zhang, Y.-B., Sumby C. J., Doonan, C. J., A Metal-organic Framework Supported Iridium Catalyst for the Gas Phase Hydrogenation of Ethylene, *Chem. Commun.*, 2020, 56, 15313–15316.



Statement of Authorship

Title of Paper	A Metal-organic Framework Supported Iridium Catalyst for the Gas Phase Hydrogenation of Ethylene
Publication Status	<input checked="" type="checkbox"/> Published <input type="checkbox"/> Accepted for Publication <input type="checkbox"/> Submitted for Publication <input type="checkbox"/> Unpublished and Unsubmitted work written in manuscript style
Publication Details	Peralta, R. A., Huxley, M. T., Shi, Z., Zhang, Y.-B., Sumbly C. J., Doonan, C. J., A Metal-organic Framework Supported Iridium Catalyst for the Gas Phase Hydrogenation of Ethylene, Chem. Commun., 2020, 56, 15313–15316.

Principal Author

Name of Principal Author (Candidate)	Ricardo A. Peralta
Contribution to the Paper	Design and development of the project. Preparation of samples and collection of data. Analysis and interpretation of gas-phase NMR and X-Ray crystallography data. Preparation and drafting of the manuscript.
Overall percentage (%)	70%
Certification:	This paper reports on original research I conducted during the period of my Higher Degree by Research candidature and is not subject to any obligations or contractual agreements with a third party that would constrain its inclusion in this thesis. I am the primary author of this paper.
Signature	Date 23/2/21

Co-Author Contributions

By signing the Statement of Authorship, each author certifies that:

- i. the candidate's stated contribution to the publication is accurate (as detailed above);
- ii. permission is granted for the candidate to include the publication in the thesis; and
- iii. the sum of all co-author contributions is equal to 100% less the candidate's stated contribution.

Name of Co-Author	Michael T. Huxley
Contribution to the Paper	Assisted with the conception of the project, sample preparation, collection of X-Ray crystallography data and drafting the manuscript.
Signature	Date 19/03/2021

Name of Co-Author	Zhaolin Shi
Contribution to the Paper	Assisted with collection of X-Ray crystallography data.
Signature	Date

Name of Co-Author	Yue-Biao Zhang		
Contribution to the Paper	Assisted with collection of X-Ray crystallography data.		
Signature		Date	

Name of Co-Author	Christopher J. Sumbly		
Contribution to the Paper	Assisted with the conception of the project, analysis of data and preparation of the manuscript.		
Signature		Date	17/01/2021

Name of Co-Author	Christian J. Doonan		
Contribution to the Paper	Assisted with the conception of the project, analysis of data and preparation of the manuscript.		
Signature		Date	17/01/2021

Statement of Authorship

Title of Paper	A Metal-organic Framework Supported Iridium Catalyst for the Gas Phase Hydrogenation of Ethylene
Publication Status	<input checked="" type="checkbox"/> Published <input type="checkbox"/> Accepted for Publication <input type="checkbox"/> Submitted for Publication <input type="checkbox"/> Unpublished and Unsubmitted work written in manuscript style
Publication Details	Peralta, R. A., Huxley, M. T., Shi, Z., Zhang, Y.-B., Sumbly C. J., Doonan, C. J., A Metal-organic Framework Supported Iridium Catalyst for the Gas Phase Hydrogenation of Ethylene, Chem. Commun., 2020, 56, 15313–15316

Principal Author

Name of Principal Author (Candidate)	Ricardo A. Peralta		
Contribution to the Paper	Design and development of the project. Preparation of samples and collection of data. Analysis and interpretation of gas-phase NMR and X-Ray crystallography data. Preparation and drafting of the manuscript.		
Overall percentage (%)	70%		
Certification	This paper reports on original research I conducted during the period of my Higher Degree by Research candidature and is not subject to any obligations or contractual agreements with a third party that would constrain its inclusion in this thesis. I am the primary author of this paper.		
Signature		Date	23/2/21

Co-Author Contributions

By signing the Statement of Authorship, each author certifies that

the candidate's **stated contribution to the publication is accurate (as detailed above)**;

permission is granted for the candidate to include the publication in the thesis, and

the sum of all co-author contributions is equal to 100% less the candidate's **stated contribution**.

Name of Co-Author	Zhaolin Shi		
Contribution to the Paper	Assisted with collection of X-Ray crystallography data		
Signature		Date	2021.3.17

Name of Co-Author	Yue-Biao Zhang		
Contribution to the Paper	Assisted with collection of X-Ray crystallography data		
Signature		Date	

v

4.1 Abstract

The mutable structures of Metal-organic Frameworks (MOFs) allow their use as novel supports for transition metal catalysts. Herein we prepare an iridium bis(ethylene) catalyst bound to the neutral N-donors of a MOF structure and show that the compound is a stable gas phase ethylene hydrogenation catalyst. The data illustrate the need to carefully consider the inner sphere (support) and outer sphere (anion) chemistry.

4.2 Introduction

Metal-organic Frameworks (MOFs) are a class of porous, crystalline materials, that are comprised of metal nodes interconnected by organic linkers to produce open networked structures.^{1,2} Due to their modular synthesis, crystallinity and high porosity, MOFs are attractive platform materials for exploring the gas phase activity of well-defined molecular catalysts in a heterogeneous environment.³ Two strategies that have been employed to successfully incorporate discrete organometallic catalysts within MOF pores are: 1) anchoring to the metal oxide nodes;⁴⁻⁶ and 2) binding to donor sites built into the organic linkers.^{3,7-12} Examples of the former have been reported by the groups of Gates, Gagliardi and Farha who showed that the nature of the support has a marked influence on the chemistry of Ir and Ni ethylene hydrogenation catalysts bound to the metal nodes of Zr and Hf-based MOFs.⁴⁻⁶ Recently, we showed that a Rh(I) organometallic catalyst, **1**·[Rh(C₂H₄)₂]X (X=Cl, BF₄), bound to the organic backbone of a manganese-based MOF (**1**, [Mn₃L₃] (L = bis-(4-carboxyphenyl-3,5-dimethyl-pyrazol-1-yl)methane)) via bispyrazole moieties was also active for the gas phase hydrogenation of ethylene.³ In contrast to the aforementioned Ir and Ni systems, the Rh cation is supported by neutral nitrogen donors rather than charged oxygen atoms and thus a counter anion is required for charge balance. Interestingly, we found that the activity of the catalyst was highly anion dependent; the [rhodium]BF₄ showed much greater activity than the [rhodium]Cl complex. Additionally, we observed that the Rh centers were prone to deactivation via the formation of nanoparticles under an excess of hydrogen. To further explore gas phase hydrogenation chemistry in **1** and expand our fundamental knowledge of MOFs as supports for site-isolated molecular catalysts we installed an Ir(I) bis-ethylene organometallic catalyst into the pores of **1** and examined its reactivity towards ethylene

hydrogenation in the gas phase. We found that the Ir catalyst is more stable towards hydrogen gas than the corresponding Rh species. Furthermore, we again observed that the catalytic activity is anion dependent, however, for the Ir catalyst the chloride complex shows greater reactivity than the BF_4 species.

4.3 Results and discussion

Using a post-synthetic metalation (PSMet) process developed to prepare $\mathbf{1}\cdot[\text{Rh}(\text{C}_2\text{H}_4)_2]\text{X}$ ($\text{X} = [\text{RhCl}_2(\text{C}_2\text{H}_4)_2]^-$, Cl^- , BF_4^-),³ we reacted MOF **1** with $[\text{Ir}(\text{C}_2\text{H}_4)_2\text{Cl}]_2$ in ethanol at 65 °C under an ethylene atmosphere for three days (Figure 4.1 and 7.3.5.3). This provided the iridium metalated MOF, $\mathbf{1}\cdot\text{IrCl}$ (Figure 4.1). To determine the extent of metalation, the yellow crystals of $\mathbf{1}\cdot\text{IrCl}$ were examined by Energy Dispersive X-ray (EDX) analysis. The data indicated ca. 85% occupancy of the chelation sites in **1**, and an Ir:Cl ratio of 1:1. Furthermore, the bulk crystallinity of $\mathbf{1}\cdot\text{IrCl}$, post metalation, was confirmed by Powder X-ray Diffraction (PXRD) data (Figure 7.3.4.1).

The excellent condition of $\mathbf{1}\cdot\text{IrCl}$ single crystals prompted us to investigate the coordination sphere of the iridium centers using single crystal X-ray diffraction (SCXRD). However, refinement of the structure indicated considerable disorder of the metalation site (Figure 4.1b). With the MOF backbone in place, a structural model was developed of the disordered metalation site by considering the electron density map and considering spectroscopic data for the sample. This reveals the main species is a bis(ethylene) complex of iridium, $\mathbf{1}\cdot[\text{Ir}(\text{C}_2\text{H}_4)_2\text{Cl}]$ (referred to from this point as $\mathbf{1}\cdot\text{IrCl}(\text{ETH})$); the Ir3B atom is modelled with a site occupancy factor of 0.25, 50% occupancy of the metalation site due to the mirror plane. An ethylene ligand is bonded with Ir3B-C with bond lengths of 2.256(19) and 2.25(2) Å and slightly canted, as observed for the Rh(I) complex.³ A Cl atom was modelled with 0.25 occupancy bound to an axial coordination site of the iridium center (Ir3B-Cl 2.646(13) Å). Unusually for this MOF, the linker where post-synthetic metalation occurs is identifiably disordered (B:A = 0.75:0.25) and the electron density map supports a second, low occupancy Ir position (Ir3A, 0.05, 10% occupancy) giving a total Ir occupancy of 0.6 that is slightly less than that determined by EDX analysis. Another Cl site, also refined at 0.05 to match the Ir3A occupancy, was located in the MOF pore in the pocket normally occupied by anions.^{3,13} The coordination

environment of this second component could not be determined but partially occupied CO and ethylene ligands were included in the formula based on the spectroscopic evidence (see below). Together, these components suggest that the Ir center in $\mathbf{1}\cdot\text{IrCl}$ is a mixture of the target bis-ethylene complex ($\mathbf{1}\cdot\text{IrCl}(\text{ETH})$) and a potential carbonyl ethylene Ir(I) complex ($\mathbf{1}\cdot\text{IrCl}(\text{ETH}/\text{CO})$) (Figure 4.1b).

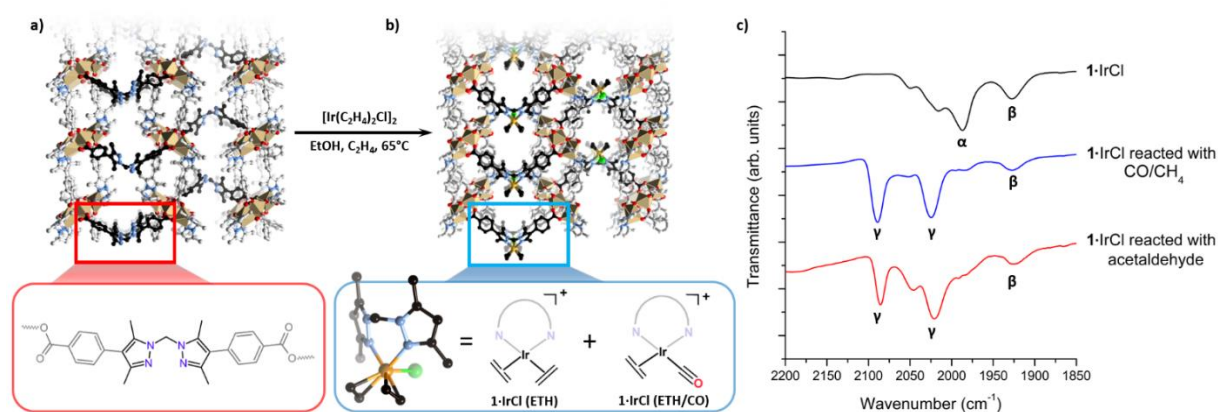


Figure 4.1. (a) A perspective view of the X-ray crystal structure of MOF **1** and a representation of the ligand moiety shown in the enlargement. (b) Post-synthetic metalation of **1** with $[\text{Ir}(\text{C}_2\text{H}_4)_2\text{Cl}]_2$ yields $\mathbf{1}\cdot\text{IrCl}$, while the expanded panel shows that the chelated Ir center can be modelled as a bis-ethylene Ir(I) chloride complex ($\mathbf{1}\cdot\text{IrCl}(\text{ETH})$) with an adjacent low occupancy Ir center with an un-resolved coordination sphere, likely corresponding to the monocarbonyl ethylene Ir(I) ($\mathbf{1}\cdot\text{IrCl}(\text{ETH}/\text{CO})$) complex observed via IR spectroscopy (Ir, orange; Cl, green; C, black/grey; N, blue; O, red; Mn, beige; H omitted for clarity). (c) IR spectra of $\mathbf{1}\cdot\text{IrCl}$ as synthesized, following exposure to CO/CH₄ and following reaction with acetaldehyde in ethanol, displaying the changes in the CO stretching region. Bands attributed to Ir(I) monocarbonyl complexes are labelled α and β while the gem dicarbonyl stretches of $\mathbf{1}\cdot[\text{Ir}(\text{CO})_2]$ are labelled γ .

To probe the coordination sphere of the Ir sites, we activated samples of $\mathbf{1}\cdot\text{IrCl}$ and analyzed the headspace above the sample with gas phase NMR following exposure to CO and H₂, respectively. The enhanced binding strength of CO in comparison to ethylene will convert putative $\mathbf{1}\cdot\text{IrCl}(\text{ETH})$ to $\mathbf{1}\cdot[\text{Ir}(\text{CO})_2]$ and allow direct measurement of bound ethylene in the reaction headspace. Furthermore, bound ethylene can be measured by the introduction of H₂ which will reduce the ethylene ligand to ethane. These experiments confirmed the presence of slightly more than one molecule of ethylene per Ir site (see Chapter 7.3.7.2). Thus, these

data are consistent with a significant proportion of the iridium in **1**·IrCl being **1**·IrCl(ETH) but also support the formation of the additional **1**·IrCl(ETH/CO) species observed by SCXRD.

To investigate this second Ir species, IR spectroscopy measurements were conducted on the metalated MOF crystals. The presence of weak stretches between 1925-2080 cm^{-1} that could not be assigned to **1**·IrCl(ETH) (Figure 4.2a, C=C stretches typically observed below 1600 cm^{-1})¹⁴⁻¹⁶ also indicate an additional species is present. Although bis-ethylene Ir(I) complexes of substituted tris-pyrazolylborates and tris-pyrazolylmethanes are known to form Ir(III) alkyl hydride complexes upon heating,¹⁷⁻¹⁹ the Ir-H stretches (or the crotyl hydrides that subsequently form) appear at higher wavenumbers (2100 to 2200 cm^{-1})¹⁷ and are thus inconsistent with the data for **1**·IrCl. As eluded to in the structural discussion above, we advance that the IR stretches observed in the spectrum of **1**·IrCl correspond to C≡O stretches from an Ir-CO moiety formed via the decarbonylation of ethanol during the PSMet of **1**.^{20-22,15} We note that this chemistry has been observed for P,N,P-pincer complexes of Ir(I).^{20,22} Alcohol decarbonylation by simple Ir(I) complexes is thought to proceed via dehydrogenation of the alcohol to form the corresponding aldehyde which can subsequently undergo decarbonylation to form an Ir(III) monocarbonyl complex (Figure 4.2b).²⁰⁻²² The three day reaction time and relatively high temperature (65 °C) needed for metalation of **1** with $[\text{Ir}(\text{C}_2\text{H}_4)_2\text{Cl}]_2$ would provide suitable conditions for this reaction. To confirm that the CO originates from decarbonylation of ethanol, we performed two experiments: first, we metalated **1** with $[\text{Ir}(\text{C}_2\text{H}_4)_2\text{Cl}]_2$ in the presence of the expected aldehyde intermediate, acetaldehyde. After three days at 65 °C, the MOF crystals were analyzed by IR spectroscopy which revealed a more pronounced monocarbonyl C≡O stretching band at 1980 cm^{-1} (Figure 7.3.8.2) and additional bands centered at 2088 and 2024 cm^{-1} which correspond to an Ir(I) dicarbonyl species (See Figure 4.2b for proposed reaction mechanism). Secondly, we reacted **1**·IrCl crystals with acetaldehyde at 65 °C in ethanol and observed a similar increase in the intensity of the CO stretches and formation of the dicarbonyl complex (Figure 4.2a). The appearance of higher intensity CO stretching bands in the presence of acetaldehyde supports the hypothesis that ethanol decarbonylation is the origin of the unexpected carbonyl species present in **1**·IrCl.

The relatively low intensity of the $\nu(\text{C}\equiv\text{O})$ stretches indicates that carbonyl complexes are a minor component of the Ir species in **1**·IrCl. Thus, the combination of SCXRD, NMR and IR evidence suggests that **1**·IrCl is mainly the targeted **1**·IrCl(ETH) species (ca. 66%), which is

anticipated to be a promising catalyst for gas-phase hydrogenation, and a mixture of Ir carbonyl complexes formed during synthesis, predominantly $\mathbf{1}\cdot\text{IrCl}(\text{ETH}/\text{CO})$ (ca. 34%). Despite extensive attempts to form pure $\mathbf{1}\cdot[\text{Ir}(\text{C}_2\text{H}_4)_2]$, metalation in solvents other than ethanol was unsuccessful either due to decomposition of the Ir(I) precursor or the unfavorable arrangement of the pyrazole sites of the MOF in these solvents.²³

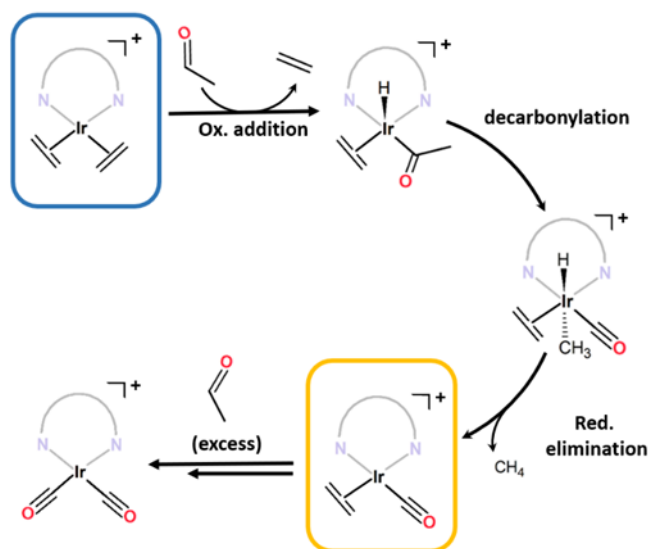


Figure 4.2. The proposed mechanism via which mono- and dicarbonyl complexes are generated from decarbonylation of acetaldehyde. The target bis(ethylene) complex $\mathbf{1}\cdot\text{IrCl}(\text{ETH})$ and the $\mathbf{1}\cdot\text{IrCl}(\text{ETH}/\text{CO})$ by product that is also observed are shown in the blue and yellow boxes. Acetaldehyde can be formed by dehydrogenation of ethanol.

Given our previous observation that the coordinating tendency of the anion can significantly impact the catalytic activity of organometallic catalysts loaded into $\mathbf{1}$,³ we exchanged the chloride anion in $\mathbf{1}\cdot\text{IrCl}$ for tetrafluoroborate using facile anion exchange with NaBF_4 in methanol under an ethylene atmosphere (Chapter 7.3.1.3). EDX analysis confirmed complete removal of chloride from the sample (Table 7.3.1). IR spectroscopy revealed minor changes in the position of the CO stretches (2020 cm^{-1}) (Figure 7.3.8.1). The sample was determined to be ca. 58% $\mathbf{1}\cdot\text{IrBF}_4(\text{ETH})$ and 42% $\mathbf{1}\cdot\text{IrBF}_4(\text{ETH}/\text{CO})$ based on spectroscopic analysis, noting that this might be a slight over estimation of the latter due to facile loss of ethylene in $\mathbf{1}\cdot\text{IrBF}_4$.

With an enhanced understanding of the sample composition, we investigated the stability of **1**·IrCl and **1**·IrBF₄ towards activation and hydrogen exposure. Activation from dry pentane at room temperature for 2 hr yielded surface areas of 575 and 462 m²g⁻¹, for **1**·IrCl and **1**·IrBF₄ respectively, which are consistent with that observed for other metalated samples of **1**.²⁴ Activated samples of **1**·IrCl and **1**·IrBF₄ were exposed to pure hydrogen (1 bar), and unlike the analogous **1**·[Rh(C₂H₄)₂]X samples,³ the crystals did not become black (due to formation of Rh nanoparticles) but instead transformed from pale yellow to off-white. Furthermore, Transition Electron Microscopy (TEM) analysis of the sample showed no evidence of Ir nanoparticles (see Chapter 7.3.3). We then studied the gas-phase hydrogenation of ethylene using **1**·IrCl and **1**·IrBF₄ in a 1:1 mixture of ethylene and hydrogen (2 bar) at 46 °C. Using gas-phase NMR to monitor the evolution of the reaction within a sealed high-pressure NMR tube, we observed the conversion of ethylene to ethane and consumption of hydrogen (**1**·IrCl: initial TOF^{15%} 44 hr⁻¹, average TOF^{15%} over four cycles: 49 hr⁻¹). Both catalysts are active with the **1**·IrCl material retaining consistent activity over the course of four successive cycles (Figure 4.3b). The BF₄ derivative is more active initially (TOF^{20%} of 95 hr⁻¹) but loses some activity on cycling (average TOF^{15%} over cycles 2-4: 24 hr⁻¹). This suggests that the chloride anion plays a role in stabilizing the active catalyst, as has been observed in alcohol decarbonylation catalysis using molecular iridium catalysts.²¹

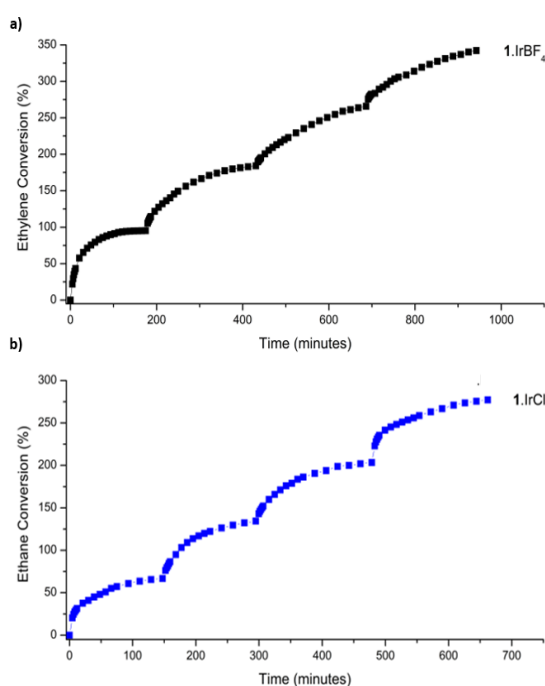


Figure 4.3. Catalysis data for the hydrogenation of ethylene at 46°C (2 bar) using (a) **1**·IrBF₄ and (b) **1**·IrCl

The average TOF^{15%} over four cycles of 49 hr⁻¹ demonstrated by **1**·IrCl is comparable to the activity reported for MOF-node supported [Ir(C₂H₄)₂] species,⁴ although it most likely underestimates the activity of **1**·IrCl(ETH) due to the presence of less active carbonyl species.²⁵ Various studies have investigated the gas phase ethylene hydrogenation activity of [Ir(C₂H₄)₂] complexes supported on the inorganic nodes of the MOFs UiO-66, UiO-67 and NU-1000, as well as zeolite and MgO supports.^{4,25-28} Under flow-reaction conditions operating at room temperature, these systems typically display TOFs up to 62 hr⁻¹ for the MOF supported systems and up to 2160 hr⁻¹ on HY Zeolite.²⁶ Notably, these complexes are rendered charge neutral via the support, negating the need for the charge balancing anions employed in **1**·IrCl and **1**·IrBF₄. Furthermore, the electron donating or withdrawing ability of the support plays a significant role in the catalytic activity of the supported Ir complex.^{25,26} The highly acidic Al sites in HY Zeolite generate electron deficient Ir centers which promote rapid hydrogenation (TOF 2160 hr⁻¹) due to their tendency to interact with and activate several reagent molecules simultaneously.^{25,29} Based on comparison of the $\nu(\text{C}\equiv\text{O})$ stretching frequencies of zeolite-supported gem-dicarbonyl complexes (2109, 2038 cm⁻¹)²⁵ and our system (2088, 2025 cm⁻¹), the Ir center in **1**·IrCl is more electron rich and therefore less active in hydrogenation (although it appears intermediate between Zeolite and MOF-node supported Ir centres,^{4,26} for example UiO-66 node-supported [Ir(CO)₂]: $\nu(\text{C}\equiv\text{O})$ 2074 cm⁻¹, 1996 cm⁻¹).

4.4 Conclusions

In conclusion, metalation of a porous MOF with [Ir(C₂H₄)₂Cl]₂ resulted in a solid-state catalyst active towards ethylene hydrogenation. A combination of SCXRD, IR and NMR spectroscopy, and EDX analysis elucidated that the MOF pores were decorated with non-homogeneous single-atom active sites including **1**·IrCl(ETH) and carbonyl ligated by-products e.g. **1**·IrCl(ETH/CO). The Ir(I) ethylene complexes are stable catalysts (cycled 4 times with retention of activity) that compare favorably with MOF node supported variants in terms of activity. Furthermore, we found that the use of a neutral support allows for modulation of catalyst activity and stability via the counter anion. This work expands our knowledge of MOFs as

supports for single site catalysts and shows how the chemistry can be tuned by both inner and outer-sphere effects.

4.5 Associated content

Supporting information: characterization data for the MOF samples, IR spectroscopic data, gas adsorption data, additional gas phase NMR spectroscopy, powder X-ray diffraction data and details of the SCXRD and tables of crystallography data collection and refinement parameters, crystallographic information file (cif).

4.6 Acknowledgment

CJS and CJD gratefully acknowledge the Australian Research Council for funding (DP190101402). This research was undertaken in part using the MX1 and MX2 beamlines at the Australian Synchrotron, part of ANSTO, and made use of the Australian Cancer Research Foundation (ACRF) detector. RAP gratefully acknowledges Adelaide Scholarship International.

4.7 References

1. H. Furukawa, K. E. Cordova, M. O'Keeffe and O. M. Yaghi, *Science*, 2013, **341**, 974-985.
2. O. M. Yaghi, M. O'Keeffe, N. W. Ockwig, H. K. Chae, M. Eddaoudi and J. Kim, *Nature*, 2003, **423**, 705-714.
3. R. A. Peralta, M. T. Huxley, J. D. Evans, T. Fallon, H. Cao, M. He, X. S. Zhao, S. Agnoli, C. J. Sumby and C. J. Doonan, *J. Am. Chem. Soc.*, 2020, **142**, 13533-13543.
4. D. Yang, S. O. Odoh, T. C. Wang, O. K. Farha, J. T. Hupp, C. J. Cramer, L. Gagliardi and B. C. Gates, *J. Am. Chem. Soc.*, 2015, **137**, 7391-7396.
5. X. Wang, X. Zhang, R. Pandharkar, J. Lyu, D. Ray, Y. Yang, S. Kato, J. Liu, M. C. Wasson, T. Islamoglu, Z. Li, J. T. Hupp, C. J. Cramer, L. Gagliardi and O. K. Farha, *ACS Catalysis*, 2020, **10**, 8995-9005.

6. V. Bernales, D. Yang, J. Yu, G. Gümüşlü, C. J. Cramer, B. C. Gates and L. Gagliardi, *ACS Appl. Mater. Interfaces*, 2017, **9**, 33511-33520.
7. X. Feng, Y. Song, Z. Li, M. Kaufmann, Y. Pi, J. S. Chen, Z. Xu, Z. Li, C. Wang and W. Lin, *J. Am. Chem. Soc.*, 2019, **141**, 11196-11203.
8. T. Sawano, Z. Lin, D. Boures, B. An, C. Wang and W. Lin, *J. Am. Chem. Soc.*, 2016, **138**, 9783-9786.
9. T. Sawano, P. Ji, A. R. Mclsaac, Z. Lin, C. W. Abney and W. Lin, *Chem Sci*, 2015, **6**, 7163-7168.
10. A. Burgun, C. J. Coghlan, D. M. Huang, W. Chen, S. Horike, S. Kitagawa, J. F. Alvino, G. F. Metha, C. J. Sumbly and C. J. Doonan, *Angew. Chem., Int. Ed. Engl.*, 2017, **56**, 1-6.
11. R. J. Young, M. T. Huxley, E. Pardo, N. R. Champness, C. J. Sumbly and C. J. Doonan, *Chem. Sci.*, 2020, **11**.
12. M. I. Gonzalez, E. D. Bloch, J. A. Mason, S. J. Teat and J. R. Long, *Inorg. Chem.*, 2015, **54**, 2995-3005.
13. M. T. Huxley, R. J. Young, W. M. Bloch, N. R. Champness, C. J. Sumbly and C. J. Doonan, *Organometallics*, 2019, **38**, 3412-3418.
14. H. Huber, G. A. Ozin and W. J. Power, *J. Am. Chem. Soc.*, 1976, **98**, 6508-6511.
15. J. Hirsch, S. DeBeer George, E. I. Solomon, B. Hedman, K. O. Hodgson and J. N. Burstyn, *Inorganic Chemistry*, 2001, **40**, 2439-2441.
16. S. B. Mohsin, M. Trenary and H. J. Robota, *The Journal of Physical Chemistry*, 1991, **95**, 6657-6661.
17. I. I. Padilla-Martínez, M. L. Poveda, E. Carmona, M. A. Monge and C. Ruiz-Valero, *Organometallics*, 2002, **21**, 93-104.
18. C. K. Ghosh, J. K. Hoyano, R. Krentz and W. A. G. Graham, *J. Am. Chem. Soc.*, 1989, **111**, 5480-5481.
19. Y. Alvarado, O. Boutry, E. Gutiérrez, A. Monge, M. C. Nicasio, M. L. Poveda, P. J. Pérez, C. Ruíz, C. Bianchini and E. Carmona, *Chemistry a European Journal*, 1997, **3**, 860-873.
20. J. G. Melnick, A. T. Radosevich, D. Villagran and D. G. Nocera, *Chem. Commun. (Camb)*, 2010, **46**, 79-81.
21. E. P. Olsen and R. Madsen, *Chemistry*, 2012, **18**, 16023-16029.
22. S. M. H. Kloek, D.M.; Goldberg, K.I, *Organometallics*, 2006, **25**, 3007-3011.

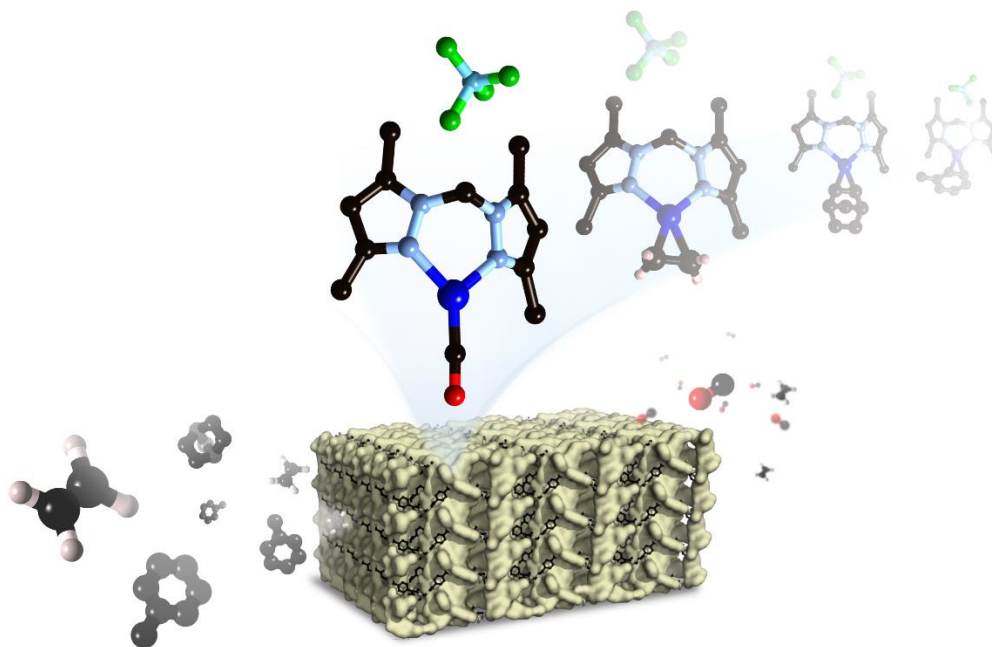
23. R. Peralta, M. Huxley, R. Young, O. M. Linder-Patton, J. D. Evans, C. J. Doonan and C. J. Sumbly, *Faraday Discuss.*, 2021, **225**, 84.
24. W. M. Bloch, A. Burgun, C. J. Coghlan, R. Lee, M. L. Coote, C. J. Doonan and C. J. Sumbly, *Nat. Chem.*, 2014, **6**, 906-912.
25. J. Lu, P. Serna and B. C. Gates, *ACS Catalysis*, 2011, **1**, 1549-1561.
26. D. Yang, S. O. Odoh, J. Borycz, T. C. Wang, O. K. Farha, J. T. Hupp, C. J. Cramer, L. Gagliardi and B. C. Gates, *ACS Catal.*, 2016, **6**, 235-247.
27. A. G. Uzun, B.C., *J. Am. Chem. Soc.*, 2009, **131**, 15887-15894.
28. A. Uzun, V. A. Bhirud, P. W. Kletnieks, J. F. Haw and B. C. Gates, *The Journal of Physical Chemistry C*, 2007, **111**, 15064-15073.
29. J. Lu, P. Serna, C. Aydin, N. D. Browning and B. C. Gates, *J. Am. Chem. Soc.*, 2011, **133**, 16186-16195.

Chapter 5: Single-crystal to Single-crystal transformations of MOF-supported, site-isolated trigonal planar Cu(I) complexes with labile ligands

Ricardo A. Peralta,^a Michael T. Huxley,^a Jorge Albalad,^a Christopher J. Sumbly^{a*}
and Christian J. Doonan^{a*}

^a Centre for Advanced Nanomaterials and Department of Chemistry, The University of Adelaide, North Terrace, Adelaide, SA 5000, Australia. Email: (CJS); (CJD)

Paper submitted to Inorganic Chemistry.



Statement of Authorship

Title of Paper	Single-crystal to Single-crystal transformations of MOF-supported, site-isolated trigonal planar Cu(I) complexes with labile ligands
Publication Status	<input type="checkbox"/> Published <input type="checkbox"/> Accepted for Publication <input checked="" type="checkbox"/> Submitted for Publication <input type="checkbox"/> Unpublished and Unsubmitted work written in manuscript style
Publication Details	Paper submitted to Inorganic Chemistry

Principal Author

Name of Principal Author (Candidate)	Ricardo A. Peralta
Contribution to the Paper	Design, development, and subsequent characterization of the samples for this project. Analysis and interpretation of the crystal structures. Preparation of the manuscript.
Overall percentage (%)	70%
Certification:	This paper reports on original research I conducted during the period of my Higher Degree by Research candidature and is not subject to any obligations or contractual agreements with a third party that would constrain its inclusion in this thesis. I am the primary author of this paper.
Signature	_____ Date _____

Co-Author Contributions

By signing the Statement of Authorship, each author certifies that:

- i. the candidate's stated contribution to the publication is accurate (as detailed above);
- ii. permission is granted for the candidate to include the publication in the thesis; and
- iii. the sum of all co-author contributions is equal to 100% less the candidate's stated contribution.

Name of Co-Author	Michael T. Huxley
Contribution to the Paper	Assisted with the conception of the project, sample preparation, collection of X-Ray crystallography data and drafting the manuscript.
Signature	_____ Date <u>19/03/2021</u>

Name of Co-Author	Jorge Albalad
Contribution to the Paper	Assisted with sample preparation and collection of X-Ray crystallography data.
Signature	_____ Date <u>18/3/2021</u>

Name of Co-Author	Christian J. Doonan		
Contribution to the Paper	Assisted with the conception of the project, analysis of data and preparation of the manuscript.		
Signature		Date	17/03/2021

Name of Co-Author	Christopher J. Sumbly		
Contribution to the Paper	Assisted with the conception of the project, analysis of data and preparation of the manuscript.		
Signature		Date	17/03/2021

5.1 Abstract

Transition metal complexes bearing labile ligands can be difficult to isolate and study in solution due to unwanted dinucleation or ligand substitution reactions. Metal-organic Frameworks (MOFs) provide a unique matrix that allows site isolation and stabilization of well-defined transition metal complexes that may be of importance as moieties for gas adsorption or catalysis. Herein we report the development of an *in-situ* anion metathesis strategy which facilitates the post-synthetic modification of Cu(I) complexes appended to a porous, crystalline MOF. By exchanging coordinated chloride for weakly coordinating anions in the presence of carbon monoxide or ethylene, a series of labile MOF-appended Cu(I) complexes featuring carbon monoxide or ethylene ligands are prepared and structurally characterized using X-ray crystallography. These complexes have an uncommon trigonal planar geometry due to the absence of coordinating solvents. The porous host framework allows small and moderately sized molecules to access the isolated Cu(I) sites and displace the “place-holder” CO ligand, mirroring the ligand exchange processes involved in Cu-centered catalysis.

5.2 Introduction

Metal-organic frameworks (MOFs) are a class of porous, crystalline materials that are assembled via a building block approach from metal-based nodes and organic links.¹⁻³ This synthetic strategy allows for metal-binding ligand moieties such as, 2,2'-bipyridine,⁴⁻⁸ porphyrins,⁹ bis and tris pyrazoles¹⁰⁻¹⁴ and phosphorous-based systems,¹⁵⁻¹⁷ to be readily incorporated into the MOF architecture as structural units.^{18, 19} As a result, the MOF pore network can be furnished with transition metal complexes to enhance specific performance characteristics, e.g., gas adsorption⁴ and catalysis.^{7, 12, 14, 17, 20} The chemistry of metal complexes anchored to a MOF lattice is distinct from the solution phase as it provides a pathway to site-isolation that obviates, typically, undesired dinucleation reactions and can facilitate site-selective chemistry.^{4, 11, 15, 18, 19, 21, 22} Furthermore, in the crystalline solid-state well-defined complexes replete with weakly coordinating ligands, that would be displaced by solvent molecules in solution, can be accessed and precisely characterized via diffraction

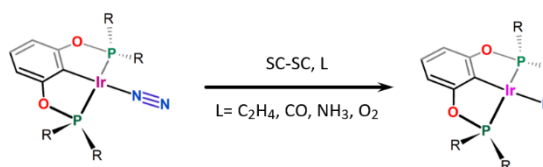
methods.²³⁻²⁶ Thus, such metalated MOFs represent excellent structural models for studying the fundamental inorganic reaction processes that underpin catalytic reactions.²⁷

Previous work has shown that the stabilization of labile ligands and their chemistry can be structurally elucidated by examining single-crystal to single-crystal (SC-SC) reactions in solid-state molecular systems.²⁸⁻³⁰ For example, Brookhart and co-workers reported that the labile dinitrogen ligand of an Ir (I) pincer complex, $[\text{Ir}(\text{L}^{\text{PCP}})(\text{N}_2)]$ (Figure 5.1a, where $\text{L}^{\text{PCP}} = \text{C}_6\text{H}_4\text{-1,3-}[\text{OP}(\text{C}_6\text{H}_2\text{-2,4,6-(CF}_3)_3)_2]_2$), underwent exchange via a dissociative mechanism.³¹ In addition, Weller and co-workers showed that a Rhodium σ -alkane complex could be synthesized by carrying out a solid-gas reaction on crystals of $[\text{Rh}(\text{dcype})(\text{norbornane})][\text{BAR}^{\text{F}_4}]$ (Figure 5.1b, where $\text{dcype} = 1,2\text{-bis(dicyclohexylphosphino)ethane}$).²³ Both examples highlight that to explore the reactivity of metal centers isolated within a crystalline matrix, pore networks that allow for the diffusion of molecular substrates are required.^{24, 28} In molecular crystals, pore structures are generated by crystal packing forces and thus cannot be tailored via *a priori* design principles. Additionally, they are unstable towards a broad spectrum of reaction conditions.²⁸ In contrast to molecular crystals, MOFs offer robust architectures and the potential to control pore dimensions and functionality through careful selection of the organic building units. Indeed, we have demonstrated that a Mn(II)-based MOF, **MnMOF-1**; $([\text{Mn}_3\text{L}_2\text{L}'])$ (where $\text{L} = \text{L}' = \text{bis(4-carboxyphenyl-(3,5-dimethylpyrazol-1-yl))methane}$) is an excellent platform material to study inorganic chemistry in the crystalline solid-state. Due to the flexibility of the N,N'-chelating ligand, **MnMOF-1** readily accommodates the subtle structural transformations that accompany post-synthetic metalation and subsequent metal-centered reactions^{10, 12-14, 32} without losing long-range order.

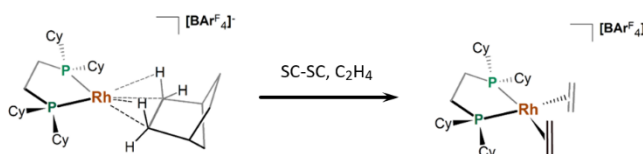
Copper(I) complexes are of great interest in homogeneous catalysis due to their versatility, relative earth abundance, compared to precious metal systems, and low toxicity. In MOF chemistry, copper(I) cations have been employed to enhance gas separation performance³³ and as single atom catalytic sites,^{11, 34} in both cases free coordination sites are crucial to functionality. Thus, developing synthetic methods that lead to the isolation of coordinatively unsaturated copper(I) sites within MOFs is an important step towards expanding this chemistry. Herein, we employ an *in-situ* anion metathesis strategy to realize a series of trigonal

planar Cu(I) complexes (Figure 5.2) bearing weakly coordinated ligands. The crystallographic characterization of such Cu(I) complexes is typically elusive; however, the MOF matrix offers a unique environment for their isolation and stabilization. By dint of the highly crystalline and robust host framework we were able to map the ligand exchange processes at the site-isolated Cu(I) moieties within **MnMOF-1** via single crystal X-ray crystallography (SCXRD) and thus advance the fundamental chemistry required to explore novel Cu centered chemistry in MOFs.

Exchange of ligated N₂ in molecular crystal (ref. 31)



Exchange of norbornane in molecular crystal (ref. 23)



THIS WORK: Exchange of labile CO in MnMOF-1

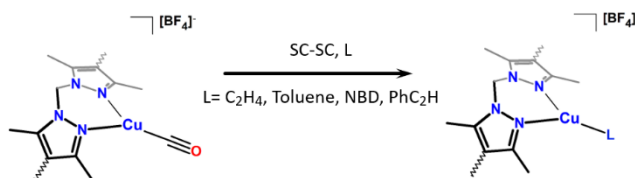


Figure 5.1. Examples of previous SC-SC studies of ligand exchange at labile transition metal complexes in the solid state; exchange of small gaseous molecules at an Ir(I) dinitrogen complex and a Rh(I) σ -alkane complex reported by Brookhart *et al.* and Weller *et al.* respectively. This work involves ligand exchange occurring at a labile Cu(I) carbonyl complex housed within **MnMOF-1**.

5.3 Results and Discussion

5.3.1 Synthesis of labile Cu(I) complexes in MnMOF-1

A promising facet of MOF chemistry is their potential as platforms for studying the exchange of small, labile molecules bound to well-defined, site isolated complexes; a role foreshadowed by their intrinsically high crystallinity, tunable structure metrics and permanent porosity.³⁵⁻³⁹

Indeed, such insights can inform the development of MOFs for applications in selective gas adsorption and heterogeneous catalysts. We envisaged that an *in situ* anion metathesis strategy could generate open coordination sites within **MnMOF-1** by directly exchanging coordinated halide anions for weakly coordinating anions. By carrying out anion exchange in the presence of small gas molecules a variety metal complexes with highly labile ligands can be realized. This approach is effectively a MOF-centric adaptation of anion metathesis, a pervasive process in organometallic chemistry.⁴⁰ The preponderance of Cu(I) to adopt a wide range of coordination geometries^{41, 42} (tetrahedral,⁴³⁻⁴⁶ trigonal planar,^{43, 44} digonal^{47, 48}) and the weak interaction between Cu(I) and classic, small gaseous ligands such as carbon monoxide and ethylene; motivated us to explore our strategy using Cu(I) functionalized **MnMOF-1**. Many Cu(I) catalysts, such as those studied for carbene and nitrene insertion, are based on complexes featuring labile ligands which allow facile binding and activation of the reagent molecules such as organic azides and diazoacetates.^{11, 49-54} As such, stabilizing weakly-ligated complexes via site-isolation within a robust crystalline host is of significant interest.¹¹

Our entry point to Cu(I) chemistry in **MnMOF-1** was via direct metalation with CuCl. Exposure of **MnMOF-1** to CuCl in acetonitrile at 4°C resulted in a color change in the crystals from colorless to pale yellow. SCXRD revealed the formation of a tetrahedral N,N'-chelated Cu(I) complex, which exists as a mixture of the charged bis-acetonitrile and neutral mono-acetonitrile complexes **MnMOF-1**·[Cu(MeCN)₂]Cl and **MnMOF-1**·[CuCl(MeCN)], respectively. The material, designated **MnMOF-1**·[CuCl(MeCN)] for simplicity, crystallizes in the space group *P2₁/m* (Figure 5.2). The crystallographically distinct Cu(I) centers are highly disordered (See Chapter 7.4.3.2 for refinement details), precluding analysis of the respective bond lengths; however analogous structural motifs have been reported.^{46, 55} Energy Dispersive X-ray (EDX) analysis confirmed quantitative metalation (Mn:Cu:Cl = 3:1:1, see Table 7.4.1).

To examine the potential of the *in-situ* anion metathesis methodology in MOFs, tetrafluoroborate was introduced as the weakly-coordinating anion and ethylene as the labile placeholder ligand. **MnMOF-1**·[CuCl(MeCN)] crystals were soaked in a saturated methanol solution of NaBF₄ under 4 bar of ethylene for 3 days. Following anion metathesis, the resulting colorless MOF crystals were subjected to EDX analysis to ascertain the extent of Cl⁻ substitution

by tetrafluoroborate. The data showed a Mn:Cu:Cl ratio of 3:1:0, confirming quantitative anion exchange and retention of the Cu center within the host framework (see Table 7.4.1). The bulk crystallinity and phase purity of the material was confirmed by PXRD data (Figure 7.4.2.1). To elucidate the Cu(I) coordination environment, SCXRD data was collected using Synchrotron radiation.^{56, 57} Close inspection of the diffraction data revealed a trigonal planar Cu(I) complex comprised of two N atoms from L and an ethylene ligand; **MnMOF-1**·[Cu(C₂H₄)]BF₄. The Cu–C bond lengths of 2.125(16) and 2.036(15) Å are comparable with analogous molecular complexes.⁵⁸⁻⁶⁰ Analogous to our previous studies,^{10, 12, 61} the charge balancing anion (BF₄⁻) occupies a pocket within the MOF pore adjacent to the N,N'-chelated Cu(I) center. Numerous three coordinate, N,N'-chelated Cu(I) ethylene complexes have been reported in literature and structurally characterized,^{44, 58, 60, 62} highlighting the relative stability of the copper-ethylene bond when suitably protected.

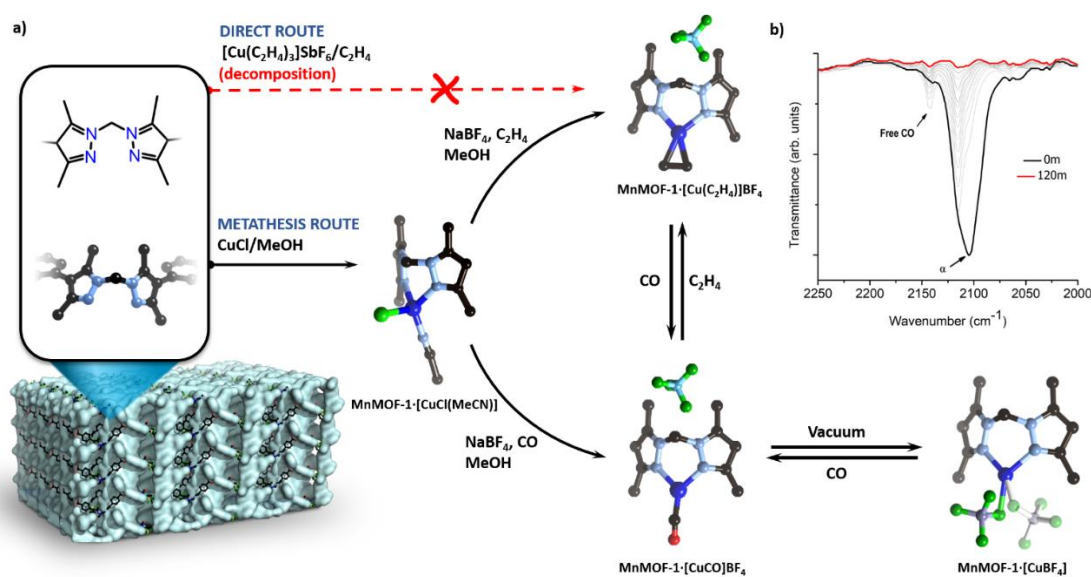


Figure 5.2. (a) Accessing **MnMOF-1**·[Cu(C₂H₄)]BF₄ via the direct route leads to decomposition of [Cu(C₂H₄)₃]SbF₆. Only *via* the metathesis route, which involves metalation of **MnMOF-1** with CuCl and subsequent anion metathesis with NaBF₄ in the presence of ethylene or CO, can the corresponding labile complexes be obtained. **MnMOF-1**·[CuCO]BF₄ loses CO under vacuum to yield the BF₄ complex **MnMOF-1**·[CuBF₄], with the coordinated BF₄ is disordered over four crystallographically distinct positions (two generated by a mirror plane that bisects the Cu center). IR spectra collected under vacuum clearly indicates the quantitative loss of coordinated CO and transient formation of free CO in the MOF pores (b). Hydrogen atoms have been omitted for clarity; the MOF backbone is represented by a blue Van der Waals surface. (C, black; N, lavender; O, red; Cu, blue; B, pale blue; F, green; S, yellow; Cl, lime-green; P, pink).

Simultaneously, we explored the direct metalation of **MnMOF-1** with the precursor $[\text{Cu}(\text{C}_2\text{H}_4)_3]\text{SbF}_6$ to generate **MnMOF-1** $\cdot[\text{Cu}(\text{C}_2\text{H}_4)]\text{SbF}_6$. Despite this being a viable approach for synthesis of molecular complexes,⁶³ efforts to metalate **MnMOF-1** with $[\text{Cu}(\text{C}_2\text{H}_4)_3]\text{SbF}_6$ proved unsuccessful due to decomposition of the tris-ethylene precursor in solution. Next, we expanded our methodology to a more labile ligand, carbon monoxide (CO).⁶⁴⁻⁶⁶ Cu(I) exhibits a weak interaction with CO due to negligible backbonding, making it an ideal 'placeholder' ligand. This property is emphasized by the observation of $\nu(\text{C}\equiv\text{O})$ stretches which are higher than that of free CO (2143 cm^{-1}) in several reported Cu(I) carbonyl complexes.^{65, 67, 68} **MnMOF-1** $\cdot[\text{CuCl}]$ crystals were exposed to CO (4 bar) during ion-exchange with NaBF_4 , during which a new stretch appeared at 2105 cm^{-1} in the IR spectrum, indicating formation of a new Cu(I) carbonyl species. As anticipated, the $\nu(\text{C}\equiv\text{O})$ stretch is close to that of free CO due to minimal backbonding from Cu(I) to the CO π^* orbital.^{43, 69, 70} To establish the extent of anion exchange, EDX analysis was performed which revealed the absence of chloride within the sample (see Table 7.4.1). Additionally, PXRD confirmed that bulk crystallinity is retained after the ligand exchange process. (Figure 7.4.2.1). We note that exposure of **MnMOF-1** $\cdot[\text{CuCl}]$ to a CO atmosphere only (i.e., no anion present) failed to elicit formation of a carbonyl complex; the IR spectra showed an absence of $\nu(\text{C}\equiv\text{O})$ stretches. This suggests that the replacement of Cl by CO occurs via a dissociative pathway and provides confirmation of the weak Cu(I)–CO interaction. Following anion exchange chemistry under CO, the crystals remained in satisfactory condition for SCXRD studies. Careful analysis of the data revealed the formation of a trigonal planar Cu(I) carbonyl complex, **MnMOF-1** $\cdot[\text{CuCO}]\text{BF}_4$ (Figure 5.1b). The Cu–C bond length of $1.781(15)\text{ \AA}$, is comparable with other known molecular carbonyl complexes.^{43, 64, 65, 71} As per the analogous Cu(I)-ethylene complex, **MnMOF-1** $\cdot[\text{Cu}(\text{C}_2\text{H}_4)]\text{BF}_4$, the charge balancing anion (BF_4^-) occupies a pocket in the MOF pore adjacent to the N,N'-chelated Cu(I) site.

The capacity of anion exchange to generate trigonal planar Cu(I) complexes within **MnMOF-1** led us to explore the use of other anions that are known to be very weakly coordinating.⁷² Both hexafluorophosphate (PF_6^-) and triflate (OTf^-) analogues can be prepared via anion exchange in the presence of CO gas, giving **MnMOF-1** $\cdot[\text{CuCO}]\text{PF}_6$ and **MnMOF-1** $\cdot[\text{CuCO}]\text{OTf}$,

respectively. As anticipated **MnMOF-1**·[CuCO]PF₆ and **MnMOF-1**·[CuCO]OTf both show $\nu(\text{C}\equiv\text{O})$ stretches close to free CO (2108 cm⁻¹ for both complexes). SCXRD studies confirmed a trigonal planar geometry for both complexes (Cu-C = 1.819(16) Å for the OTf derivative; the PF₆ derivative possesses two crystallographically distinct Cu(I) carbonyl sites with 1.782(15) and 1.828(17) Å Cu-C bonds). Again, the respective anions located in a pocket adjacent to the Cu(I) center (Figure 5.3, note the triflate derivative is very hydroscopic and preventing formation of an aquo complex is extremely challenging, see 7.4.6 for details). This family of carbonyl complexes further supports the use of *in-situ* anion metathesis as a general method for producing site-isolated, Cu(I) centers possessing highly labile ligands within **MnMOF-1**.

To the best of our knowledge, the only other structurally characterized examples of trigonal planar N,N'-chelated Cu(I) carbonyl complexes have been reported in 2019 by Parasar *et al.*,⁶⁵ in 2004 by Dias *et al.*⁷¹ and in 2020 by Huse *et al.*⁶⁴ These compounds are supported by polyfluorinated co-ligands based on pyrazolyl, triazapentadienyl or β -diketimate motifs, producing charge neutral complexes with reduced π -backbonding contributions, as evidenced by high $\nu(\text{C}\equiv\text{O})$ stretches (above 2100 cm⁻¹). However, these complexes are unstable, losing coordinated CO if not kept under a CO atmosphere. For comparison, analogous tetrahedral complexes are significantly more stable towards CO loss than the three-coordinate derivatives.⁷³ Thus, we were interested to explore the stability of the MOF-supported three-coordinate complexes. To this end, storage of **MnMOF-1**·[CuCO]BF₄ in a non-coordinating solvent for several days, under an inert atmosphere, does not result in loss of CO. This difference emphasizes that site isolation in the MOF framework exerts a stabilizing effect on the Cu(I) carbonyl moiety, reducing CO loss.

Motivated by these results, we turned our attention to carrying out simple ligand exchange reactions on the CO and C₂H₄ ligated complexes. **MnMOF-1**·[CuCO]BF₄ crystals were soaked in a non-coordinating solvent under ethylene atmosphere (2 bar). After two days SCXRD was performed and revealed the formation of **MnMOF-1**·[Cu(C₂H₄)]BF₄ indicating that substitution of the carbonyl ligand can be achieved via a SC-SC crystal process. Furthermore, dosing crystals of **MnMOF-1**·[Cu(C₂H₄)]BF₄ with CO (2 bar) lead to formation of **MnMOF-1**·[CuCO]BF₄ ($\nu(\text{C}\equiv\text{O})$ stretch at 2105 cm⁻¹) over 48 hours. We then examined the stability of **MnMOF-1**·[Cu(C₂H₄)]BF₄ via gas phase NMR. Samples of **MnMOF-1**·[Cu(C₂H₄)]BF₄ were loaded into an

NMR fitted with a Young's tap and were activated at temperatures between 30 °C and 100 °C. After each activation, the tube was dosed with CO and the headspace analyzed via gas phase NMR to determine if ethylene was still present in the complex. The results showed that the ethylene required activation at 100°C to be removed.

To assess the stability of **MnMOF-1**·[CuCO]BF₄ towards loss of CO, a sample was loaded into an *in situ* FTIR cell (developed in-house, for details see 7.4.7) connected to a vacuum. During the first 5 minutes, the sample underwent a color change from pale yellow to colorless, with a concomitant diminishing of the CO stretch at 2105 cm⁻¹; after 2 hours evidence of CO bands were absent in the IR (Figure 5.2). Loss of coordinated CO is accompanied by the temporary appearance of free CO in the FTIR spectra, presumably due to gas being trapped in the MOF pellet; however, the signal quickly dissipates upon gas escape (Figure 5.2). To determine whether the process is reversible, CO (1 bar) was dosed back into the IR cell. Analysis of the IR data showed that the CO stretch at 2105 cm⁻¹ was regenerated (Figure 7.4.5.1), suggesting that the Cu(I) center is stabilized upon CO loss. The *reversible* loss of coordinated CO under vacuum led us to postulate that the anion (BF₄ in this case) binds to, and thereby stabilizes the resulting unsaturated Cu(I) center. We note that in a pertinent report, Fianchini *et al.* characterized the SbF₆ bound complex [Cu(*trans,trans,trans*-1,5,9-cyclododecatriene)(SbF₆)] which features an SbF₆ anion bound by a single fluorine to the Cu(I) center; additionally the anion is readily displaced by CO.⁶⁷

Next, we aimed to structurally characterize **MnMOF-1**·[CuCO]BF₄ following removal of the CO ligand. Crystals of **MnMOF-1**·[CuCO]BF₄ were placed under vacuum for two hours to remove CO, 'backfilled' with dried cyclohexane to protect against moisture and subjected to SCXRD analysis. The crystal structure revealed, as expected from FTIR spectroscopy, an absence of coordinated CO. Furthermore, the charge balancing anion (BF₄) could not be observed in the MOF pore but was instead located in the coordination sphere of the Cu(I) center, albeit disordered over two crystallographically distinct positions (a further two symmetry-generated sites are generated by a mirror plane). This represents a rare example of a Cu(I) complex bearing a coordinated BF₄ anion, of which we are aware of only one other example.⁷⁴ Although the formation of this moiety could be posited from the IR spectra, this is an excellent example

of how MOFs can be employed as a matrix to facilitate the structural characterization of reactive species via SCXRD.

To assess the porosity of **MnMOF-1**·[Cu(CO)]X (X = BF₄, OTf, PF₆) and **MnMOF-1**·[Cu(C₂H₄)]BF₄ we performed 77 K N₂ gas adsorption isotherms. Activation of **MnMOF-1**·[Cu(CO)]X (X = BF₄, OTf, PF₆) from pentane at room temperature and **MnMOF-1**·[Cu(C₂H₄)]BF₄ from pentane at 100 °C yielded permanently porous materials with BET surface areas of 788, 735, 916 and 754 m²·g⁻¹, respectively. We note that these values agree with those observed for other metalated derivatives of **MnMOF-1**. Given the activation conditions employed we anticipate that the CO and ethylene were removed, and that the Cu species consist of anion-bound complexes. In summary, these studies confirm that coordinated CO in **MnMOF-1**·[CuCO]BF₄ is more labile and thus the better ‘placeholder’ ligand for supported Cu(I) sites in **MnMOF-1**.

5.3.2 Ligand exchange chemistry using **MnMOF-1**·[CuCO]BF₄

The lability of the CO ligand in **MnMOF-1**·[CuCO]BF₄ encouraged us to explore its ligand exchange chemistry. As discussed earlier, Brookhart and coworkers elegantly employed SCXRD to capture small molecule exchange at a cationic Ir(I) dinitrogen complex in the solid-state (Figure 5.1).³¹ However, in contrast to solid-state molecular crystals; **MnMOF-1** presents a permanently porous matrix within which exchange processes involving larger molecules can be conveniently studied via crystallography. As a proof of principle, **MnMOF-1**·[CuCO]BF₄ was soaked in toluene under an argon atmosphere for 2 days. IR spectroscopy performed on the toluene-soaked samples revealed the disappearance of the CO stretch at 2105 cm⁻¹. SCXRD experiments revealed that the CO had been replaced with a η²-toluene ligand bound by C2 and C3 of the toluene ring (Figure 5.3) with the Cu–C bond lengths (Cu–C = 2.146(4), 2.105(4) Å) commensurate with those reported in literature for other Cu η²-arene complexes.^{64, 75-79} Structurally characterized Cu(I) η²-arene complexes are rare and have been used as precursors for nitrene transfer and Cu(I) borohydride chemistry.^{80, 81}

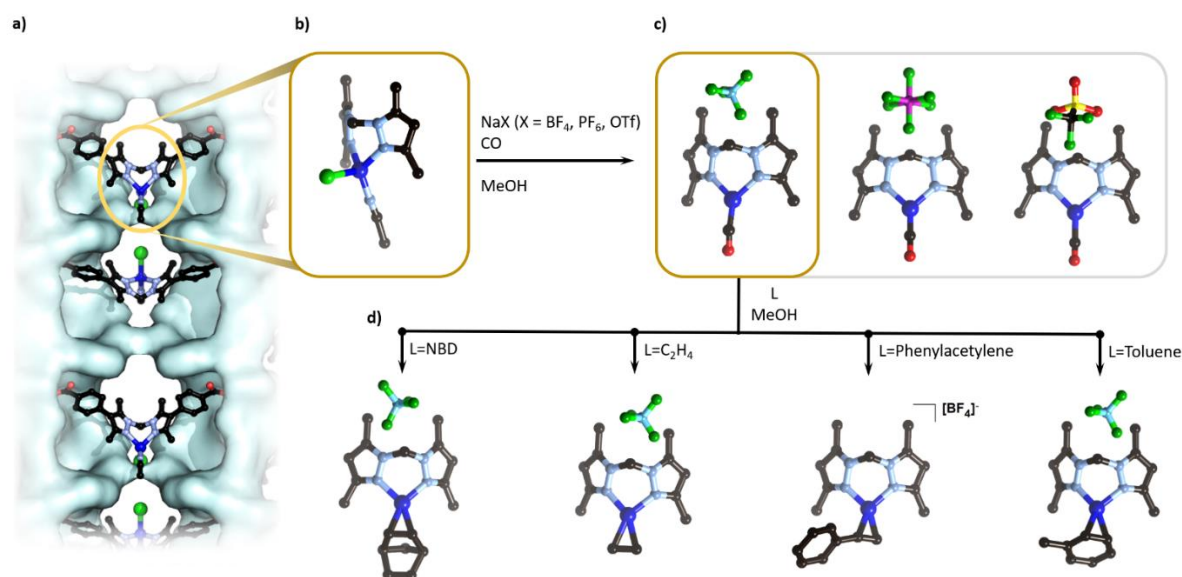


Figure 5.3. Metalation of **MnMOF-1** with CuCl yields **MnMOF-1·[CuCl(MeCN)]** (a) which undergoes quantitative anion exchange (b) with NaX (X = BF₄, PF₆, OTf) under an atmosphere of CO to yield the corresponding carbonyl complexes **MnMOF-1·[CuCO]BF₄**, **MnMOF-1·[CuCO]PF₆** and **MnMOF-1·[CuCO]OTf** (c). **MnMOF-1·[CuCO]BF₄** undergoes ligand exchange with norbornadiene (NBD), ethylene (C₂H₄), phenylacetylene and toluene to yield the respective π-complexes (d). All carbonyl and π-complexes were structurally characterized after solvent exchange with cyclohexane to ensure clean formation of the trigonal planar derivatives. Hydrogen atoms have been omitted for clarity; the MOF backbone is represented by a blue Van der Waals surface. (C, black; N, lavender; O, red; Cu, blue; B, pale blue; F, green; S, yellow; Cl, lime-green; P, pink).

We further explored the substitution chemistry of CO using other ligands. For example, **MnMOF-1·[CuCO]BF₄** crystals were soaked in a cyclohexane solution of norbornadiene (NBD) or phenylacetylene (HC≡CPh). In both cases IR spectroscopy confirmed the absence of CO stretches; concurrently SCXRD analysis verified the formation of trigonal planar complexes **MnMOF-1·[Cu(η²-NBD)]BF₄** and **MnMOF-1·[Cu(η²-HC≡CPh)]BF₄**. **MnMOF-1·[Cu(η²-NBD)]BF₄** features a BF₄ counterion in the MOF pore adjacent to the N,N'-chelated Cu(I) site; however, the anion in **MnMOF-1·[Cu(η²-HC≡CPh)]BF₄** could not be adequately resolved in the structural model. In the particular case of **MnMOF-1·[Cu(η²-NBD)]BF₄**, NBD coordinates through only one alkene moiety (Figure 5.3) with Cu–C distances of 2.026(8) and 2.051(9) Å.^{82, 83} In the analogous system, **MnMOF-1·[Cu(η²-HC≡CPh)]BF₄**, the alkyne coordinates to the Cu(I) center in an η²-fashion with Cu–C bond lengths of 1.947(14) and 1.88(12) Å.^{79, 84} These results emphasize that CO is an excellent 'placeholder' ligand in site-isolated Cu (I) complexes.

5.4 Conclusions

Here we showed that ion exchange in the presence of gas molecules facilitates the stabilization of Cu(I) complexes with labile ligands (CO, ethylene) within the porous, crystalline, MOF matrix of **MnMOF-1**. Due to their instability in coordinating solvents and sensitivity to air/moisture, molecular analogues of these complexes are challenging to characterize via SCXRD. We also explored the ligand exchange chemistry of **MnMOF-1**·[CuCO]BF₄ and showed that these SC-SC process could be followed by SCXRD. The inherent characteristics of the **MnMOF-1**; high crystallinity, permanent robust porosity, and large pore apertures, renders it an excellent platform to access a broad range of complexes with labile ligands and further, to study ligand substitution processes. We envisage that this chemistry is an important fundamental step towards the synthesis of novel Cu-based species and the exploration of their reactivity within the nanoporous environment of MOF pores.

5.5 Experimental

5.5.1. General Considerations

Unless otherwise stated, all chemicals were obtained from commercial sources and used as received. Solvents were dried using literature procedures and degassed with Ar prior to use. Specifically, acetonitrile (MeCN) was dried from CaH₂ under nitrogen; methanol (MeOH) was dried by refluxing them over Mg under N₂; acetone was dried from CaSO₄ under nitrogen; and toluene and cyclohexane was dried over Na/benzophenone. NaBF₄ used for anion exchange were stored in a 120 °C drying oven. The ligand bis-(4-carboxyphenyl-3,5-dimethylpyrazolyl) and **MnMOF-1** were synthesized as previously reported. [Cu(C₂H₄)₃]SbF₆ complex was synthesized as reported in the literature.⁸⁵ The chemicals carbon monoxide, ethylene, phenylacetylene, norbornadiene and CuCl was obtained from commercial vendors and used without purification.

Powder X-ray diffraction (PXRD) data were collected on a Bruker Advanced D8 diffractometer (capillary stage) using Cu K α radiation ($\lambda = 1.5456 \text{ \AA}$, 40 kW/ 40mA, $2\theta = 2 - 52.94^\circ$, ϕ rotation = 20 rotation/min, at 1 sec exposure per step with 5001 steps and using 0.5 mm glass capillaries). Infrared (IR) spectra were collected on a Perkin-Elmer Spectrum Two, with the sample distributed between two NaCl disks in Nujol. Energy dispersive X-ray spectroscopy (EDX) was performed on a Philips XL30 field emission scanning electron microscope. Gas adsorption isotherm measurements were performed on an ASAP 2020 Surface Area and Pore Size Analyzer. Activation of samples was carried out as described.

5.5.2 Preparation of **MnMOF-1**·[CuClMeCN]

Single crystals of **MnMOF-1** (~24 mg) were placed in a 4 ml glass vial and washed with freshly distilled acetonitrile under Ar flow a total of 5 times (the solution was degassed with Ar after each exchange and the sample was allowed to soak for 1 hr between washings). Under Ar flow, CuCl (30 mg) was added, the vial was sealed under Ar and heated at 4 °C for 3 days. The resulting pale green crystals were washed with freshly distilled acetonitrile five times under Ar

flow to give **MnMOF-1**·[Cu(CH₃CN)(Cl)]. IR ν_{\max} (nujol, cm⁻¹): 2289 (w, Cu-N≡CCH₃), 2250 (free, Cu-N≡CCH₃), 1607 (s, C=C), 1550 (m, C=C), 1510 (m, C=C) 1406.

5.5.3 *In situ* anion metathesis to form **MnMOF-1**·[CuCO]BF₄

Single crystals of **MnMOF-1**·[Cu(CH₃CN)(Cl)] (~24 mg) were placed in a 20 ml glass pressure vessel fitted with a pressure gauge and Swagelok tap assembly.¹² The crystals were washed with freshly distilled methanol (5 x 5 ml) under Ar flow a total of 5 times (the solution was degassed with Ar after each exchange and the sample was allowed to soak for 1 hr between washings). Excess oven dried NaBF₄ was added to a small glass ampule which was subsequently submerged in the glass pressure tube containing the MOF sample. The solution was degassed with Ar and the pressure tube was sealed under carbon monoxide ($P_T = 4$ bar) and allowed them to stand at RT for 3 days. Under argon flow the ampule containing undissolved salt was removed. Finally, the MOF crystals were washed with freshly distilled methanol (5 ml) five times under argon to form **MnMOF-1**·[CuCO]BF₄ as pale-yellow crystals. The samples can be stored under CO atmosphere for 2 weeks. IR ν_{\max} (nujol, cm⁻¹): 2105 (m, CO), 1613 (s, C=C), 1549 (m, C=C), 1511 (m, C=C) 1408.

5.5.4 *In-situ* anion metathesis to form **MnMOF-1**·[Cu(CO)]PF₆ and **MnMOF-1**·[Cu(CO)]OTf.

Crystals of **MnMOF-1**·[CuCl(MeCN)] (~24 mg) were placed in a 20 ml glass pressure vessel fitted with a pressure gauge and Swagelok tap assembly.¹² The crystals were washed with freshly distilled MeOH (5 x 5 ml) under Ar flow (the solution was degassed with Ar after each exchange and the sample was allowed to soak for 1 h between washings). A stock solution of dry NaPF₆ or NaOTf in distilled MeOH (35 mg, 5 ml) was added to the 20 ml glass tube containing the MOF sample. The solution was degassed with Ar, the pressure tube was sealed under CO atmosphere ($P_T = 4$ bar), and allowed to stand at room temperature for 72 h. Under Ar flow, the ampule containing undissolved salt was removed and the resulting colorless crystals were washed with freshly distilled methanol (5 x 5 ml), acetone (5 x 5 ml) and *n*-pentane (5 x 5 ml). **MnMOF-1**·[Cu(CO)]PF₆ and **MnMOF-1**·[Cu(CO)]OTf can be stored under CO

atmosphere up to two weeks. **MnMOF-1**·[CuCO]PF₆: IR ν_{\max} (nujol, cm⁻¹): 2108 (m, CO), 1615 (s, C=C), 1550 (m, C=C), 1511 (m, C=C) 1408. **MnMOF-1**·[CuCO]OTf: IR ν_{\max} (nujol, cm⁻¹): 2108 (m, CO), 1618 (s, C=C), 1552 (m, C=C), 1513 (m, C=C) 1408.

5.5.5 *In-situ* anion metathesis to form **MnMOF-1**·[Cu(C₂H₄)]BF₄

Single crystals of MnMOF-1·[Cu(CH₃CN)(Cl)] (~24 mg) were placed in a 20 ml glass pressure vessel fitted with a pressure gauge and Swagelok tap assembly.¹² The crystals were washed with freshly distilled methanol (5 x 5 ml) under Ar flow a total of 5 times (the solution was degassed with Ar after each exchange and the sample was allowed to soak for 1 hr between washings). Excess oven dried NaBF₄ was added to a small glass ampule which was subsequently submerged in the glass pressure tube containing the MOF sample. The solution was degassed with C₂H₄ and the pressure tube was sealed under ethylene (P_T = 4 bar) and allowed the sample to stand at RT for 3 days. Under ethylene flow **MnMOF-1**·[Cu(C₂H₄)]BF₄ the ampule containing undissolved salt was removed. Finally, the MOF crystals were washed with freshly distilled methanol (5 ml) five times under argon to form **MnMOF-1**·[Cu(C₂H₄)]BF₄ as pale-yellow crystals. The samples can be stored under ethylene atmosphere for 2 weeks. IR ν_{\max} (nujol, cm⁻¹): 1615 (s, C=C), 1549 (m, C=C), 1512 (m, C=C) 1407.

5.5.6 Preparation of **MnMOF-1**·[Cu(η^2 -Toluene)]BF₄

Single crystals of **MnMOF-1**·[CuCO]BF₄ (~24 mg) were placed in a 4 ml glass vial and washed with freshly distilled toluene under Ar flow a total of 5 times (the solution was degassed with Ar after each exchange and the sample was allowed to soak for 1 hr between washings). Finally, the vial was sealed under Ar for 2 days to give **MnMOF-1**·[Cu(η^2 -Toluene)]BF₄. IR ν_{\max} (nujol, cm⁻¹): 1938, 1805, 1797 (m, C=C, toluene), 1616 (s, C=C), 1551 (m, C=C), 1514 (m, C=C) 1413.

5.5.6 Preparation of **MnMOF-1**·[Cu(η^2 -NBD)]BF₄ and **MnMOF-1**·[Cu(HC≡CPh)]BF₄

Single crystals of **MnMOF-1**·[CuCO]BF₄ (~24 mg) were placed in a 4 ml glass vial and washed with freshly distilled acetone under Ar flow a total of 5 times. Consequently, the crystals were washed with distilled cyclohexane (the solutions were degassed with Ar after each exchange and the sample was allowed to soak for 1 hr between washings) five times under argon. Finally, 1 ml of norbornadiene or phenylacetylene were added and the vial was sealed under argon for 2 days to give **MnMOF-1**·[Cu(η^2 -NBD)]BF₄ and **MnMOF-1**·[Cu(HC≡CPh)]BF₄ respectively. **MnMOF-1**·[Cu(η^2 -NBD)]BF₄: IR ν_{\max} (nujol, cm⁻¹): 1619 (s, C=C), 1553 (m, C=C), 1515 (m, C=C) 1415. **MnMOF-1**·[Cu(HC≡CPh)]BF₄: IR ν_{\max} (nujol, cm⁻¹): 1936 (w, C≡C), 1622 (s, C=C), 1555 (m, C=C), 1516 (m, C=C) 1416.

5.6 Associated content

Supporting information: characterization data for the MOF samples, IR spectroscopic data, gas adsorption data, powder X-ray diffraction data and details of the SCXRD and tables of crystallography data collection and refinement parameters, crystallographic information file (cif).

5.7 Acknowledgements

CJS and CJD gratefully acknowledge the Australian Research Council for funding (DP190101402). This research was undertaken in part using the MX1 and MX2 beamlines at the Australian Synchrotron, part of ANSTO, and made use of the Australian Cancer Research Foundation (ACRF) detector. RAP gratefully acknowledges Adelaide Scholarship International. We acknowledge the contribution of Peter Apoeffis in developing the in-situ infra-red spectroscopy cell (SI. 7.0) and high-pressure reaction vessels used in this work.

5.8 References

1. Furukawa, H.; Cordova, K. E.; O'Keeffe, M.; Yaghi, O. M., The chemistry and applications of metal-organic frameworks. *Science* **2013**, *341* (6149), 974-985.
2. Yaghi, O. M.; O'Keeffe, M.; Ockwig, N. W.; Chae, H. K.; Eddaoudi, M.; Kim, J., Reticular synthesis and the design of new materials. *Nature* **2003**, *423* (6941), 705-714.
3. Kitagawa, S.; Kitaura, R.; Noro, S., Functional porous coordination polymers. *Angew. Chem., Int. Ed.* **2004**, *43* (18), 2334-75.
4. Bloch, E. D.; Britt, D.; Lee, C.; Doonan, C. J.; Uribe-Romo, F. J.; Furukawa, H.; Long, J. R.; Yaghi, O. M., Metal Insertion in a Microporous Metal-Organic Framework Lined with 2,2'-Bipyridine. *J. Am. Chem. Soc.* **2010**, *132*, 14382-14384.
5. Gonzalez, M. I.; Bloch, E. D.; Mason, J. A.; Teat, S. J.; Long, J. R., Single-crystal-to-single-crystal metalation of a metal-organic framework: a route toward structurally well-defined catalysts. *Inorg. Chem.* **2015**, *54* (6), 2995-3005.
6. Zhang, T.; Manna, K.; Lin, W., Metal-Organic Frameworks Stabilize Solution-Inaccessible Cobalt Catalysts for Highly Efficient Broad-Scope Organic Transformations. *J. Am. Chem. Soc.* **2016**, *138* (9), 3241-9.
7. Manna, K.; Zhang, T.; Greene, F. X.; Lin, W., Bipyridine- and Phenanthroline-Based Metal-Organic Frameworks for Highly Efficient and Tandem Catalytic Organic Transformations via Directed C-H Activation. *J. Am. Chem. Soc.* **2015**, *137* (7), 2665-2673.
8. Manna, K.; Zhang, T.; Lin, W., Postsynthetic metalation of bipyridyl-containing metal-organic frameworks for highly efficient catalytic organic transformations. *J. Am. Chem. Soc.* **2014**, *136* (18), 6566-9.
9. Morris, W.; Voloskiy, B.; Demir, S.; Gándara, F.; McGrier, P. L.; Furukawa, H.; Cascio, D.; Stoddart, J. F.; Yaghi, O. M., Synthesis, Structure, and Metalation of Two New Highly Porous Zirconium Metal-Organic Frameworks. *Inorg. Chem.* **2012**, *51* (12), 6443-6445.
10. Bloch, W. M.; Burgun, A.; Coghlan, C. J.; Lee, R.; Coote, M. L.; Doonan, C. J.; Sumbly, C. J., Capturing snapshots of post-synthetic metallation chemistry in metal-organic frameworks. *Nat. Chem.* **2014**, *6* (10), 906-912.
11. Sun, C.; Skorupskii, G.; Dou, J. H.; Wright, A. M.; Dinca, M., Reversible Metallation and Catalysis with a Scorpionate-like Metallo-ligand in a Metal-Organic Framework. *J. Am. Chem. Soc.* **2018**, *140* (50), 17394-17398.

12. Peralta, R. A.; Huxley, M. T.; Evans, J. D.; Fallon, T.; Cao, H.; He, M.; Zhao, X. S.; Agnoli, S.; Sumbly, C. J.; Doonan, C. J., Highly Active Gas Phase Organometallic Catalysis Supported Within Metal-organic Framework Pores. *J. Am. Chem. Soc.* **2020**, *142* (31), 13533-13543.
13. Huxley, M. T.; Burgun, A.; Ghodrati, H.; Coghlan, C. J.; Lemieux, A.; Champness, N. R.; Huang, D. M.; Doonan, C. J.; Sumbly, C. J., Protecting-Group-Free Site-Selective Reactions in a Metal-Organic Framework Reaction Vessel. *J. Am. Chem. Soc.* **2018**, *140* (20), 6416-6425.
14. Burgun, A.; Coghlan, C. J.; Huang, D. M.; Chen, W.; Horike, S.; Kitagawa, S.; Alvino, J. F.; Metha, G. F.; Sumbly, C. J.; Doonan, C. J., Mapping-Out Catalytic Processes in a Metal-Organic Framework with Single-Crystal X-ray Crystallography. *Angew. Chem., Int. Ed.* **2017**, *56*, 1-6.
15. Dunning, S. G.; Nandra, G.; Conn, A. D.; Chai, W.; Sikma, R. E.; Lee, J. S.; Kunal, P.; Reynolds, J. E., 3rd; Chang, J. S.; Steiner, A.; Henkelman, G.; Humphrey, S. M., A Metal-Organic Framework with Cooperative Phosphines That Permit Post-Synthetic Installation of Open Metal Sites. *Angew. Chem., Int. Ed.* **2018**, *57* (30), 9295-9299.
16. Feng, X.; Song, Y.; Li, Z.; Kaufmann, M.; Pi, Y.; Chen, J. S.; Xu, Z.; Li, Z.; Wang, C.; Lin, W., Metal-Organic Framework Stabilizes a Low-Coordinate Iridium Complex for Catalytic Methane Borylation. *J. Am. Chem. Soc.* **2019**, *141* (28), 11196-11203.
17. Sawano, T.; Lin, Z.; Boures, D.; An, B.; Wang, C.; Lin, W., Metal-Organic Frameworks Stabilize Mono(phosphine)-Metal Complexes for Broad-Scope Catalytic Reactions. *J. Am. Chem. Soc.* **2016**, *138* (31), 9783-6.
18. Evans, J. D.; Sumbly, C. J.; Doonan, C. J., Post-synthetic metalation of metal-organic frameworks. *Chem. Soc. Rev.* **2014**, *43* (16), 5933-51.
19. Young, R. J.; Huxley, M. T.; Pardo, E.; Champness, N. R.; Sumbly, C. J.; Doonan, C. J., Isolating reactive metal-based species in Metal–Organic Frameworks – viable strategies and opportunities. *Chem. Sci.* **2020**, *11*, 4031-4050.
20. Gonzalez, M. I.; Oktawiec, J.; Long, J. R., Ethylene oligomerization in metal-organic frameworks bearing nickel(II) 2,2'-bipyridine complexes. *Faraday Discuss.* **2017**, *201*, 351-367.
21. Drake, T.; Ji, P.; Lin, W., Site Isolation in Metal–Organic Frameworks Enables Novel Transition Metal Catalysis. *Acc. Chem. Res.* **2018**, *51* (9), 2129-2138.
22. Sikma, R. E.; Kunal, P.; Dunning, S. G.; Reynolds, J. E., 3rd; Lee, J. S.; Chang, J. S.; Humphrey, S. M., Organoarsine Metal-Organic Framework with cis-Diarsine Pockets for the

Installation of Uniquely Confined Metal Complexes. *J. Am. Chem. Soc.* **2018**, *140* (31), 9806-9809.

23. Pike, S. D.; Thompson, A. L.; Algarra, A. G.; Apperley, D. C.; Macgregor, S. A.; Weller, A. S., Synthesis and Characterization of a Rhodium(I) σ -Alkane Complex in the Solid State. *Science* **2012**, *337* (6102), 1648-1651.

24. Pike, S. D.; Krämer, T.; Rees, N. H.; Macgregor, S. A.; Weller, A. S., Stoichiometric and Catalytic Solid–Gas Reactivity of Rhodium Bis-phosphine Complexes. *Organometallics* **2015**, *34* (8), 1487-1497.

25. Chadwick, F. M.; Rees, N. H.; Weller, A. S.; Kramer, T.; Iannuzzi, M.; Macgregor, S. A., A Rhodium-Pentane Sigma-Alkane Complex: Characterization in the Solid State by Experimental and Computational Techniques. *Angew. Chem., Int. Ed.* **2016**, *55* (11), 3677-81.

26. Boyd, T. M.; Tegner, B. E.; Tizzard, G. J.; Martinez-Martinez, A. J.; Neale, S. E.; Hayward, M. A.; Coles, S. J.; Macgregor, S. A.; Weller, A. S., A Structurally Characterized Cobalt(I) sigma-Alkane Complex. *Angew. Chem., Int. Ed.* **2020**, *59*, 6177-6181.

27. Ikemoto, K.; Inokuma, Y.; Rissanen, K.; Fujita, M., X-ray Snapshot Observation of Palladium-Mediated Aromatic Bromination in a Porous Complex. *J. Am. Chem. Soc.* **2014**, *136* (19), 6892-6895.

28. Pike, S. D.; Weller, A. S., Organometallic synthesis, reactivity and catalysis in the solid state using well-defined single-site species. *Phil. Trans. R. Soc. A* **2015**, *373* (2037).

29. Chadwick, F. M.; McKay, A. I.; Martinez-Martinez, A. J.; Rees, N. H.; Kramer, T.; Macgregor, S. A.; Weller, A. S., Solid-state molecular organometallic chemistry. Single-crystal to single-crystal reactivity and catalysis with light hydrocarbon substrates. *Chem. Sci.* **2017**, *8* (9), 6014-6029.

30. Albrecht, M.; Lutz, M.; Spek, A. L.; van Koten, G., Organoplatinum crystals for gas-triggered switches. *Nature* **2000**, *406* (6799), 970-974.

31. Huang, Z.; White, P. S.; Brookhart, M., Ligand exchanges and selective catalytic hydrogenation in molecular single crystals. *Nature* **2010**, *465* (7298), 598-601.

32. Huxley, M. T.; Young, R. J.; Bloch, W. M.; Champness, N. R.; Sumbly, C. J.; Doonan, C. J., Isomer Interconversion Studied through Single-Crystal to Single-Crystal Transformations in a Metal–Organic Framework Matrix. *Organometallics* **2019**, *38* (18), 3412-3418.

33. Mohamed, M. H.; Yang, Y.; Li, L.; Zhang, S.; Ruffley, J. P.; Jarvi, A. G.; Saxena, S.; Vesper, G.; Johnson, J. K.; Rosi, N. L., Designing Open Metal Sites in Metal–Organic Frameworks for Paraffin/Olefin Separations. *J. Am. Chem. Soc.* **2019**, *141* (33), 13003-13007.
34. Wright, A. M.; Sun, C.; Dincă, M., Thermal Cycling of a MOF-Based NO Disproportionation Catalyst. *J. Am. Chem. Soc.* **2021**, *143* (2), 681-686.
35. Gonzalez, M. I.; Mason, J. A.; Bloch, E. D.; Teat, S. J.; Gagnon, K. J.; Morrison, G. Y.; Queen, W. L.; Long, J. R., Structural characterization of framework-gas interactions in the metal-organic framework Co₂(dobdc) by in situ single-crystal X-ray diffraction. *Chem. Sci.* **2017**, *8* (6), 4387-4398.
36. Runcevski, T.; Kapelewski, M. T.; Torres-Gavosto, R. M.; Tarver, J. D.; Brown, C. M.; Long, J. R., Adsorption of two gas molecules at a single metal site in a metal-organic framework. *Chem. Commun.* **2016**, *52* (53), 8251-4.
37. Bloch, E. D.; Hudson, M. R.; Mason, J. A.; Chavan, S.; Crocella, V.; Howe, J. D.; Lee, K.; Dzubak, A. L.; Queen, W. L.; Zadrozny, J. M.; Geier, S. J.; Lin, L. C.; Gagliardi, L.; Smit, B.; Neaton, J. B.; Bordiga, S.; Brown, C. M.; Long, J. R., Reversible CO binding enables tunable CO/H₂ and CO/N₂ separations in metal-organic frameworks with exposed divalent metal cations. *J. Am. Chem. Soc.* **2014**, *136* (30), 10752-61.
38. Zhang, J.-P.; Liao, P.-Q.; Zhou, H.-L.; Lin, R.-B.; Chen, X.-M., Single-crystal X-ray diffraction studies on structural transformations of porous coordination polymers. *Chem. Soc. Rev.* **2014**, *43* (16), 5789-5814.
39. Easun, T. L.; Moreau, F.; Yan, Y.; Yang, S.; Schröder, M., Structural and dynamic studies of substrate binding in porous metal–organic frameworks. *Chem. Rev.* **2017**, *46* (1), 239-274.
40. van Dijkman, T. F.; Siegler, M. A.; Bouwman, E., Copper(I) Complexes of Naphthyl-Substituted Fluorinated Trispyrazolylborate Ligands with Ethene and Carbon Monoxide. *Eur. J. Inorg. Chem.* **2016**, *2016* (15-16), 2586-2594.
41. Carvajal, M. A.; Novoa, J. J.; Alvarez, S., Choice of Coordination Number in d¹⁰ Complexes of Group 11 Metals. *J. Am. Chem. Soc.* **2004**, *126* (5), 1465-1477.
42. Fujisawa, K.; Noguchi, Y.; Miyashita, Y.; Okamoto, K.-i.; Lehnert, N., Mononuclear and Binuclear Copper(I) Complexes Ligated by Bis(3,5-diisopropyl-1-pyrazolyl)methane: Insight into the Fundamental Coordination Chemistry of Three-Coordinate Copper(I) Complexes with a Neutral Coligand. *Inorg. Chem.* **2007**, *46* (25), 10607-10623.

43. Chou, C.-C.; Su, C.-C.; Yeh, A., Mononuclear and Dinuclear Copper(I) Complexes of Bis(3,5-dimethylpyrazol-1-yl)methane: Synthesis, Structure, and Reactivity. *Inorg. Chem.* **2005**, *44* (17), 6122-6128.
44. Adiraju, V. A. K.; Flores, J. A.; Yousufuddin, M.; Dias, H. V. R., Copper(I) Ethylene Complexes Supported by 1,3,5-Triazapentadienyl Ligands with Electron-Withdrawing Groups. *Organometallics* **2012**, *31* (22), 7926-7932.
45. Wang, D.; Jahan, F.; Meise, K. J.; Lindeman, S. V.; Gardinier, J. R., Silver(I) and Copper(I) Complexes of Semi-Bulky Nitrogen-Confused C-Scorpionates. *Eur. J. Inorg. Chem.* **2020**, *2020* (20), 1964-1978.
46. Zelenay, B.; Frutos-Pedreño, R.; Markalain-Barta, J.; Vega-Isa, E.; White, A. J. P.; Díez-González, S., Homo- and Heteroleptic Copper(I) Complexes with Diazabutadiene Ligands: Synthesis, Solution- and Solid-State Structural Studies. *Eur. J. Inorg. Chem.* **2016**, *2016* (28), 4649-4658.
47. Trose, M.; Nahra, F.; Cordes, D. B.; Slawin, A. M. Z.; Cazin, C. S. J., Cu-NHC azide complex: synthesis and reactivity. *Chem Commun* **2019**, *55* (80), 12068-12071.
48. Danopoulos, A. A.; Simler, T.; Braunstein, P., N-Heterocyclic Carbene Complexes of Copper, Nickel, and Cobalt. *Chem. Rev.* **2019**, *119* (6), 3730-3961.
49. Díaz-Requejo, M. M.; Pérez, P. J., Coinage Metal Catalyzed C-H Bond Functionalization of Hydrocarbons. *Chem. Rev.* **2008**, *108* (8), 3379-3394.
50. Carsch, K. M.; DiMucci, I. M.; Iovan, D. A.; Li, A.; Zheng, S.-L.; Titus, C. J.; Lee, S. J.; Irwin, K. D.; Nordlund, D.; Lancaster, K. M.; Betley, T. A., Synthesis of a copper-supported triplet nitrene complex pertinent to copper-catalyzed amination. *Science* **2019**, *365* (6458), 1138-1143.
51. Muñoz-Molina, J. M.; Belderrain, T. R.; Pérez, P. J., Trispyrazolylborate coinage metals complexes: Structural features and catalytic transformations. *Coord. Chem. Rev.* **2019**, *390*, 171-189.
52. Dias, H. V. R.; Lu, H.-L.; Kim, H.-J.; Polach, S. A.; Goh, T. K. H. H.; Browning, R. G.; Lovely, C. J., Copper(I) Ethylene Adducts and Aziridination Catalysts Based on Fluorinated Tris(pyrazolyl)borates [HB(3-(CF₃),5-(R)Pz)₃]- (where R = CF₃, C₆H₅, H; Pz = pyrazolyl). *Organometallics* **2002**, *21* (7), 1466-1473.

53. Flores, J. A.; Dias, H. V. R., Gold(I) Ethylene and Copper(I) Ethylene Complexes Supported by a Polyhalogenated Triazapentadienyl Ligand. *Inorg. Chem.* **2008**, *47* (11), 4448-4450.
54. Flores, J. A.; Badarinarayana, V.; Singh, S.; Lovely, C. J.; Dias, H. V. R., Synthesis and catalytic activity of an electron-deficient copper–ethylene triazapentadienyl complex. *Dalton Trans.* **2009**, (37), 7648-7652.
55. Gustafsson, B.; Håkansson, M.; Jagner, S., Complexes between copper(I) chloride and polydentate aromatic amines. *Inorganica Chim. Acta* **2003**, *350*, 209-214.
56. Cowieson, N. P.; Aragao, D.; Clift, M.; Ericsson, D. J.; Gee, C.; Harrop, S. J.; Mudie, N.; Panjekar, S.; Price, J. R.; Riboldi-Tunnicliffe, A.; Williamson, R.; Caradoc-Davies, T., MX1: a bending-magnet crystallography beamline serving both chemical and macromolecular crystallography communities at the Australian Synchrotron. *J. Synchrotron Radiat.* **2015**, *22* (1), 187-190.
57. Aragao, D.; Aishima, J.; Cherukuvada, H.; Clarken, R.; Clift, M.; Cowieson, N. P.; Ericsson, D. J.; Gee, C. L.; Macedo, S.; Mudie, N.; Panjekar, S.; Price, J. R.; Riboldi-Tunnicliffe, A.; Rostan, R.; Williamson, R.; Caradoc-Davies, T. T., MX2: a high-flux undulator microfocus beamline serving both the chemical and macromolecular crystallography communities at the Australian Synchrotron. *J. Synchrotron Rad.* **2018**, *25* (3), 885-891.
58. Dias, H. V. R.; Wu, J., Structurally Characterized Coinage-Metal–Ethylene Complexes. *Eur. J. Inorg. Chem.* **2008**, *2008* (4), 509-522.
59. Ridlen, S. G.; Kulkarni, N. V.; Dias, H. V. R., Monoanionic, Bis(pyrazolyl)methylborate $[(\text{Ph}_3\text{B})\text{CH}(\text{3,5-(CH}_3)_2\text{Pz})_2]](-)$ as a Supporting Ligand for Copper(I)-ethylene, cis-2-Butene, and Carbonyl Complexes. *Inorg. Chem.* **2017**, *56* (12), 7237-7246.
60. Dias, H. V. R.; Lovely, C. J., Carbonyl and Olefin Adducts of Coinage Metals Supported by Poly(pyrazolyl)borate and Poly(pyrazolyl)alkane Ligands and Silver Mediated Atom Transfer Reactions. *Chem. Rev.* **2008**, *108* (8), 3223-3238.
61. Peralta, R.; Huxley, M.; Young, R.; Linder-Patton, O. M.; Evans, J. D.; Doonan, C. J.; Sumbly, C. J., MOF Matrix Isolation: Cooperative Conformational Mobility Enables Reliable Single Crystal Transformations. *Faraday Discuss.* **2020**, *225*, 84-99.
62. Masuda, H. Y., N.; Taga, T.; Machida, K., Structural Studies of Copper(I) complexes with ethylene. Crystal Structures of $[\text{Cu}(2,2'\text{-bipyridine})(\text{ethylene})]\text{ClO}_4$, and $[\text{Cu}(1,10\text{-phenanthroline})(\text{ethylene})]\text{ClO}_4$. *J. Organomet. Chem.* **1987**, *322*, 121-129.

63. Klimovica, K.; Kirschbaum, K.; Daugulis, O., Synthesis and Properties of “Sandwich” Diimine-Coinage Metal Ethylene Complexes. *Organometallics* **2016**, *35* (17), 2938-2943.
64. Huse, K.; Weinert, H.; Wölper, C.; Schulz, S., Electronic effect of a perfluorinated β -diketiminato ligand on the bonding nature of copper carbonyl complexes. *Dalton Trans.* **2020**, *49* (28), 9773-9780.
65. Parasar, D.; Jayaratna, N. B.; Muñoz-Castro, A.; Conway, A. E.; Mykhailiuk, P. K.; Dias, H. V. R., Carbonyl complexes of copper(i) stabilized by bridging fluorinated pyrazolates and halide ions. *Dalton Trans.* **2019**, *48* (19), 6358-6371.
66. Bruce, M. I.; Ostaszewski, A. P. P., Group IB metal chemistry. Part I. Preparation and reactions of the carbonyl(hydrotripyrazol-1-ylborato)copper(I) complex. *Dalt. Trans.* **1973**, (22), 2433-2436.
67. Fianchini, M.; Cundari, T. R.; DeYonker, N. J.; Dias, H. V. R., A non-classical copper carbonyl on a tri-alkene hydrocarbon support. *Dalton Trans.* **2009**, (12), 2085-2087.
68. Ivanova, S. M.; Ivanov, S. V.; Miller, S. M.; Anderson, O. P.; Solntsev, K. A.; Strauss, S. H., Mono-, Di-, Tri-, and Tetracarbonyls of Copper(I), Including the Structures of $\text{Cu}(\text{CO})_2(1\text{-Bn-CB}_{11}\text{F}_{11})$ and $[\text{Cu}(\text{CO})_4][1\text{-Et-CB}_{11}\text{F}_{11}]$. *Inorg. Chem.* **1999**, *38* (17), 3756-3757.
69. Papish, E. T.; Donahue, T. M.; Wells, K. R.; Yap, G. P. A., How are tris(triazolyl)borate ligands electronically different from tris(pyrazolyl)borate ligands? A study of $(\text{TtztBu,Me})\text{CuCO}[\text{TtztBu,Me}]$ = tris(3-t-butyl-5-methyl-1,2,4-triazolyl)borate]. *Dalton Trans.* **2008**, (22), 2923-2925.
70. Pike, R. D., Structure and Bonding in Copper(I) Carbonyl and Cyanide Complexes. *Organometallics* **2012**, *31* (22), 7647-7660.
71. Dias, H. V. R.; Singh, S., Copper(I) Complexes of Fluorinated Triazapentadienyl Ligands: Synthesis and Characterization of $[\text{N}\{(\text{C}_3\text{F}_7)\text{C}(\text{Dipp})\text{N}\}_2]\text{CuL}$ (Where L = NCCH_3 , CNBut , CO ; Dipp = 2,6-Diisopropylphenyl). *Inorg. Chem.* **2004**, *43* (19), 5786-5788.
72. Strauss, S. H., The search for larger and more weakly coordinating anions. *Chem. Rev.* **1993**, *93* (3), 927-942.
73. Pampaloni, G.; Peloso, R.; Belletti, D.; Graiff, C.; Tiripicchio, A., Trifluoromethyl-Substituted Bis(pyrazolyl)methanes as Ligands for Copper and Silver: Synthesis and Spectroscopic and Structural Characterization. *Organometallics* **2007**, *26* (17), 4278-4286.

74. Gandhi, B. A.; Green, O.; Burstyn, J. N., Facile Oxidation-Based Synthesis of Sterically Encumbered Four-Coordinate Bis(2,9-di-tert-butyl-1,10-phenanthroline)copper(I) and Related Three-Coordinate Copper(I) Complexes. *Inorg. Chem.* **2007**, *46* (10), 3816-3825.
75. Parvin, N.; Hossain, J.; George, A.; Parameswaran, P.; Khan, S., N-heterocyclic silylene stabilized monocordinated copper(i)-arene cationic complexes and their application in click chemistry. *Chem. Commun.* **2020**, *56* (2), 273-276.
76. Dines, M. B.; Bird, P. H., Aromatic complexes of copper(I) trifluoromethanesulphonate. *Chem. Commun.* **1973**, (1), 12-12.
77. R. Conry, R., Synthesis of copper(I) complexes with a novel naphthyl-appended macrocyclic ligand, including the crystal and molecular structure of the first copper(I)- η^2 -naphthyl complex. *Chem. Commun.* **1998**, (5), 555-556.
78. Lee, S. Y.; Na, S. J.; Kwon, H. Y.; Lee, B. Y.; Kang, S. O., Syntheses and Structures of a Macrocyclic β -Diketimine and Its Zinc and Copper Complexes. *Organometallics* **2004**, *23* (23), 5382-5385.
79. Badiei, Y. M.; Warren, T. H., Electronic structure and electrophilic reactivity of discrete copper diphenylcarbenes. *J. Organomet. Chem.* **2005**, *690* (24), 5989-6000.
80. Badiei, Y. M.; Dinescu, A.; Dai, X.; Palomino, R. M.; Heinemann, F. W.; Cundari, T. R.; Warren, T. H., Copper-nitrene complexes in catalytic C-H amination. *Angew. Chem., Int. Ed.* **2008**, *47* (51), 9961-4.
81. Nako, A. E.; White, A. J.; Crimmin, M. R., Bis(σ -B-H) complexes of copper(i): precursors to a heterogeneous amine-borane dehydrogenation catalyst. *Dalton Trans.* **2015**, *44* (28), 12530-4.
82. Speier, G.; Szabó, L.; Fülöp, V., Preparation and molecular structure of an adipinato copper norbornadiene complex. *J. Organomet. Chem.* **1993**, *462* (1), 375-378.
83. Stricker, M.; Oelkers, B.; Rosenau, C. P.; Sundermeyer, J., Copper(I) and Silver(I) Bis(trifluoromethanesulfonyl)imide and Their Interaction with an Arene, Diverse Olefins, and an NTF²-Based Ionic Liquid. *Chem. Eur. J.* **2013**, *19* (3), 1042-1057.
84. Dias, H. V. R.; Flores, J. A.; Wu, J.; Kroll, P., Monomeric Copper(I), Silver(I), and Gold(I) Alkyne Complexes and the Coinage Metal Family Group Trends. *J. Am. Chem. Soc.* **2009**, *131* (31), 11249-11255.

85. Fianchini, M.; Campana, C. F.; Chilukuri, B.; Cundari, T. R.; Petricek, V.; Dias, H. V. R., Use of $[\text{SbF}_6]^-$ to Isolate Cationic Copper and Silver Adducts with More than One Ethylene on the Metal Center. *Organometallics* **2013**, 32 (10), 3034-3041.

Chapter 6: Conclusion and Future outlook

This thesis has demonstrated the enormous potential of MOFs as both catalytic platforms and as crystalline matrices within which to study reactive transition metal complexes via X-ray crystallography. Until now, most of the investigations using MOFs for catalysis have been dedicated to the synthesis of fine chemicals in solution. However, the judicious choice of chemistry and reaction conditions can showcase the unique properties of MOFs, such as high surface area, crystallinity, and reticular design. Specifically, carrying out chemistry in solution does not take full advantage of these intrinsic characteristics. Therefore, this thesis explored novel systems where these MOF characteristics can be exploited to characterize site isolated transition metal catalysts and study their activity in gas phase catalysis.

The key approach employed in this thesis was the heterogenization of well-defined homogeneous catalysts within the bespoke MOF, **MnMOF-1**, via postsynthetic modification. This required the fundamental properties of the MOF, namely its dynamic response of the material to solvent exchange, to be elucidated; while new techniques were developed in order to facilitate metalation (and subsequent chemistry) using highly reactive organometallic complexes. The structural flexibility of the linker site and framework are critical to achieving high levels of metal loading. Metalation in **MnMOF-1** has proven to be facile for most transition metals when those reactions are conducted in coordinating solvents such as acetonitrile (CH_3CN) or ethanol (EtOH). A major problem is that many organometallic compounds could react with coordinating solvents and form undesirable moieties within the MOF (e.g. when using precursor complexes with labile ligands such as ethylene). In Chapter 2 new methodologies were developed to allow postsynthetic metalation chemistry to occur in non-coordinating solvents. However, direct solvent exchange of **MnMOF-1** starting from certain polar solvents led to loss of single crystallinity. Thus, an indirect solvent exchange methodology via acetone was successfully implemented, expanding the range of solvents that can be employed for decorating the pores of the MOF with reactive transition metal complexes without losing single crystallinity or generating undesirable solvated complexes. Remarkably, this methodology was shown to be a useful way to metalate **MnMOF-1** with

reactive metal complexes in non-coordinating solvents and elucidate the coordination environment via X-ray crystallography.

MnMOF-1 has proved to be an excellent platform to characterize reactive metal complexes ordered throughout the framework via SCXRD. In Chapter 3 and 4, a postsynthetic metalation strategy was developed to facilitate metalation with highly reactive precursors. Direct metalation of **MnMOF-1** with reactive $[\text{Rh}(\text{ETH})_2\text{Cl}]_2$ or $[\text{Ir}(\text{ETH})_2\text{Cl}]_2$ under an inert atmosphere resulted in the formation of nanoparticles. To prevent this decomposition, a new approach was developed; specifically, the metalation was carried out in the presence of excess alkene, preventing the decomposition of the metal moiety in solution and thereby allowing metalation to take place. By keeping the samples under an ethylene atmosphere, the coordination sphere of the MOF-bound complex could be manipulated by anion exchange to generate the corresponding tetrafluoroborate (BF_4) or chloride (Cl) complexes. Through judicious choice of the conditions, the MOF retained single crystallinity during the metalation and anion exchange steps, allowing the coordination sphere of the reactive metal complexes to be elucidated via SCXRD.

It has been previously demonstrated that homogeneous catalytic moieties can be introduced into MOF structures to realize the benefits of a heterogenization. However, examples where well-defined MOF catalyst systems have been used for commercially desirable, gas phase catalysis are exceedingly rare. In Chapter 3 and 4, industrially attractive gas phase reactions were carried out with site-isolated, well-defined reactive metal complexes located in the MOF architecture. Gas-phase NMR spectroscopy was utilized to monitor 1-butene isomerization and ethylene hydrogenation catalyzed by the Rh(I) and Ir(I) ethylene complexes. **MnMOF-1**· $[\text{Rh}(\text{C}_2\text{H}_4)_2\text{BF}_4]$ was found to be a highly efficient catalyst for 1-butene isomerization (average $\text{TOF}^{90\%}$ ca. 2000 hr^{-1}) and ethylene hydrogenation, while the chloride derivative displays negligible activity for isomerization. Moreover, the material can be cycled over 5 cycles without a measurable loss of activity. Overall, the work presented in those Chapters demonstrated the powerful platform of **MnMOF-1** is effectively able to transpose well-defined organometallic systems to the solid-state and to facilitate commercially attractive reactions within the MOF pore environment in the absence of solvent.

To expand our knowledge of MOFs as supports for single site catalysts, in Chapter 4, metalation of **MnMOF-1** was conducted with $[\text{Ir}(\text{C}_2\text{H}_4)_2\text{Cl}]_2$ under ethylene. The reaction

mainly results in formation of the neutral bis-ethylene complex of iridium, **MnMOF-1**·[Ir(C₂H₂)₂Cl]. Similar methodology to that developed in Chapter 3 was applied to exchange the coordinating anion (Cl) for non-coordinating anion (BF₄). Again, the hydrogenation of ethylene was observed to be anion dependent; however, for the Ir catalyst, the chloride complex shows greater reactivity than the BF₄ species. These findings advance our comprehension of using MOFs as platforms for gas-phase heterogeneous catalysis and provides insight into how these materials can be best developed as materials for industrial catalysis.

As described in Chapters 3 and 4, site isolation is a key factor in accessing and stabilizing labile complexes, which are of interest in catalysis. In the homogenous phase, characterizing these species is challenging due to their short solution lifetimes. Building on the knowledge attained from the Rh(I) and Ir(I) focused projects, in Chapter 5, **MnMOF-1** was used as support for labile copper(I) complexes, particularly Cu(I) carbonyl complexes. The metalation of **MnMOF-1** with CuCl led to the formation of **MnMOF-1**·[Cu(CH₃CN)(Cl)] with a tetrahedral coordination geometry at the added Cu(I) moiety. In order to convert this species into a labile Cu(I) site, a new methodology was introduced “*in-situ* anion metathesis”, in which anion exchange with non-coordinating anions was performed in the presence of small gas molecules that could bind to the newly formed coordination site. The formation of the **MnMOF-1** [CuCO]X (X = BF₄, PF₆, OTf) and **MnMOF-1**·[Cu(C₂H₄)]BF₄ complexes using this strategy was confirmed by SCXRD and IR spectroscopy. Remarkably this new methodology facilitated the incorporation of weakly coordinating ligands into the Cu(I) coordination sphere, producing otherwise difficult to access complexes.

Well-defined, discrete transition metal complexes with labile ligands crystallized in the solid-state can undergo the same reaction processes as organometallic compounds in solution, such as ligand substitution. By judicious choice of anions or fortuitous crystal packing these materials can possess a degree of porosity towards small gaseous reagents; however, the innately non-porous nature of the molecular crystals makes it difficult for larger reagents to access the metal centers. Therefore, in catalysis applications involving larger substrates, the intrinsic characteristics of crystalline porous 3D materials such as MOFs makes them superior materials. **MnMOF-1**·[CuCO]BF₄ proved to be an excellent candidate for studying ligand substitution. The carbonyl ligand was successfully substituted for ethylene to give **MnMOF-**

$1 \cdot [\text{Cu}(\text{C}_2\text{H}_4)]\text{BF}_4$. In order to prove the advantage of using an innately porous material, **MnMOF-1**· $[\text{CuCO}]\text{BF}_4$ was reacted with larger molecules such as toluene, norbornadiene (NBD) and phenylacetylene ($\text{PhC}\equiv\text{CH}$) to yield **MnMOF-1**· $[\text{Cu}(\eta^2\text{-toluene})]\text{BF}_4$, **MnMOF-1**· $[\text{Cu}(\eta^2\text{-NBD})]\text{BF}_4$ and **MnMOF-1**· $[\text{Cu}(\text{HC}\equiv\text{CPh})]\text{BF}_4$ respectively. Intriguingly, under an inert gas and non-coordinating solvent, the Cu(I) carbonyl complex did not lose coordinated CO, demonstrating that the framework of the MOF provides extra stability to the Cu(I) carbonyl moiety relative to molecular analogues. This material proved to be an excellent platform to access a broad range of labile complexes and study their substitution chemistry.

Future work will aim to use the isolated copper(I) centers in **MnMOF-1**· $[\text{CuL}]\text{X}$ (L= ethylene, CO; X= BF_4 , PF_6 , OTf) for applications such as gas separation and catalysis. The Cu(I) carbonyl complex was demonstrated to be a labile complex where the CO can be treated as a “placeholder” ligand. A potential application of the isolated MOF-tethered Cu(I) that has received considerable attention is gas separation. The separation of gas molecules with similar physicochemical properties is of great industrial importance. Structural characterization of the adsorption sites provides insights into how these materials interact with the gas molecules and can be best developed as future platform materials for gas sorption. Separation of olefin from paraffin mixtures (e.g. ethylene from ethane) is an important industrial process for which the efficacy of Cu(I) functionalized **MnMOF-1** will be studied. Besides gas separation, Cu(I) moieties within **MnMOF-1** can act as active sites for catalysis. Due to the intrinsic characteristics of **MnMOF-1** and the isolated labile Cu(I) complex, the material can be used as a platform to trap catalytic intermediates and characterize them via X-ray crystallography. In particular, nitrene/carbene transfer are promoted by labile Cu(I) complexes and proceed through highly reactive intermediates which could potentially be elucidated by crystallography using **MnMOF-1** as a host.

The work described in this thesis has established **MnMOF-1** as an exceptional platform to isolate well-defined organometallic species and employ them for commercially desirable gas phase catalysis. **MnMOF-1** is a unique porous material that possess a flexible linker and framework which are critical to achieving high levels of metalation while preserving single-crystallinity. The salient features of **MnMOF-1** such as high crystallinity and porosity, allow the coordination environment of the host metal to be structurally characterized. This work has contributed to our understanding of **MnMOF-1** and MOF-based catalysis generally by

developing new strategies for the incorporation and manipulation of site-isolated reactive metal complexes and confirming the capacity of MOFs to act as platforms for gas-phase catalysis. Future work will expand on these principles, particularly the use of MOF-bound labile Cu(I) complexes as earth-abundant catalysts.

Chapter 7: Appendices

7.1. Supplementary information for Chapter 2

7.1.1 Monitoring solvent exchange within MnMOF-1

Herein, X-ray crystallography was employed to study the effects of solvation in **MnMOF-1**, in particular the effect of solvent on the conformation of the free pyrazole sites within the material. Although it is clear that solvent exchange induces structural transformations (e.g. 'syn' and 'anti' conformation) over the course of 24 hr (5 washes), it is not clear how long it takes to fully exchange the solvent within the MOF pores and whether the solvent is fully exchanged within the cavities of framework. To investigate these factors, key solvent exchange processes from DMF to acetone, acetone to diethyl ether, acetone to DCM, acetone to THF and acetone to *p*-xylene were monitored via NMR spectroscopy. For example, **MnMOF-1-as** was exchanged with fresh acetone a number of times over the course of 90 minutes, and after each exchange a portion of the MOF crystals was removed, dried briefly under a flow of Ar and digested in *d*₆-DMSO/DCI for analysis by NMR spectroscopy. This allowed the proportion of DMF and acetone to be determined, revealing that solvent exchange takes place rapidly and is complete within three solvent exchanges.

In the other solvent exchange processes the same method was applied. The trend was similar to the first experiment described above; the solvent exchange occurs rapidly and is complete within the first three exchanges. These experiments verify that the solvent exchange procedure used to prepare samples for crystallographic studies successfully substitute the solvent within the MOF pores.

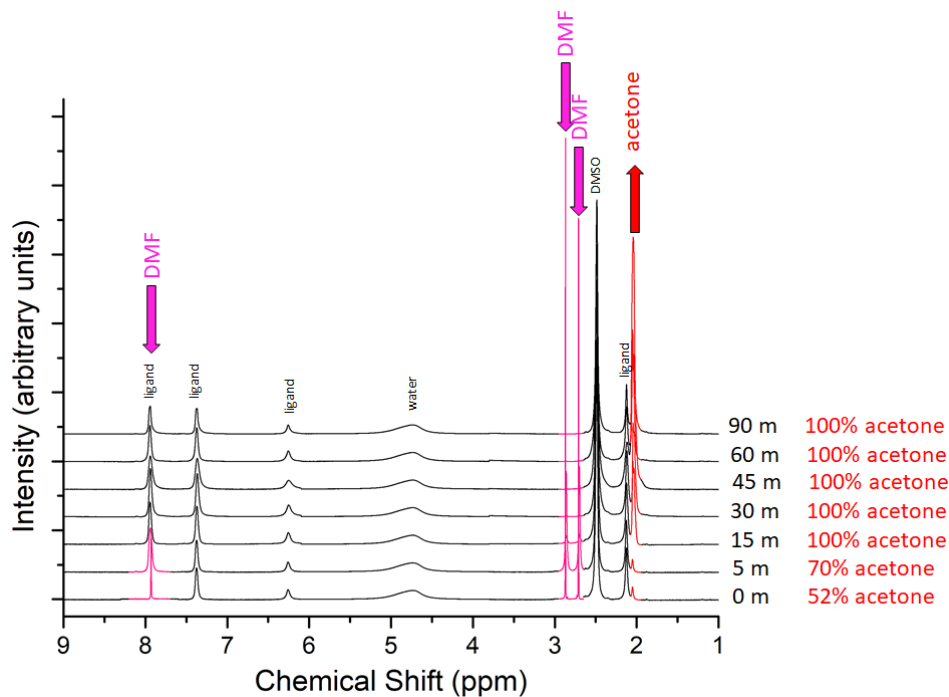


Figure 7.1.1.1. Sample MnMOF-1-DMF was washed recurrently 6 times with acetone during the course of 90 minutes, each time the sample was allowed to soak for the specified time before the next solvent exchange was performed. After the solvent was changed, a portion of the MOF material was dried briefly under Ar flow and analyzed by NMR (digested in d_6 -DMSO/DCI) to quantify the proportions of DMF and acetone present within the MOF pores.

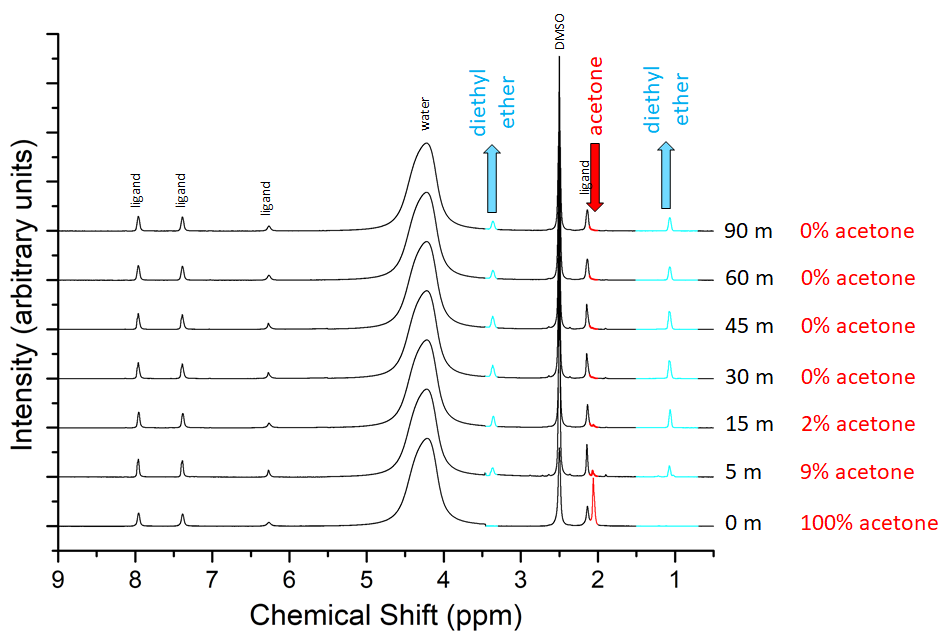


Figure 7.1.1.2. Sample MnMOF-1-ace was washed recurrently 6 times with diethyl ether during the course of 90 minutes, each time the sample was allowed to soak certain time before adding new solvent. After the solvent was changed, a portion of the material was dried softly under Ar flow and analyzed by NMR (digested in d_6 -DMSO/DCI) to quantify the amount of acetone remained in each washed.

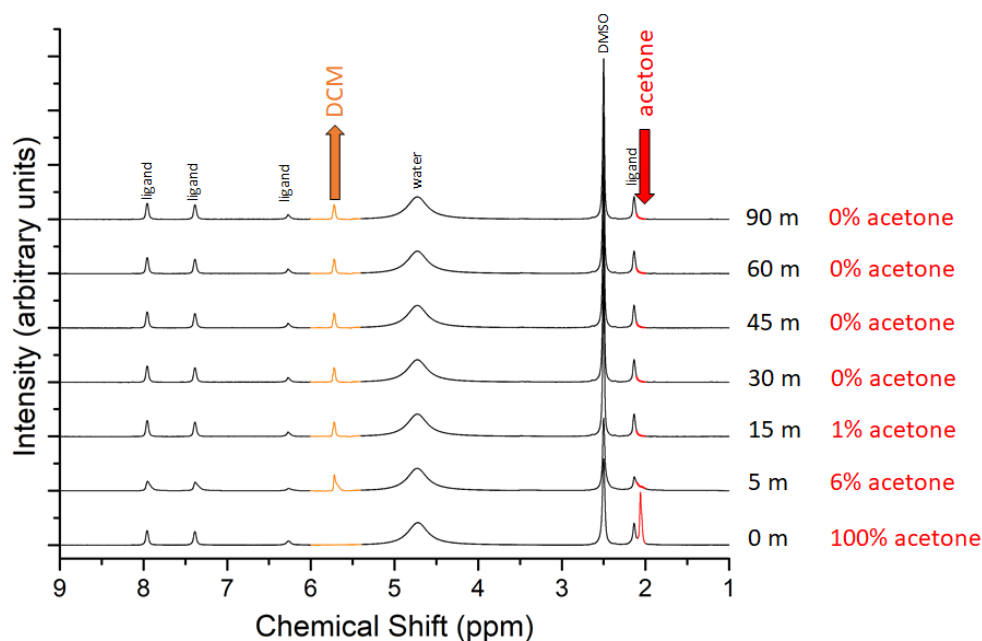


Figure 7.1.1.3. Sample MnMOF-1-ace was washed recurrently 6 times with DCM during the course of 90 minutes, each time the sample was allowed to soak certain time before adding new solvent. After the solvent was changed, a portion of the material was dried softly under Ar flow and analyzed by NMR (digested in d_6 -DMSO/DCI) to quantify the amount of acetone remained in each washed.

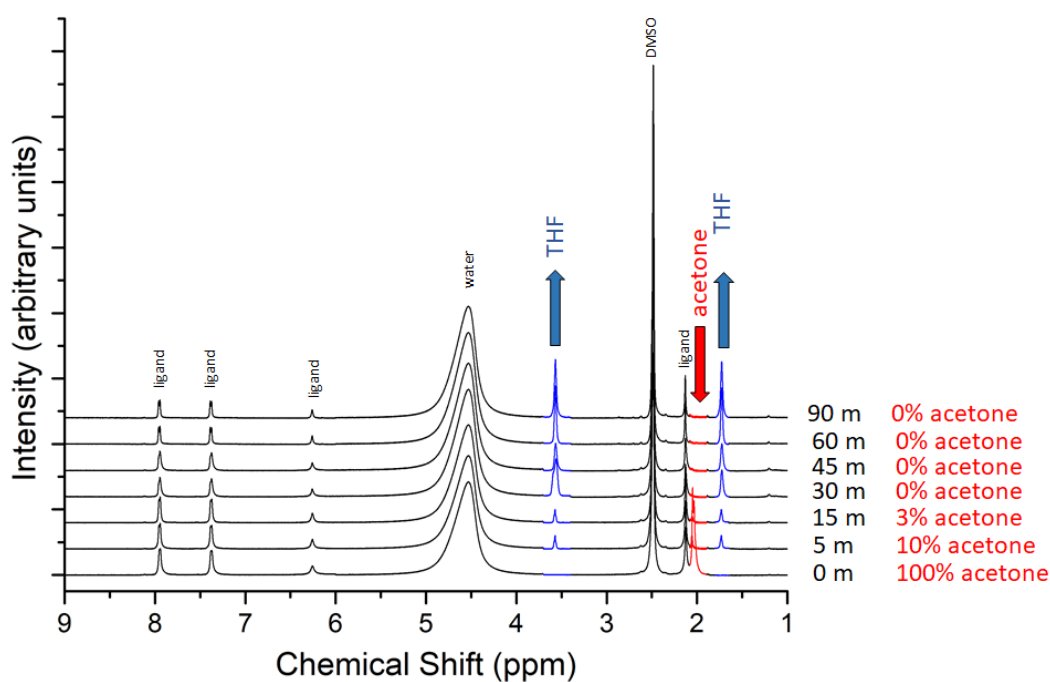


Figure 7.1.1.4. Sample MnMOF-1-ace was washed recurrently 6 times with THF during the course of 90 minutes, each time the sample was allowed to soak certain time before adding new solvent. After the solvent was changed, a portion of the material was dried softly under Ar flow and analyzed by NMR (digested in d_6 -DMSO/DCI) to quantify the amount of acetone remained in each washed.

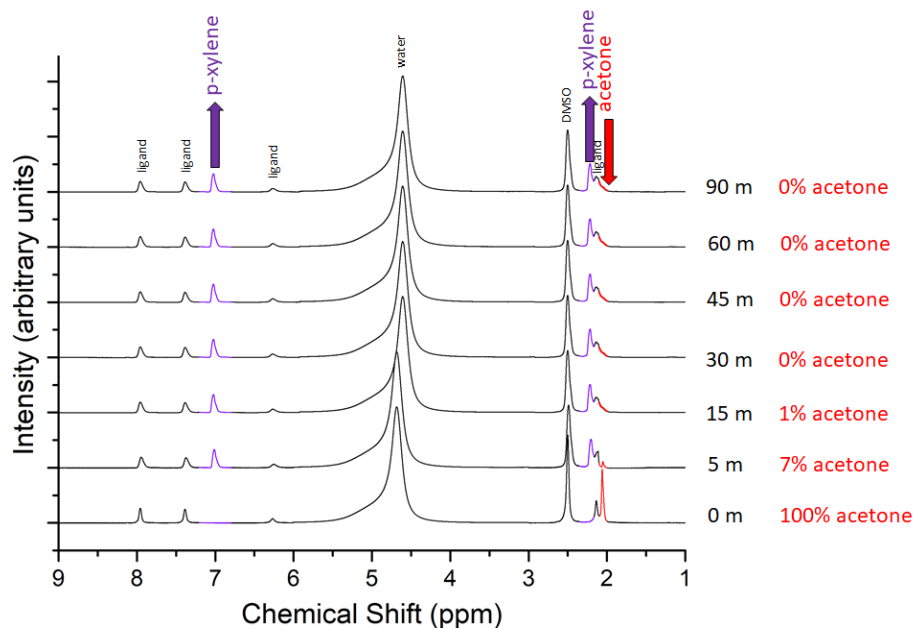


Figure 7.1.1.5. Sample MnMOF-1-ace was washed recurrently 6 times with p-xylene during the course of 90 minutes, each time the sample was allowed to soak for the specified time before adding new solvent. After the solvent was changed, a portion of the material was dried softly under Ar flow and analyzed by NMR (digested in d_6 -DMSO/DCI) to quantify the amount of acetone remained in each washed.

7.1.2. IR spectroscopy following reaction between solvated MnMOF-1 and $[\text{Rh}(\text{CO})_2\text{Cl}]_2$

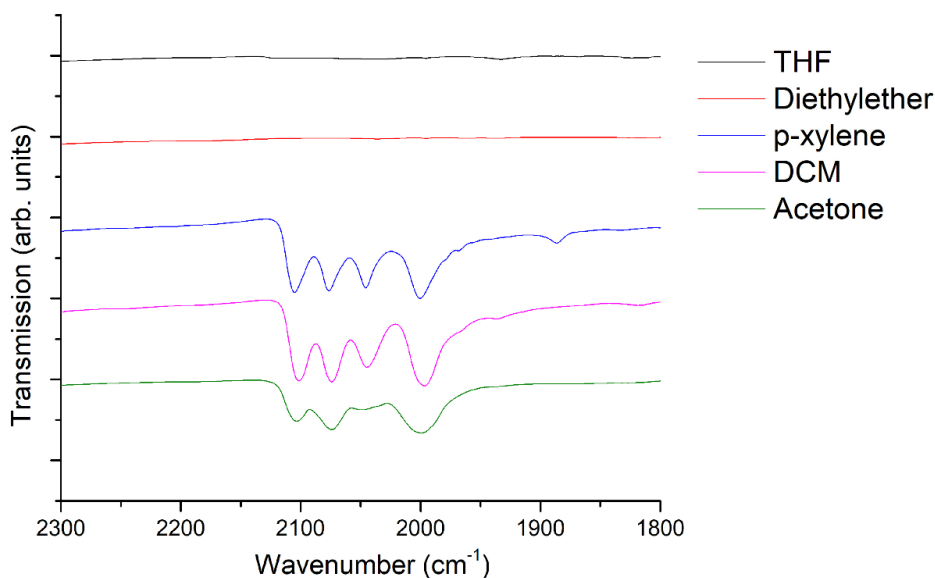


Figure 7.1.2. IR spectra of MnMOF-1 after reaction with $[\text{Rh}(\text{CO})_2\text{Cl}]_2$ in different solvents. The presence of strong CO stretching bands near 2000 cm^{-1} confirms the successful metalation of MnMOF-1 to form MnMOF-1- $[\text{Rh}(\text{CO})_2][\text{Rh}(\text{CO})_2\text{Cl}]_2$ in p-Xylene, DCM and acetone. The same reaction performed in THF or diethylether does not result in metalation, as evidenced by the absence of CO stretching bands in the IR spectrum.

7.1.3. Powder X-ray diffractograms of each sample

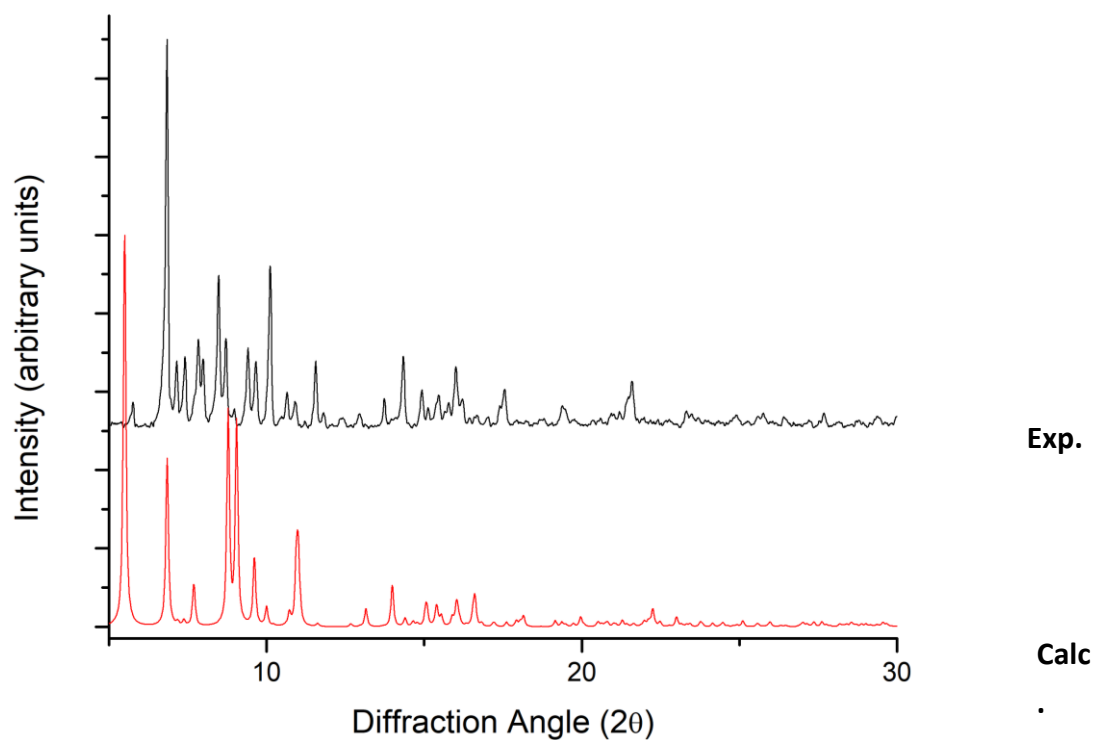


Figure 7.1.3.1. PXRD pattern obtained for **MnMOF-1-MeOH** (exp) and simulated PXRD pattern generated from the single crystal X-ray structure (calc).

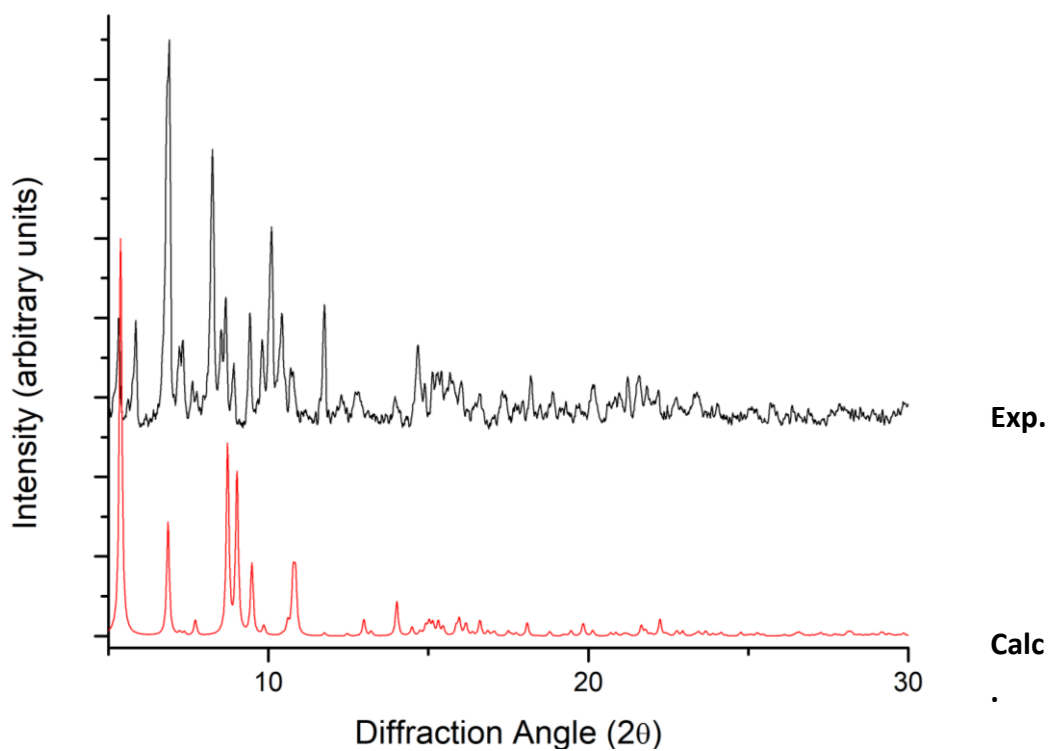


Figure 7.1.3.2. PXRD pattern obtained for **MnMOF-1-EtOH** (exp) and simulated PXRD pattern generated from the single crystal X-ray structure (calc).

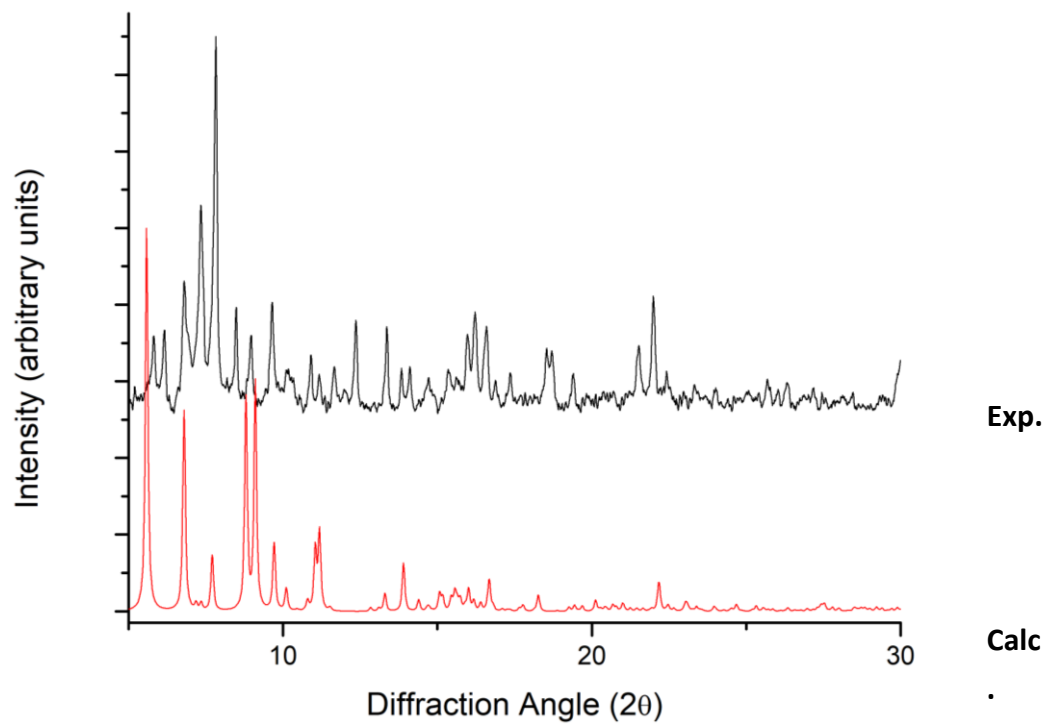


Figure 7.1.3.3. PXRD pattern obtained for **MnMOF-1-ace** (exp) and simulated PXRD pattern generated from the single crystal X-ray structure (calc).

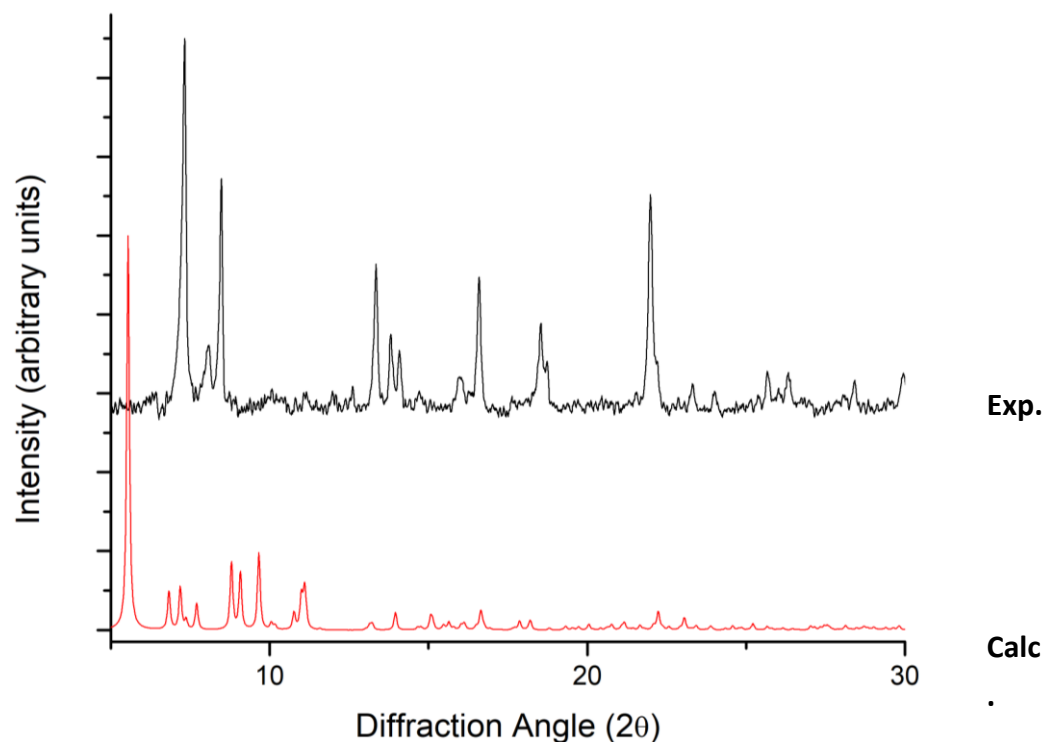


Figure 7.1.3.4. PXRD pattern obtained for **MnMOF-1-DCM** (exp) and simulated PXRD pattern generated from the single crystal X-ray structure (calc).

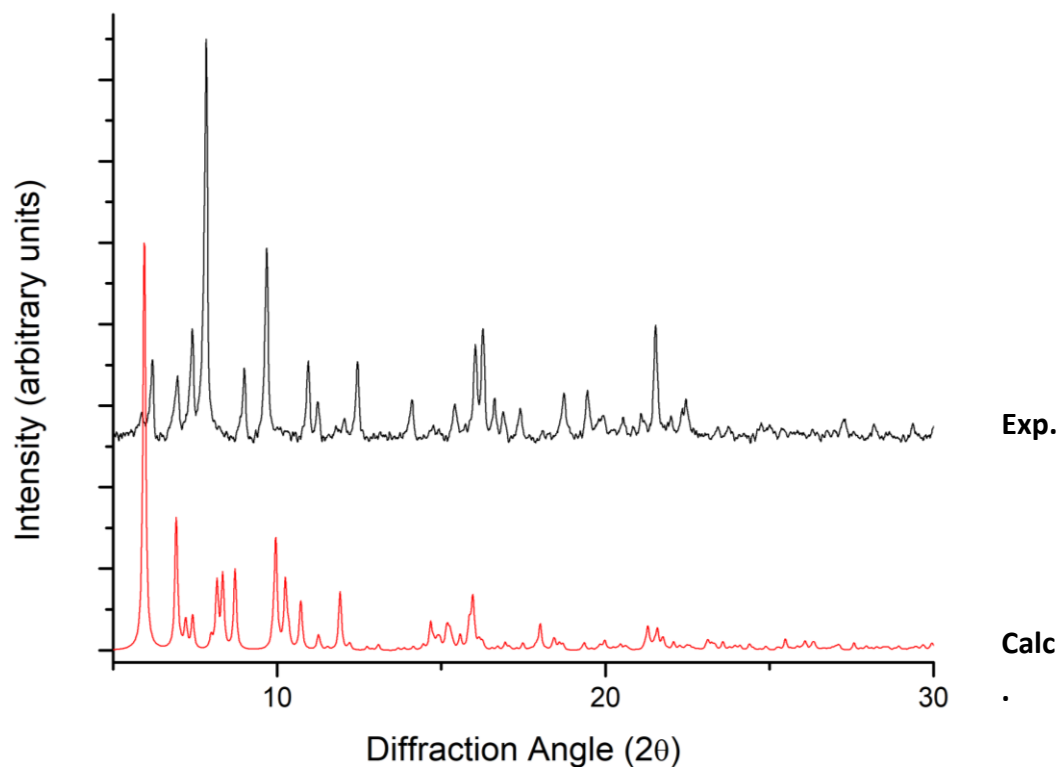


Figure 7.1.3.5. PXRD pattern obtained for **MnMOF-1-DEE** (exp) and simulated PXRD pattern generated from the single crystal X-ray structure (calc).

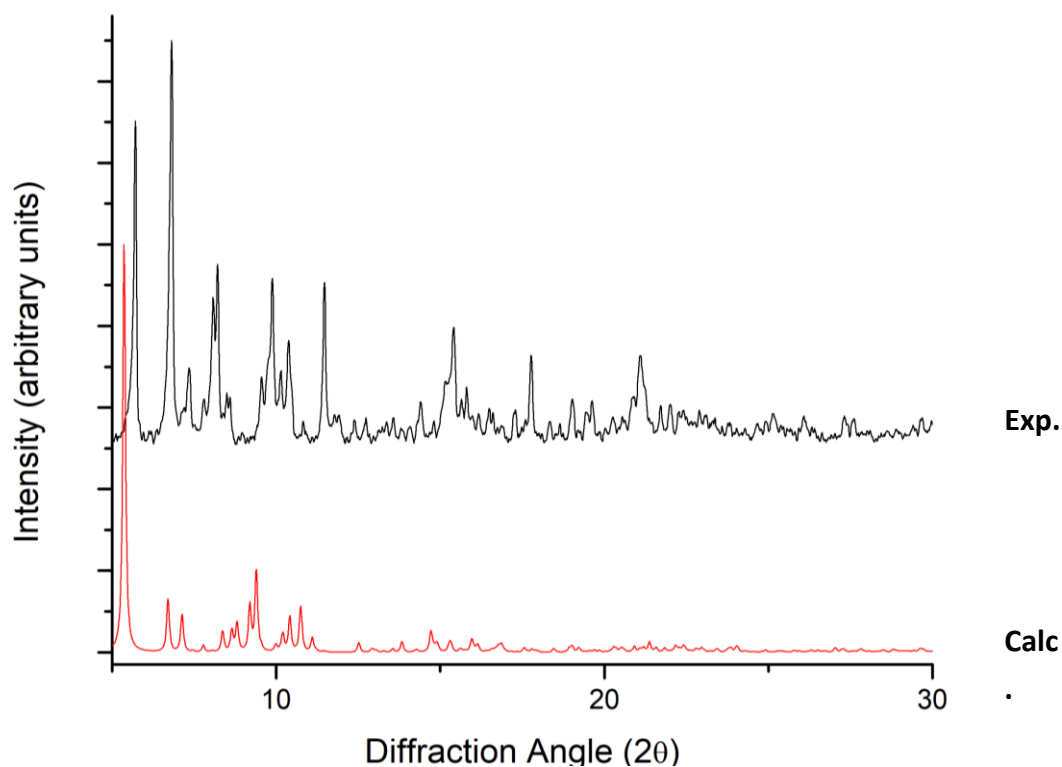


Figure 7.1.3.6. PXRD pattern obtained for **MnMOF-1-THF** (exp) and simulated PXRD pattern generated from the single crystal X-ray structure (calc).

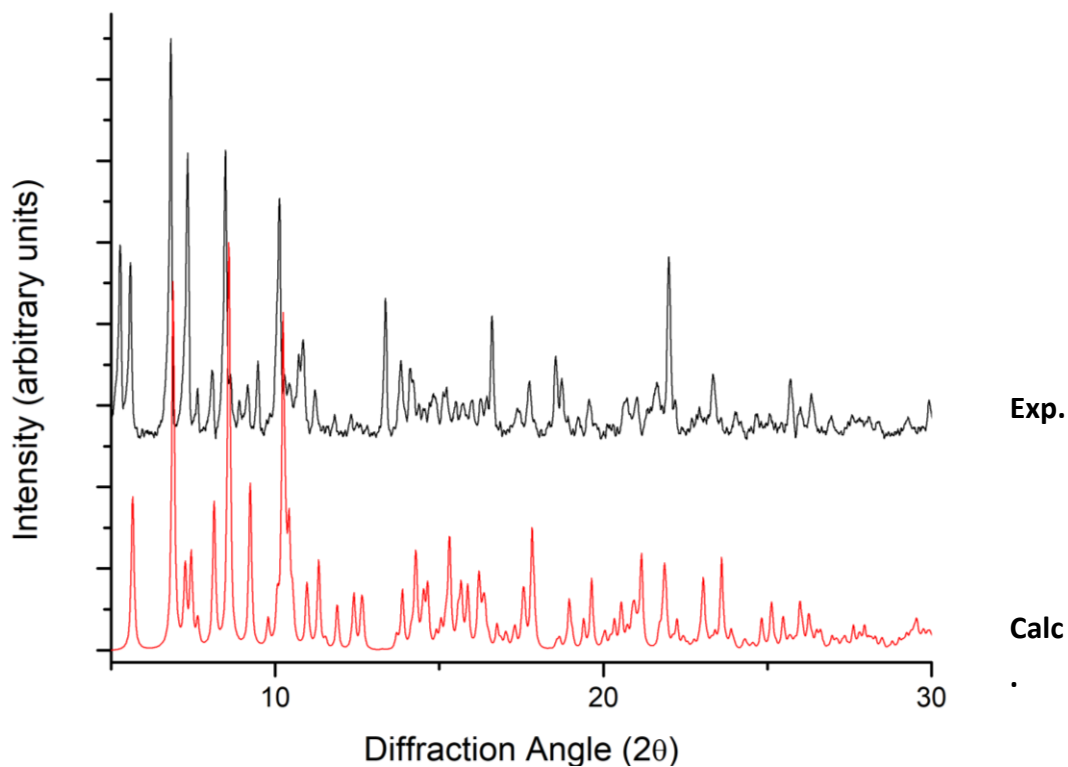


Figure 7.1.3.7. PXRD pattern obtained for **MnMOF-1-*p*-xylene** (exp) and simulated PXRD pattern generated from the single crystal X-ray structure (calc).

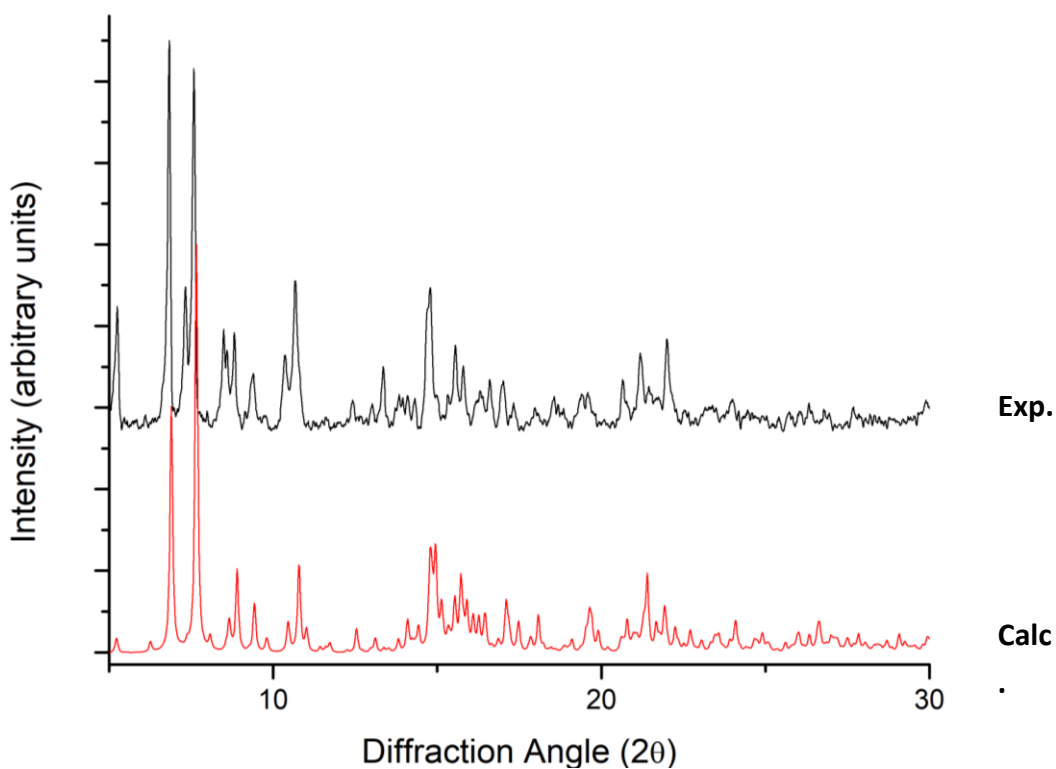


Figure 7.1.3.8. PXRD pattern obtained **MnMOF-1·[Rh(CO)₂][RhCl₂(CO)₂]** formed in *p*-xylene (exp) and simulated PXRD pattern generated from the single crystal X-ray structure (calc).

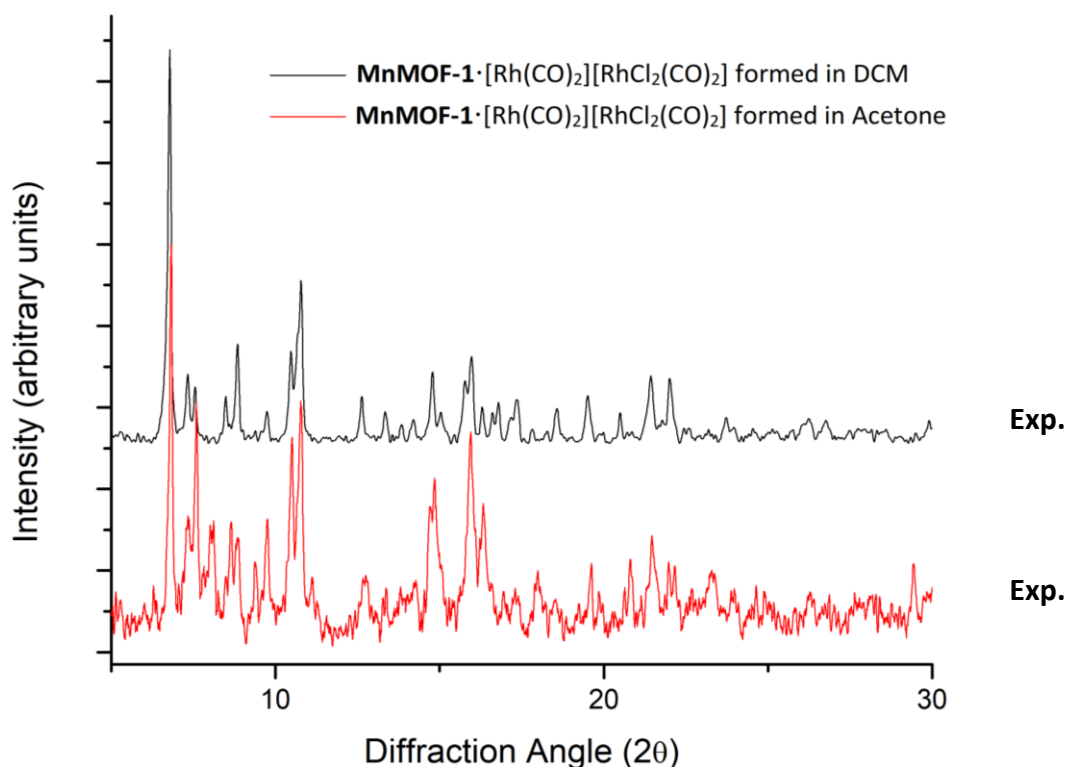


Figure 7.1.3.9. PXRD pattern obtained **MnMOF-1**·[Rh(CO)₂][RhCl₂(CO)₂] formed in DCM (exp) and PXRD pattern obtained **MnMOF-1**·[Rh(CO)₂][RhCl₂(CO)₂] formed in (exp).

7.1.4. Structure refinement details and tables of crystallographic parameters for the structures specific refinement details

MnMOF-1(MeOH). The structure possessed solvent accessible pores and in order to subtract the contribution from the disordered solvent, the SQUEEZE routine available in Platon¹ was applied to the data. Refinement against the new HKL file gave an improvement in *R*₁, *wR*₂ and *Goof*. The disorder of the bispyrazole site was modelled through the use of DFIX, EADP, EXYZ, FLAT and SIMU restraints.

MnMOF-1(*p*-xylene). The MOF structure and the solvate *p*-xylene were well ordered in this structure. A FLAT restraint was used to help the refinement of a xylene molecule.

MnMOF-1(DEE). The structure possessed solvent accessible pores and in order to subtract the contribution from the disordered solvent, the SQUEEZE routine available in Platon¹ was applied to the data. Refinement against the new HKL file gave an improvement in *R*₁, *wR*₂ and *Goof*.

MnMOF-1(EtOH). Like the methanol solvate, the structure possessed solvent accessible pores and in order to subtract the contribution from the disordered solvent, the SQUEEZE routine available in Platon¹ was applied to the data. Refinement against the new HKL file gave an improvement in *R1*, *wR2* and *GooF*. The disorder of the bispyrazole site was modelled through the use of DFIX, EADP, EXYZ, FLAT and SIMU restraints.

MnMOF-1(DCM). Like the methanol solvate, the structure possessed solvent accessible pores and in order to subtract the contribution from the disordered solvent, the SQUEEZE routine available in Platon¹ was applied to the data. Refinement against the new HKL file gave an improvement in *R1*, *wR2* and *GooF*. The disorder of the bispyrazole site was modelled through the use of DFIX, EADP, EXYZ, FLAT and SIMU restraints.

MnMOF-1(acetone). Like the methanol solvate, the structure possessed solvent accessible pores and in order to subtract the contribution from the disordered solvent, the SQUEEZE routine available in Platon¹ was applied to the data. Refinement against the new HKL file gave an improvement in *R1*, *wR2* and *GooF*. The disorder of the bispyrazole site was modelled through the use of DFIX, EADP, EXYZ, FLAT and SIMU restraints.

MnMOF-1(THF). The structure possessed solvent accessible pores and in order to subtract the contribution from the disordered solvent, the SQUEEZE routine available in Platon¹ was applied to the data. Refinement against the new HKL file gave an improvement in *R1*, *wR2* and *GooF*. DFIX restraints were used to aid the refinement of THF molecules located in the structure.

1. Spek, A. L. PLATON SQUEEZE: a tool for the calculation of the disordered solvent contribution to the calculated structure factors. *Acta. Crystallogr. C Struct. Chem.* **2015**, *71*, 9-18.

Table 7.1.4.1. X-ray experimental data for **MnMOF-1(MeOH)**, and **MnMOF-1(p-xylene)**

Compound	MnMOF-1(MeOH)	MnMOF-1(p-xylene)
CCDC #	1977797	1977798
Empirical formula	C ₁₆ H ₂₁ BO ₂	C ₂₂ H ₃₂ B ₂ O ₄
Formula weight	256.14	382.09
Crystal system	monoclinic	monoclinic
Space group	<i>P</i> 2 ₁ / <i>n</i>	<i>P</i> 2 ₁ / <i>c</i>
<i>a</i> /Å	13.6508(5)	16.4821(11)
<i>b</i> /Å	6.5437(2)	11.7361(7)
<i>c</i> /Å	16.0430(5)	12.1569(7)
α /°	90	90
β /°	96.376(3)	110.168(7)
γ /°	90	90
Volume/Å ³	1424.20(8)	2207.4(3)
Z	4	4
$\rho_{\text{calc}}/\text{cm}^3$	1.195	1.150
μ/mm^{-1}	0.075	0.075
F(000)	552.0	824.0
Crystal size/mm ³	0.49 × 0.3 × 0.27	0.45 × 0.35 × 0.25
2 θ range for data collection/°	6.73 to 58.652	6.944 to 58.648
Reflections collected	10719	7619
Independent reflections	3452 [<i>R</i> _{int} = 0.0343, <i>R</i> _{sigma} = 0.0397]	7619 [<i>R</i> _{sigma} = 0.0519]
Data/restraints/parameters	3452/0/176	7619/0/261
Goodness-of-fit on F ²	1.031	0.990
Final R indexes [<i>I</i> ≥ 2 σ (<i>I</i>)]	<i>R</i> ₁ = 0.0504, <i>wR</i> ₂ = 0.1082	<i>R</i> ₁ = 0.0713, <i>wR</i> ₂ = 0.1815
Final R indexes [all data]	<i>R</i> ₁ = 0.0681, <i>wR</i> ₂ = 0.1172	<i>R</i> ₁ = 0.0936, <i>wR</i> ₂ = 0.1906
Largest diff. peak/hole / e Å ⁻³	0.29/-0.24	0.82/-0.29

Table 7.1.4.1. (cont'd). X-ray experimental data for **MnMOF-1(DEE)** and **MnMOF-1(EtOH)**.

Compound	MnMOF-1(DEE)	MnMOF-1(EtOH)
CCDC #	1977799	1977800
Empirical formula	C ₁₇ H ₁₃ F ₃	C ₁₇ H ₁₆ O
Formula weight	274.27	236.30
Crystal system	monoclinic	monoclinic
Space group	<i>P</i> 2 ₁ / <i>c</i>	<i>P</i> 2 ₁
a/Å	12.6555(4)	6.1082(2)
b/Å	11.1090(4)	7.4449(2)
c/Å	9.1227(4)	13.4770(5)
α/°	90	90
β/°	98.759(4)	94.885(3)
γ/°	90	90
Volume/Å ³	1267.60(8)	610.64(3)
Z	4	2
ρ _{calc} /cm ³	1.437	1.285
μ/mm ⁻¹	0.113	0.078
F(000)	568.0	252.0
Crystal size/mm ³	0.6 × 0.28 × 0.21	0.46 × 0.2 × 0.08
2θ range for data collection/°	6.998 to 58.596	7.112 to 58.524
Reflections collected	14693	10936
Independent reflections	3100 [R _{int} = 0.0462, R _{sigma} = 0.0358]	2939 [R _{int} = 0.0439, R _{sigma} = 0.0450]
Data/restraints/parameters	3100/0/181	2939/1/164
Goodness-of-fit on F ²	1.063	1.026
Final R indexes [I ≥ 2σ (I)]	R ₁ = 0.0464, wR ₂ = 0.0975	R ₁ = 0.0425, wR ₂ = 0.0871
Final R indexes [all data]	R ₁ = 0.0629, wR ₂ = 0.1063	R ₁ = 0.0518, wR ₂ = 0.0907
Largest diff. peak/hole / e Å ⁻³	0.27/-0.26	0.19/-0.25

Table 7.1.4.1. (cont'd). X-ray experimental data for **MnMOF-1**[Rh(CO)₂][RhCl₂(CO)₂](p-xylene), and **MnMOF-1(DCM)**.

Compound	MnMOF-1 [Rh(CO) ₂][RhCl ₂ (CO) ₂](p-xylene)	MnMOF-1(DCM)
CCDC #	1977801	1977802
Empirical formula	C ₁₄ H ₁₂ S	C ₂₄ H ₁₆ F ₆
Formula weight	212.30	418.37
Crystal system	monoclinic	orthorhombic
Space group	<i>I</i> 2	<i>Pbca</i>
<i>a</i> /Å	14.0151(5)	9.8589(7)
<i>b</i> /Å	6.2442(2)	7.7089(5)
<i>c</i> /Å	24.7473(8)	48.243(3)
α /°	90	90
β /°	101.462(4)	90
γ /°	90	90
Volume/Å ³	2122.52(13)	3666.6(4)
<i>Z</i>	8	8
ρ_{calc} /cm ³	1.329	1.516
μ /mm ⁻¹	0.264	0.130
F(000)	896.0	1712.0
Crystal size/mm ³	0.53 × 0.1 × 0.06	0.5 × 0.1 × 0.08
2 θ range for data collection/°	6.72 to 58.774	6.756 to 58.656
Reflections collected	12935	16973
Independent reflections	4914 [<i>R</i> _{int} = 0.0350, <i>R</i> _{sigma} = 0.0461]	4462 [<i>R</i> _{int} = 0.0768, <i>R</i> _{sigma} = 0.1020]
Data/restraints/parameters	4914/9/285	4462/4/327
Goodness-of-fit on <i>F</i> ²	1.028	1.110
Final <i>R</i> indexes [<i>I</i> ≥ 2 σ (<i>I</i>)]	<i>R</i> ₁ = 0.0397, <i>wR</i> ₂ = 0.0832	<i>R</i> ₁ = 0.0879, <i>wR</i> ₂ = 0.1446
Final <i>R</i> indexes [all data]	<i>R</i> ₁ = 0.0478, <i>wR</i> ₂ = 0.0870	<i>R</i> ₁ = 0.1475, <i>wR</i> ₂ = 0.1673
Largest diff. peak/hole / e Å ⁻³	0.26/-0.22	0.31/-0.29

Table 7.1.4.1. (cont'd). Table S1 (cont'd). X-ray experimental data for **MnMOF-1(acetone)** and **MnMOF-1(THF)**.

Compound	MnMOF-1(acetone)	MnMOF-1(THF)
CCDC #	1977803	1977804
Empirical formula	C ₂₂ H ₁₆ N ₂ O ₄	C ₁₈ H ₁₄ N ₄
Formula weight	372.37	286.33
Crystal system	monoclinic	triclinic
Space group	<i>P</i> 2 ₁ / <i>c</i>	<i>P</i> -1
<i>a</i> /Å	10.5980(4)	5.9688(3)
<i>b</i> /Å	11.5690(5)	9.4191(5)
<i>c</i> /Å	14.0558(6)	12.8890(6)
α /°	90	109.120(5)
β /°	91.353(4)	92.769(4)
γ /°	90	96.001(4)
Volume/Å ³	1722.88(12)	678.27(6)
<i>Z</i>	4	2
ρ_{calc} /cm ³	1.436	1.402
μ /mm ⁻¹	0.100	0.087
<i>F</i> (000)	776.0	300.0
Crystal size/mm ³	0.4 × 0.36 × 0.08	0.5 × 0.18 × 0.07
2 θ range for data collection/°	6.786 to 58.378	6.718 to 58.82
Reflections collected	15710	15131
Independent reflections	4107 [<i>R</i> _{int} = 0.0651, <i>R</i> _{sigma} = 0.0889]	3346 [<i>R</i> _{int} = 0.0446, <i>R</i> _{sigma} = 0.0440]
Data/restraints/parameters	4107/0/253	3346/0/199
Goodness-of-fit on <i>F</i> ²	1.007	1.039
Final <i>R</i> indexes [<i>I</i> ≥ 2 σ (<i>I</i>)]	<i>R</i> ₁ = 0.0557, <i>wR</i> ₂ = 0.0943	<i>R</i> ₁ = 0.0473, <i>wR</i> ₂ = 0.0912
Final <i>R</i> indexes [all data]	<i>R</i> ₁ = 0.1072, <i>wR</i> ₂ = 0.1125	<i>R</i> ₁ = 0.0741, <i>wR</i> ₂ = 0.1007
Largest diff. peak/hole / e Å ⁻³	0.26/-0.23	0.30/-0.21

7.1.5. Thermal ellipsoid plots for all structures at the 50% probability level

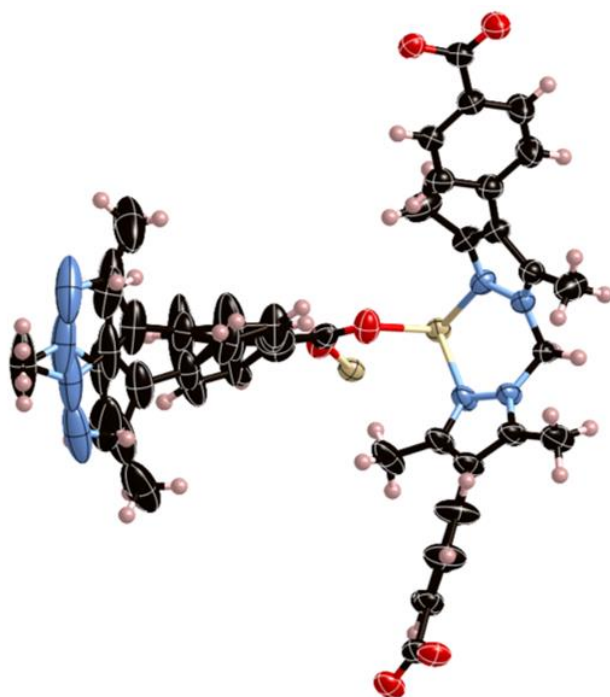


Figure 7.1.5.1. The asymmetric unit of **MnMOF-1-EtOH**, with all non-hydrogen atoms represented by ellipsoids at the 50% probability level (C, black; H, white; N, aqua; O, red; Rh, orange; Mn, beige).

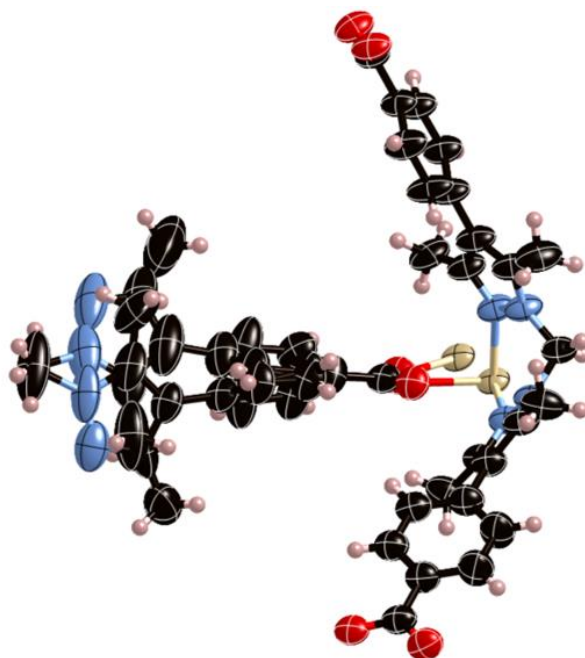


Figure 7.1.5.2. The asymmetric unit of **MnMOF-1-MeOH**, with all non-hydrogen atoms represented by ellipsoids at the 50% probability level (C, black; H, white; N, aqua; O, red; Rh, orange; Mn, beige).

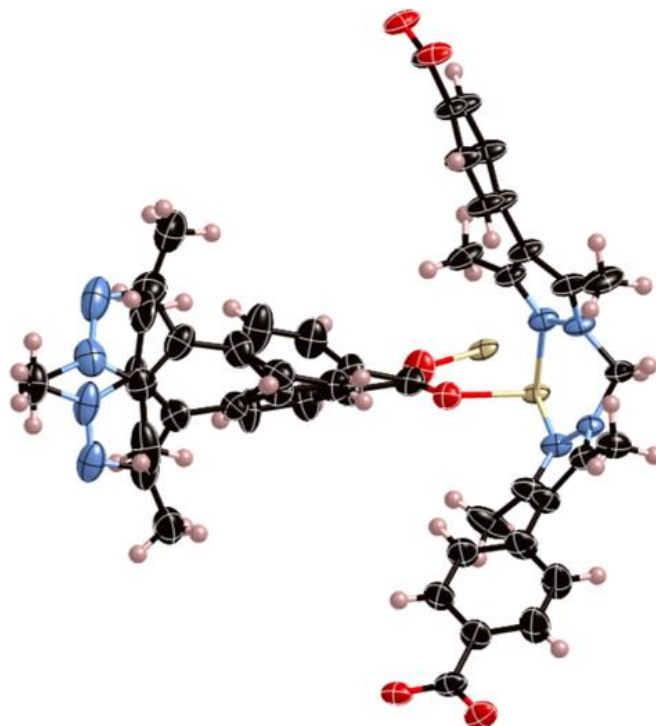


Figure 7.1.5.3. The asymmetric unit of **MnMOF-1-ace**, with all non-hydrogen atoms represented by ellipsoids at the 50% probability level (C, black; H, white; N, aqua; O, red; Rh, orange; Mn, beige).

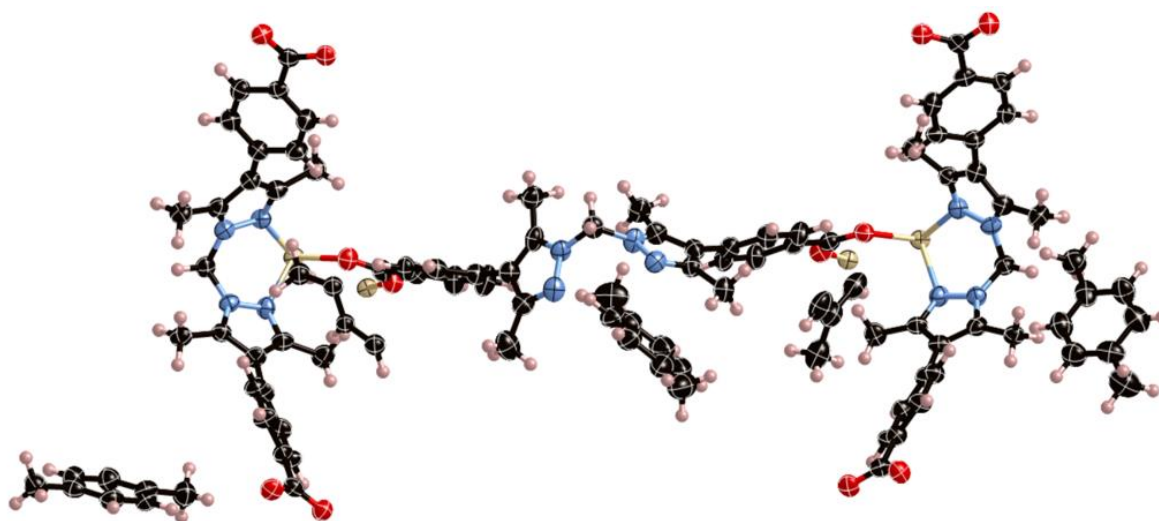


Figure 7.1.5.4 The asymmetric unit of **MnMOF-1-pXylene**, with all non-hydrogen atoms represented by ellipsoids at the 50% probability level (C, black; H, white; N, aqua; O, red; Rh, orange; Mn, beige).

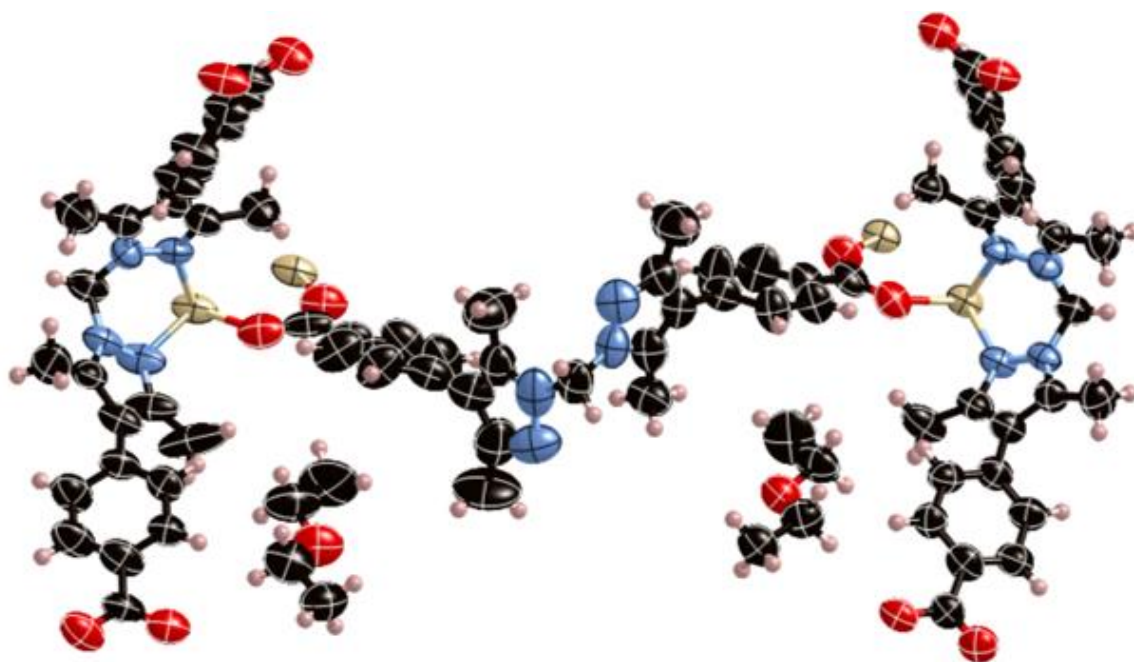


Figure 7.1.5.5. The asymmetric unit of **MnMOF-1-DEE**, with all non-hydrogen atoms represented by ellipsoids at the 50% probability level (C, black; H, white; N, aqua; O, red; Rh, orange; Mn, beige).

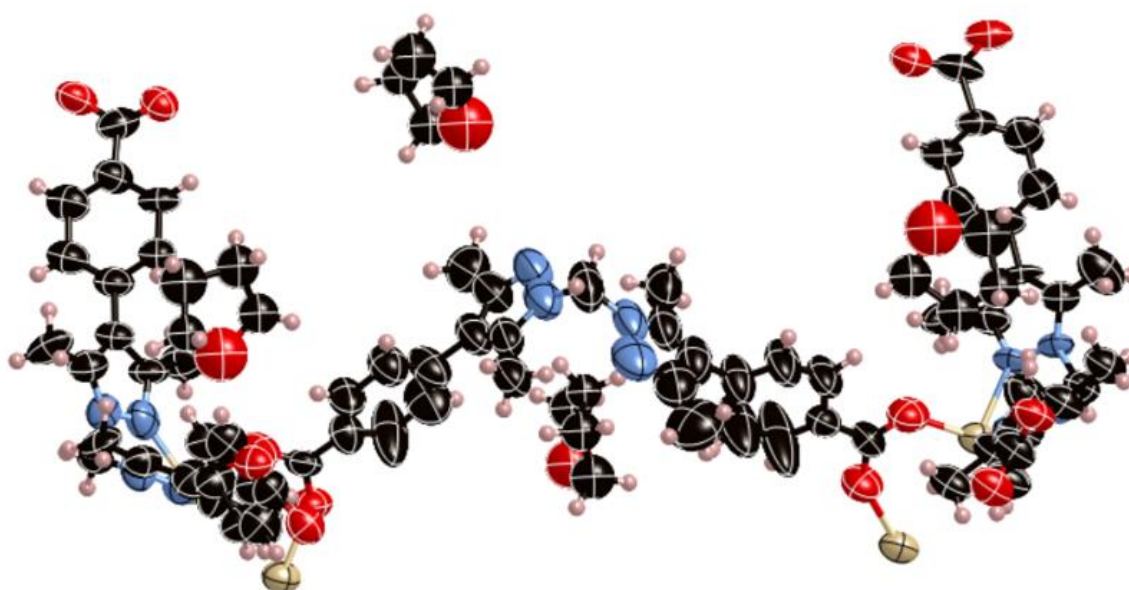


Figure 7.1.5.6. The asymmetric unit of **MnMOF-1-THF**, with all non-hydrogen atoms represented by ellipsoids at the 50% probability level (C, black; H, white; N, aqua; O, red; Rh, orange; Mn, beige).

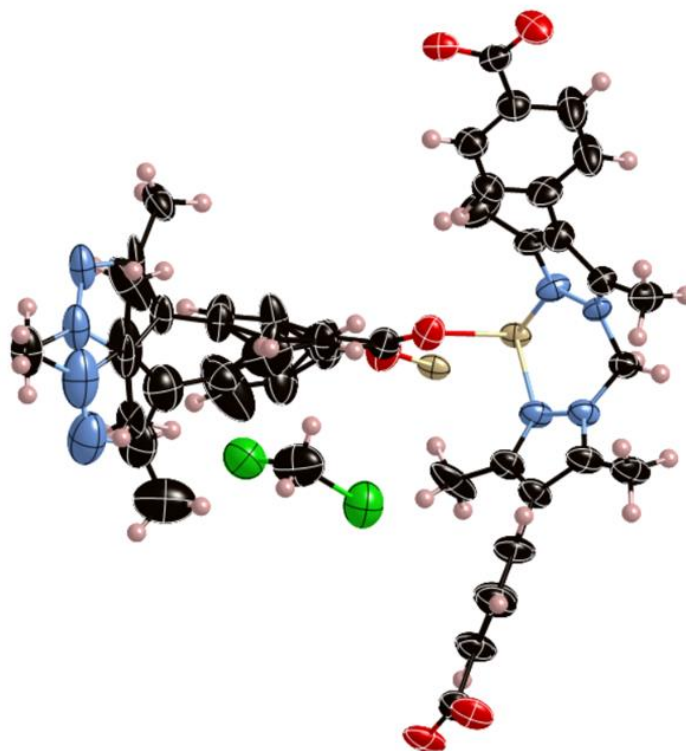


Figure 7.1.5.7. The asymmetric unit of **MnMOF-1-DCM**, with all non-hydrogen atoms represented by ellipsoids at the 50% probability level (C, black; H, white; N, aqua; O, red; Rh, orange; Mn, beige).

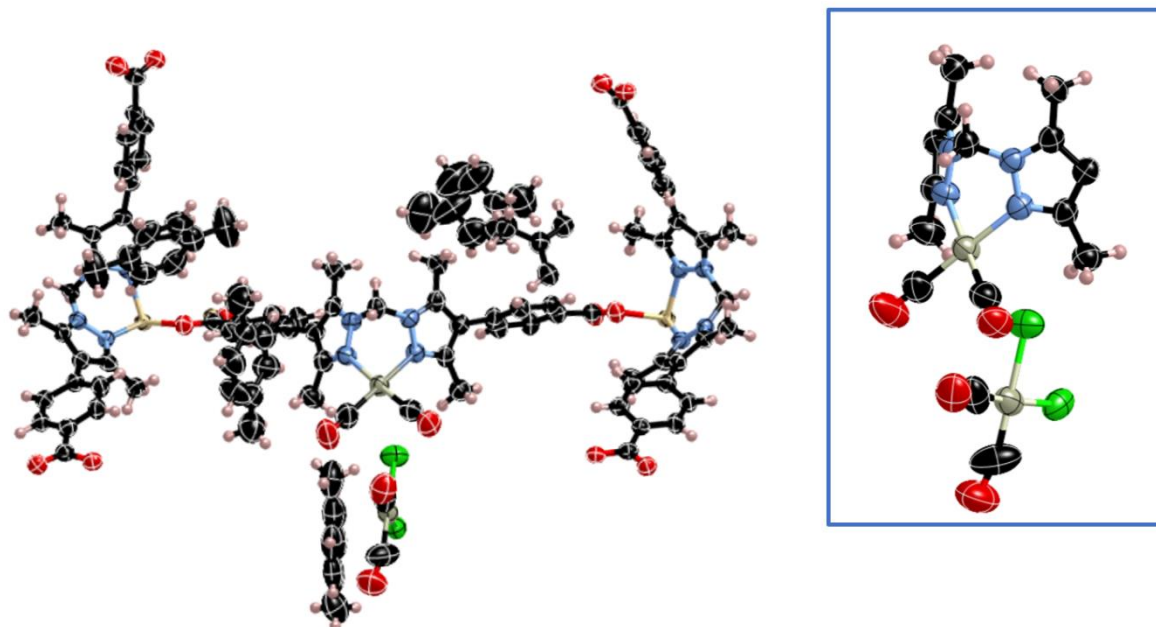


Figure 7.1.5.8. (left) The asymmetric unit of **MnMOF-1-[Rh(CO)₂][Rh(CO)₂Cl₂]**, with all non-hydrogen atoms represented by ellipsoids at the 50% probability level (C, black; H, pink; N, aqua; O, red; Rh, orange; Mn, beige; Rh, white). **(Right)** A perspective view of the chelating site, displaying the coordinating sphere of the Rh(I) centre and its associated [Rh(CO)₂Cl₂] anion.

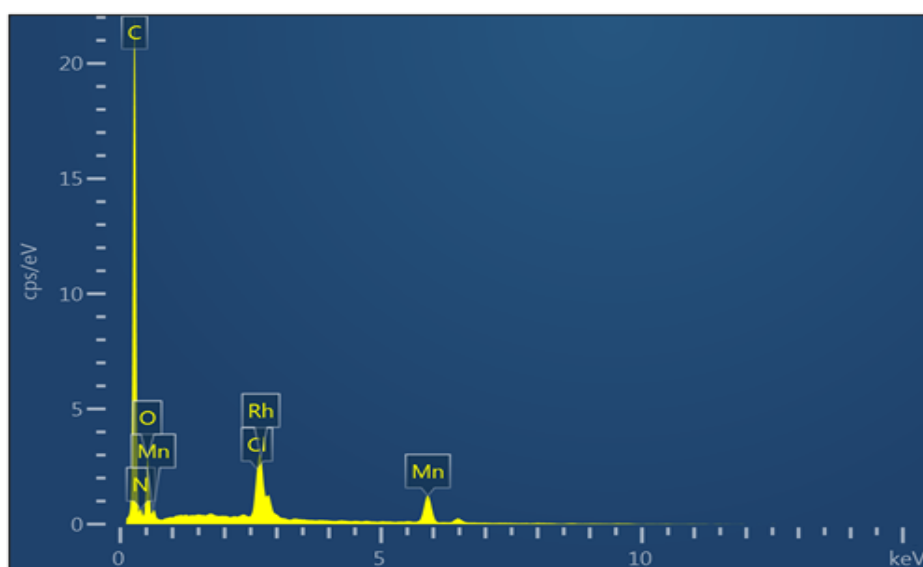
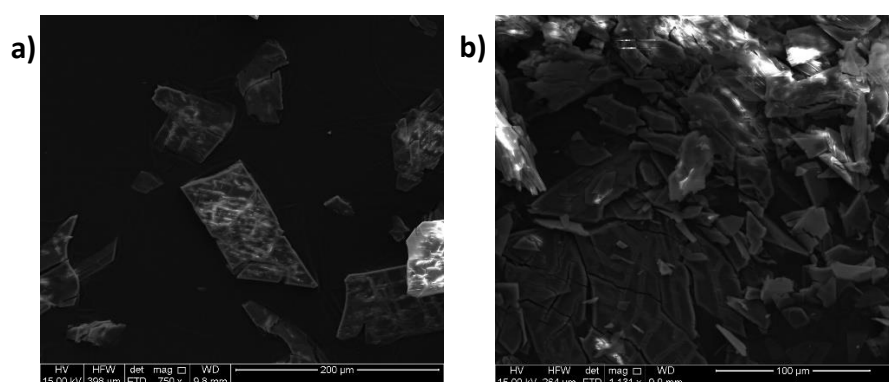
7.1.6. Energy Dispersive X-ray Analysis (EDX)

Table 7.1.6.1. Rh(I) occupancy determined via measurement of the Mn:Rh ratio using EDX analysis.

Sample	Rh, Chloride occupancy (%) ^{a,b}	Std error (%)
MnMOF-1-ace	210	4.7
MnMOF-1-DCM	198	4.3
MnMOF-1-DEE	3	2.5
MnMOF-1THF	5	1.5

^a Average atomic% obtained from four crystals.

^b Relative to full occupancy of the free chelation sites in **1**.

**Figure 7.1.6.1.** Representative raw EDX spectra for MnMOF-1·[Rh(CO)₂][RhCl₂(CO)₂] in acetone**Figure 7.1.6.2.** SEM images of MnMOF-1·[Rh(CO)₂][RhCl₂(CO)₂] in acetone showing (a) an example of a single crystal (b) a group of crystals.

7.2. Supplementary information for Chapter 3

7.2.1. Energy Dispersive X-ray (EDX) Analysis

Table 7.2.1.1. Rh(I) and associated anion occupancy determined via measurement of the Mn:Rh ratio and the Rh:Cl ratio using EDX analysis.

Sample	Rh, Chloride occupancy (%) ^{a,b}		Std error (%)
1 ·[Rh(C ₂ H ₄) ₂][Rh(C ₂ H ₄) ₂ Cl ₂]	198.6	202.1	4.7
1 ·ETH-Cl	104.2	106.6	5.4
1 ·ETH-BF ₄	101.3	0.8	1.2
1 ·[Rh(NBD)][Rh(NBD)Cl ₂]	203.6	206.3	4.1
1 ·NBD-BF ₄	100.8	0.05	0.8
1 ·NBD-Cl	103.2	101.4	3.6
1 ·MeCN-Cl	101.7	98.7	1.4

^a Average atomic% obtained from three areas.

^b Relative to full occupancy of the bis(pyrazole)methane coordinating sites in **1**.

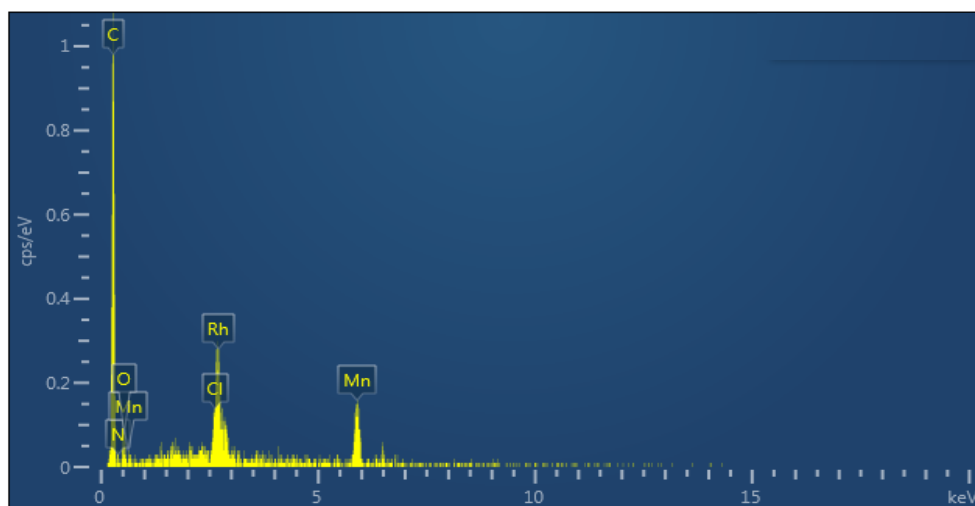


Figure 7.2.1.1. Representative raw EDX spectra for **1**·[Rh(C₂H₄)₂][Rh(C₂H₄)₂Cl₂].

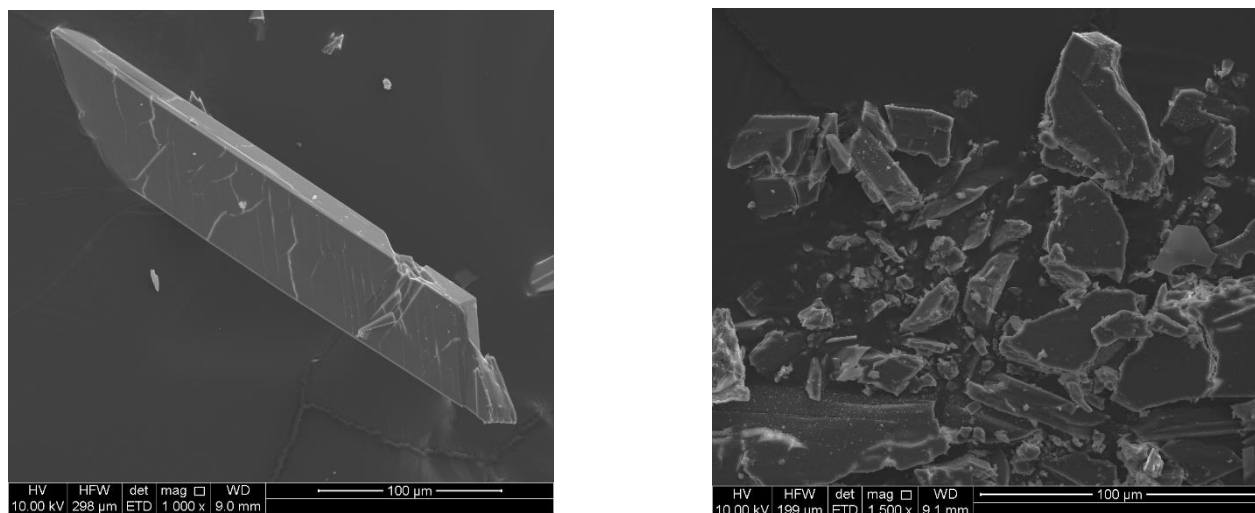


Figure 7.2.1.2. SEM images of metalated **1** showing (left) a single crystal and (right) an area of crushed crystals used for EDX analysis.

7.2.2. High Resolution Transmission Electron Microscopy (HR-TEM), Selected Area Electron Diffraction (SAED) and EDX analysis for 1-NBD-Cl after the hydrogenation

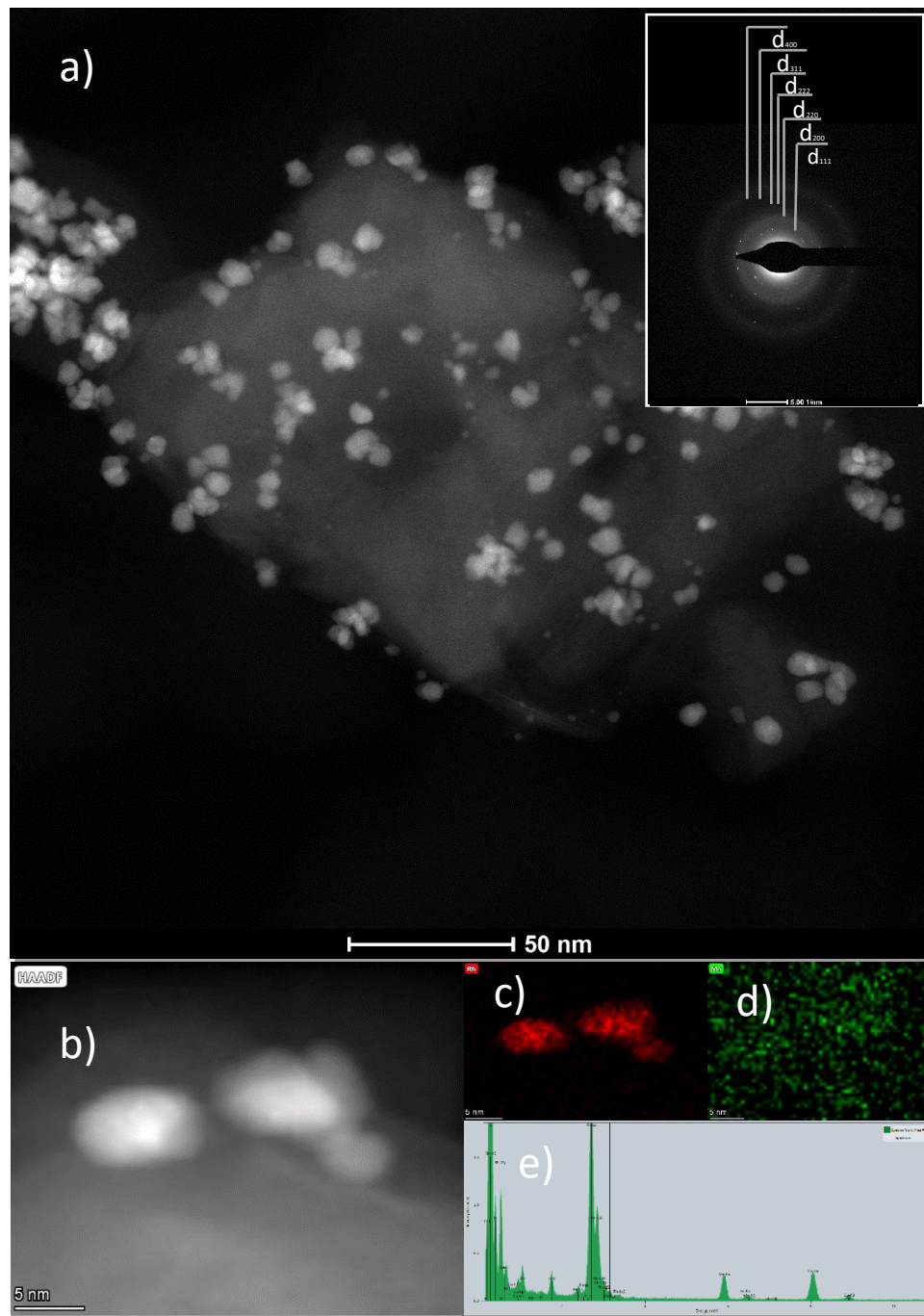


Figure 7.2.2.1. Characterization of 1-NBD-Cl after the hydrogenation. a) HR-TEM image with the corresponding SAED as an inset. Nanoparticles show the diffraction from hkl planes which match with corresponding metallic rhodium cubic structure. b) Sketch map of the area selected for EDX element mapping of c) Rhodium, d) Manganese and e) the corresponding spectra.

7.2.3. Transmission Electron Microscopy (TEM) data and particle size analysis for 1·NBD-Cl after the hydrogenation

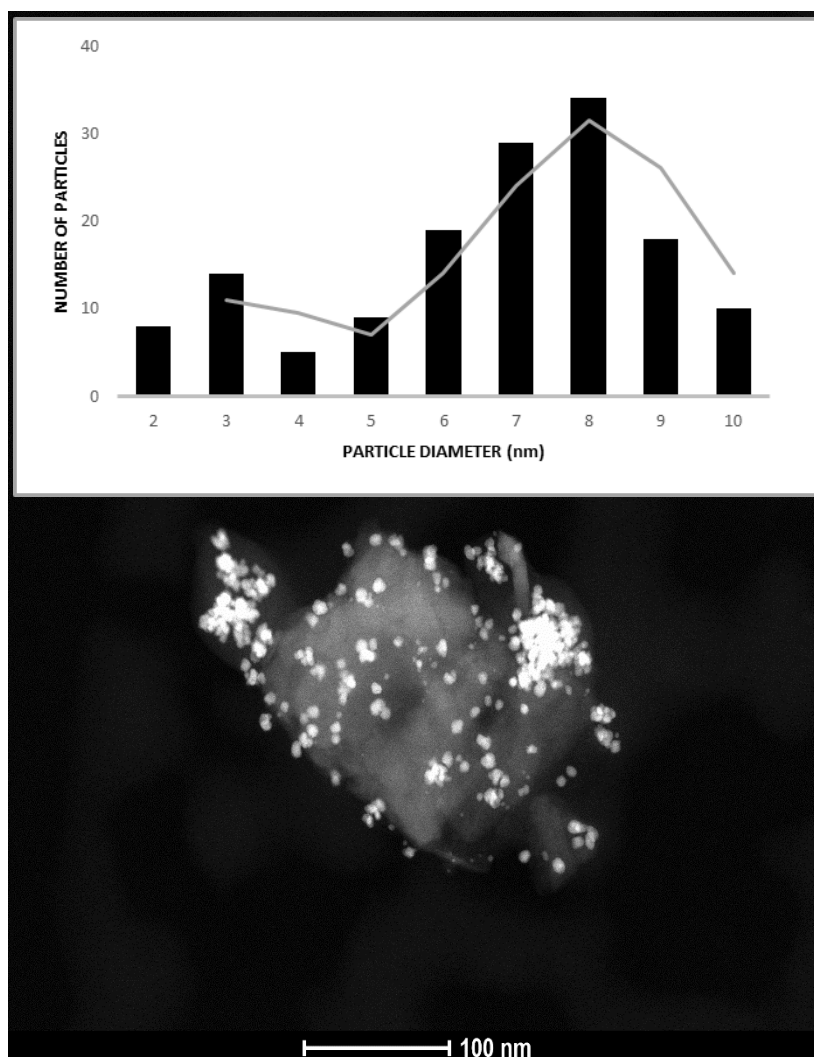


Figure 7.2.3.1. HR-TEM image revealing the formation of nanoparticles after the hydrogenation of 1·NBD-Cl (bottom). The insert image (top) is the size distribution histogram of the 1·NP with an average of 7 nm.

7.2.4. Powder X-ray Diffraction (PXRD) plots

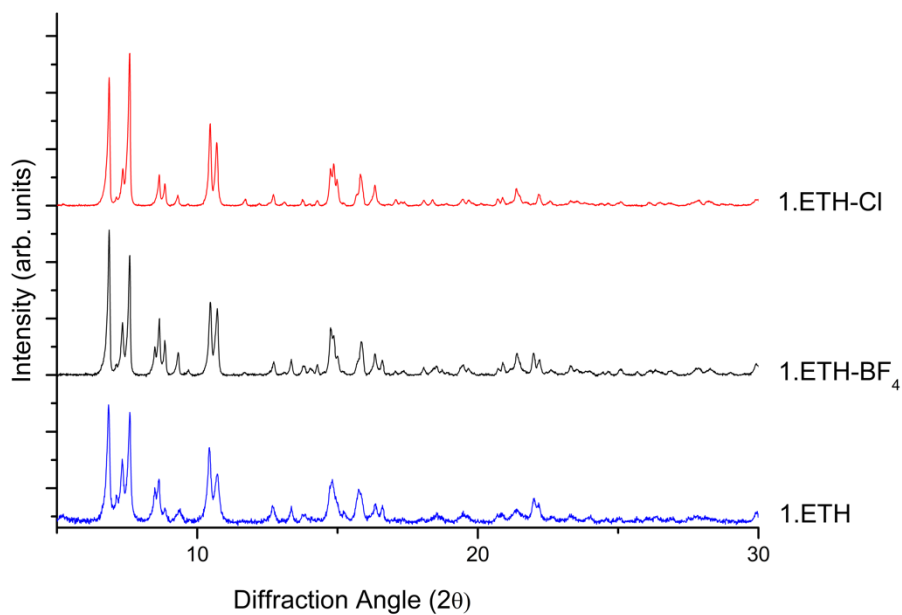


Figure 7.2.4.1. Experimental PXRD plots for 1·ETH, 1·ETH-BF₄ and 1·ETH-Cl.

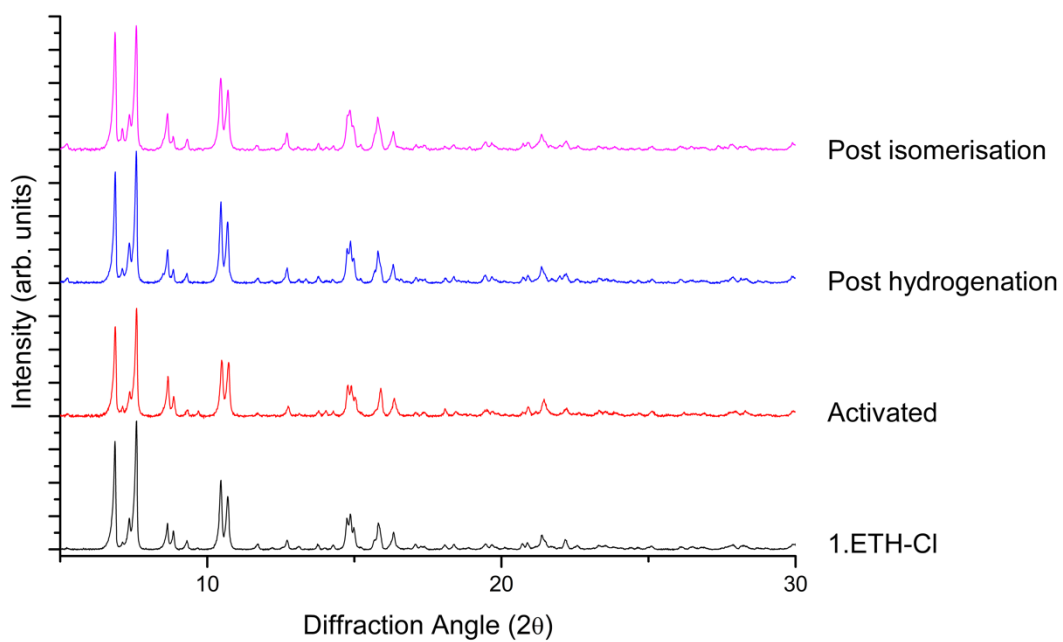


Figure 7.2.4.2. Experimental PXRD plots for 1·ETH-Cl after activation, hydrogenation and butene isomerisation catalysis.

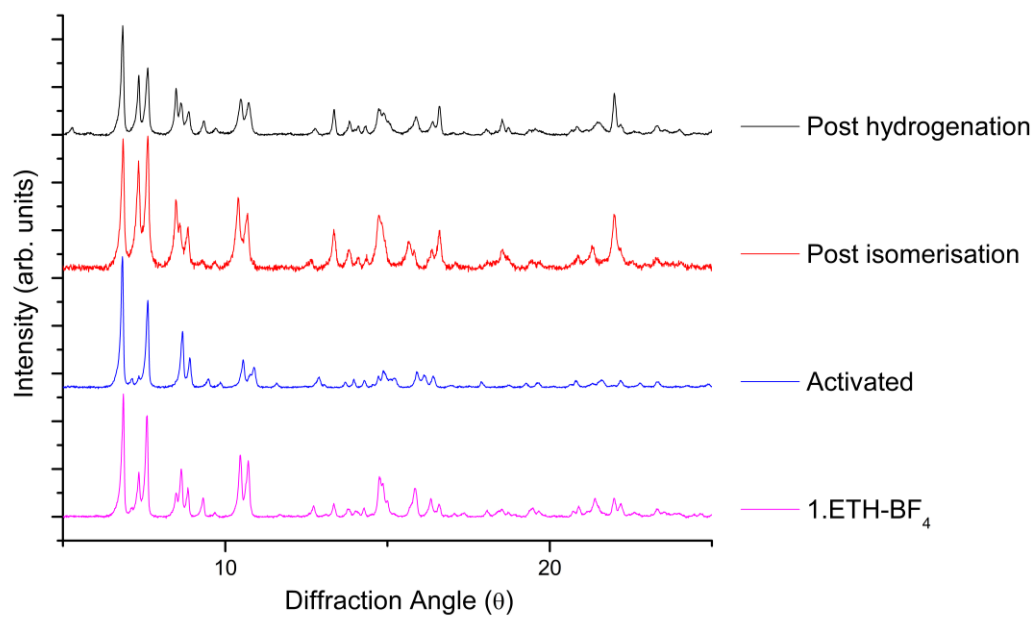


Figure 7.2.4.3. Experimental PXRD plots for 1·ETH-BF₄ after activation, hydrogenation and butene isomerization catalysis.

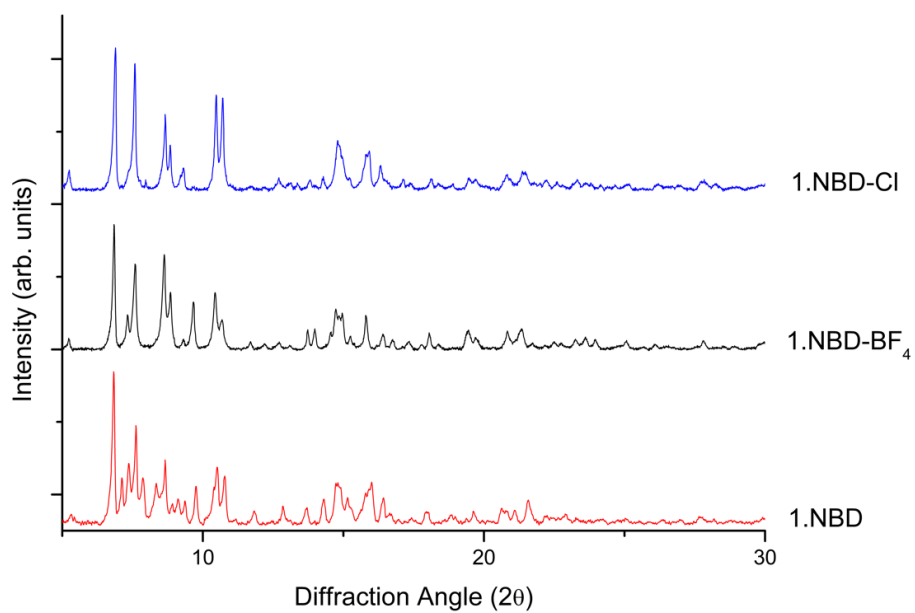


Figure 7.2.4.4. Experimental PXRD plots for 1·NBD, 1·NBD-BF₄ and 1·NBD-Cl.

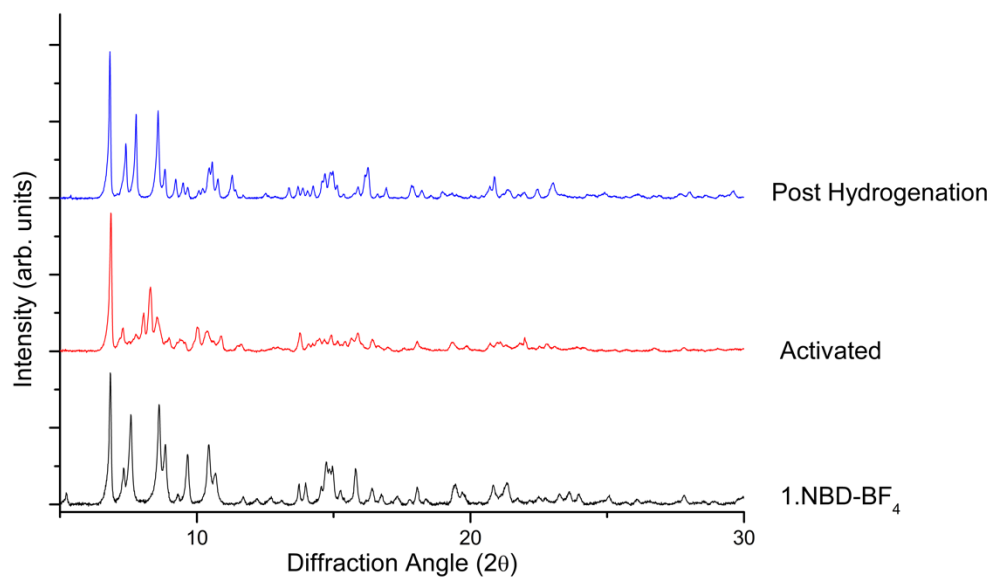


Figure 7.2.4.5. Experimental PXRD plots for 1·NBD-BF₄ after activation and hydrogenation.

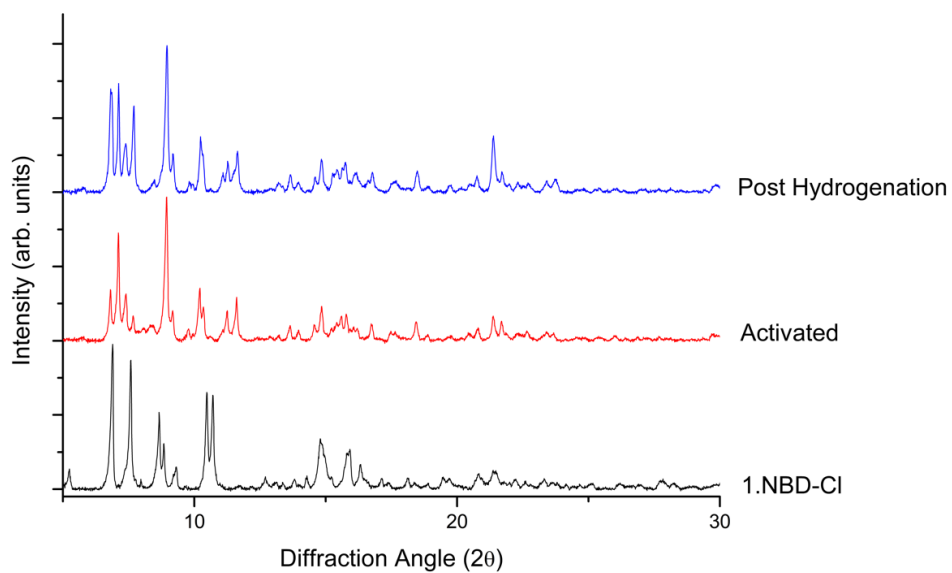


Figure 7.2.4.6. Experimental PXRD plots for 1·NBD-Cl after activation and hydrogenation.

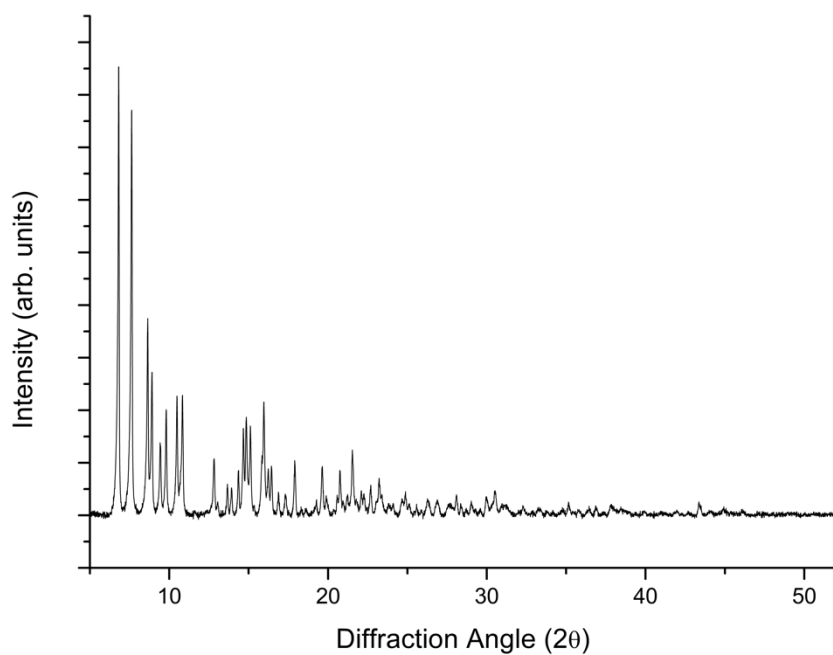


Figure 7.2.4.7. Experimental PXRD plot for 1-NP. The rhodium nanoparticles formed during hydrogenation are too small to produce discernible peaks in the PXRD pattern.

7.2.5. Single Crystal X-ray Crystallography

7.2.5.1. General Procedures

Single crystals were mounted in Paratone-N oil on a MiTeGen micromount. Single-crystal X-ray data were collected at 100 K on the MX1 or MX2 beamlines of the Australian Synchrotron¹ using the Blue-ice software interface,² $\lambda = 0.71073 \text{ \AA}$. Absorptions corrections were applied using empirical methods using SHELXS³ or SHELXT⁴ and refined by full-matrix least squares on F^2 by SHELXL,⁵ interfaced through the program X-Seed⁶ or OLEX.⁷ In general, all atoms were refined anisotropically and hydrogens atoms were included as invariants at geometrically estimated positions, unless specified otherwise in additional details in supporting information. Where noted, the data was treated with the SQUEEZE routine available in Platon.⁸ Figures were produced using the program CrystalMaker. X-ray experimental data is given in Tables S7.2.5.5.1- S7.2.5.5.4. CIF data have been deposited with the Cambridge Crystallographic Data Centre, CCDC reference numbers CCDC 2003247-2003253.

7.2.5.2. Specific Refinement Details

1·[Rh(NBD)][Rh(NBD)Cl₂] (1·NBD). The crystals were mounted from acetonitrile (MeCN). A series of DFIX, SIMU, RIGU and ISOR restraints were used to model the NBD ligands of the main moiety and the anion. The [Rh(NBD)Cl₂] anion is disordered over two sites but the NBD ligand of the minor component could not be located in the difference map (one Cl ligand lies in the anion pocket of the MOF and is not disordered). The SQUEEZE routine available in Platon was applied to the data, which gave a new HKL file. The number of located electrons was 72 and electron density equating to approximately 1.5 additional MeCN (22e) molecules per formula unit were removed by the SQUEEZE routine. There are also 3 MeCN molecules per formula unit that were located in the structure and refined.

1·[Rh(NBD)]Cl (1·NBD-Cl). The crystals were mounted from methanol (MeOH). A series of DFIX, SIMU, and ISOR restraints were used to model the NBD ligands of the main moiety. The chloride anion is disordered over two sites. The SQUEEZE routine available in Platon was applied to the data, which gave a new HKL file. The number of located electrons was 1188 and electron density equating to approximately 16.5 additional MeOH (18e) molecules per formula unit were removed by the SQUEEZE routine.

1·[Rh(NBD)]BF₄ (1·NBD-BF₄). The crystals were mounted from methanol (MeOH). The data was of sufficient quality to allow the location and refinement of the methanol (and what appears to be water molecules). A series of DFIX, EADP, and ISOR restraints were used to model the solvate molecules. The hydrogen atoms associated with the water molecules were added to the formula.

1·[Rh(CH₂CH₂)₂][Rh(CH₂CH₂)Cl₂] (1·ETH). The crystals were mounted from ethanol (EtOH). A series of DFIX and SIMU restraints were used to model the primary coordination sphere of the Rh in the main moiety and the anion. FLAT and SIMU restraints were used to model an aryl ring of the ligand. The SQUEEZE routine available in Platon was applied to the data, which gave a new HKL file. The number of located electrons was 573 and electron density equating to approximately 11 EtOH (26e) molecules per formula unit were removed by the SQUEEZE routine.

1·[Rh(CH₂CH₂)₂]Cl (1·ETH-Cl). The crystals were mounted from pentane. A series of DFIX and SIMU restraints were used to model the primary coordination sphere of the Rh in the main moiety. SIMU restraints were used to model the chelating site of the MOF. The SQUEEZE routine available in Platon was applied to the data, which gave a new HKL file. The number of located electrons was 455 and electron density equating to approximately 5.5 pentane (42e) molecules per formula unit were removed by the SQUEEZE routine.

1·[Rh(CH₂CH₂)₂]BF₄ (1·ETH-BF₄). The crystals were mounted from pentane. A series of DFIX and EADP restraints were used to model the disordered tetrafluoroborate anion (across two sites). The SQUEEZE routine available in Platon was applied to the data, which gave a new HKL file. The number of located electrons was 468 and electron density equating to approximately 5.5 pentane (42e) molecules per formula unit were removed by the SQUEEZE routine.

1·[Rh(MeCN)₂]Cl. The crystals were mounted from tetrahydrofuran (THF). The Rh(MeCN)₂Cl moiety was modelled at 70% occupancy (0.35 due to the mirror plane) despite EDX data supporting quantitative metalation. The SQUEEZE routine available in Platon was applied to the data, which gave a new HKL file. The number of located electrons was 443 and electron density equating to approximately 5.5 THF (40e) molecules per formula unit were removed by the SQUEEZE routine.

7.2.5.3. Thermal ellipsoid plots for all structures at the 50% probability level

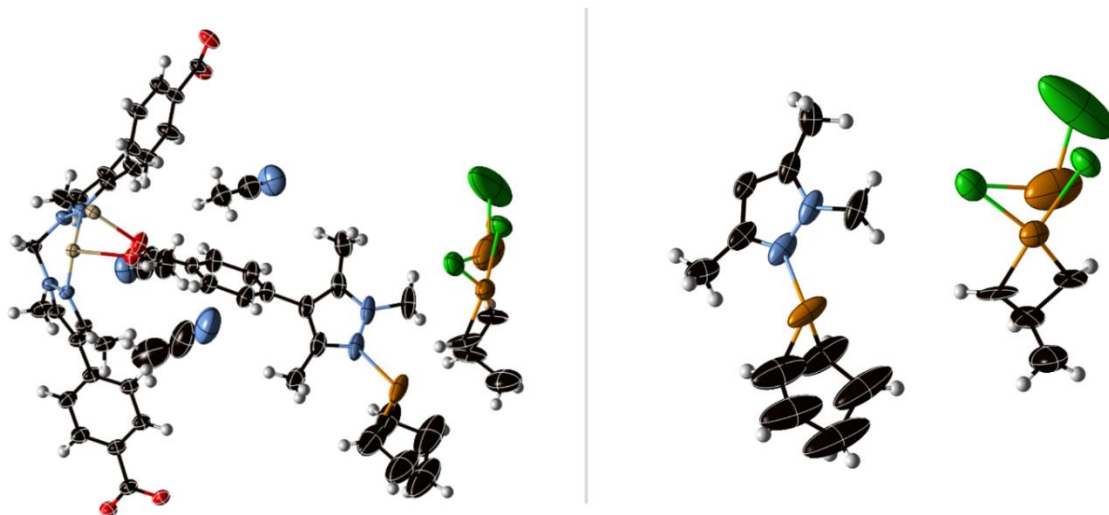


Figure 7.2.5.3.1. (left) The asymmetric unit of $1 \cdot [\text{Rh}(\text{NBD})][\text{Rh}(\text{NBD})\text{Cl}_2]$, with all non-hydrogen atoms represented by ellipsoids at the 50% probability level (C, black; H, white; N, light blue; O, red; Rh, orange; Mn, beige; Cl, green). (right) A perspective view of the Rh(I) chelation site and associated $[\text{Rh}(\text{NBD})\text{Cl}_2]$ anion (disorder shown) in $1 \cdot [\text{Rh}(\text{NBD})][\text{Rh}(\text{NBD})\text{Cl}_2]$ with all non-hydrogen atoms represented by ellipsoids at the 50% probability level.

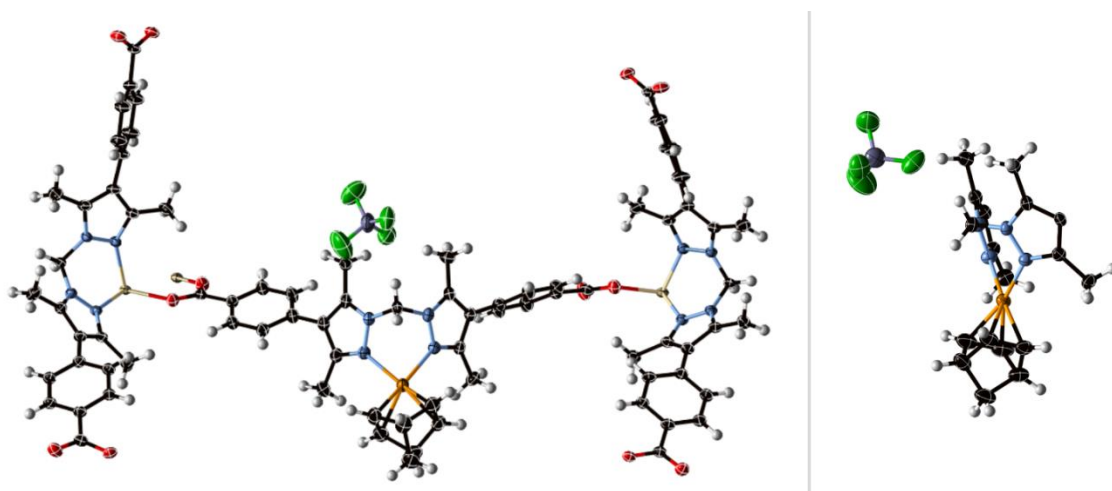


Figure 7.2.5.3.2. (left) The asymmetric unit of $1 \cdot \text{NBD} \cdot \text{BF}_4$, with all non-hydrogen atoms represented by ellipsoids at the 50% probability level (C, black; H, white; N, light blue; O, red; Rh, orange; Mn, beige; B, dark blue; F, green). (right) A perspective view of the Rh(I) site in $1 \cdot \text{NBD} \cdot \text{BF}_4$ with all non-hydrogen atoms represented by ellipsoids at the 50% probability level.

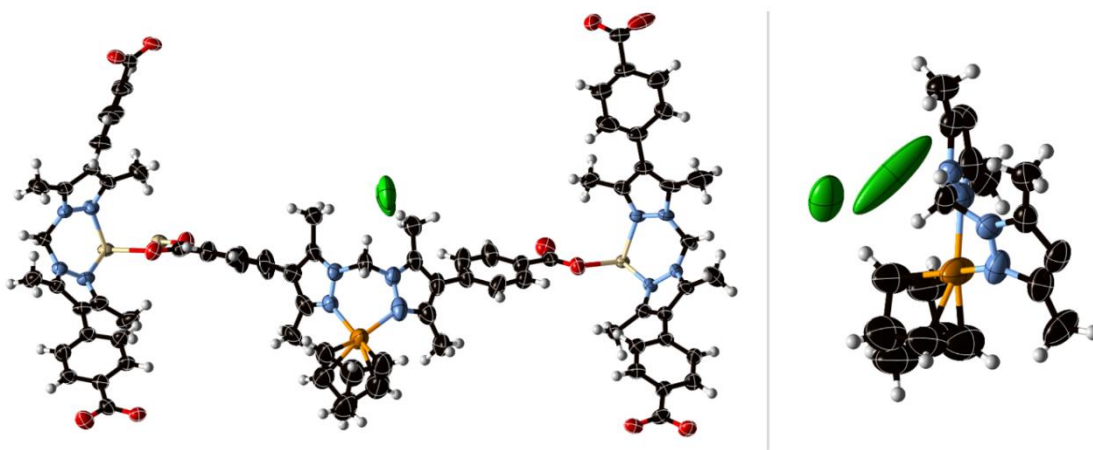


Figure 7.2.5.3.3. (left) The asymmetric unit of **1-NBD-Cl**, with all non-hydrogen atoms represented by ellipsoids at the 50% probability level (C, black; H, white; N, light blue; O, red; Rh, orange; Mn, beige; Cl, green). (right) A perspective view of the Rh(I) site and associated chloride anion (disordered over two positions) in **1-NBD-Cl** with all non-hydrogen atoms represented by ellipsoids at the 50% probability level.

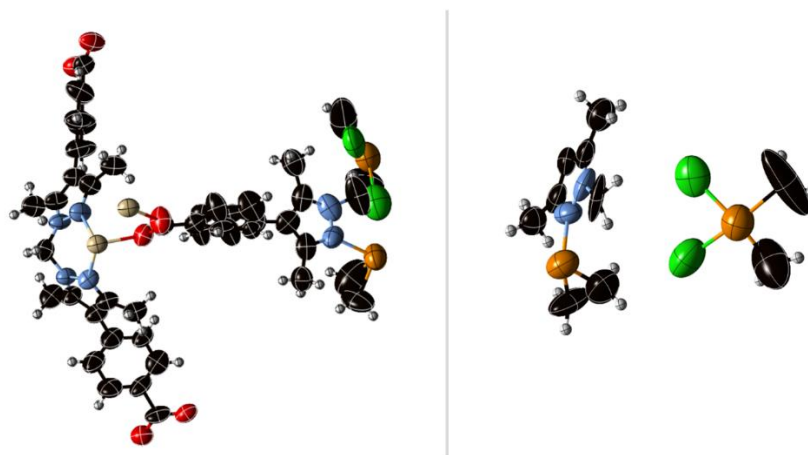


Figure 7.2.5.3.4. (left) The asymmetric unit of **1·[Rh(C₂H₄)₂][Rh(C₂H₄)₂Cl₂] (1-ETH)**, with all non-hydrogen atoms represented by ellipsoids at the 50% probability level (C, black; H, white; N, light blue; O, red; Rh, orange; Mn, beige; Cl, green). (right) A perspective view of the Rh(I) chelation site and associated [Rh(C₂H₄)₂Cl₂] anion in **1·[Rh(C₂H₄)₂][Rh(C₂H₄)₂Cl₂] (1-ETH)** with all non-hydrogen atoms represented by ellipsoids at the 50% probability level.

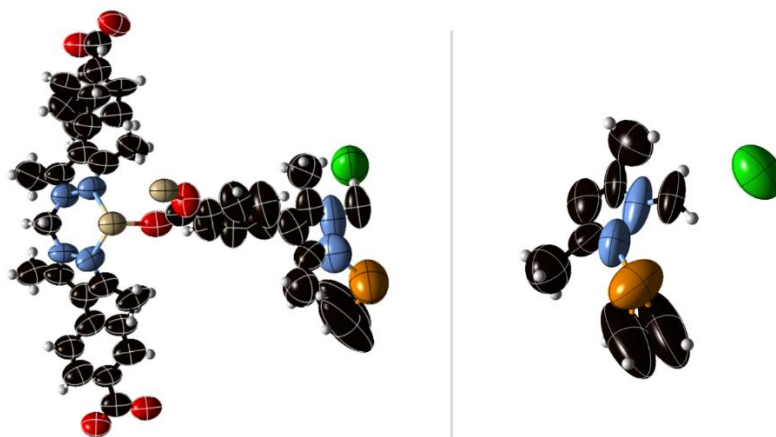


Figure 7.2.5.3.5.: (left) The asymmetric unit of **1·ETH-Cl**, with all non-hydrogen atoms represented by ellipsoids at the 50% probability level (C, black; H, white; N, light blue; O, red; Rh, orange; Mn, beige; Cl, green). (right) A perspective view of the Rh(I) site and associated chloride anion in **1·ETH-Cl** with all non-hydrogen atoms represented by ellipsoids at the 50% probability level.

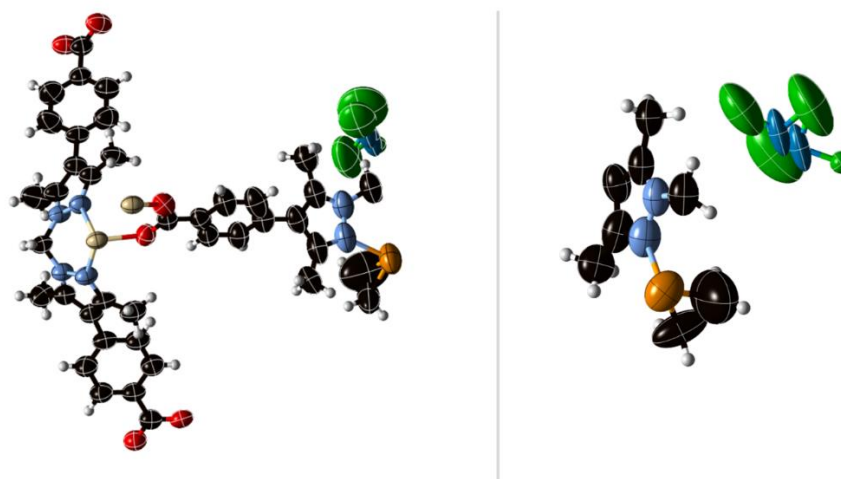


Figure 7.2.5.3.6. (left) The asymmetric unit of **1·ETH-BF₄**, with all non-hydrogen atoms represented by ellipsoids at the 50% probability level (C, black; H, white; N, light blue; O, red; Rh, orange; Mn, beige; B, dark blue; F, green). (right) A perspective view of the Rh(I) site in **1·ETH-BF₄** with all non-hydrogen atoms represented by ellipsoids at the 50% probability level (disorder of the tetrafluoroborate anion shown).

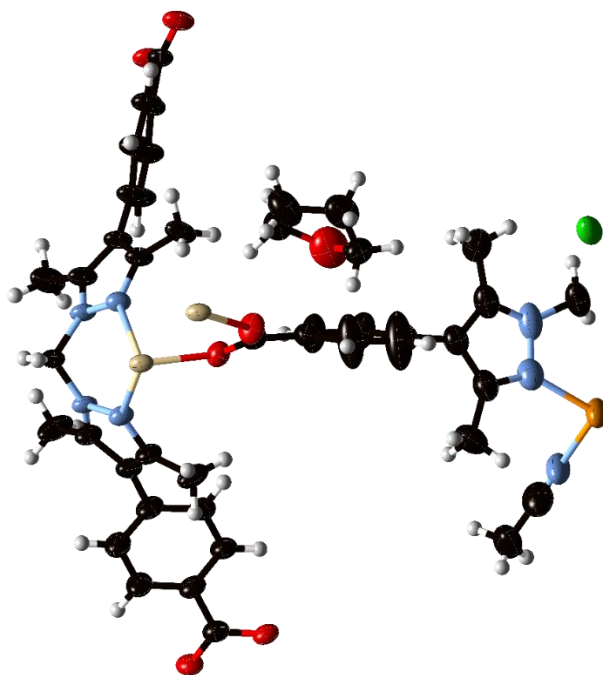


Figure 7.2.5.3.7. The asymmetric unit of $1 \cdot [\text{Rh}(\text{MeCN})_2]\text{Cl}$, with all non-hydrogen atoms represented by ellipsoids at the 50% probability level (C, black; H, white; N, light blue; O, red; Rh, orange; Mn, beige; Cl, green).

7.2.5.4 F_{obs} Electron Density Maps for all structures

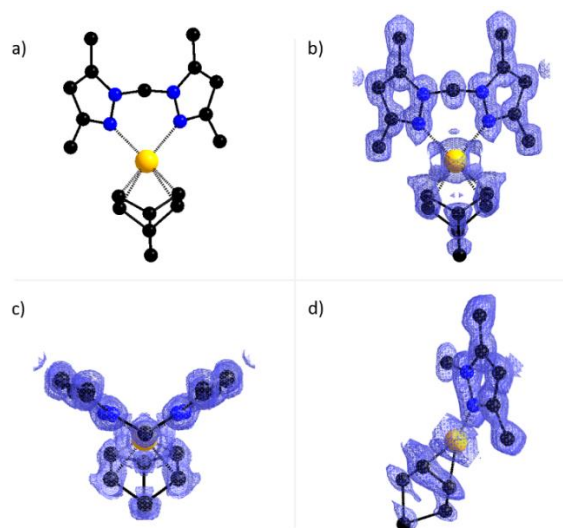


Figure 7.2.5.4.1. (a) A perspective view of the chelated Rh(I) complex in $1 \cdot [\text{Rh}(\text{NBD})][\text{Rh}(\text{NBD})\text{Cl}_2]$ and the overlaid electron density map as viewed from the (b) front, (c) top and (d) side of the complex.

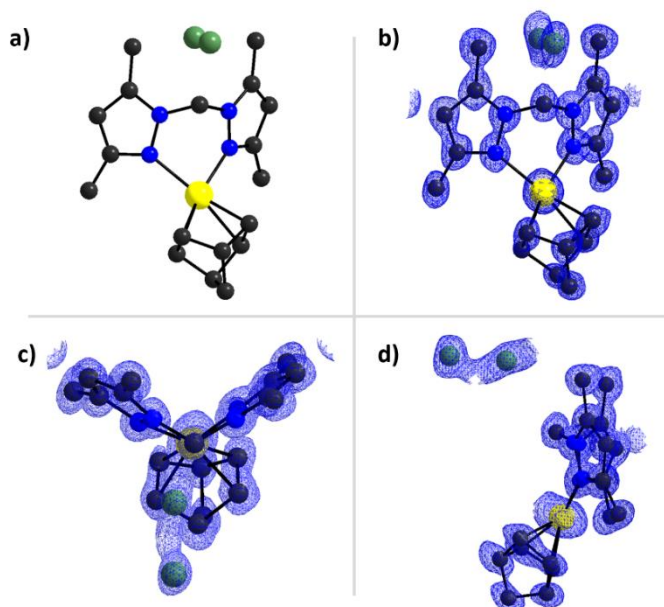


Figure 7.2.5.4.2. (a) A perspective view of the chelated Rh(I) complex in **1·NBD-Cl** and the overlaid electron density map as viewed from the (b) front, (c) top and (d) side of the complex.

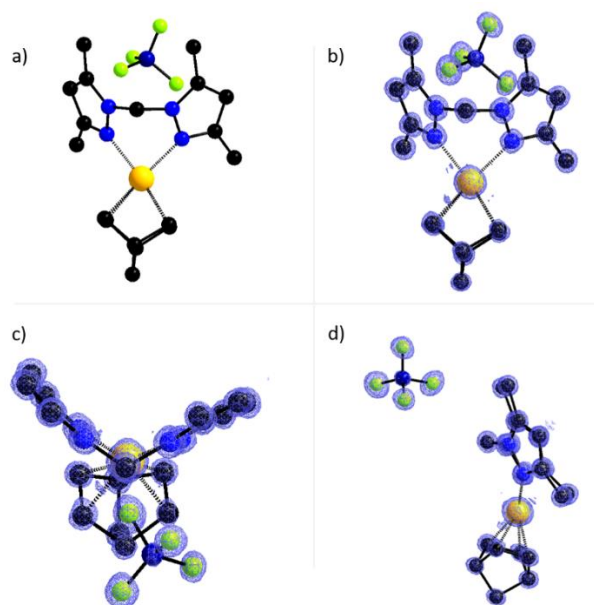


Figure 7.2.5.4.3. (a) A perspective view of the chelated Rh(I) complex in **1·NBD-BF₄** and the overlaid electron density map as viewed from the (b) front, (c) top and (d) side of the complex.

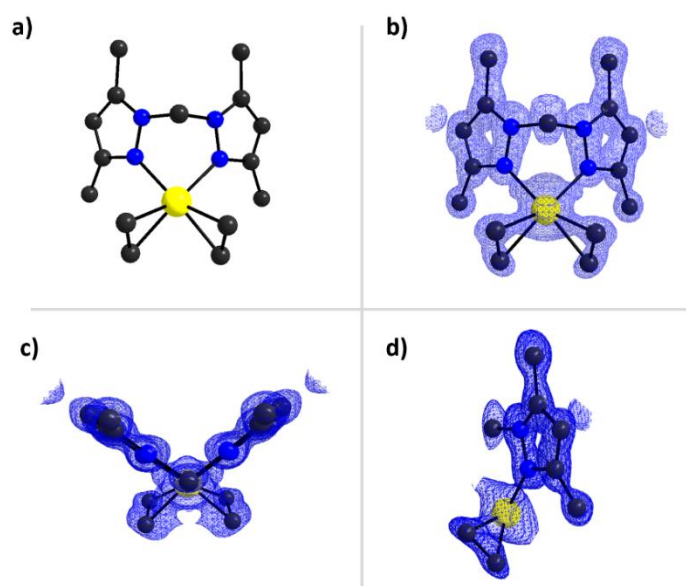


Figure 7.2.5.4.4. (a) A perspective view of the chelated Rh(I) complex in $1 \cdot [\text{Rh}(\text{C}_2\text{H}_4)_2][\text{Rh}(\text{C}_2\text{H}_4)_2\text{Cl}_2]$ ($1 \cdot \text{ETH}$) and the overlaid electron density map as viewed from the (b) front, (c) top and (d) side of the complex.

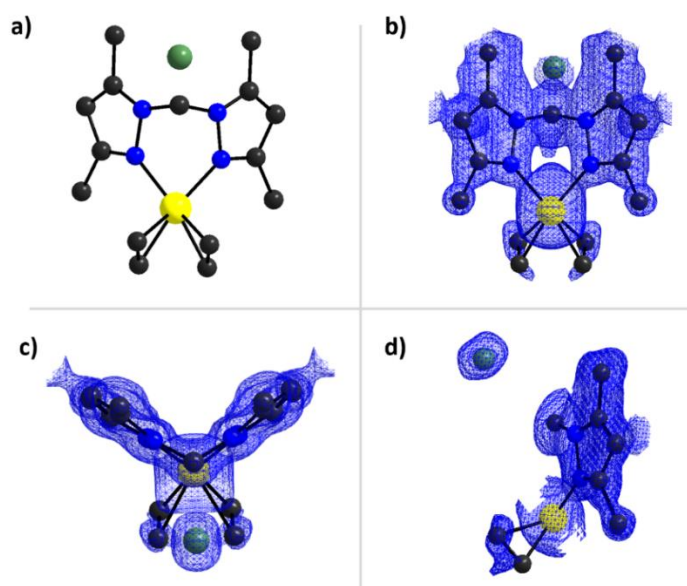


Figure 7.2.5.4.5. (a) A perspective view of the chelated Rh(I) complex in $1 \cdot \text{ETH-Cl}$ and the overlaid electron density map as viewed from the (b) front, (c) top and (d) side of the complex.

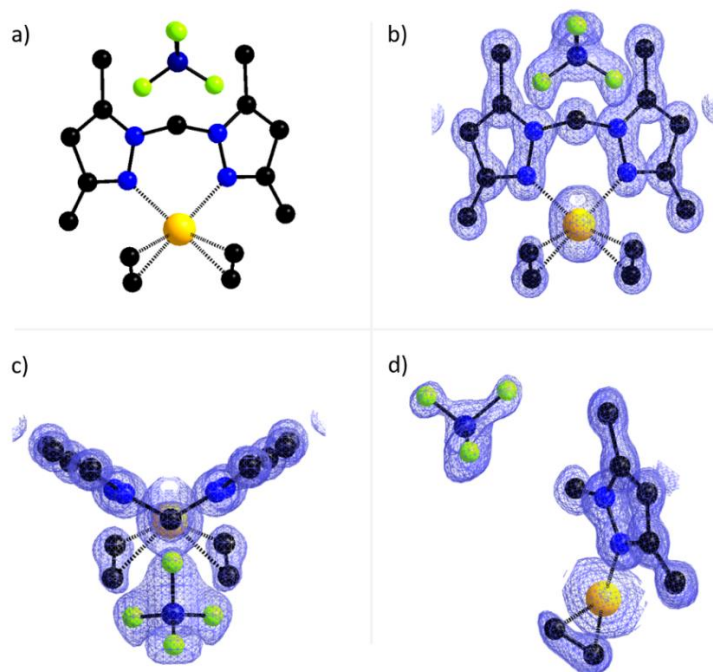


Figure 7.2.5.4.6. (a) A perspective view of the chelated Rh(I) complex in 1-ETH-BF_4 and the overlaid electron density map as viewed from the (b) front, (c) top and (d) side of the complex.

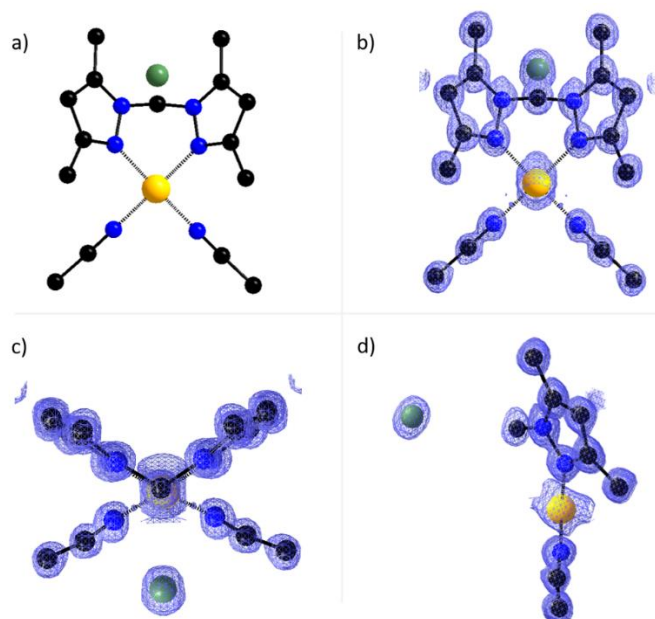


Figure 7.2.5.4.7. (a) A perspective view of the chelated Rh(I) complex in $1\text{-[Rh(MeCN)}_2\text{]Cl}$ and the overlaid electron density map as viewed from the (b) front, (c) top and (d) side of the complex.

Table S7.2.5.5.1. Crystallographic data collection and refinement parameters for the metalated forms of **1**.

Sample	1·[Rh(NBD)][Rh(NBD)Cl ₂]	1·NBD-Cl
Crystallographic Parameter		
Formula	C ₁₀₄ H _{104.5} Cl ₂ Mn ₃ N _{19.5} O ₁₂ Rh ₂	C _{98.5} H ₁₄₀ ClMn ₃ N ₁₂ O _{28.5} Rh
FW	2261	2251.40
T, K	100(2)	100(2)
Wavelength, Å	Synchrotron (0.71073)	Synchrotron ($\lambda = 0.71073$)
Crystal system, space group	Monoclinic <i>P</i> 2 ₁ / <i>m</i>	Monoclinic <i>P</i> 2 ₁ / <i>c</i>
Z	2	4
a, Å	12.336(3)	12.453(3)
b, Å	33.362(7)	33.266(7)
c, Å	13.082(3)	25.637(5)
α , °	90	90
β , °	95.42(3)	96.44(3)
γ , °	90	90
V, Å ³	5359.9(19)	10553(4)
d_{calc} , g/cm ³	1.401	1.417
Absorption coefficient, mm ⁻¹	0.762	0.611
<i>F</i> (000)	2320.0	4720
Crystal size, mm ³	0.3 × 0.15 × 0.06	0.2 × 0.11 × 0.04
2 θ range for data collection	2.442 to 64.242	2.014 to 63.75
Index range	-15 ≤ <i>h</i> ≤ 15, -44 ≤ <i>k</i> ≤ 44, -18 ≤ <i>l</i> ≤ 18	-18 ≤ <i>h</i> ≤ 18, -49 ≤ <i>k</i> ≤ 49, -35 ≤ <i>l</i> ≤ 35
Reflections collected	94565	194532
Independent reflections	14404 [R _{int} =0.0400, R _{sigma} =0.0229]	29921 [R _{int} =0.1146, R _{sigma} =0.0844]
Data/restraints/parameters	14404/84/658	29921/113/1022
GOF on F ²	1.025	1.150
Largest diff. peak and hole, eÅ ⁻³	3.96/-3.67	2.22/-2.95
R ₁ , [<i>I</i> > 2 σ (<i>I</i>)]	0.0948	0.1240
wR ₂ , all data	0.2830	0.3722
CCDC Number	2003248	2003247

Table S7.2.5.5.2. Crystallographic data collection and refinement parameters for the metalated forms of **1**.

Sample	1·NBD-BF ₄	1·[Rh(C ₂ H ₄) ₂][Rh(CH ₂ CH ₂) ₂ Cl ₂]
Crystallographic Parameter		
Formula	C _{91.75} H _{126.25} BF ₄ Mn ₃ N ₁₂ O _{27.25} Rh	C ₁₀₅ H ₁₅₂ Cl ₂ Mn ₃ N ₁₂ O ₂₃ Rh ₂
FW	2187.83	2391.92
T, K	100(2)	100(2)
Wavelength, Å	Synchrotron ($\lambda = 0.71073$)	Synchrotron ($\lambda = 0.71073$)
Crystal system, space group	Monoclinic <i>P</i> 2 ₁ / <i>c</i>	Monoclinic <i>P</i> 2 ₁ / <i>m</i>
Z	4	2
a, Å	12.462(3)	12.362(3)
b, Å	34.572(7)	33.404(7)
c, Å	25.460(5)	13.013(3)
α , °	90	90
β , °	98.63(3)	97.03(3)
γ , °	90	90
V, Å ³	10845(4)	5333.2(19)
d_{calc} , g/cm ³	1.340	1.489
Absorption coefficient, mm ⁻¹	0.572	0.776
F(000)	4559.0	2498.0
Crystal size, mm ³	0.25 × 0.13 × 0.04	0.4 × 0.25 × 0.05
2 θ range for data collection	2.002 to 63.698	2.438 to 58.41
Index range	-18 ≤ h ≤ 18, -51 ≤ k ≤ 51, -33 ≤ l ≤ 33	-14 ≤ h ≤ 14, -39 ≤ k ≤ 39, -17 ≤ l ≤ 17
Reflections collected	197727	55421
Independent reflections	30418 [R _{int} =0.0610, R _{sigma} =0.0337]	10199 [R _{int} = 0.0729, R _{sigma} = 0.0498]
Data/restraints/parameters	30418/35/1368	10199/58/566
GOF on F ²	1.147	1.755
Largest diff. peak and hole, eÅ ⁻³	2.10/-1.30	1.91/-3.13
R ₁ , [$I > 2\sigma(I)$]	0.0719	0.1840
wR ₂ , all data	0.2124	0.4706
CCDC Number	2003249	2003252

Table S7.2.5.5.3. Crystallographic data collection and refinement parameters for the metalated forms of **1**.

Sample	1·ETH-Cl	1·ETH-BF ₄
Crystallographic Parameter		
Formula	C _{106.5} H ₁₄₀ ClMn ₃ N ₁₂ O ₁₂ Rh	C ₇₉ H ₇₄ BF ₄ Mn ₃ N ₁₂ O ₁₂ Rh
FW	2083.48	2134.84
T, K	100(2)	100(2)
Wavelength, Å	Synchrotron ($\lambda = 0.71073$)	Synchrotron ($\lambda = 0.71073$)
Crystal system, space group	Monoclinic <i>P2₁/m</i>	Monoclinic <i>P2₁/m</i>
Z	2	2
a, Å	12.288(3)	12.239(2)
b, Å	32.624(7)	34.061(7)
c, Å	12.928(3)	12.913(3)
α , °	90	90
β , °	95.46(3)	99.45(3)
γ , °	90	90
V, Å ³	5159.1(18)	5310.1(19)
d_{calc} , g/cm ³	1.341	1.335
Absorption coefficient, mm ⁻¹	0.607	0.572
<i>F</i> (000)	2192.0	2240.0
Crystal size, mm ³	0.4 × 0.25 × 0.06	0.40 × 0.20 × 0.05
2 θ range for data collection	2.496 to 64.324	2.392 to 56.37
Index range	-16 ≤ <i>h</i> ≤ 16, -44 ≤ <i>k</i> ≤ 44, -16 ≤ <i>l</i> ≤ 18	-14 ≤ <i>h</i> ≤ 15, -42 ≤ <i>k</i> ≤ 42, -16 ≤ <i>l</i> ≤ 15
Reflections collected	51436	52134
Independent reflections	11410 [<i>R</i> _{int} = 0.0973, <i>R</i> _{sigma} = 0.0949]	10266 [<i>R</i> _{int} = 0.0616, <i>R</i> _{sigma} = 0.0495]
Data/restraints/parameters	11410/110/536	10266/5/526
GOF on <i>F</i> ²	0.959	1.120
Largest diff. peak and hole, eÅ ⁻³	1.11/-0.94	1.17/-0.91
<i>R</i> ₁ , [<i>I</i> > 2 σ (<i>I</i>)]	0.1497	0.0975
w <i>R</i> ₂ , all data	0.3869	0.3240
CCDC Number	2003251	2003253

Table S7.2.5.5.4. Crystallographic data collection and refinement parameters for the metalated forms of **1**.

Sample	1·[Rh(MeCN) ₂]Cl
Crystallographic Parameter	
Formula	C ₁₀₉ H ₁₃₂ ClMn ₃ N ₁₄ O _{19.5} Rh
FW	2253.46
T, K	100(2)
Wavelength, Å	Synchrotron ($\lambda = 0.71073$)
Crystal system, space group	Monoclinic <i>P2₁/m</i>
Z	2
a, Å	12.329(3)
b, Å	32.790(7)
c, Å	13.037(3)
α°	90
β°	94.16(3)
γ°	90
V, Å ³	5256.6(18)
d_{calc} , g/cm ³	1.424
Absorption coefficient, mm ⁻¹	0.608
F(000)	2354.0
Crystal size, mm ³	0.22 × 0.13 × 0.03
Theta range for data collection	2.484 to 63.618
Index range	-15 ≤ h ≤ 15, -43 ≤ k ≤ 43, -17 ≤ l ≤ 17
Reflections collected	95799
Independent reflections	14009 [R _{int} = 0.0501, R _{sigma} = 0.0302]
Data/restraints/parameters	14009/0/554
GOF on F ²	1.044
Largest diff. peak and hole, e·Å ⁻³	3.47/-2.04
R ₁ , [I > 2σ(I)]	0.1009
wR ₂ , all data	0.2896
CCDC Number	2003250

7.2.6. Isotherm data

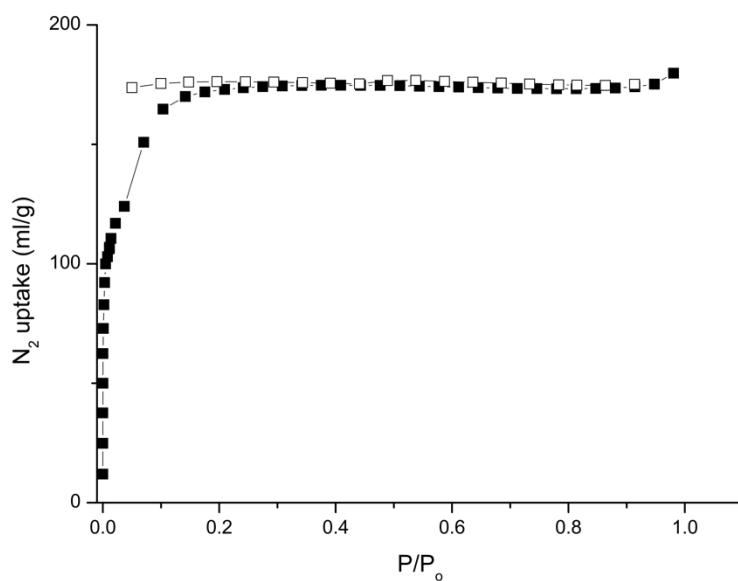


Figure 7.2.6.1. N_2 isotherm data collected on 1-NP at 77K, after activation from dry acetone at 80°C for 20 hr. Black squares represent adsorption, open squares represent desorption.

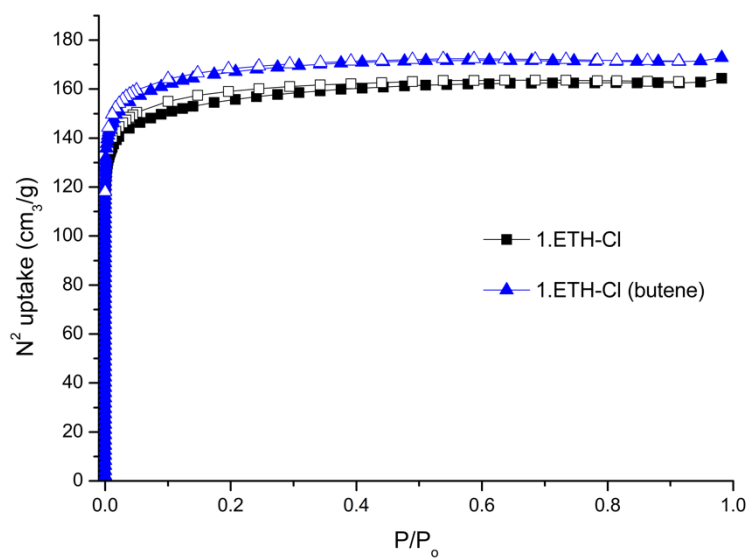


Figure 7.2.6.2. N_2 isotherm data collected on 1-ETH-Cl at 77K, after activation from dry pentane at RT for 2 hr (black squares) and following reaction with 1-butene for 3 hr (blue triangles). Colored squares/triangles represent adsorption, open squares/triangles represent desorption.

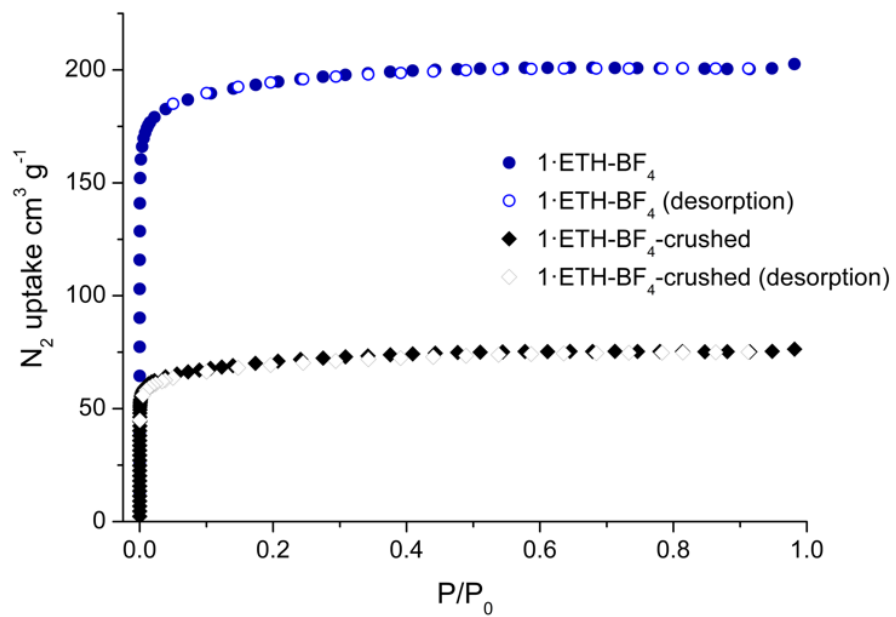


Figure 7.2.6.3. isotherms collected at 77K for 1-ETH-BF₄ and 1-ETH-BF₄-crushed, displaying the significant loss of surface area in the crushed sample.

7.2.7. Nuclear Magnetic Resonance (NMR) data

7.2.7.1 Time resolved NMR data for ethylene hydrogenation

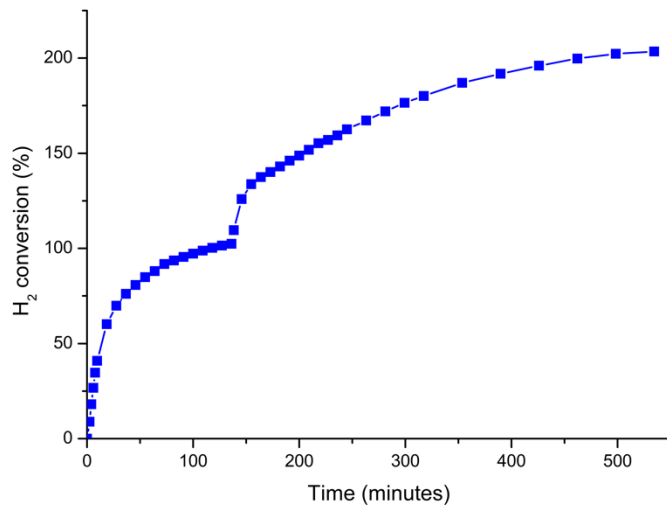


Figure 7.2.7.1.1. The hydrogenation of ethylene over 1-NP at 46°C proceeds rapidly in the first cycle but slows down significantly in the second cycle.

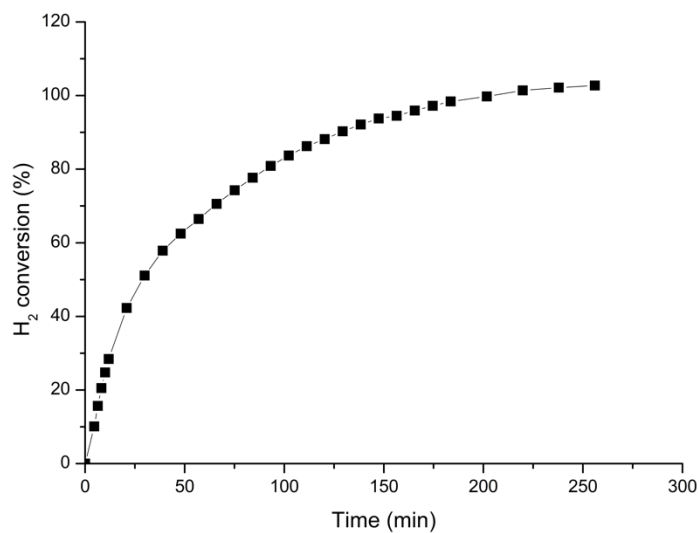


Figure 7.2.7.1.2. The hydrogenation of ethene over a crushed sample of 1-ETH-BF₄ at 46°C.

7.2.7.2 Time resolved NMR data for butene isomerization

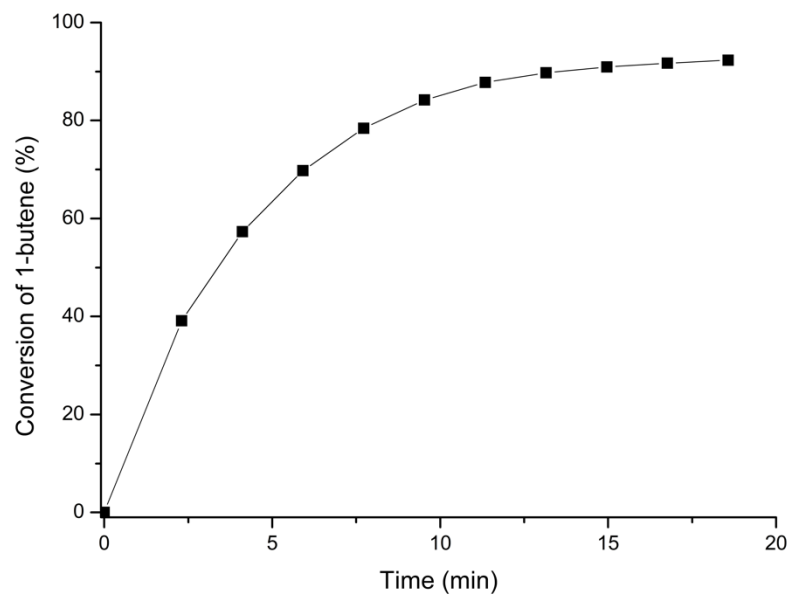


Figure 7.2.7.2.2. Butene isomerization catalyzed by a crushed sample of 1·ETH-BF₄ as determined by gas-phase NMR.

7.2.7.3. Sample composition analysis using a CO/CH₄ probe

Samples of **1**·ETH-BF₄ and **1**·ETH-Cl were activated in a high-pressure NORELL NMR tube using the same protocol described in the experimental. Following activation, the NMR tube was dosed with a mixture of 1 bar of CH₄ and 1 bar of CO. The tube was sealed and transferred to a Varian Gemini 600 MHz NMR.

Exposure to CO/CH₄ results in an instantaneous color change from yellow to off-white, which, in conjunction with the presence of CO stretching bands in the IR spectrum of the MOF crystals, verified that **1**·[Rh(CO)₂]BF₄ and **1**·[Rh(CO)₂]Cl were formed (SI Figure 7.3.2-3). Gas-phase NMR spectra of the head-space in the NMR tube revealed the amount of ethylene displaced from the Rh(I) centre (SI Figure 7.3.4-5) via integration of the ethylene and methane signals; the result is consistent with retention of ~90% for both samples.

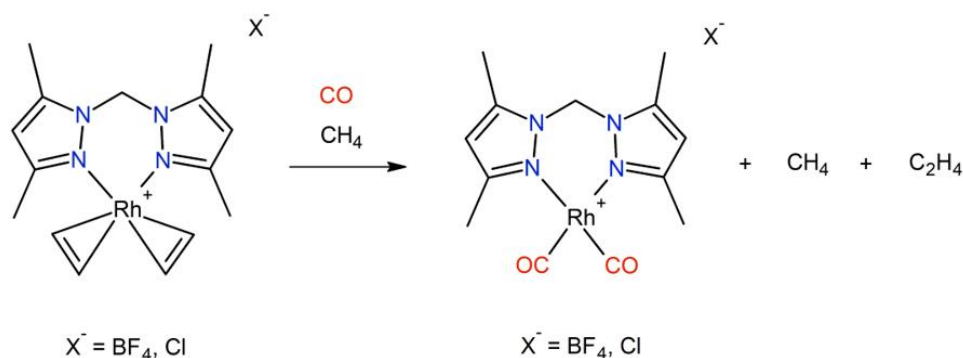


Figure 7.2.7.3.1. Reaction scheme showing the displacement of the ethylene from the Rh(I) center in **1**·ETH-BF₄ or **1**·ETH-Cl in presence of CO/CH₄.

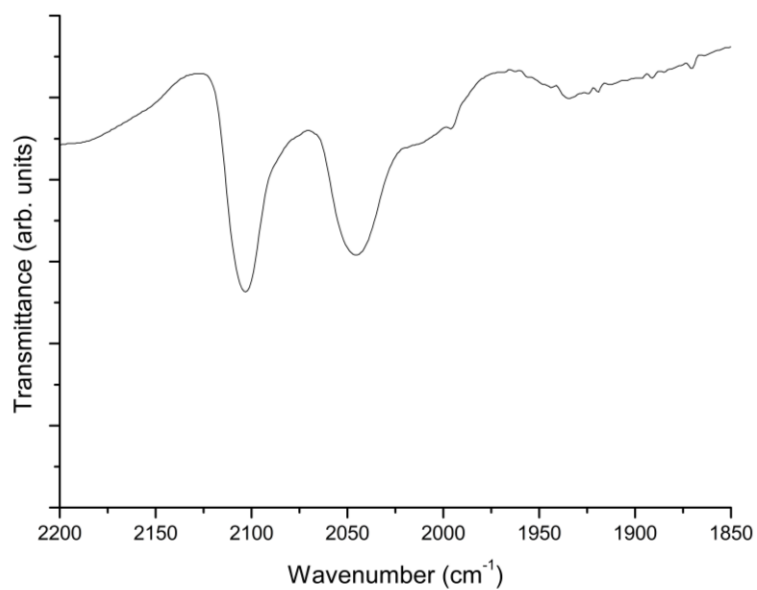


Figure 7.2.7.3.2. Infra-red spectrum of **1**·ETH-BF₄ crystals following exposure to CO/CH₄, displaying the strong CO stretches corresponding to the formation of **1**·[Rh(CO)₂]BF₄.

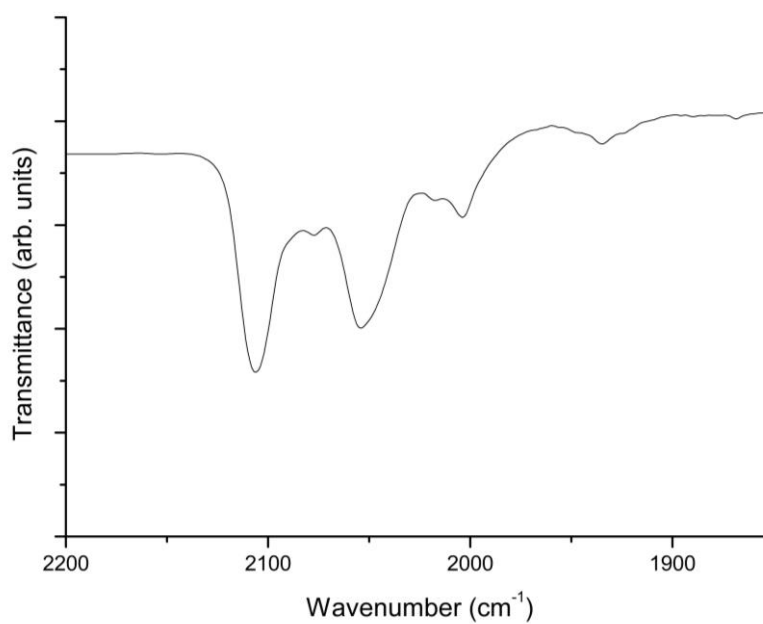


Figure 7.2.7.3.3. Infra-red spectrum of **1**·ETH-Cl crystals following exposure to CO/CH₄, displaying the strong CO stretches corresponding to the formation of **1**·[Rh(CO)₂]Cl.

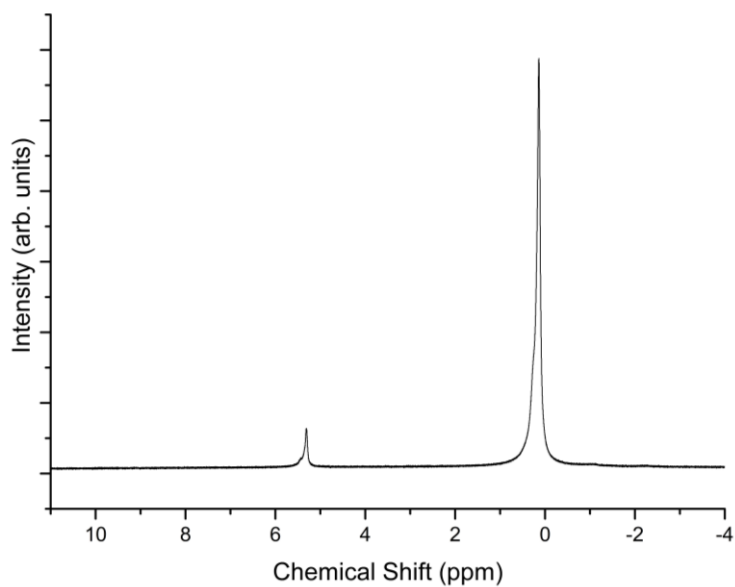


Figure 7.2.7.3.4. ¹H NMR spectrum obtained from the headspace of an NMR tube containing 1·ETH-BF₄ crystals following exposure to CO/CH₄, displaying the ethylene (5.31 ppm) and methane (0.14 ppm) resonances.

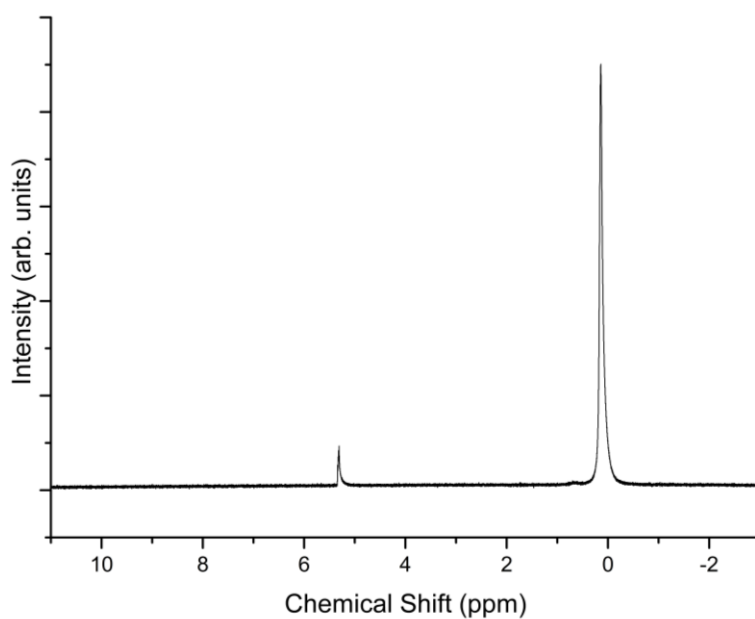


Figure 7.2.7.3.5. ¹H NMR spectrum obtained from the headspace of an NMR tube containing 1·ETH-Cl crystals following exposure to CO/CH₄, displaying the ethylene (5.31 ppm) and methane (0.14 ppm) resonances.

7.2.8. Infrared (IR) Spectroscopy

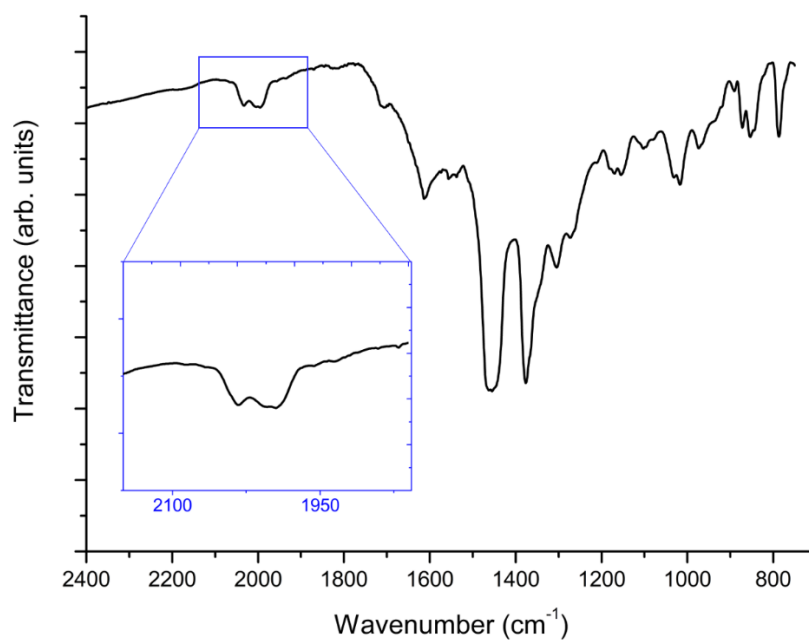


Figure 7.2.8.1. Infra-red spectrum (nujol) of 1-ETH-Cl crystals following exposure to 1-butene at 46°C, displaying the weak rhodium hydride stretches observed at 2034 and 2000 cm^{-1} .

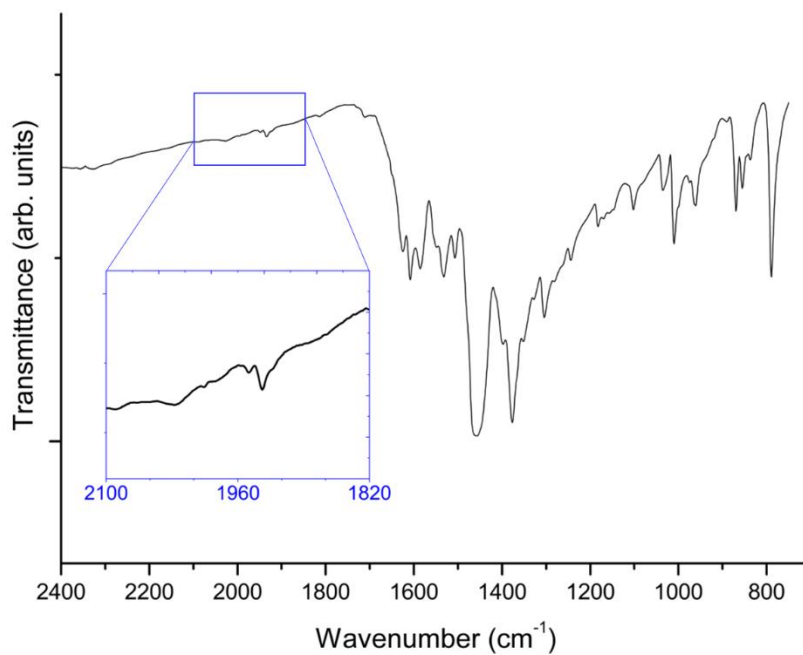


Figure 7.2.8.2. Infra-red spectrum (nujol) of 1-ETH-Cl crystals following ethylene hydrogenation (1.2 bar ethylene, 0.8 bar H_2) at 46°C, displaying the weak rhodium hydride stretches observed at 2026 and 1934 cm^{-1} .

7.2.9. High Pressure Reaction Vessel Details

The high-pressure reactors (Figure SI 9.1) used for post-synthetic metalation of **1** under ethylene were developed in-house. A 20 ml high-pressure glass tube from Ace glass Inc. (item 7644-15, 15mm thread) sealed via a threaded PTFE plug was drilled to accommodate a pressure gauge and tap assembly (SI Figure 9.1).

The PTFE solid plug (item 5845-47) with O-RING back seal was modified to add an O-RING front seal (VITON BS010) and a 1/4" diameter hole was bored through the plug such that the tube could be evacuated and filled with an appropriate atmosphere.

A flange screw nut #15mm Ace Thread with flange diameter 1.5" x 3/8" thick was 3D printed in PLA and used to modify the 5845-47 PTFE Solid Plug.

A flanged stud was prepared for insertion through the PTFE lid using a 1/4" UNF x 1.5" long 304 Stainless Steel, hexagon head bolt. The bolt head was modified to accommodate the flange (flange diameter 0.669" x .109" thickness with 2 x flat edges, 15mm A/F, and 1/8" hole bored through).

This was assembled by inserting the 5845-47 PTFE solid plug into the 1/4" UNF flanged stud, via the front seal end, and was screwed together by a 1/4 UNF female to 1/4" NPT, female 304 stainless steel bush adapter, with 2 flat edges, 5/8" A/F.

A Swagelok 1/4" NPT male x 1/4" NPT male stainless-steel hex nipple fitted into bush adapter with PTFE tape, before the 7644-15 glass connector is assembled to 5845-47 PTFE solid plug.

Swagelok fittings used in the assembly are as follows:

SS-4-HN (Stainless Steel Pipe Fitting, Hex Nipple, 1/4 in. Male NPT)

SS-4-T (Stainless Steel Pipe Fitting, Tee, 1/4 in. Female NPT)

PGI-63B-BG16-LOAX (PGI Series gauge 0-16 bar Lower mount 1/4" male NP)

SS-400-1-4 (SS Swagelok Tube Fitting, Male Connector, 1/4 in. Tube OD x 1/4 in. Male NP)

SS-4P4T (SS Quarter-Turn Instrument Plug Valve, 1/4 in. Swagelok Tube Fitting, 1.6 Cv)

Chapter 7

Teflon tape was applied to all Swagelok fittings with NPT male threads before assembly.

The pressure vessel was pressure tested to 80 psi (5.5 bar) with compressed air for 24 hours.

The glass pressure tube was stored in a 120°C drying oven between use.



Figure 7.2.9.1. Glass pressure vessel fitted with a pressure gauge and tap assembly.

7.2.10. X-ray Photoelectron Spectroscopy (XPS) Experiments

XPS spectra were acquired in a custom designed UHV systems equipped with an Omicron EA125 electron analyser and a dual anode X-ray source (Omicron DAR 400). The samples were dispersed onto carbon tape under N_2 atmosphere and then left to outgas overnight prior to the measurements. Due to the insulating nature of the samples, a flood gun was used to compensate charging effects. The binding energy scale was calibrated used the C 1s spectrum, which was positioned at 284.8 eV.

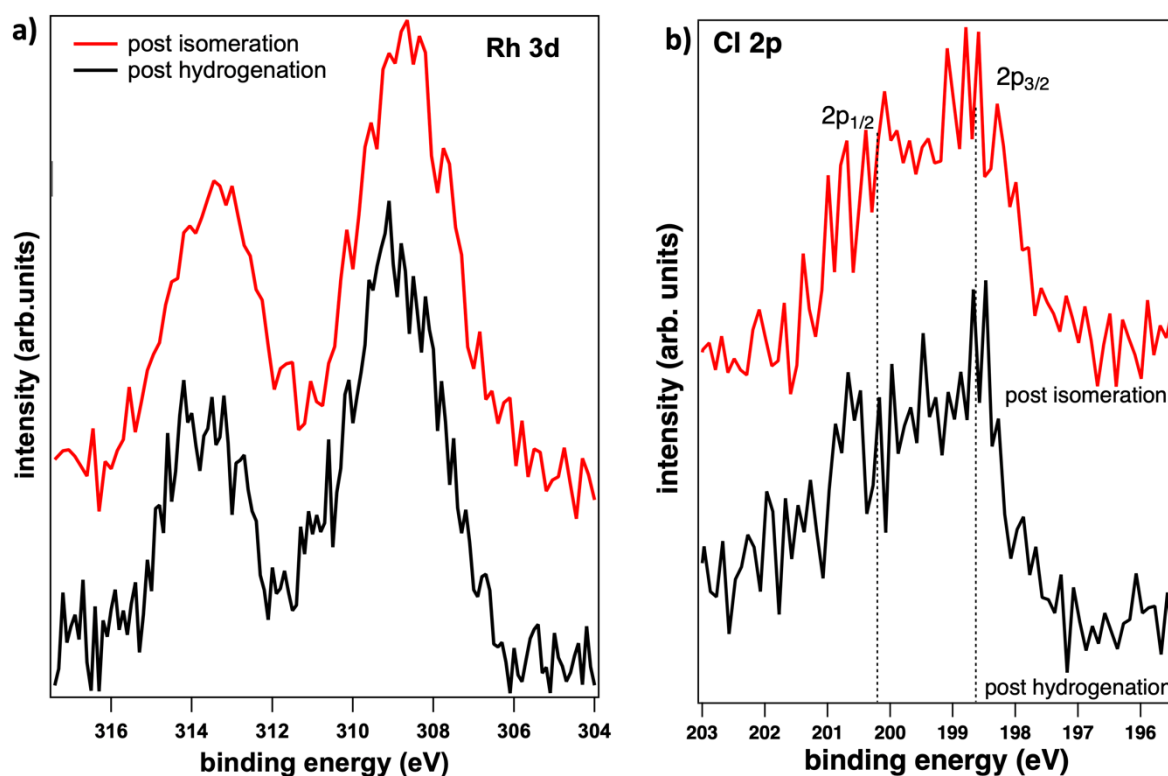


Figure 7.2.10.1. (a) Rh 3d and (b) Cl 2p photoemission spectra of 1-ETH-Cl crystals after butene isomerization (red) and ethylene hydrogenation (black).

7.2.11. Computational Supplementary Information

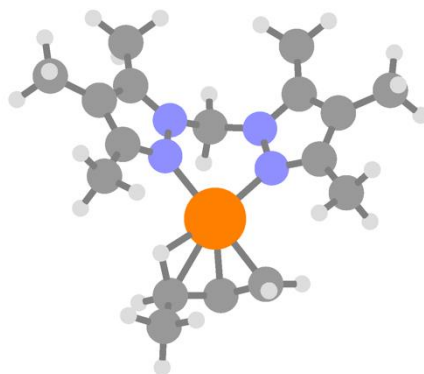


Figure 7.2.9.11.1. Structure of the representative Rh complex with bound 1-butene. Rh, orange; C, gray; N, blue; H, white.

Table S7.2.9.11.1. Relative free energies of the Rh complexes for the proposed mechanism butene isomerization.

Complex	$\Delta G / \text{kJ mol}^{-1}$
I	4.95
II	12.2
III	0.00

Table S7.2.9.11.2. Energy barriers obtained by climbing image nudged elastic band for the Rh complexes.

Barrier	$\Delta E / \text{kJ mol}^{-1}$
I→II	36.6
II→III	14.7

Table S7.2.9.11.3. Relative free energies of the Rh complexes with Cl present for the proposed mechanism butene isomerization.

Complex	$\Delta G / \text{kJ mol}^{-1}$
I-Cl	3.58
II-Cl	-82.5
III-Cl	0.00

Table S7.2.9.11.4. Relative free energies of the Rh complexes with BF_4 present for the proposed mechanism butene isomerization.

Complex	$\Delta G / \text{kJ mol}^{-1}$
I- BF_4	-1.08
II- BF_4	-32.2
III- BF_4	0.00

Table S7.2.9.11.5. Simulated surface areas (SA) and probe occupiable pore volumes (PV).

Sample	SA / $\text{m}^2 \text{g}^{-1}$	PV / $\text{m}^3 \text{g}^{-1}$
1·ETH- BF_4 (disorder 1)	973	0.30
1·ETH- BF_4 (disorder 2)	913	0.28
1·ETH-Cl (disorder 1)	893	0.29
1·ETH-Cl (disorder 2)	867	0.29
1·NBD- BF_4 (disorder 1)	989	0.29
1·NBD- BF_4 (disorder 2)	989	0.29
1·NBD-Cl (disorder 1)	871	0.27
1·NBD-Cl (disorder 2)	850	0.26

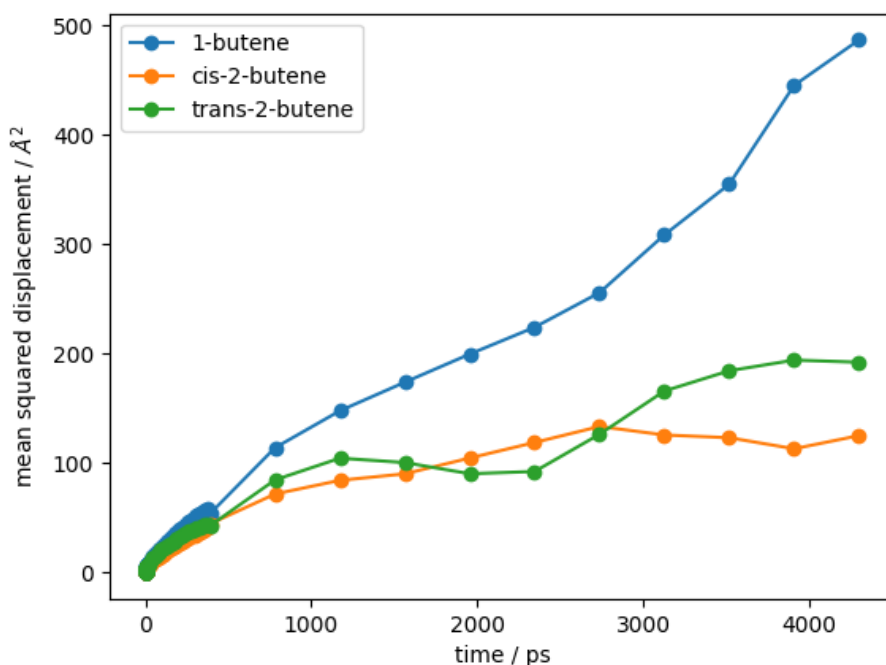


Figure 7.2.9.11.2. Mean squared displacement of butane species at 300 K using the NVT ensemble within the rigid structure of 1·ETH- BF_4 .

7.2.11.1 DFT Calculations on butene transport within 1·ETH-X

7.2.11.1.1 Computational details

Despite the above technological methods, first principles were employed to reveal the catalytic enhancement mechanism of 1-butene isomerization. All the simulations were carried out using density functional theory (DFT) on the Vienna *Ab initio* Simulation Package (VASP).⁹¹⁰ The interaction between ions and electrons was described by projector-augmented wave (PAW) method. The electron exchange-correlation energy is performed using generalized gradient approximation functional with the Perdew-Burke-Ernzerh correction.¹¹ The energy-cutoffs for all systems were set to be 400 eV. The whole model for the Rh/Mn MOF contains 372 atoms. The criteria for the relaxation of the electronic SC-loop was set to be 1×10^{-6} eV \AA^{-1} . And the relaxation will be stopped after the convergence of forces reached 0.03 eV \AA^{-1} . The *k*-points grid was set as (1×1×1) and generated with Gamma centered points. During the geometry optimization, the ions in reactants, intermediates and products were fully relaxed. The transition states were located by climbing images nudged elastic band (CI-NEB)¹²⁻¹³ and dimmer methods.¹⁴

7.2.11.1.2 Results and discussion

DFT calculations were carried out to gain deep insight into the catalytic action of MOFs in the isomerization of 1-butene. Figure 7.2.11.1.1 illustrates the potential energy surfaces (PESs) of 1-butene isomerization with and without the presence of MOFs. The bond lengths as well as atom numbers are labeled in blue. Direct isomerization of 1-butene proceeds with H4 atom migrating from C3 atom to C1 atom (TS1 in Figure 7.2.11.1.1), but the energy barrier for the formation of 2-butene is as high as 2.96 eV, indicating a low feasibility of this process.

When the MOF structure exists, the process is significantly promoted. To deeply investigate the enhancement caused by Rh sites, Bader charges of active sites are analyzed. In the MOF, each fluorine ion is negatively charged by ~ 0.83 electron, each boron ion has 2.36 positive charge, hence the $[\text{BF}_4^-]$ group has ~ 0.96 negative charge. In this paper, the $[\text{BF}_4^-]$ anion will not participate in the 1-butene isomerization directly according to the special structure of MOF. Instead, the interaction between Rh and C=C double bonds play a dominant role.

As shown in blue lines in Figure 7.2.11.1.1, the isomerization of 1-butene is divided into three elementary reactions including conformation isomerization and two steps of hydrogen

migration. Analysis of the differential charge density of IM1 (Figure 7.2.11.1.2) shows that the π electrons from C=C double bonds exhibit a strong interaction with the d orbitals of Rh site, and the valence electrons of Rh somehow donate to the electron densities around C1 and C2, as observed by Douglas et al.¹⁵ Then the conformation IM1 endothermically isomerizes to IM2 with the C3–H4 bond lengthened by 0.10 Å. As shown in Figure 7.2.11.1.2, electron densities are mainly distributed between Rh and C1/C2/C3, which means that the π electrons are delocalized from C1/C2 to C1/C2/C3. The dehydrogenation of 1-butene (IM2 \rightarrow TS2) takes place with a moderate energy barrier of 0.31 eV, and IM3 is formed after the H4 atom migrating to Rh. The significantly reduced energy barrier is ascribed to the reduced electrophilicity of C3 atom which causes bond energy of C3–H4 decrease, and hence the cleavage of C3–H4 bond becomes easier. The Bader charge analysis also shows few electrons are transferred from H4 to C3.

In IM3, the Rh site loses more electrons, and the Rh–H bonds is unstable especially with the presence of delocalized π electrons. Hence, the negatively charged H4 atom is reactive to associated with C1 to stabilize the system. Compared to re-isomerize back to C3 atom, H4 favors to transfer to C1 atom (IM3 \rightarrow IM4) because of high thermodynamic feasibility. The formation of IM4 owns a moderate energy barrier of 0.17 eV and is exothermic by releasing energy of 0.88 eV. This process is driven by the symmetry effect. When H4 transfers to C1, 2-butene is produced with high symmetry. The charges of C2 and C3 are similar. The differential charge density of IM4 also shows a symmetrically contribution of the molecules. Along the total pathways of 1-butene (from IM1 to IM4), we can conclude that the H4 migration to the Rh site is rate-determining step as it occupies the top position in the PES file.

To conclude, the DFT simulation reveals the interaction between π electrons and d orbitals of active Rh site of MOF has a significant enhancement of the 1-butene isomerization by reducing the energy barrier from 2.96 eV to 0.68 eV in the PES. Hydrogen migration from α -C (C3) to Rh site is the rate determining step.

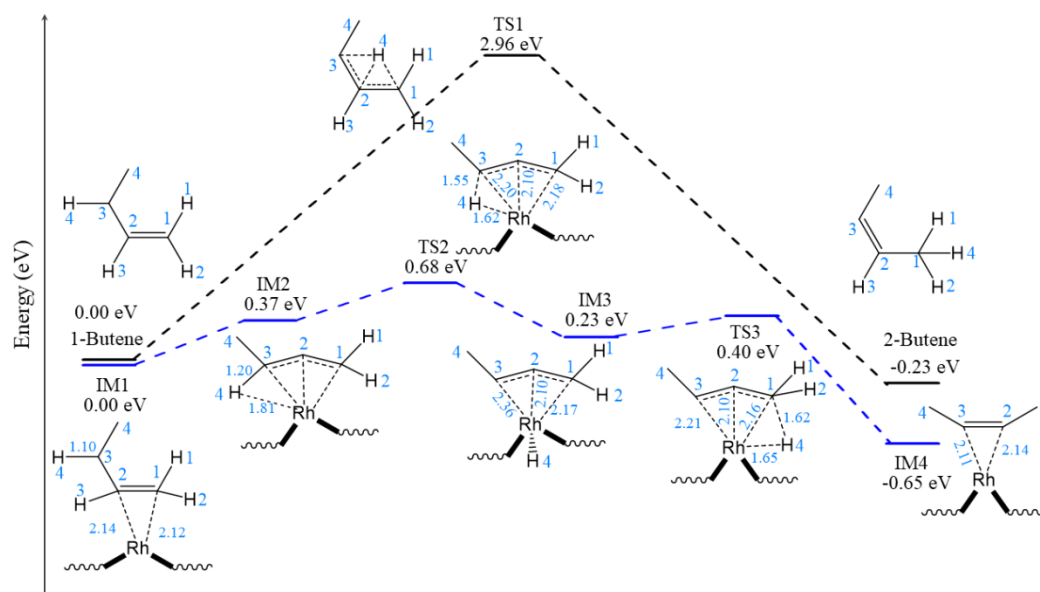
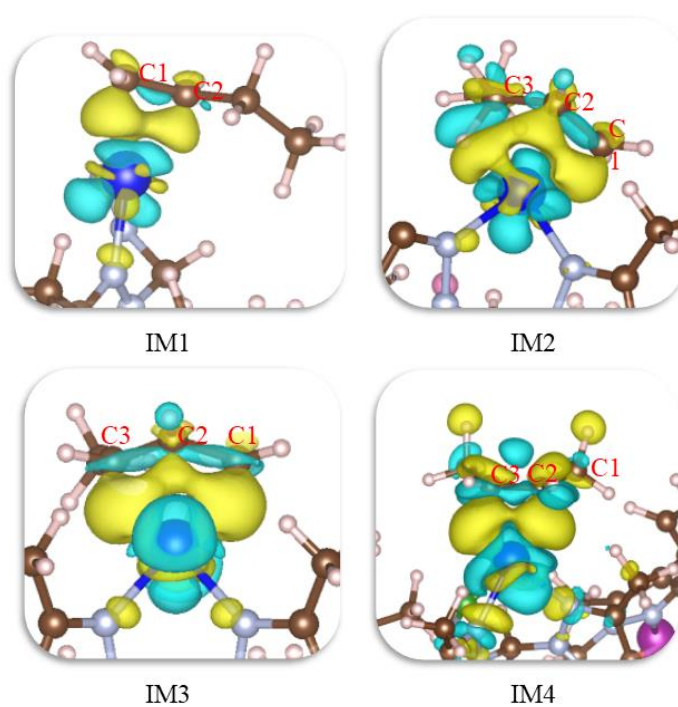


Figure 7.2.11.1.1. Potential energy surfaces of 1-butene isomerization in the absence (black line) and presence (blue line) of MOF. Bond lengths and atom numbers are labelled in blue.

Table S7.2.11.1.1. Bader charge of active sites in the intermediates and transition states.

	IM1	IM2	TS2	IM3	TS3	IM4
C1	-0.227	-0.226	-0.220	-0.223	-0.224	-0.150
C2	-0.193	-0.172	-0.197	-0.155	-0.087	-0.103
C3	-0.092	-0.076	-0.150	-0.097	-0.200	-0.113
H4	0.033	0.009	0.059	-0.038	0.053	0.092
Rh	0.410	0.436	0.464	0.531	0.478	0.363

**Figure 7.2.11.1.2.** Differential charge density of intermediates referred in the MOF-promoted 1-butene isomerization. Blue surface designates the charge density reduced area, and the yellow surface represents the charge density increased area.

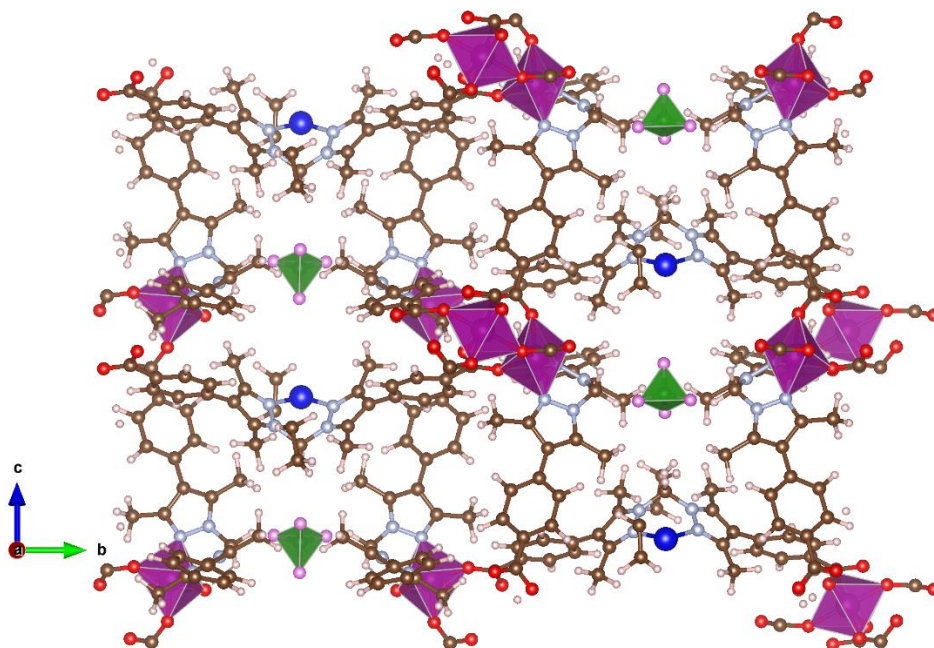


Figure 7.2.11.1.3.: Periodical structure ($1 \times 1 \times 2$) of MOF used in the DFT simulation. The atoms are colored by H in white, B in green, C in brown, N in silvery white, O in red, F in pink, Mn in purple and Rh in blue.

7.2.12. References

- (1) Cowieson, N. P.; Aragao, D.; Clift, M.; Ericsson, D. J.; Gee, C.; Harrop, S. J.; Mudie, N.; Panjikar, S.; Price, J. R.; Riboldi-Tunnicliffe, A., *et al.* MX1: a bending-magnet crystallography beamline serving both chemical and macromolecular crystallography communities at the Australian Synchrotron. *J. Synchrotron Radiat.* **2015**, *22*, 187.
- (2) McPhillips, T.; McPhillips, S.; Chiu, H.; Cohen, A. E.; Deacon, A. M.; Ellis, P. J.; Garman, E.; Gonzalez, A.; Sauter, N. K.; Phizackerley, R. P., *et al.* Blue-Ice and the Distributed Control System software for data acquisition and instrument control at macromolecular crystallography beamlines. *J. Synchrotron Radiat.* **2002**, *9*, 401.
- (3) Sheldrick, G. A short history of SHELX. *Acta. Crystallogr. A* **2008**, *64*, 112.
- (4) Sheldrick, G. SHELXT - Integrated space-group and crystal-structure determination. *Acta. Crystallogr. A* **2015**, *71*, 3.
- (5) Sheldrick, G. M. Crystal structure refinement with SHELXL. *Acta. Crystallogr. C* **2015**, *71*, 3.
- (6) Barbour, L. J. X-Seed — A Software Tool for Supramolecular Crystallography. *J. Supramol. Chem.* **2001**, *1*, 189.
- (7) Dolomanov, O. V.; Bourhis, L. J.; Gildea, R. J.; Howard, J. A. K.; Puschmann, H. OLEX2: a complete structure solution, refinement and analysis program. *J. Appl. Crystallogr.* **2009**, *42*, 339.
- (8) Spek, A. L. PLATON SQUEEZE: a tool for the calculation of the disordered solvent contribution to the calculated structure factors. *Acta. Crystallogr. C* **2015**, *71*, 9.
- (9) Hafner, J. Ab-initio simulations of materials using VASP: Density-functional theory and beyond. *J. Comput. Chem.* **2008**, *29*, 2044.
- (10) Kresse, G.; Furthmüller, J. Efficient iterative schemes for ab initio total-energy calculations using a plane-wave basis set. *Phys. Rev. B* **1996**, *54*, 11169.
- (11) Perdew, J. P.; Burke, K.; Ernzerhof, M. Generalized Gradient Approximation Made Simple. *Phys. Rev. Lett.* **1996**, *77*, 3865.
- (12) Henkelman, G.; Uberuaga, B. P.; Jónsson, H. A climbing image nudged elastic band method for finding saddle points and minimum energy paths. *J. Chem. Phys.* **2000**, *113*, 9901.
- (13) Henkelman, G.; Jónsson, H. Improved tangent estimate in the nudged elastic band method for finding minimum energy paths and saddle points. *J. Chem. Phys.* **2000**, *113*, 9978.

(14) Xiao, P.; Sheppard, D.; Rogal, J.; Henkelman, G. Solid-state dimer method for calculating solid-solid phase transitions. *J. Chem. Phys.* **2014**, *140*, 174104.

(15) Douglas, T. M.; Brayshaw, S. K.; Dallanegra, R.; Kociok-Köhn, G.; Macgregor, S. A.; Moxham, G. L.; Weller, A. S.; Wondimagegn, T.; Vadivelu, P. Intramolecular Alkyl Phosphine Dehydrogenation in Cationic Rhodium Complexes of Tris(cyclopentylphosphine). *Chem. Eur. J.* **2008**, *14*, 1004.

7.3. Supplementary information for Chapter 4

7.3.1. Experimental section

7.3.1.1. General Experimental Considerations

Single crystals of MOF **1** were prepared as previously reported.¹ The chemicals ethylene, hydrogen, $[\text{Ir}(\text{C}_2\text{H}_4)_2\text{Cl}]_2$, acetaldehyde were purchased from commercial vendors and used as received. Samples were handled under standard Schlenk techniques unless otherwise stated. Solvents were dried using literature procedures and degassed with Ar prior to use. Specifically, EtOH was dried by refluxing over Mg under N_2 ; acetone was dried from CaSO_4 under nitrogen; and pentane was dried over Na/benzophenone. NaBF_4 and NaCl used for anion exchange were stored in a 120°C drying oven.

Powder X-ray diffraction (PXRD) data were collected on a Bruker Advanced D8 diffractometer (capillary stage) using Cu $K\alpha$ radiation ($\lambda = 1.5456 \text{ \AA}$, 40 kW/ 40mA, $2\theta = 2 - 52.94^\circ$, phi rotation = 20 rotation/min, at 1 sec exposure per step with 5001 steps and using 0.5 mm glass capillaries). Solution NMR spectra were recorded on Varian 500 or 600 MHz instruments at 23°C using a 5 mm probe. Gas phase NMR spectra were collected on a Varian Gemini 600 MHz NMR spectrometer as described below. Infrared (IR) spectra were collected on a Perkin-Elmer Spectrum Two, with the sample distributed between two NaCl disks in Nujol. High-resolution transmission electron microscopy (HRTEM) images and diffraction pattern were acquired using an uncorrected FEI Titan Themis 80-200. Energy dispersive X-ray spectroscopy (EDX) was performed on a Philips XL30 field emission scanning electron microscope. Gas adsorption isotherm measurements were performed on an ASAP 2020 Surface Area and Pore Size Analyser. Activation of samples was carried out as described.

7.3.1.2. Preparation of $1 \cdot \text{IrCl}$

Single crystals of **1** (~24 mg) were placed in a 20 ml glass pressure vessel fitted with a pressure gauge and Swagelok tap assembly.² The crystals were washed with freshly distilled ethanol (5 x 5 ml) under Ar flow a total of 5 times (the solution was degassed with Ar after each exchange and the sample was allowed to soak for 1hr between washings). The solution was degassed with ethylene, excess $[\text{Ir}(\text{C}_2\text{H}_4)_2\text{Cl}]_2$ (30 mg) was added and the pressure tube was sealed under ethylene (~1.2 bar) and heated at 40°C for 24 hr. The resulting yellow crystals were washed

with freshly distilled, ethylene degassed ethanol (5 x 5 ml) to remove dissolved Ir precursor. Insoluble Ir by-products were removed by washing the MOF crystals with dry, ethylene degassed acetone (5 x 5 ml) under ethylene flow to give **1**·IrCl as yellow crystals. IR ν_{\max} (nujol, cm^{-1}): 2050, 2016, 1985, 1925, 1608, 1555, 1376, 1304, 1273, 1226, 1173, 1152, 1089, 1049.

7.3.1.3. Preparation of **1**·IrBF₄

Single crystals of **1**·IrCl (~24 mg) were placed in a 20 ml glass pressure vessel fitted pressure gauge and Swagelok tap assembly. The crystals were washed with freshly distilled methanol (5 x 5 ml) under ethylene flow a total of 5 times (the solution was degassed with ethylene after each exchange and the sample was soaked for 1 hr between washings). Excess oven dried NaBF₄ was added to a small glass ampule which was subsequently submerged in the glass pressure tube containing the **1**·IrCl crystals. The pressure tube was sealed and allowed to stand at RT for 7 days (BF₄). Under ethylene flow, the ampule containing undissolved salt was removed and the yellow MOF crystals were washed with freshly distilled, ethylene degassed methanol (5 ml) five times under ethylene flow. IR ν_{\max} (nujol, cm^{-1}): 2092, 2019, 1934, 1613, 1555, 1376, 1305, 1273, 1181, 1143, 1096, 1067, 1033, 1016.

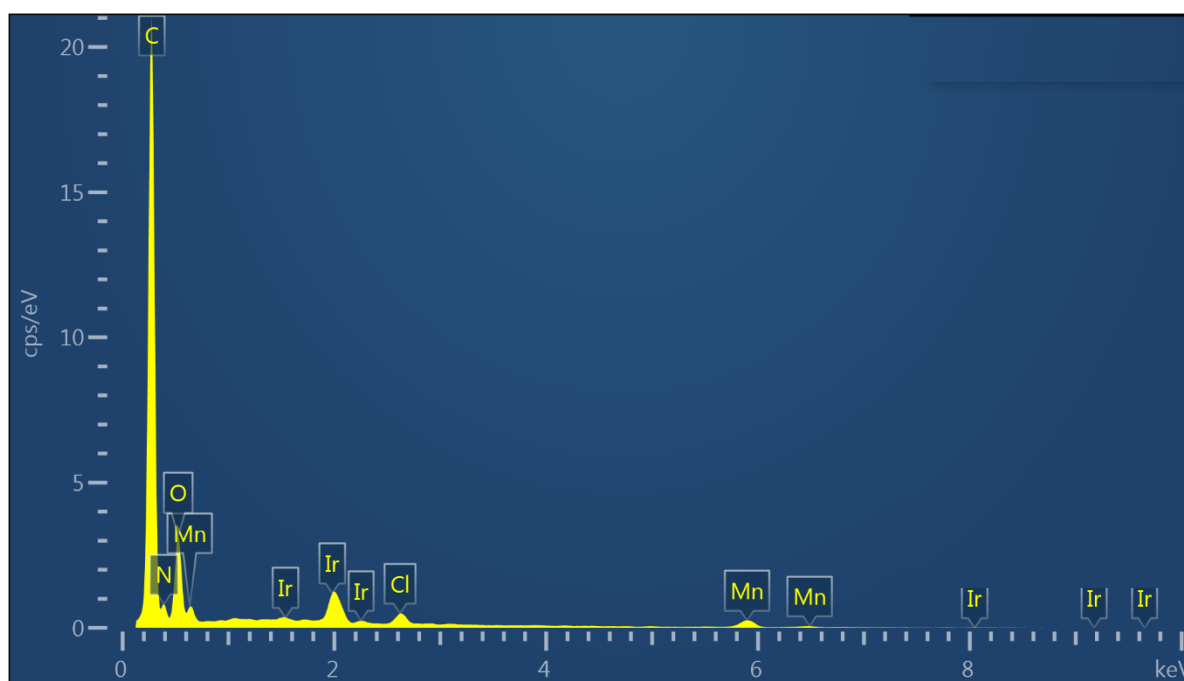
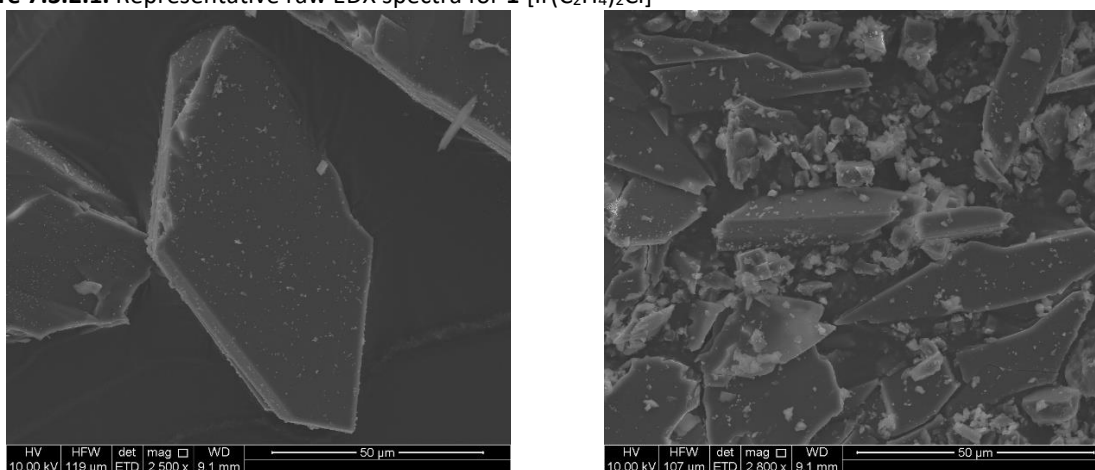
7.3.2 Energy Dispersive X-ray (EDX) Analysis

Table S7.3.2.1. EDX analysis data for the iridium and associated anion occupancy determined via measurement of the Mn:Ir and Ir:Cl ratios.

Sample	Ir occupancy (%) ^{a,b}	Cl occupancy (%) ^{a,b}	Std error (%)
1·IrCl	81.5	80.4	7.2
1·IrBF₄	78.2	0.2	5.4

^a Average atomic% obtained from three areas.

^b Relative to full occupancy of the bis(pyrazole)methane coordinating sites in **1**.

**Figure 7.3.2.1.** Representative raw EDX spectra for **1·[Ir(C₂H₄)₂Cl]****Figure 7.3.2.2.** SEM images of metalated **1** showing (left) a single crystal and (right) an area of crushed crystals used for EDX analysis.

7.3.3 High Resolution Transmission Electron Microscopy (HR-TEM) data

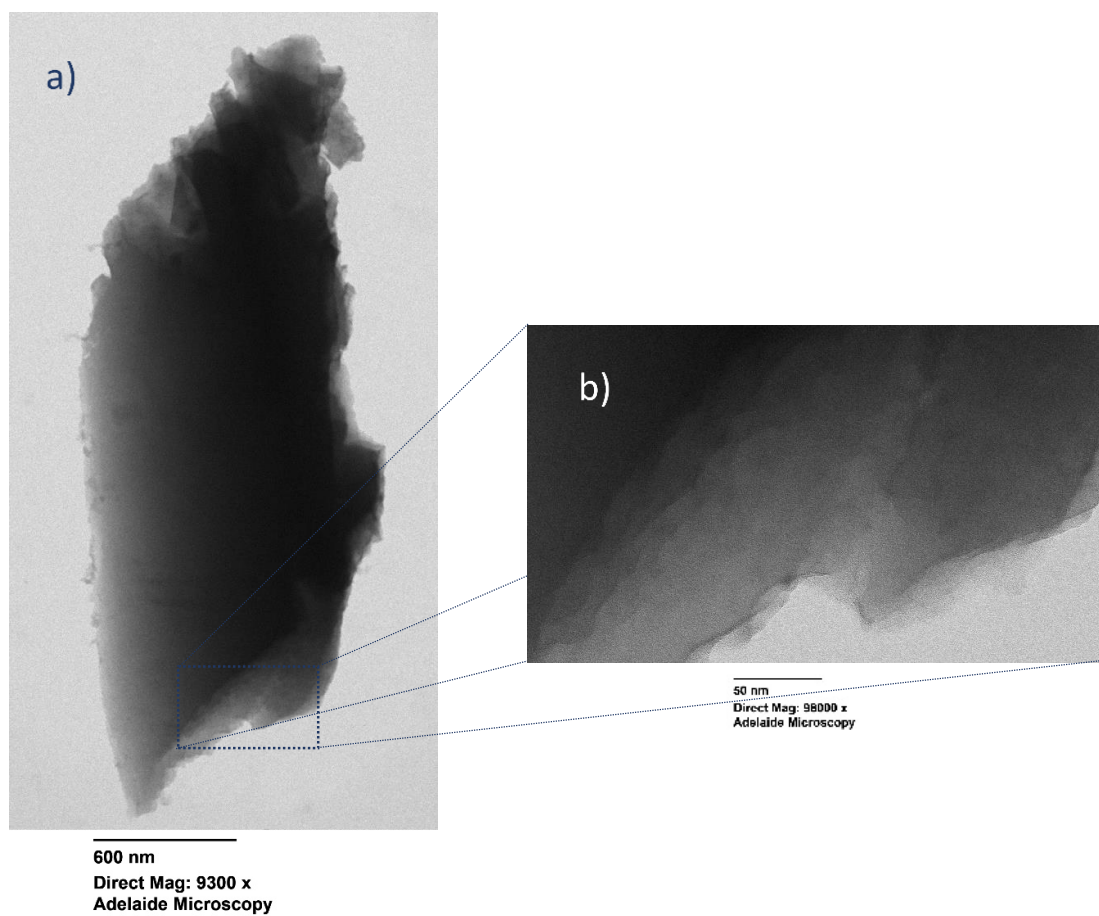


Figure 7.3.3.1. Characterization of 1-IrCl after ethylene hydrogenation experiments. a) HR-TEM image and b) locally amplified HR-TEM. The images showed no detectable iridium nanoparticles.

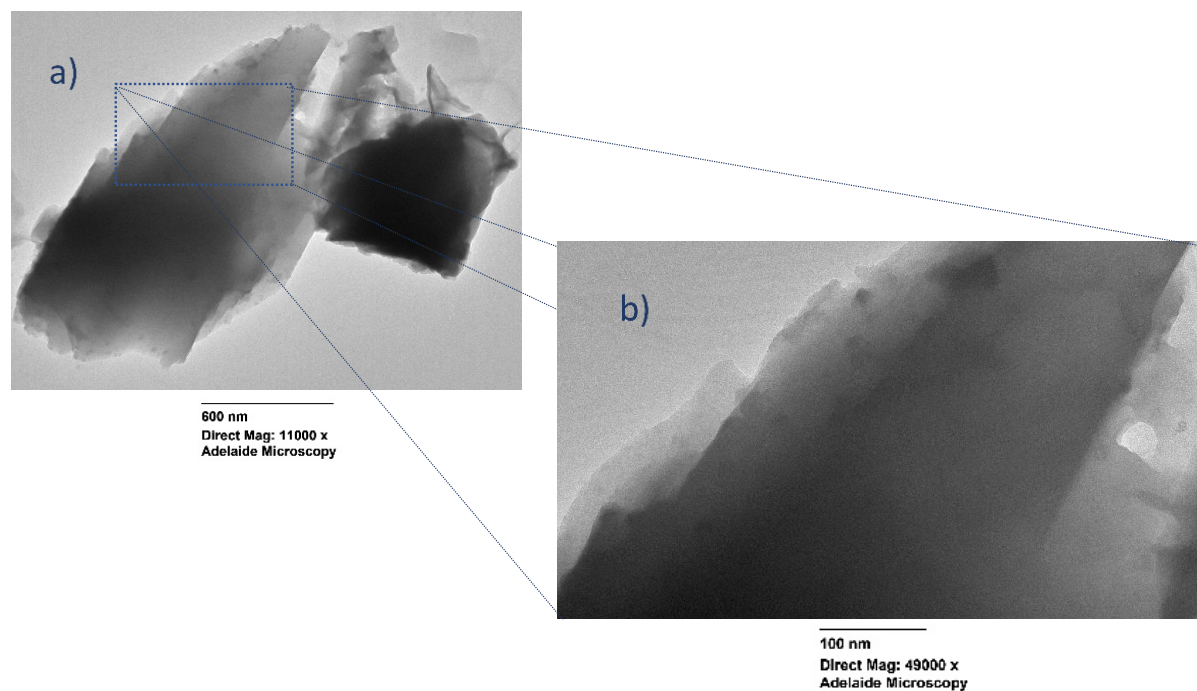


Figure 7.3.3.2. Characterization of 1-IrBF_4 after the ethylene hydrogenation experiments. a) HR-TEM image and b) locally amplified HR-TEM. The images showed no detectable iridium nanoparticles.

7.3.4. Powder X-ray Diffraction (PXRD) data

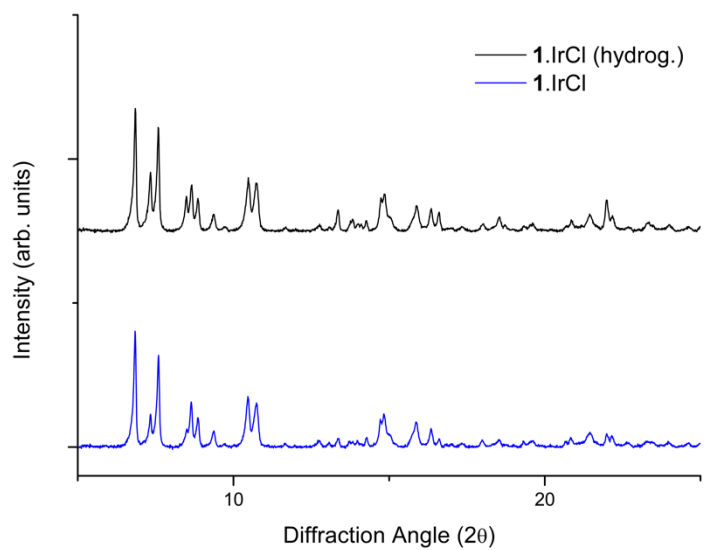


Figure 7.3.4.1. Experimental PXRD plots for 1·IrCl before and after ethylene hydrogenation experiments.

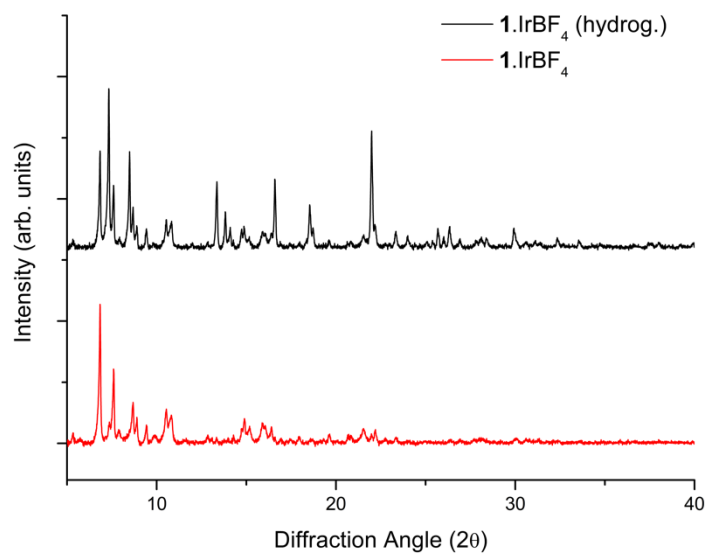


Figure 7.3.4.2. Experimental PXRD plots for 1·IrBF₄ before and after ethylene hydrogenation experiments.

7.3.5. Single Crystal X-ray Crystallography

7.3.5.1. General Procedures

Single crystals were mounted in Paratone-N oil on a MiTeGen micromount. Single-crystal X-ray data were collected at 100 K on the MX1 beamline of the Australian Synchrotron³ using the Blue-ice software interface,⁴ $\lambda = 0.71073 \text{ \AA}$. Absorption corrections were applied using empirical methods, the structure solved using SHELXT^{3,4} and refined by full-matrix least squares on F^2 by SHELXL,⁵ interfaced through the program X-Seed⁶ or OLEX.⁷ Figures were produced using the program CrystalMaker. X-ray experimental data is given in Table S2. CIF data have been deposited with the Cambridge Crystallographic Data Centre, CCDC reference numbers CCDC 2025173.

7.3.5.2. General Procedures

For most of the MOF structure the atoms were refined anisotropically and hydrogens atoms were included as invariants at geometrically estimated positions. However, for the bridging ligand (the site of post-synthetic metalation), which is disordered over two positions, the less occupied component (A, 0.25 occupancy) and its associated Ir center (Ir3A) were refined with isotropic refinement parameters. For the main component of the bridging ligand (B, 0.75 occupancy), anisotropic displacement parameters were used in the refinement. The disordered Ir centers are both on the mirror plane and combined refined to an approximately 0.3 occupancy (0.05 vs 0.25 occupancy for Ir3A vs Ir3B); this is slightly lower than the metalation yield measured by Energy Dispersive X-ray analysis of ca. 80%, i.e. 0.4 occupancy. The coordinated ethylene, which was fixed at 0.25 occupancy in line with the refined occupancy for Ir3B, was also refined with isotropic displacement parameters. The low occupancy of the Ir3A site and the disorder of the overall metalation site precluded identification of the coordination environment, but a partial CO and ethylene ligand was included in the formula in line with the data provided by IR spectroscopy. Overall this model represents the structure as a $[\text{Ir}(\text{ETH})_2\text{Cl}]$ center (Ir3B) and a possible $[\text{Ir}(\text{CO})(\text{ETH})]\text{Cl}$ center (Ir3A, this appears to have a non-coordinated Cl anion with electron density located in the “anion binding pocket” of the MOF to provide charge balance, although the presence of water in this site cannot be excluded). In addition, SIMU, FLAT and ISOR restraints were used for the refinement of the metalated linker components and the iridium centers. DFIX and EADP restraints were further used to maintain chemically sensible bond lengths for the bridging and

ethylene ligands. The data was treated with the SQUEEZE routine available in Platon to account for the large solvent accessible void volumes in the structure.⁸ To account for the removed electron density, 8 ethanol molecules (26e) per formula unit were added to the formula (16 ethanol molecules per unit cell).

7.3.5.3. Thermal ellipsoid plots for 1·IrCl

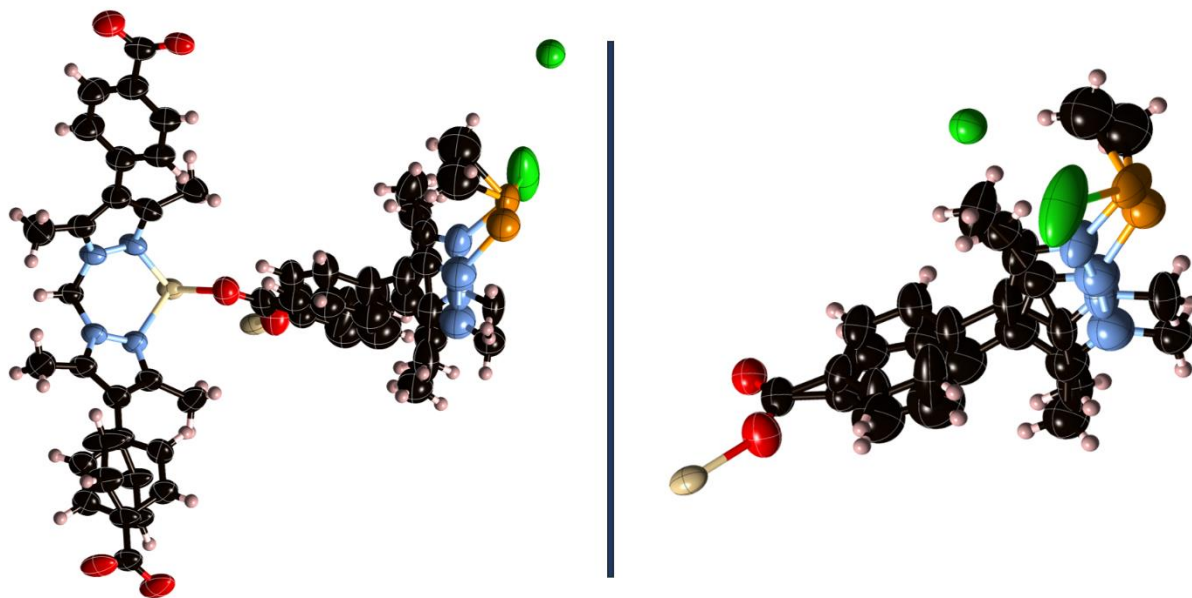


Figure 7.3.5.3.1. (left) The asymmetric unit of 1·IrCl with all non-hydrogen atoms represented by ellipsoids at the 50% probability level (Mn, beige; Ir, orange; Cl, green; C, black; N, blue; O, red; H, white). The structural model includes two disordered bridging ligand components each with a corresponding Ir center bound to the appropriate pyrazole N-donor. The coordination sphere of one of these iridium centers was refined to include coordinated ethylene and a coordinated chloride anion, while the coordination sphere of the less occupied Ir center could not be adequately modelled. (right) A perspective view of the metalated site and associated chloride anion (disorder shown) in 1·IrCl with all non-hydrogen atoms represented by ellipsoids at the 25% probability level. This view displays the disorder of the bridging ligand and associated iridium centers, as described above.

7.3.5.4. F_{obs} Electron Density Maps for 1·IrCl

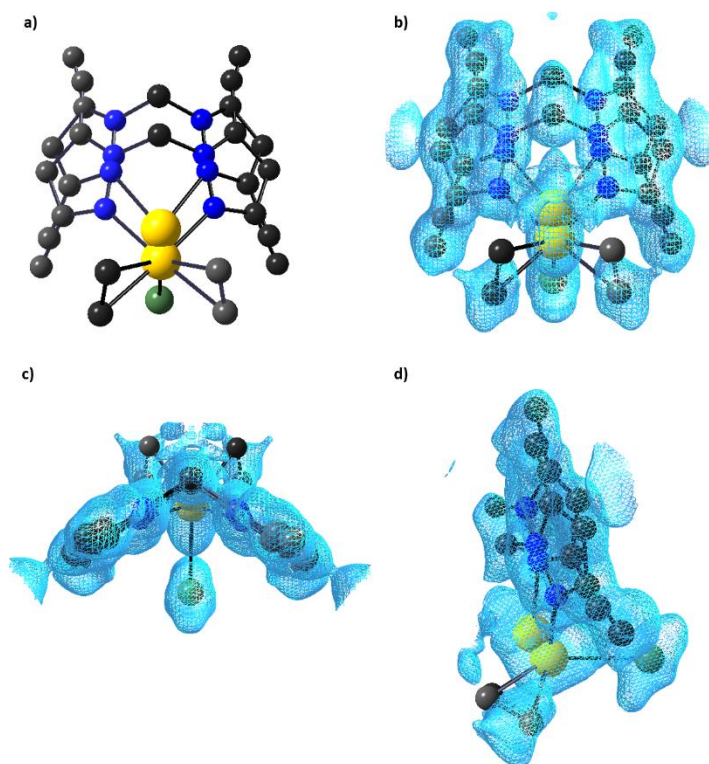


Figure 7.3.5.4.1 (a) A perspective view of the chelated Ir complex in 1·IrCl (Ir, orange; Cl, green; C, black; N, blue; O, red) and the overlaid electron density map as viewed from the (b) front, (c) top and (d) side of the complex.

7.3.5.5. X-ray crystallography data collection and refinement parameters

Table S7.3.5.5.1. Crystallographic data collection and refinement parameters for 1·IrCl.

Sample	1·IrCl
Crystallographic Parameter	
Formula	C _{90.9} H _{116.1} Cl _{0.60} Ir _{0.6} Mn ₃ N ₁₂ O _{20.0}
FW	1998.36
T, K	100(2)
Wavelength, Å	0.71037
Crystal system, space group	<i>P</i> 2 ₁ / <i>m</i>
Z	2
a, Å	12.364(3)
b, Å	33.500(7)
c, Å	12.912(3)
α, °	90
β, °	97.29(3)
γ, °	90
V, Å ³	5304.8(19)
<i>d</i> _{calc} , g/cm ³	1.251
Absorption coefficient, mm ⁻¹	1.181
<i>F</i> (000)	2074
Crystal size, mm ³	0.28 × 0.13 × 0.02
2θ range for data collection	2.432 to 58.096
Index range	-14 ≤ <i>h</i> ≤ 15, -40 ≤ <i>k</i> ≤ 40, -16 ≤ <i>l</i> ≤ 16
Reflections collected	67414
Independent reflections	10667 [<i>R</i> _{int} = 0.0387, <i>R</i> _{sigma} = 0.0223]
Data/restraints/parameters	10667/199/576
GOF on <i>F</i> ²	1.355
Largest diff. peak and hole, eÅ ⁻³	1.71/-0.53
<i>R</i> ₁ , [<i>I</i> > 2σ(<i>I</i>)]	<i>R</i> ₁ = 0.0924, <i>wR</i> ₂ = 0.3047
<i>wR</i> ₂ , all data	<i>R</i> ₁ = 0.1004, <i>wR</i> ₂ = 0.3129
CCDC Number	2025173

7.3.6. Adsorption data

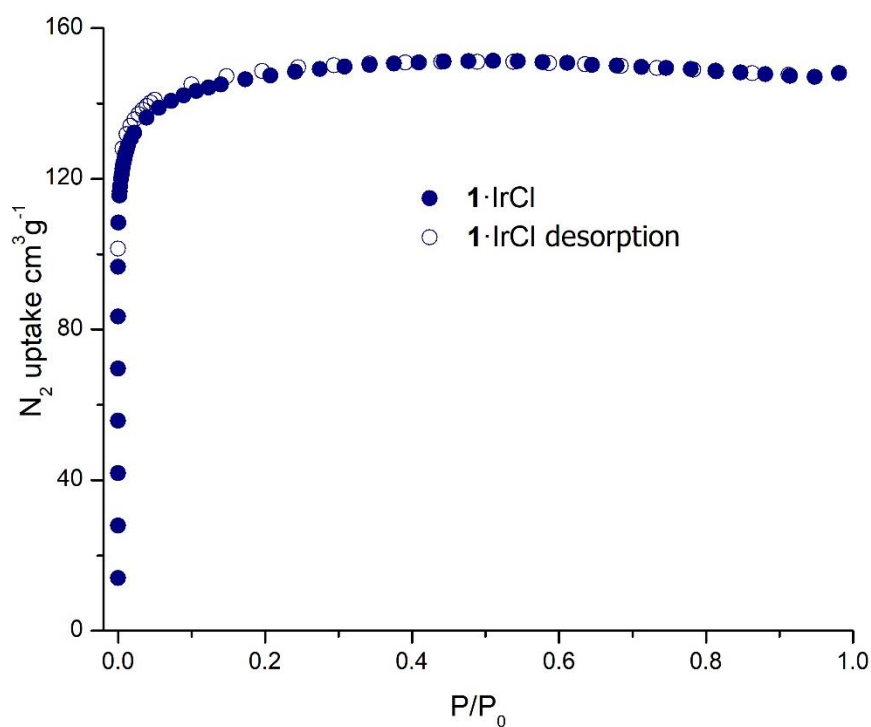


Figure 7.3.6.1. N_2 isotherm data collected on $1\cdot\text{IrCl}$ at 77 K, after activation from dry pentane at RT for 2 hr. Filled squares represent adsorption, open squares represent desorption.

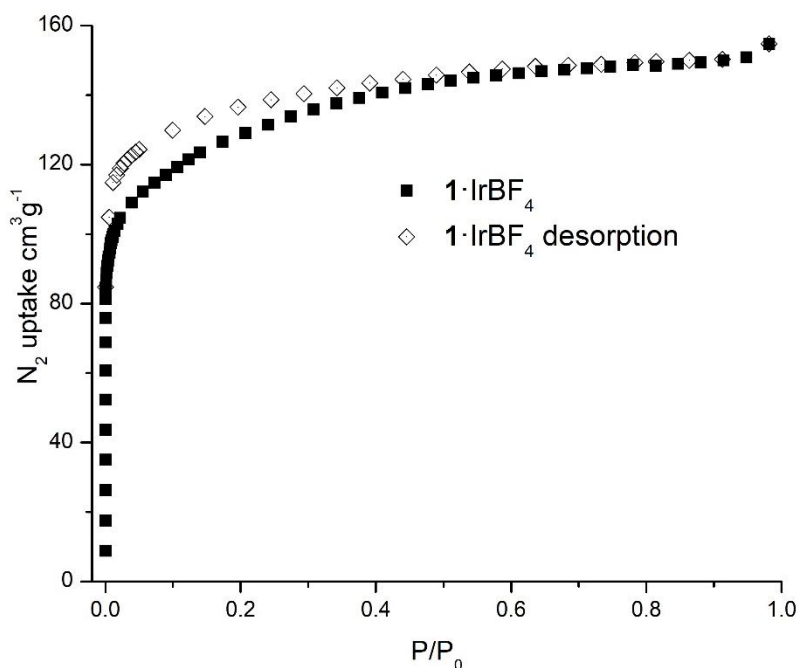


Figure 7.3.6.2. N_2 isotherm data collected on $1\cdot\text{IrBF}_4$ at 77K, after activation from dry pentane at RT for 2 hr. Filled circles represent adsorption, open circles represent desorption.

7.3.7. Nuclear Magnetic Resonance (NMR) data

7.3.7.1. Time resolved NMR data for ethylene hydrogenation experiments

1·IrCl and **1**·IrBF₄ (~2 mg) were washed with freshly distilled acetone (previously degassed with ethylene) five times under ethylene, allowing the crystals to soak for 1 hr between exchanges. Subsequently, the crystals were washed with distilled pentane (previously degassed with ethylene) five times under ethylene, soaked for 1 hr between each exchange. The sample was pipetted into a pre-weighed NORELL high-pressure NMR tube fitted with a Young's tap under ethylene flow. The excess pentane was removed before the NMR tube was placed under vacuum for 2 hrs. The NMR tube then was dosed with ethylene (1 bar, 105 μmol) followed by hydrogen (1 bar, 104 μmol). The NMR tube was sealed and placed in a Varian Gemini 600 MHz NMR spectrometer pre-heated to 46°C.

Before the collection the NMR was locked with a benzene (C₆D₆) charged NMR tube at 46 °C, which was then replaced with the pre-loaded high-pressure NMR tube. A T1 delay of 25 s was used. The extent of conversion was calculated by the comparison of the reduction/disappearance in the integral of the alkene CH₂ resonance of ethylene (5.31 ppm) and hydrogen (4.57 ppm), and the appearance of the two CH₃ alkyl resonance of ethane (0.88 ppm). The gas phase chemical shifts are referenced relative to reported data.⁵

7.3.7.2. Sample composition analysis using a CO/CH₄ probe

Samples of **1**·IrCl and **1**·IrBF₄ were activated in a high-pressure NORELL NMR tube using the same protocol described in section S7.1. Following activation, the NMR tube was dosed with a mixture of 1 bar of CH₄ and 1 bar of CO (or 1 bar of CH₄ and 1 bar of H₂ to analyze for ethane). The tube was sealed and transferred to a Varian Gemini 600 MHz NMR.

Exposure to CO/CH₄ results in an instantaneous color change from yellow to off-white, which, in conjunction with the presence of CO stretching bands in the IR spectrum of the MOF crystals, identifies the major species post CO exposure as **1**·[Ir(CO)₂Cl] and **1**·[Ir(CO)₂BF₄] (SI Figure S7.1 and 7.2-7.3). This indicates that ethylene is released into the headspace of NMR tube. Gas-phase NMR spectra of the head-space in the NMR tube revealed the amount of ethylene displaced from the Ir(I) center (SI Figure 7.4-7.5), via integration of the ethylene and methane signals; the result is consistent with retention of ~84-79% for both samples (slightly more than one equivalent per iridium atom). The amount of ethylene present in the catalyst is 84 mol% ethylene relative to iridium in **1**·IrCl (using Energy Dispersive X-ray (EDX) analysis to identify the amount of iridium); the unquantified ligand was considered as CO (i.e. 16 mol% CO relative to iridium in **1**·IrCl). This suggests a sample composition of 66% **1**·IrCl(ETH) and 34% **1**·IrCl(ETH/CO). These results are corroborated by the CO/H₂ experiments (SI Figure 7.6-7.7). The same analysis was conducted in the BF₄ derivative which was found to have 79 mol% ethylene relative to iridium and 21 mol% of CO relative to iridium; this suggests a sample composition of 58% **1**·IrBF₄(ETH) and 42% **1**·IrBF₄(ETH/CO). The slight reduction in the amount of bis-ethylene complex in the BF₄ sample may be due to enhanced sensitivity of this complex towards ethylene loss due to the charged Ir(I) center produced by the non-coordinating BF₄ anion, thereby over-estimating the proportion of CO ligated Ir sites in the sample.

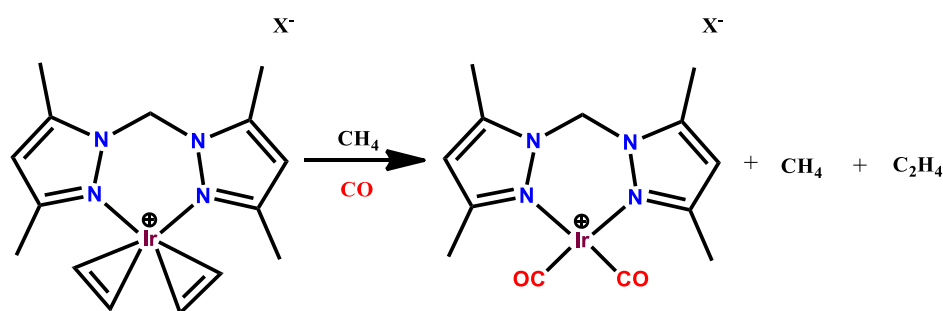


Figure 7.3.7.2.1. Reaction scheme showing the displacement of the ethylene from the Ir(I) center in **1**·IrCl or **1**·IrBF₄ in presence of CO/CH₄.

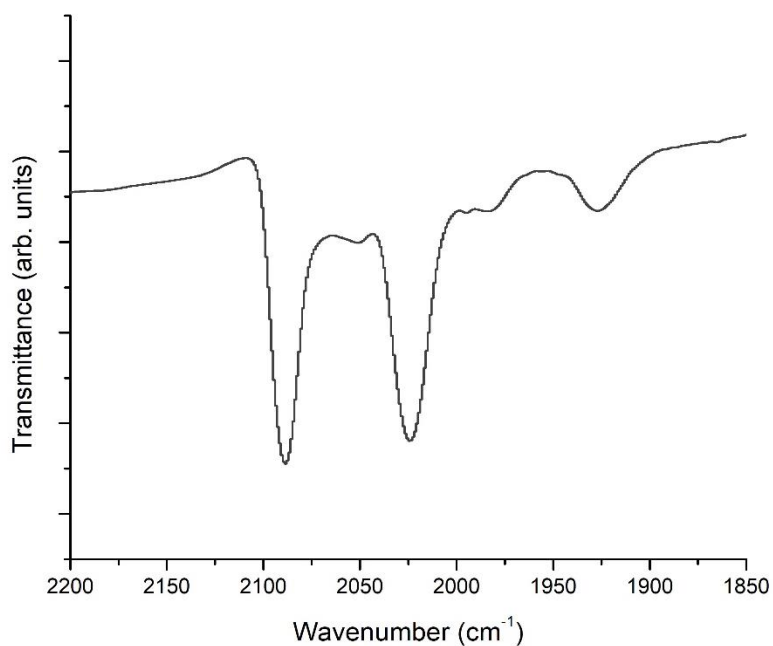


Figure 7.3.7.2.2. Infra-red spectrum of **1·IrCl** crystals following exposure to CO/CH₄, displaying the strong CO stretches corresponding to the formation of **1·[Ir(CO)₂Cl]** as the major product.

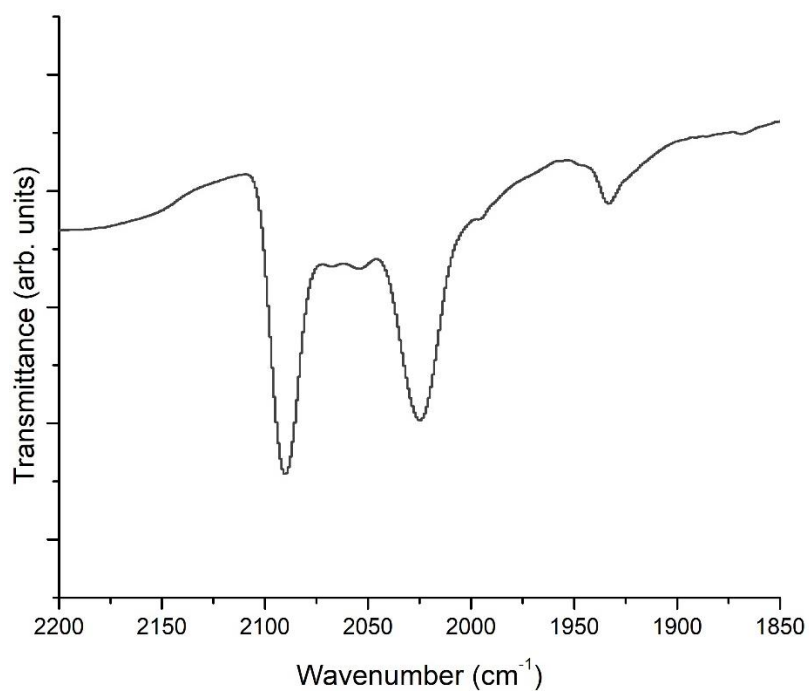


Figure 7.3.7.2.3. Infra-red spectrum of **1·IrBF₄** crystals following exposure to CO/CH₄, displaying the strong CO stretches corresponding to the formation of **1·[Ir(CO)₂BF₄]** as the major product.

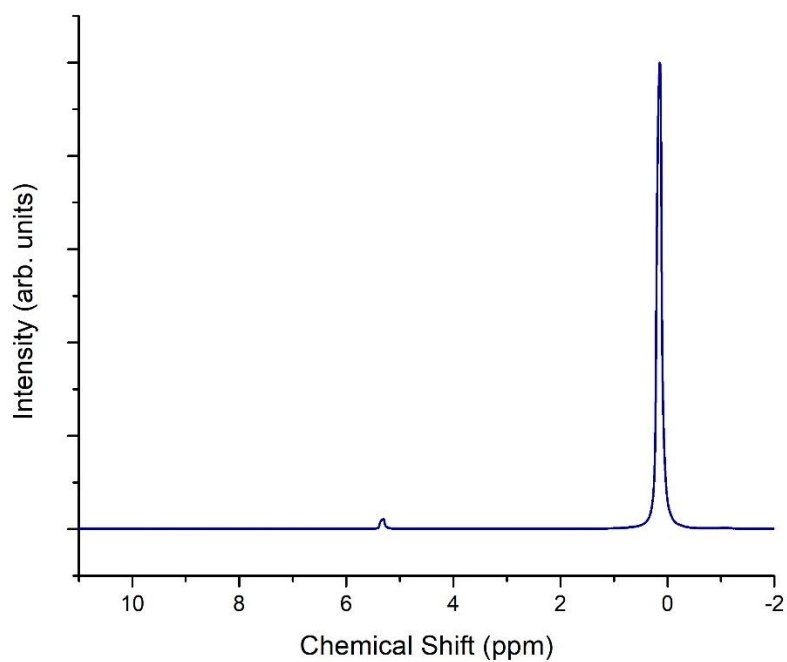


Figure 7.3.7.2.4. ^1H NMR spectrum obtained from the headspace of an NMR tube containing $1\cdot\text{IrCl}$ crystals following exposure to CO/CH_4 , displaying the ethylene (5.31 ppm) and methane (0.14 ppm) resonances.

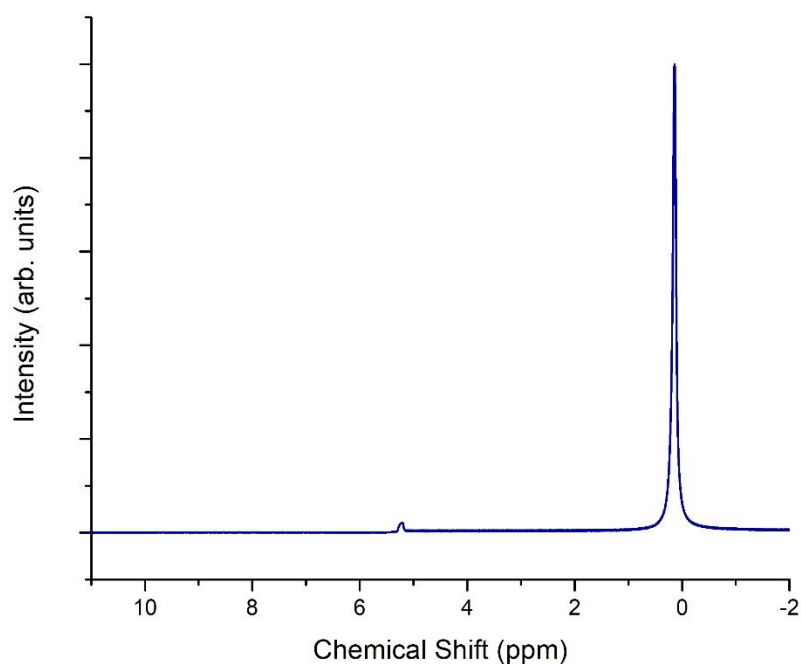


Figure 7.3.7.2.5. ^1H NMR spectrum obtained from the headspace of an NMR tube containing $1\cdot\text{IrBF}_4$ crystals following exposure to CO/CH_4 , displaying the ethylene (5.31 ppm) and methane (0.14 ppm) resonances.

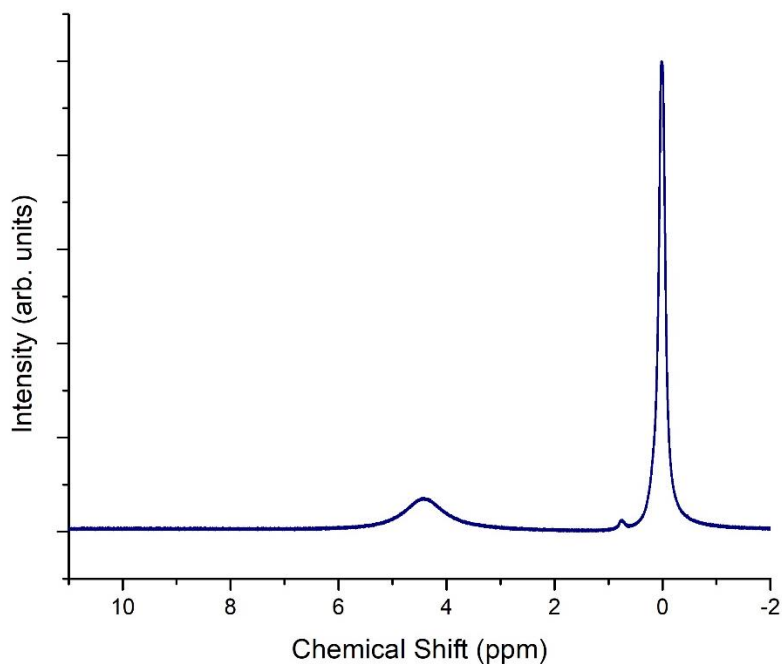


Figure 7.3.7.2.6. ¹H NMR spectrum obtained from the headspace of an NMR tube containing 1-IrCl crystals following exposure to H₂/CH₄, displaying the hydrogen (4.57 ppm), ethane (0.88) and methane (0.14 ppm) resonances.

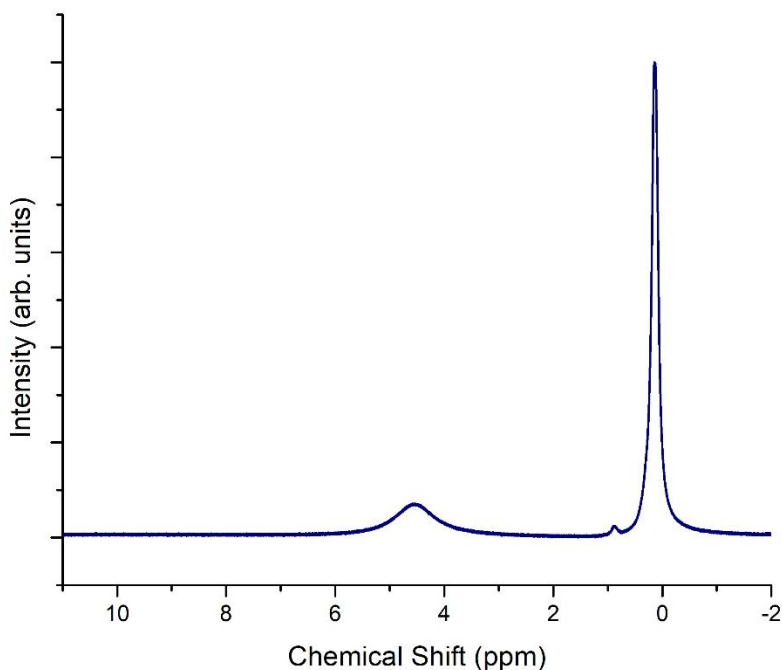


Figure 7.3.7.2.7. ¹H NMR spectrum obtained from the headspace of an NMR tube containing 1-IrBF₄ crystals following exposure to H₂/CH₄, displaying the hydrogen (4.57 ppm), ethane (0.88) and methane (0.14 ppm) resonances.

7.3.8. Infrared (IR) Spectroscopy

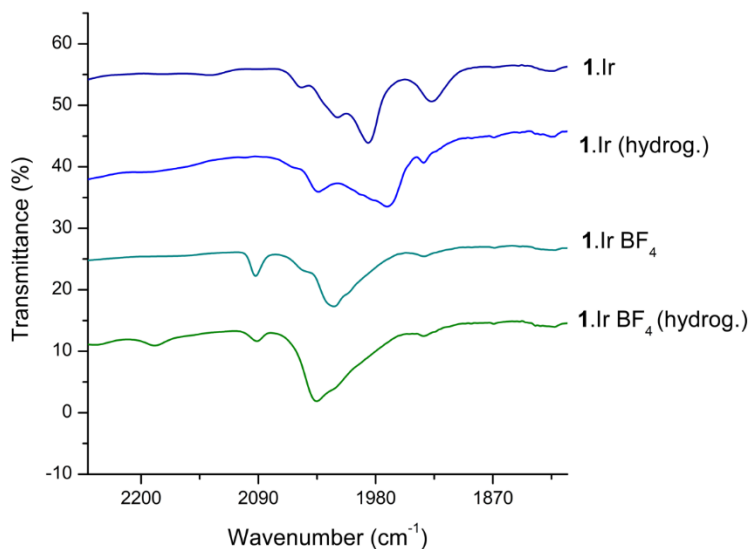


Figure 7.3.8.1. Infra-red spectrum (nujol) of **1**·IrCl and **1**·IrBF₄ crystals before and after hydrogenation catalysis, displaying minor changes in the stretching frequency of CO ligands upon exchange of the chloride anion for BF₄ and following hydrogenation.

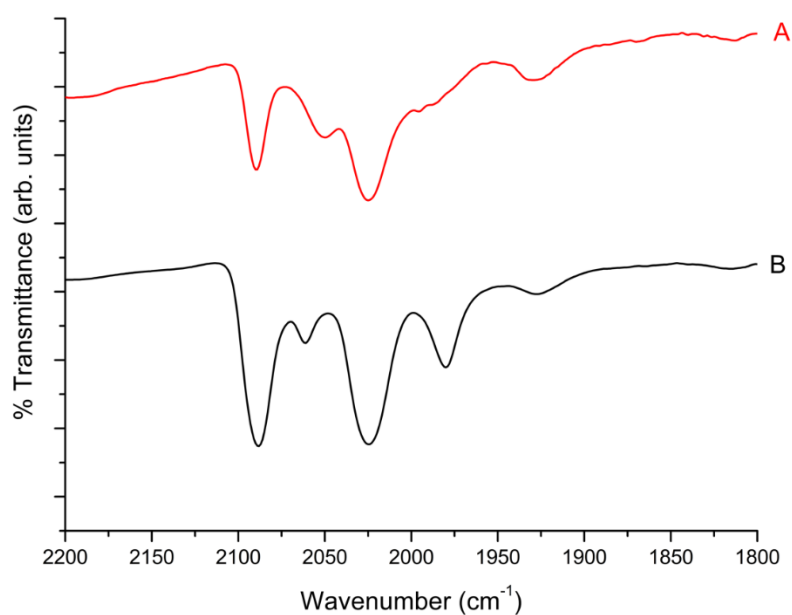


Figure 7.3.8.2. Infra-red spectrum (nujol) of an iridium metalated sample of **1** synthesized in the presence of acetaldehyde (metalation at 65°C in ethanol with acetaldehyde) (**B**) and a sample of iridium metalated **1** following exposure to acetaldehyde post-synthesis (**1**·IrCl heated at 65°C in ethanol with acetaldehyde) (**A**). In both samples, strong CO stretches are observed at 2088/2025 cm⁻¹ which indicate the formation of gem dicarbonyl complexes of iridium, supporting the proposal that the decarbonylation of acetaldehyde (generated by ethanol dehydrogenation) is the origin of the CO-ligated by-products present in **1**·IrCl.

7.3.9. References

1. Bloch, W. M.; Burgun, A.; Coghlan, C. J.; Lee, R.; Coote, M. L.; Doonan, C. J.; Sumbly, C. J., Capturing snapshots of post-synthetic metallation chemistry in metal-organic frameworks. *Nat. Chem.* **2014**, *6* (10), 906-912.
2. Peralta, R. A.; Huxley, M. T.; Evans, J. D.; Fallon, T.; Cao, H.; He, M.; Zhao, X. S.; Agnoli, S.; Sumbly, C. J.; Doonan, C. J., Highly Active Gas Phase Organometallic Catalysis Supported Within Metal-organic Framework Pores. *J. Am. Chem. Soc.* **2020**, *142* (31), 13533-13543.
3. Cowieson, N. P.; Aragao, D.; Clift, M.; Ericsson, D. J.; Gee, C.; Harrop, S. J.; Mudie, N.; Panjikar, S.; Price, J. R.; Riboldi-Tunncliffe, A.; Williamson, R.; Caradoc-Davies, T., MX1: a bending-magnet crystallography beamline serving both chemical and macromolecular crystallography communities at the Australian Synchrotron. *J. Synchrotron Rad.* **2015**, *22* (1), 187-190.
4. McPhillips, T.; McPhillips, S.; Chiu, H.; Cohen, A. E.; Deacon, A. M.; Ellis, P. J.; Garman, E.; Gonzalez, A.; Sauter, N. K.; Phizackerley, R. P.; Soltis, S. M.; Kuhn, P., Blue-Ice and the Distributed Control System software for data acquisition and instrument control at macromolecular crystallography beamlines. *J. Synchrotron Rad.* **2002**, *9*, 401-406.
5. Pike, S. D.; Krämer, T.; Rees, N. H.; Macgregor, S. A.; Weller, A. S., Stoichiometric and Catalytic Solid–Gas Reactivity of Rhodium Bis-phosphine Complexes. *Organometallics* **2015**, *34* (8), 1487-1497.

7.4. Supplementary information for Chapter 5

7.4.1. Energy Dispersive X-ray (EDX) analysis

Table 7.4.1: Cu(I) and associated anion occupancy determined via measurement of the Mn:Cu ratio and the Cu:Cl ratio using EDX analysis.

Sample	Cu, occupancy (%) ^{a,b}	Cl occupancy (%) ^{a,b}	Std error (%)
MnMOF-1 ·[Cu(CH ₃ CN)(Cl)]	101.5	110.3	7.6
MnMOF-1 ·[Cu(C ₂ H ₄)]BF ₄	102.3	0.8	1.2
MnMOF-1 ·[CuCO]BF ₄	106.2	0.2	3.5
MnMOF-1 ·[CuCO]PF ₆	104.2	0.5	4.1
MnMOF-1 ·[CuCO]OTf	99.7	0.4	3.9

^a Average atomic% obtained from three areas of crystals.

^b Relative to full occupancy of the bis(pyrazole)methane coordinating sites in **1**.

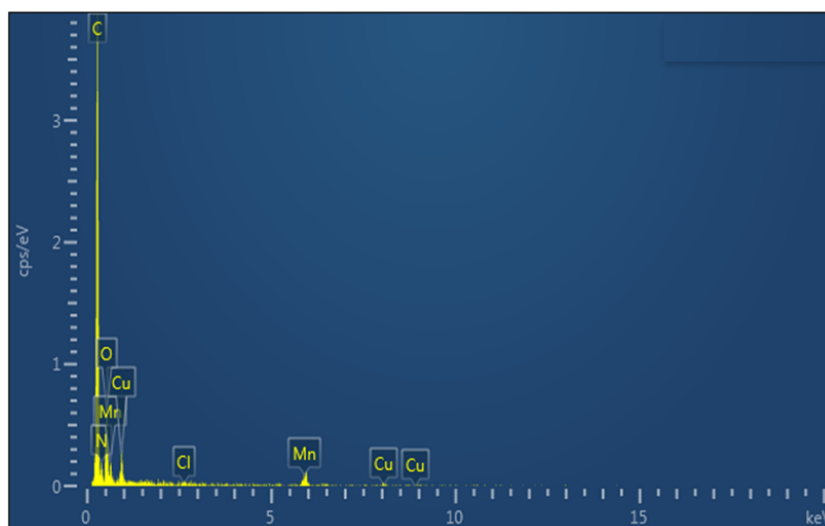


Figure 7.4.1: Representative raw EDX spectra for **MnMOF-1**·[Cu(CH₃CN)(Cl)].

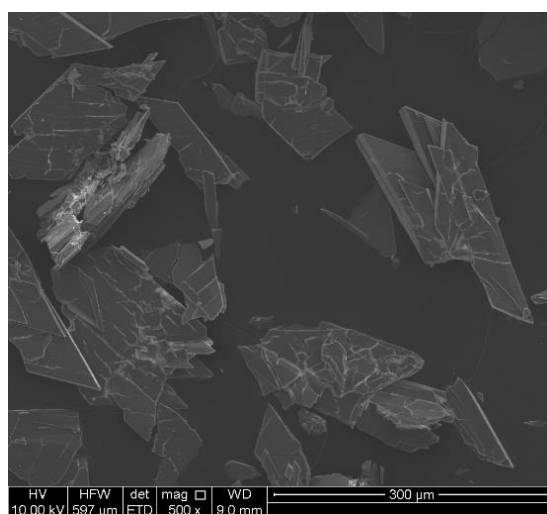


Figure 7.4.2: SEM image of metalated **MnMOF-1** showing an area of crushed crystals used for EDX analysis.

7.4.2. Powder X-ray Diffraction (PXRD) plots

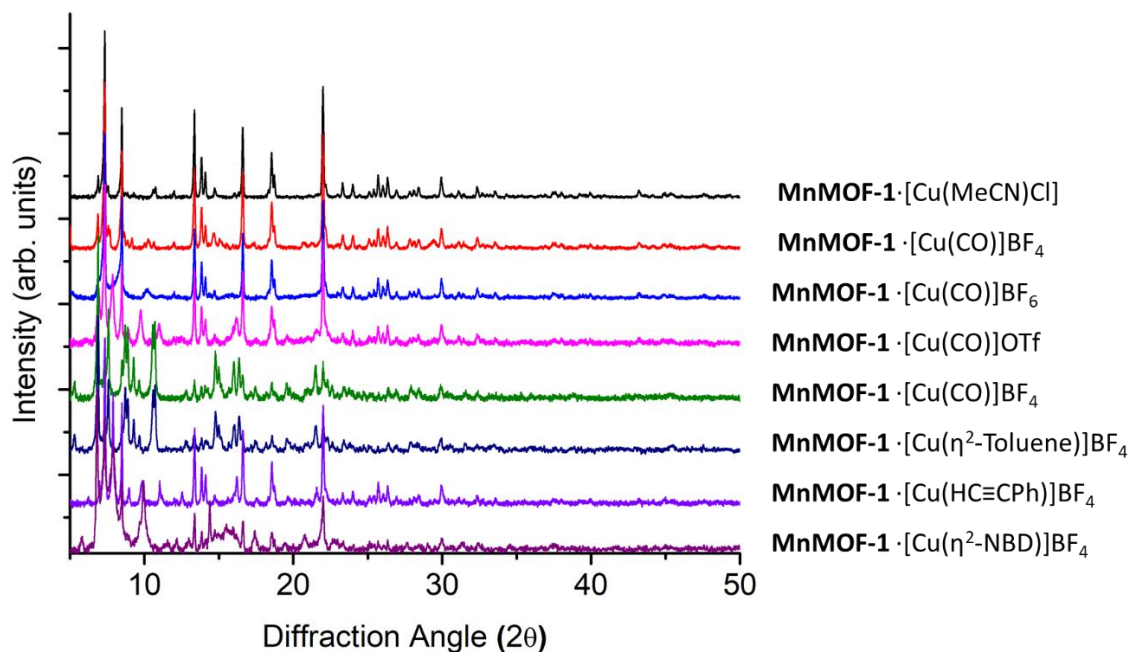


Figure 7.4.2.1: Experimental PXRD plots for **MnMOF-1**·[Cu(MeCN)Cl], **MnMOF-1**·[Cu(CO)]BF₄, **MnMOF-1**·[Cu(CO)]PF₆, **MnMOF-1**·[Cu(CO)]OTf, **MnMOF-1**·[Cu(C₂H₄)]PF₆, **MnMOF-1**·[Cu(η²-Toluene)]BF₄, **MnMOF-1**·[Cu(HC≡CPh)]BF₄ and **MnMOF-1**·[Cu(η²-NBD)]BF₄. The flexibility of the framework causes slight shifts in the PXRD peak positions and intensity upon changes in the solvent and loss of solvent during sample preparation for PXRD.

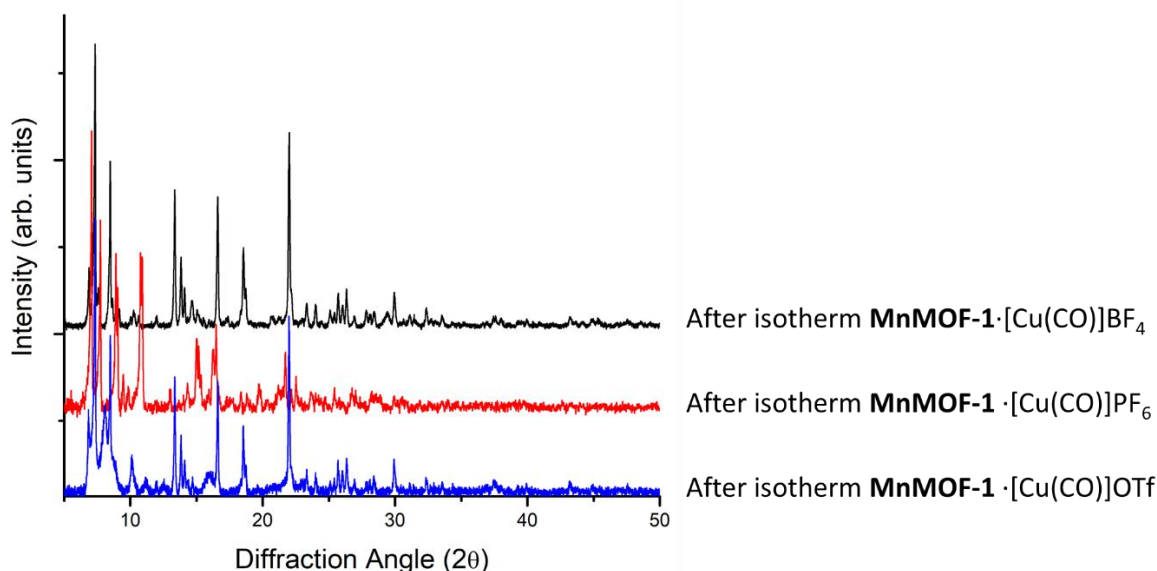


Figure 7.4.2.2: Experimental PXRD plots after the isotherms for **MnMOF-1**·[Cu(CO)]BF₄, **MnMOF-1**·[Cu(CO)]OTf, and **MnMOF-1**·[Cu(CO)]PF₆. The flexibility of the framework causes slight shifts in the PXRD peak positions and intensity upon changes in the solvent and loss of solvent during activation and/or sample preparation for PXRD.

7.4.3 Single Crystal X-ray Crystallography

7.4.3.1. General Procedures

Single crystals were mounted in Paratone-N oil on a MiTeGen micromount. Single-crystal X-ray data were collected at 100 K on the MX1 or MX2 beamlines of the Australian Synchrotron using the Blue-ice software interface,¹ $\lambda = 0.71073 \text{ \AA}$. Absorption corrections were applied using multiscan methods using XDS,^{2,3} the structures solved using SHELXS or SHELXT,^{4,5} and refined by full-matrix least squares on F^2 by SHELXL,⁶ interfaced through the program X-Seed or OLEX.^{7,8} In general, all atoms were refined anisotropically and hydrogens atoms were included as invariants at geometrically estimated positions, unless specified otherwise in additional details in supporting information. Where noted, the data was treated with the SQUEEZE routine available in Platon⁹ or using the solvent masking feature of Olex. Figures were produced using the program CrystalMaker. X-ray experimental data is given in Tables 7.4.3.5.1 – 7.4.3.5.5. CIF data have been deposited with the Cambridge Crystallographic Data Centre, CCDC reference numbers CCDC 2071194-2071203.

7.4.3.2. Specific Refinement Details

MnMOF-1·[Cu(CH₃CN)(Cl)]. The coordination environment of the added [Cu(CH₃CN)(Cl)] moieties (two independent positions with different coordination environments) is significantly disordered. A series of SIMU, RIGU, and ISOR restraints were used to allow refinement.

MnMOF-1·[CuCO]BF₄. SIMU, RIGU and DFIX restraints were used to refine the Cu-CO moiety with chemically sensible bond lengths.

MnMOF-1·[CuCO]PF₆. SIMU, RIGU and DFIX restraints were used to refine the Cu-CO moiety with chemically sensible bond lengths. Additionally, SIMU and RIGU restraints were used stabilizing the refinement and attaining chemically sensible ellipsoids for the organic linkers of the MOF.

MnMOF-1·[CuCO]OTf. SIMU, RIGU and DFIX restraints were used to refine the Cu-CO moiety with chemically sensible bond lengths. A significant proportion of the Cu centers had undergone hydrolysis to form [Cu(OH₂)]; this was approximately 50:50 in one instance and mainly the [Cu(OH₂)] complex rather than the target [CuCO]OTf species in the other crystallographically independent site. SIMU, RIGU, DFIX and ISOR restraints were also used to allow refinement of the cyclohexane solvate molecules.

MnMOF-1·[Cu(C₂H₄)]BF₄. SIMU, RIGU, ISOR and DFIX restraints were used to refine the Cu-(C₂H₄) moiety with chemically sensible bond lengths. Additional ISOR restraints were used for the fluorine atoms of the tetrafluoroborate anion.

MnMOF-1·[CuBF₄]. The BF₄ anion is disordered over four positions in the structure; two crystallographically independent sites and two sites generated by a mirror plane. Due to the relatively low occupancy in each site (0.25) a model of the BF₄ anion from the FragmentDB library was used to allow isotropic refinement (DFIX, SADI restraints). SIMU and RIGU restraints were also used for the Cu(BF₄) moiety and parts of the organic linkers of the MOF (rotational disorder). There was a small amount of residual CuCO moiety from the starting material present in the sample (**MnMOF-1**·[CuBF₄] was formed by evacuating **MnMOF-1**·[CuCO]BF₄ and resolating the crystals), but this could not be modelled.

MnMOF-1·[Cu(η²-Toluene)]BF₄. DFIX, SIMU, RIGU and ISOR restraints were used to allow the refinement of the toluene solvate molecules.

MnMOF-1·[Cu(η²-NBD)]BF₄. DFIX, SIMU, RIGU and ISOR restraints were used to allow the refinement of the coordinated norbornadiene (NBD), tetrafluoroborate anion, and toluene solvate molecules.

MnMOF-1·[Cu(η²(HC≡CPh))]BF₄. A large series of restraints (FLAT, SIMU, RIGU, EADP, ISOR and DFIX) were used to allow the refinement of the coordinated phenylacetylene (PhCCH), organic linkers, and phenylacetylene solvate molecules. The non-coordinated phenylacetylene molecules were also refined with isotropic displacement parameters (ca. 50% occupied). Finally, due to disorder, the tetrafluoroborate anion could not be located in the structure, although a possible site in the known anion pocket was identified.

7.4.3.3. Thermal ellipsoid plots for all structures at the 50% probability level

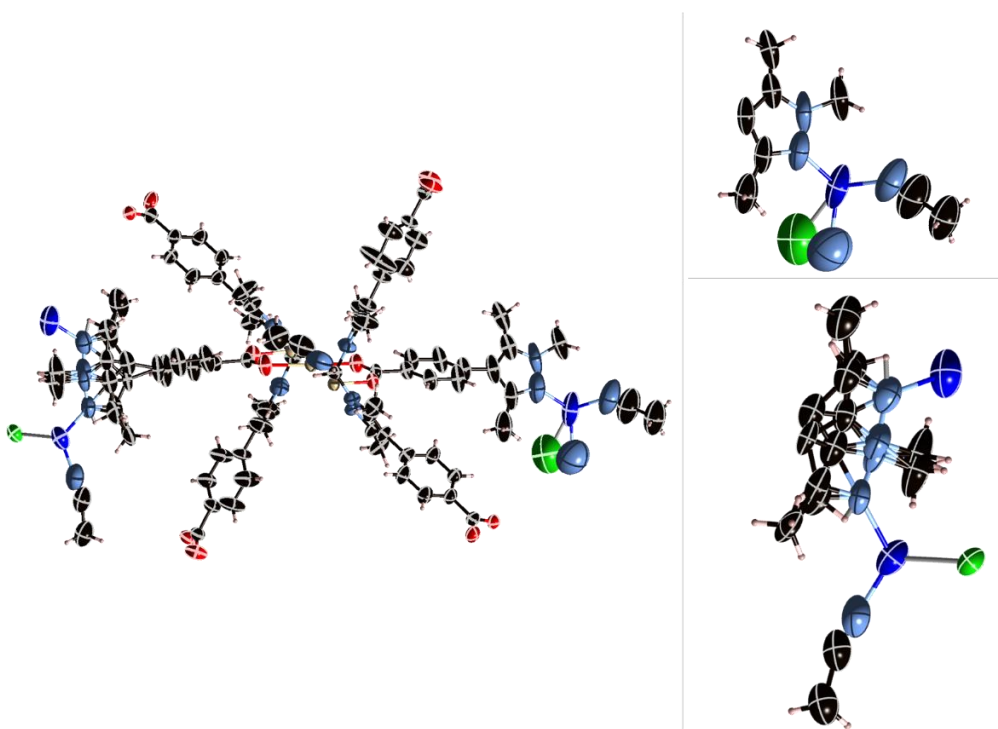


Figure 7.4.3.3.1. (left) The asymmetric unit of **MnMOF-1**-[Cu(CH₃CN)(Cl)], with all non-hydrogen atoms represented by ellipsoids at the 50% probability level (C, black; H, white; N, light blue; O, red; Cu, dark blue; Mn, beige; Cl, green). (top/bottom right) A perspective view of the crystallographically distinct Cu(I) chelation sites with all non-hydrogen atoms represented by ellipsoids at the 50% probability level.

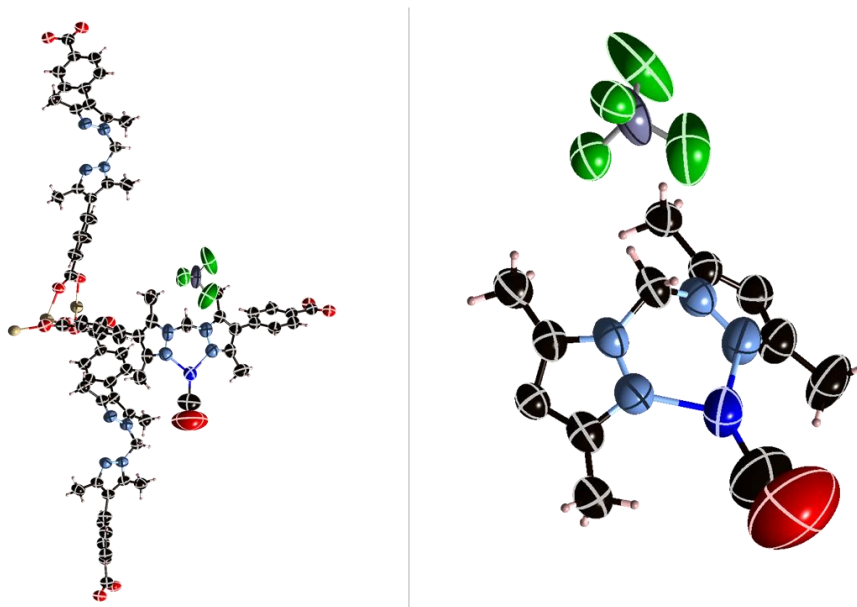


Figure 7.4.3.3.2. (left) The asymmetric unit of **MnMOF-1**-[CuCO]BF₄, with all non-hydrogen atoms represented by ellipsoids at the 50% probability level (C, black; H, white; N, light blue; O, red; Cu, dark blue; Mn, beige; B, grey; F, green). (right) A perspective view of the Cu(I) chelation site with all non-hydrogen atoms represented by ellipsoids at the 50% probability level.

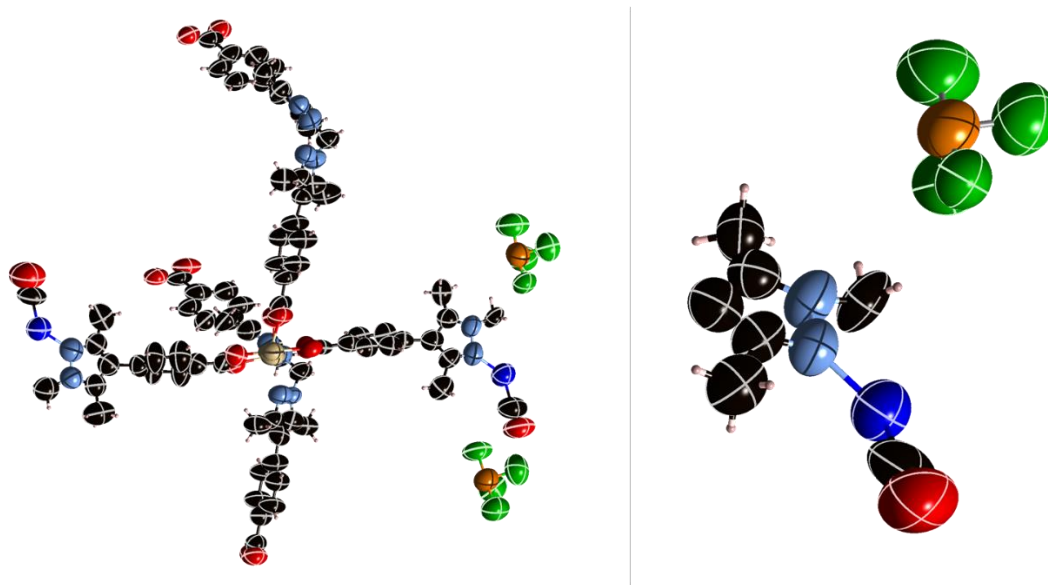


Figure 7.4.3.3. (left) The asymmetric unit of **MnMOF-1**·[CuCO]PF₆, with all non-hydrogen atoms represented by ellipsoids at the 50% probability level (C, black; H, white; N, light blue; O, red; Cu, dark blue; Mn, beige; P, orange; F, green). (right) A perspective view of the Cu(I) chelation site with all non-hydrogen atoms represented by ellipsoids at the 50% probability level.

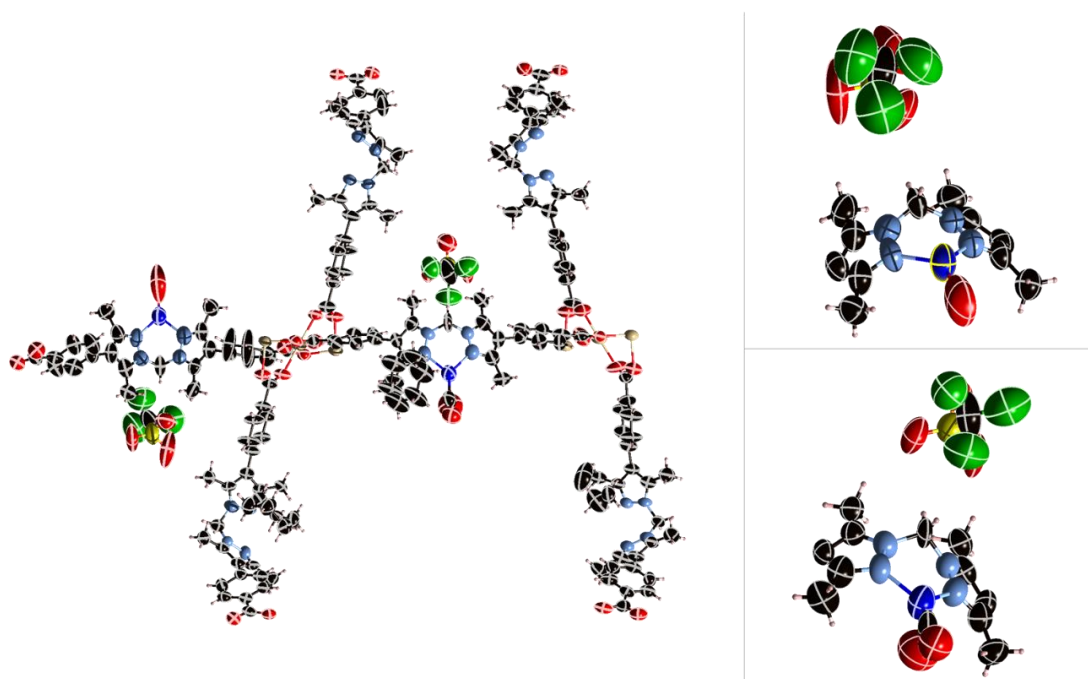


Figure 7.4.3.4. (left) The asymmetric unit of **MnMOF-1**·[CuCO]OTf, with all non-hydrogen atoms represented by ellipsoids at the 50% probability level (C, black; H, white; N, light blue; O, red; Cu, dark blue; Mn, beige; S, yellow; F, green). (right) A perspective view of the two Cu(I) chelation site with all non-hydrogen atoms represented by ellipsoids at the 50% probability level.

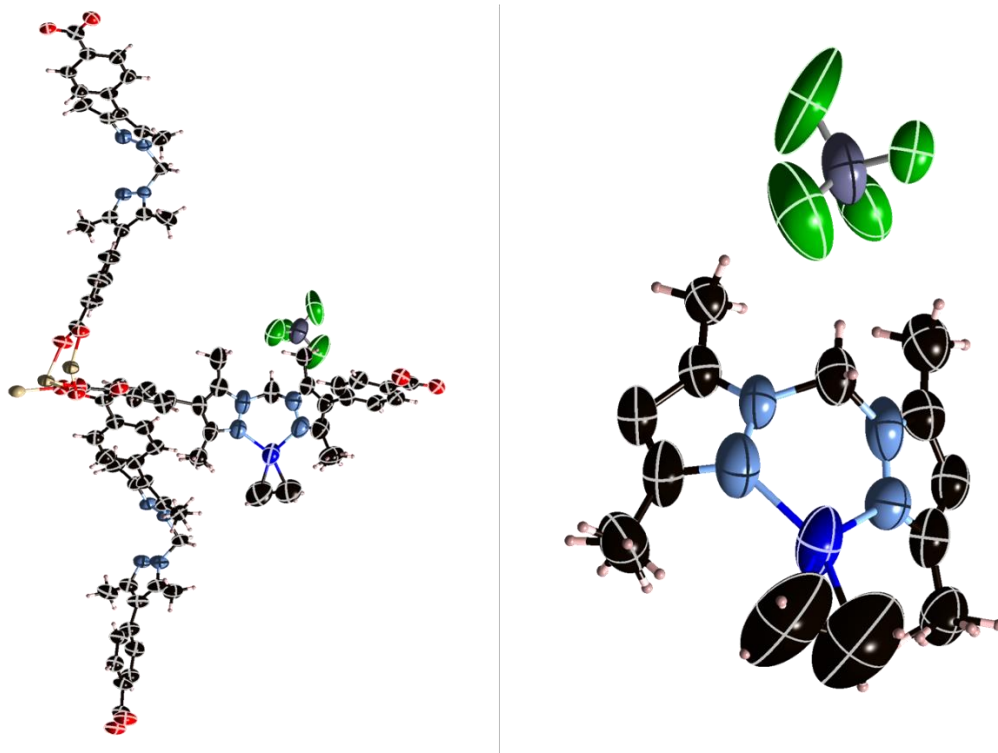


Figure 7.4.3.3.5. (left) The asymmetric unit of **MnMOF-1**·[Cu(C₂H₄)]BF₄, with all non-hydrogen atoms represented by ellipsoids at the 50% probability level (C, black; H, white; N, light blue; O, red; Cu, dark blue; Mn, beige; B, grey; F, green). (right) A perspective view of the Cu(I) chelation site with all non-hydrogen atoms represented by ellipsoids at the 50% probability level.

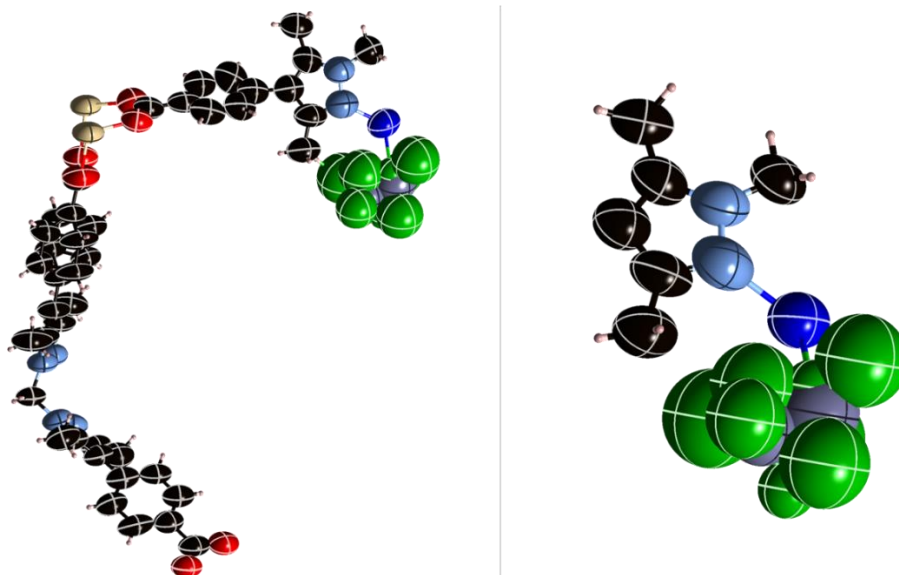


Figure 7.4.3.3.6. (left) The asymmetric unit of **MnMOF-1**·[CuBF₄], with all non-hydrogen atoms represented by ellipsoids at the 50% probability level (C, black; H, white; N, light blue; O, red; Cu, dark blue; Mn, beige; B, grey; F, green). (right) A perspective view of the Cu(I) chelation site with all non-hydrogen atoms, except the disordered tetrafluoroborate anion represented by ellipsoids at the 50% probability level.

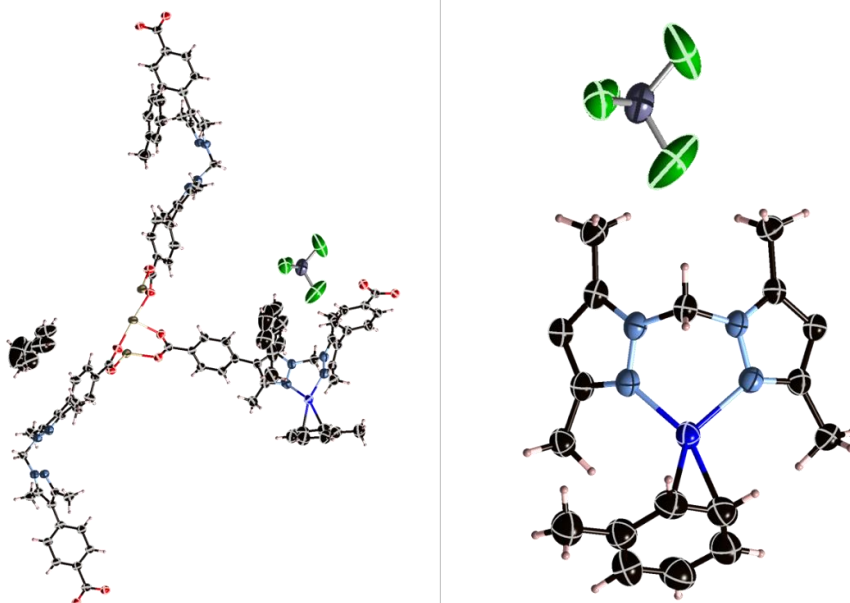


Figure 7.4.3.3.7. (left) The asymmetric unit of **MnMOF-1**·[Cu(η^2 -Toluene)]BF₄ with all non-hydrogen atoms represented by ellipsoids at the 50% probability level (C, black; H, white; N, light blue; O, red; Cu, dark blue; Mn, beige; B, grey; F, green). (right) A perspective view of the Cu(I) chelation site with all non-hydrogen atoms represented by ellipsoids at the 50% probability level.

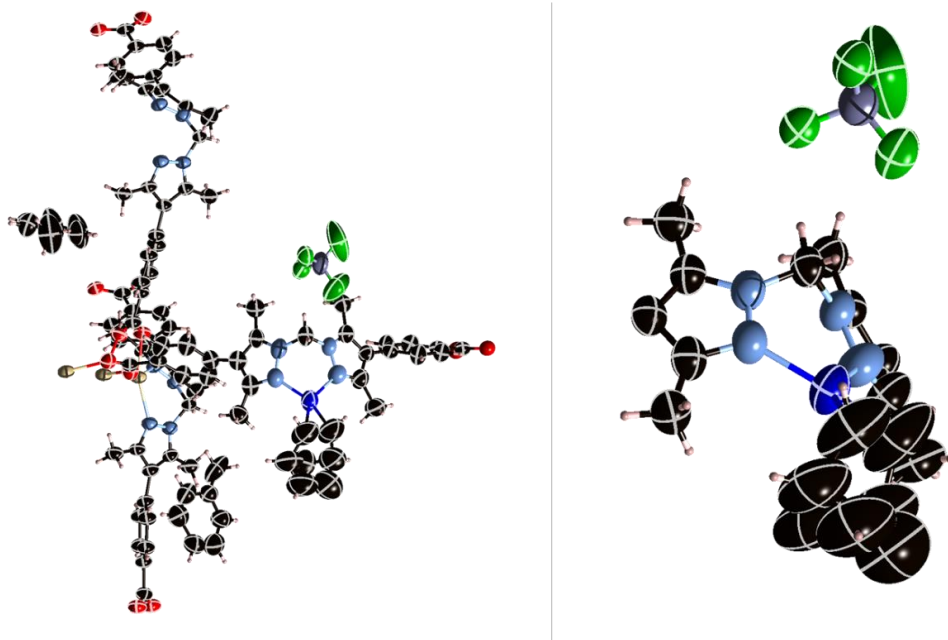


Figure SI 3.3.8: (left) The asymmetric unit of **MnMOF-1** [Cu(η^2 -NBD)]BF₄ with all non-hydrogen atoms represented by ellipsoids at the 50% probability level (C, black; H, white; N, light blue; O, red; Cu, dark blue; Mn, beige; B, grey; F, green). (right) A perspective view of the Cu(I) chelation site with all non-hydrogen atoms represented by ellipsoids at the 50% probability level.

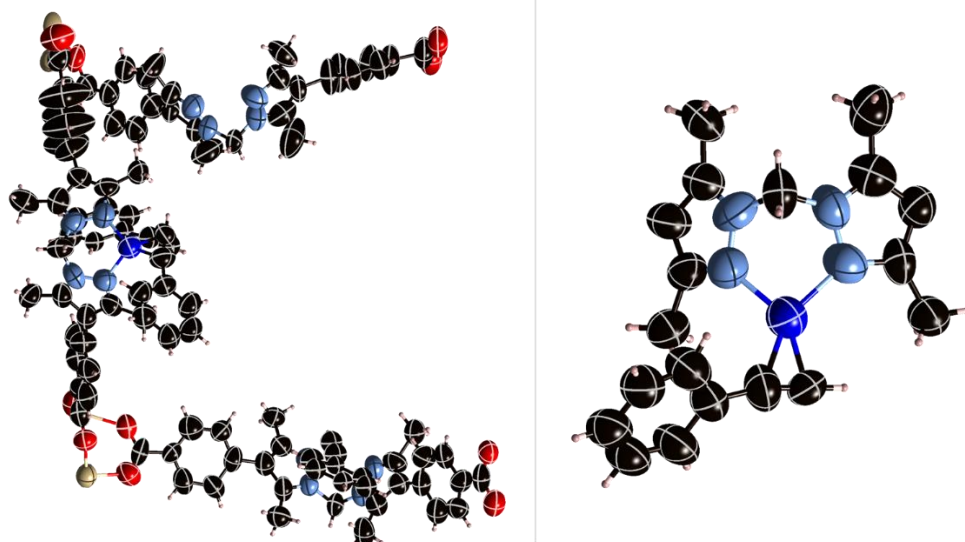


Figure 7.4.3.3.9. (left) The asymmetric unit of **MnMOF-1** [$\text{Cu}(\eta^2(\text{HC}\equiv\text{CPh}))\text{BF}_4$] with all non-hydrogen atoms represented by ellipsoids at the 50% probability level (C, black; H, white; N, light blue; O, red; Cu, dark blue; Mn, beige). (right) A perspective view of the Cu(I) chelation site with all non-hydrogen atoms represented by ellipsoids at the 50% probability level. The tetrafluoroborate anion required for charge balance could not be satisfactorily modelled due to disorder.

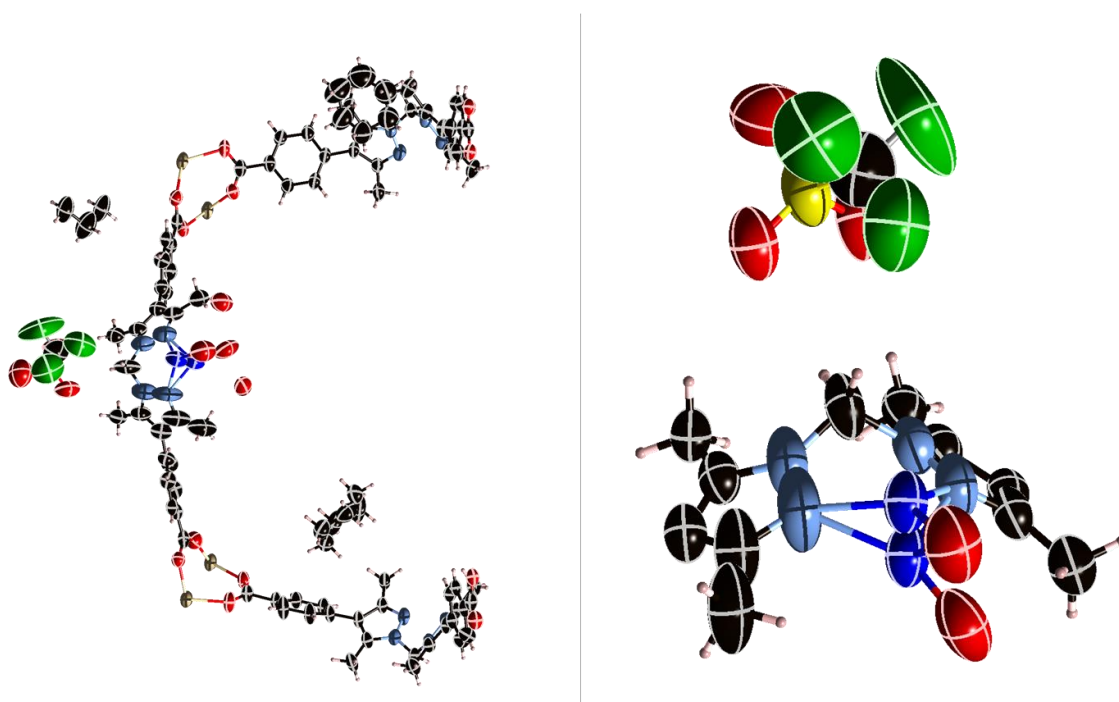


Figure 7.4.3.3.10. (left) The asymmetric unit of **MnMOF-1·[Cu(H₂O)]OTf**, with all non-hydrogen atoms represented by ellipsoids at the 50% probability level (C, black; H, white; N, light blue; O, red; Cu, dark blue; Mn, beige; S, yellow; F, green). (right) A perspective view of the two Cu(I) chelation sites with all non-hydrogen atoms represented by ellipsoids at the 50% probability level.

7.4.3.4. Electron density plots for all structures at the 50% probability level

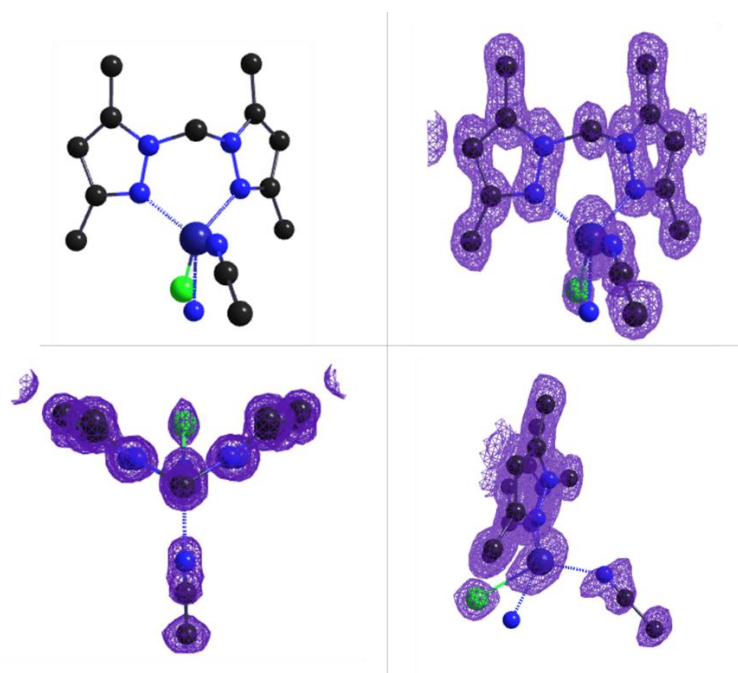


Figure 7.4.3.4.1. (a) A perspective view of the first chelated Cu(I) complex in **MnMOF-1**·[Cu(CH₃CN)(Cl)], and the overlaid electron density map as viewed from the (b) front, (c) top and (d) side of the complex.

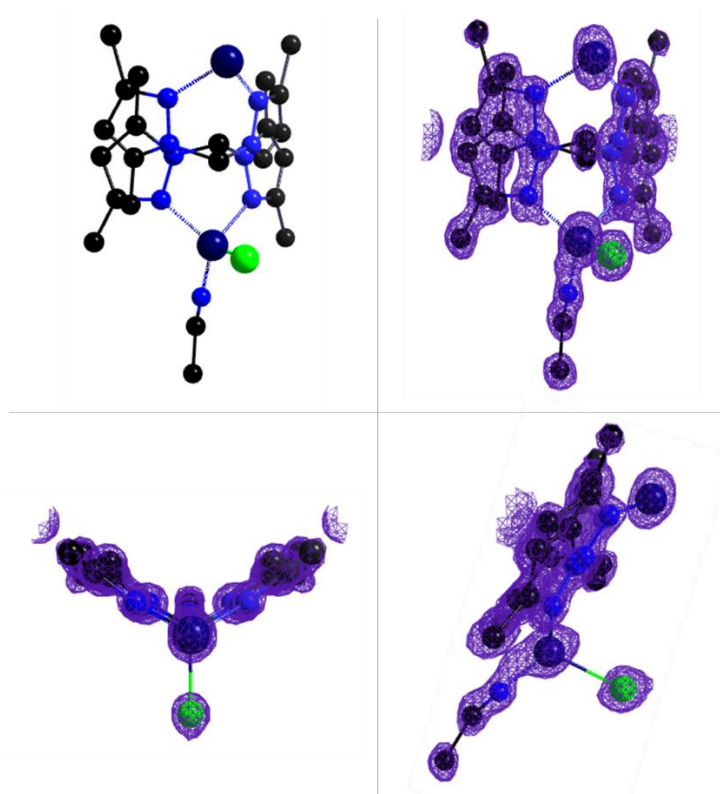


Figure 7.4.3.4.2. (a) A perspective view of the second chelated Cu(I) complex in **MnMOF-1**·[Cu(CH₃CN)(Cl)], and the overlaid electron density map as viewed from the (b) front, (c) top and (d) side of the complex.

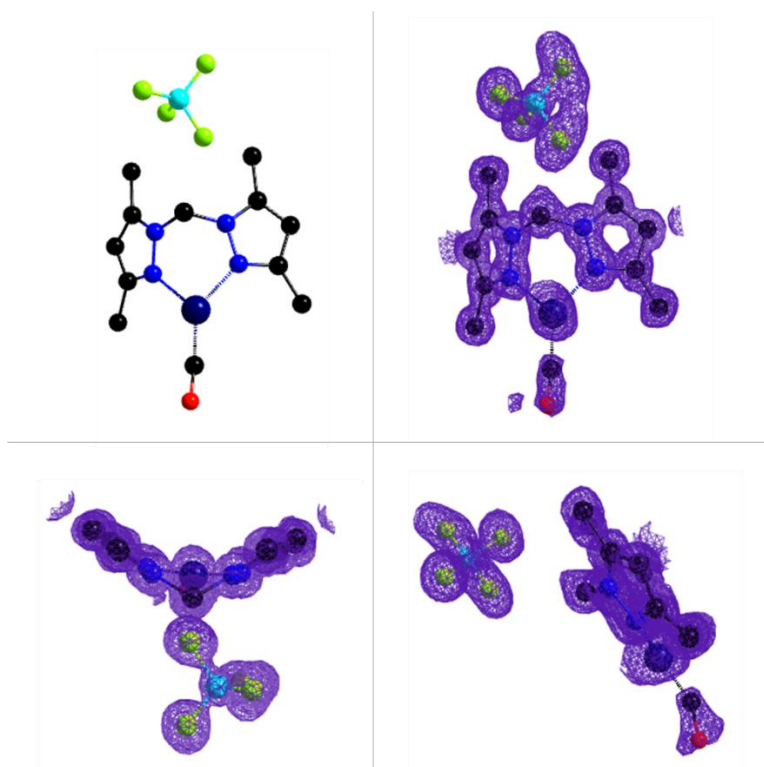


Figure 7.4.3.4.3. (a) A perspective view of the chelated Cu(I) complex in **MnMOF-1**·[CuCO]BF₄, and the overlaid electron density map as viewed from the (b) front, (c) top and (d) side of the complex.

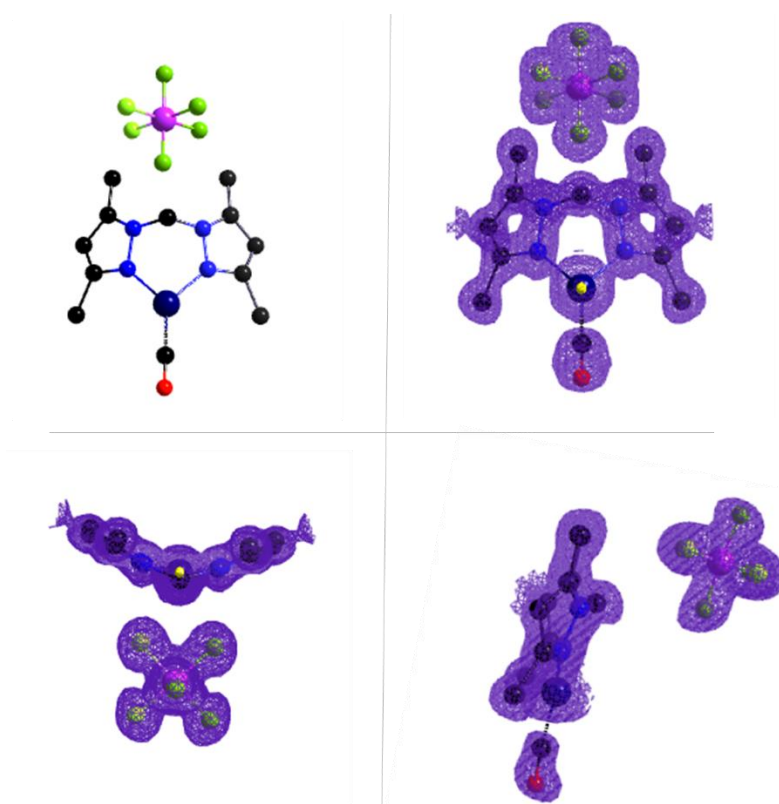


Figure 7.4.3.4.4. (a) A perspective view of the chelated Cu(I) complex in **MnMOF-1**·[CuCO]PF₆, and the overlaid electron density map as viewed from the (b) front, (c) top and (d) side of the complex.

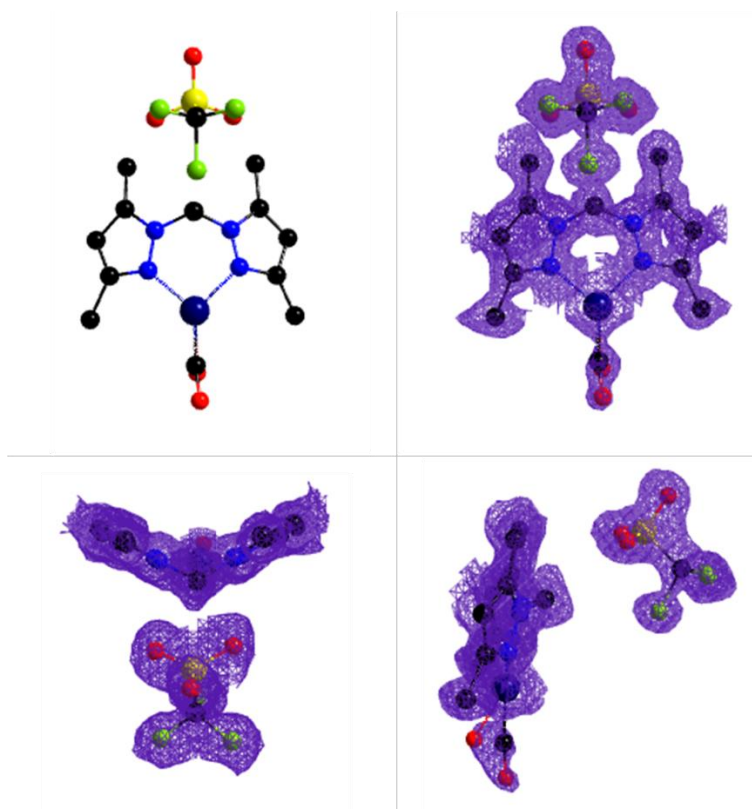


Figure 7.4.3.4.5. (a) A perspective view of the first chelated Cu(I) complex in **MnMOF-1**·[CuCO]OTf, and the overlaid electron density map as viewed from the (b) front, (c) top and (d) side of the complex.

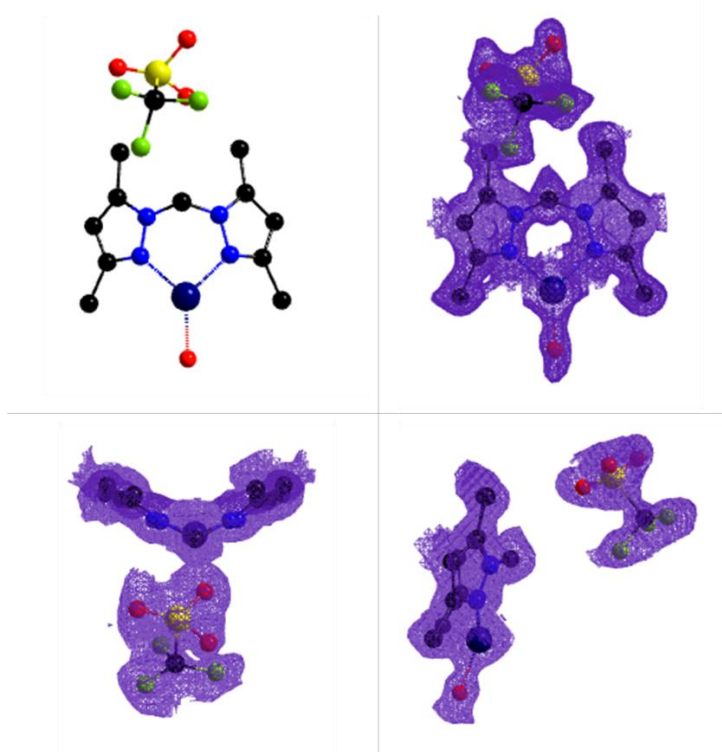


Figure 7.4.3.4.6. (a) A perspective view of the second chelated Cu(I) complex in **MnMOF-1**·[Cu(H₂O)]OTf, and the overlaid electron density map as viewed from the (b) front, (c) top and (d) side of the complex.

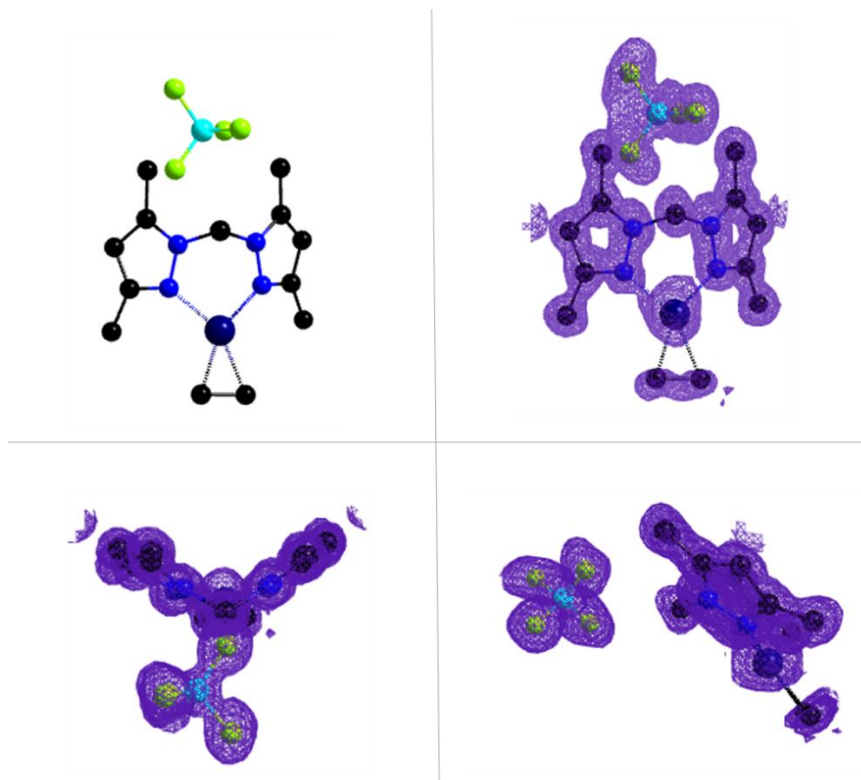


Figure 7.4.3.4.7. (a) A perspective view of the chelated Cu(I) complex in **MnMOF-1**·[Cu(C₂H₄)]BF₄, and the overlaid electron density map as viewed from the (b) front, (c) top and (d) side of the complex.

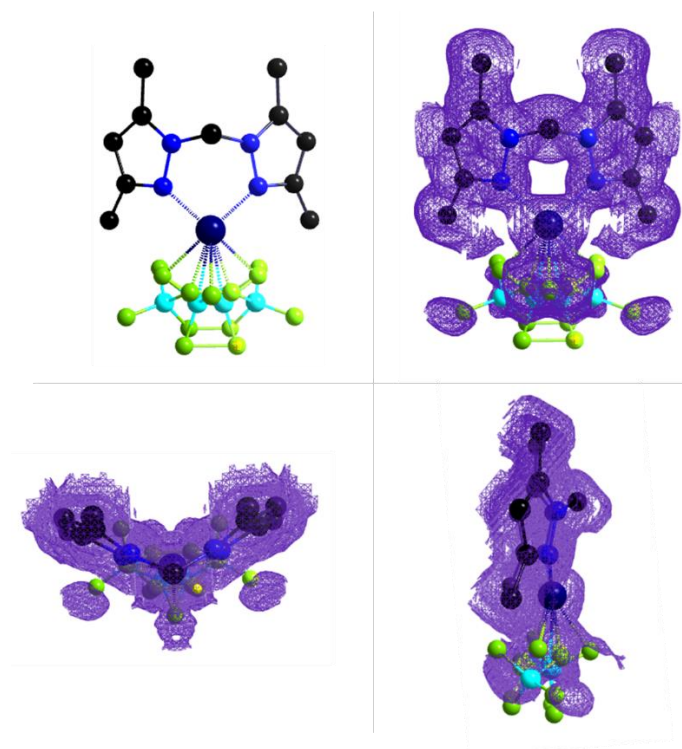


Figure 7.4.3.4.8. (a) A perspective view of the chelated Cu(I) complex in **MnMOF-1**·[Cu(BF₄)], and the overlaid electron density map as viewed from the (b) front, (c) top and (d) side of the complex. The BF₄ anion is disordered over two crystallographically distinct positions, which gives a total of four positions due to symmetry.

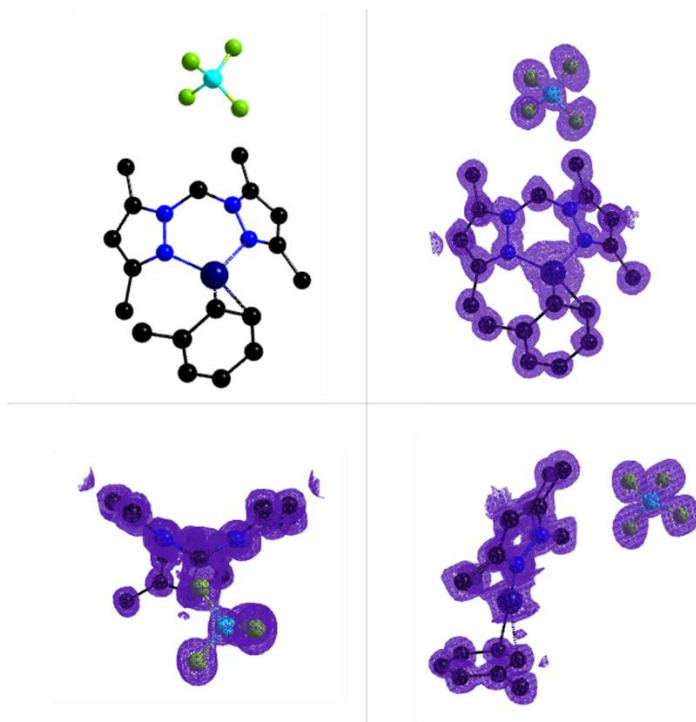


Figure 7.4.3.4.9. (a) A perspective view of the chelated Cu(I) complex in **MnMOF-1** [Cu(η^2 -Toluene)]BF₄, and the overlaid electron density map as viewed from the (b) front, (c) top and (d) side of the complex.

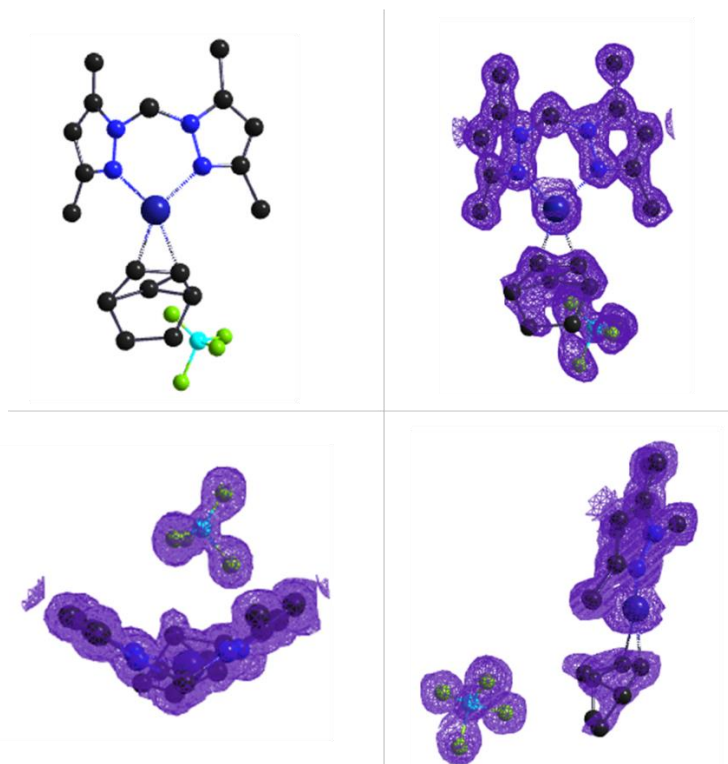


Figure 7.4.3.4.10. (a) A perspective view of the chelated Cu(I) complex in **MnMOF-1**-[Cu(η^2 -NBD)]BF₄, and the overlaid electron density map as viewed from the (b) front, (c) top and (d) side of the complex.

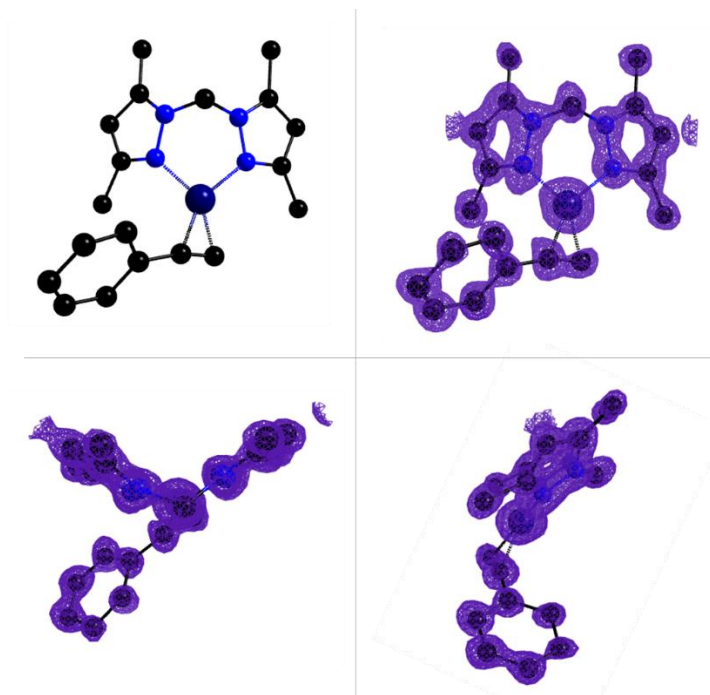


Figure 7.4.3.4.11. (a) A perspective view of the chelated Cu(I) complex in **MnMOF-1**·[Cu(η^2 (HC≡CPh))]BF₄, and the overlaid electron density map as viewed from the (b) front, (c) top and (d) side of the complex.

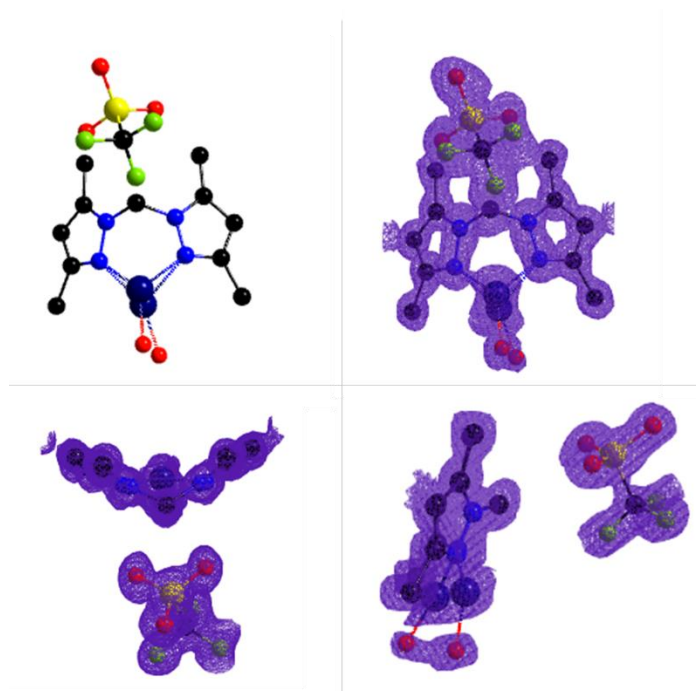


Figure 7.4.3.4.12. (a) A perspective view of the chelated Cu(I) complex in **MnMOF-1**·[Cu(H₂O)]OTf, and the overlaid electron density map as viewed from the (b) front, (c) top and (d) side of the complex.

7.4.3.5 Tables of X-ray crystallography data collection and refinement parameters

Table 7.4.3.5.1. Crystallographic data collection and refinement parameters for the metalated forms of **MnMOF-1**.

Sample	MnMOF-1·[Cu(MeCN)Cl]	MnMOF-1·[Cu(CO)]BF ₄
Crystallographic Parameter		
Formula	C ₇₉ H ₇₂ ClCuMn ₃ N ₁₄ O ₁₂	C ₇₆ H ₆₆ N ₁₂ O ₁₃ Mn ₃ CuF ₄ B
FW	1673.31	1670.57
T, K	100(2)	100(2)
Wavelength, Å	0.71073	0.71073
Crystal system, space group	Monoclinic, <i>P</i> ₂ ₁ / <i>m</i>	Monoclinic, <i>P</i> ₂ ₁ / <i>c</i>
Z	4	4
a, Å	12.349(3)	12.379(3)
b, Å	32.650(7)	34.724(7)
c, Å	25.851(5)	25.893(5)
α°	90	90
β, °	94.01(3)	97.79(3)
γ°	90	90
V, Å ³	10397(4)	11027(4)
<i>d</i> _{calc} , g/cm ³	1.069	1.006
Absorption coefficient, mm ⁻¹	0.636	0.581
<i>F</i> (000)	3444.0	3420.0
Crystal size, mm ³	0.2 × 0.14 × 0.03	0.25 × 0.14 × 0.04
2θ range for data collection	2.012 to 53.126	1.974 to 57.998
Index range	-15 ≤ <i>h</i> ≤ 15, -41 ≤ <i>k</i> ≤ 41, -31 ≤ <i>l</i> ≤ 31	-16 ≤ <i>h</i> ≤ 16, -42 ≤ <i>k</i> ≤ 42, -34 ≤ <i>l</i> ≤ 34
Reflections collected	155120	136232
Independent reflections	20537 [R _{int} = 0.0922, R _{sigma} = 0.0441]	22483 [R _{int} = 0.0687, R _{sigma} = 0.0335]
Data/restraints/parameters	20537/232/1094	22483/74/1003
GOF on F ²	1.031	1.085
Largest diff. peak and hole, eÅ ⁻³	0.93/-0.93	1.07/-1.93
R ₁ , [I > 2σ(I)]	0.0927	0.1052
wR ₂ , all data	0.2693	0.3229
CCDC Number	2071195	2071198

Table 7.4.3.5.2. Crystallographic data collection and refinement parameters for the metalated forms of **MnMOF-1**.

Sample	MnMOF-1·[Cu(CO)]PF ₆	MnMOF-1·[Cu(CO)]OTf
Crystallographic Parameter		
Formula	C ₇₆ H ₆₆ Cu ₆ Mn ₃ N ₁₂ O ₁₃ P	C _{161.5} H ₁₅₀ Cu ₂ F ₆ Mn ₆ N ₂₄ O ₃₂ S ₂
FW	1728.73	3573.89
T, K	100(2)	100(2)
Wavelength, Å	0.71073	0.71073
Crystal system, space group	Monoclinic, <i>P</i> 2 ₁ / <i>m</i>	Triclinic, <i>P</i> -1
Z	4	2
a, Å	12.373(3)	12.395(3)
b, Å	35.910(7)	25.853(5)
c, Å	25.894(5)	35.414(7)
α°	90	87.98(3)
β, °	97.46(3)	88.86(3)
γ°	90	81.34(3)
V, Å ³	11408(4)	11211(4)
<i>d</i> _{calc} , g/cm ³	1.007	1.059
Absorption coefficient, mm ⁻¹	0.580	0.594
<i>F</i> (000)	3532.0	3674.0
Crystal size, mm ³	0.19 × 0.12 × 0.02	0.22 × 0.14 × 0.03
2θ range for data collection	1.586 to 59.55	1.594 to 64.368
Index range	-16 ≤ <i>h</i> ≤ 16, -42 ≤ <i>k</i> ≤ 43, -34 ≤ <i>l</i> ≤ 35	-14 ≤ <i>h</i> ≤ 14, -34 ≤ <i>k</i> ≤ 34, -47 ≤ <i>l</i> ≤ 47
Reflections collected	138660	172176
Independent reflections	22998 [R _{int} = 0.1823, R _{sigma} = 0.1023]	55852 [R _{int} = 0.0897, R _{sigma} = 0.1035]
Data/restraints/parameters	22998/1587/1042	55852/298/2195
GOF on F ²	1.262	1.368
Largest diff. peak and hole, eÅ ⁻³	0.71/-0.82	2.30/-1.10
R ₁ , [I > 2σ(I)]	0.1657	0.1698
wR ₂ , all data	0.4992	0.4640
CCDC Number	2071196	2071197

Table 7.4.3.5.3. Crystallographic data collection and refinement parameters for the metalated forms of **MnMOF-1**.

Sample	MnMOF-1·[Cu(BF ₄)]	MnMOF-1·[Cu(NBD)]BF ₄
Crystallographic Parameter		
Formula	C ₇₅ H ₆₀ B _{0.8} CuF _{3.2} Mn ₃ N ₁₂ O ₁₂	C _{92.5} H ₈₃ BCuF ₄ Mn ₃ N ₁₂ O ₁₂
FW	1619.15	1869.87
T, K	100(2)	100.0
Wavelength, Å	0.71073	0.71073
Crystal system, space group	Monoclinic, <i>P</i> ₂ ₁ / <i>m</i>	Monoclinic, <i>P</i> ₂ ₁ / <i>c</i>
Z	2	4
a, Å	12.437(3)	12.356(3)
b, Å	34.935(7)	34.639(7)
c, Å	12.903(3)	25.985(5)
α°	90	90
β, °	98.27(3)	96.94(3)
γ°	90	90
V, Å ³	5548(2)	11040(4)
<i>d</i> _{calc} , g/cm ³	0.969	1.125
Absorption coefficient, mm ⁻¹	0.574	0.587
<i>F</i> (000)	1654.0	3852.0
Crystal size, mm ³	0.18 × 0.11 × 0.02	0.19 × 0.09 × 0.04
2θ range for data collection	2.332 to 63.762	1.968 to 64.284
Index range	-16 ≤ <i>h</i> ≤ 16, -47 ≤ <i>k</i> ≤ 47, -15 ≤ <i>l</i> ≤ 15	-17 ≤ <i>h</i> ≤ 17, -46 ≤ <i>k</i> ≤ 46, -35 ≤ <i>l</i> ≤ 34
Reflections collected	85376	189007
Independent reflections	14627 [R _{int} = 0.0994, R _{sigma} = 0.0699]	29194 [R _{int} = 0.0955, R _{sigma} = 0.0573]
Data/restraints/parameters	14627/141/539	29194/251/1157
GOF on F ²	1.351	1.040
Largest diff. peak and hole, eÅ ⁻³	0.83/-1.22	1.05/-1.17
R ₁ , [I > 2σ(I)]	0.1432	0.0892
wR ₂ , all data	0.4647	0.2966
CCDC Number	2071201	2071194

Table 7.4.3.5.4. Crystallographic data collection and refinement parameters for the metalated forms of **MnMOF-1**.

Sample	MnMOF-1·[Cu(Tol)]BF ₄	MnMOF-1·[Cu(PhC ₂ H)]BF ₄
Crystallographic Parameter		
Formula	C ₁₀₃ H ₉₅ BCuF ₄ Mn ₃ N ₁₂ O ₁₂	C ₉₁ H ₇₈ CuMn ₃ N ₁₂ O ₁₂
FW	2008.07	1760.01
T, K	100	100.15
Wavelength, Å	0.71073	0.71073
Crystal system, space group	Monoclinic, <i>P</i> 2 ₁ / <i>c</i>	Triclinic, <i>P</i> -1
Z	4	2
a, Å	12.367(3)	12.325(3)
b, Å	34.582(7)	12.935(3)
c, Å	25.915(5)	34.437(7)
α°	90	90.50(3)
β, °	97.89(3)	92.33(3)
γ°	90	99.98(3)
V, Å ³	10978(4)	5402(2)
<i>d</i> _{calc} , g/cm ³	1.215	1.082
Absorption coefficient, mm ⁻¹	0.595	0.591
<i>F</i> (000)	4152.0	1816.0
Crystal size, mm ³	0.19 × 0.08 × 0.03	0.17 × 0.07 × 0.03
2θ range for data collection	1.976 to 64.316	2.368 to 63.708
Index range	-14 ≤ <i>h</i> ≤ 14, -46 ≤ <i>k</i> ≤ 46, -35 ≤ <i>l</i> ≤ 35	-18 ≤ <i>h</i> ≤ 18, -17 ≤ <i>k</i> ≤ 17, -46 ≤ <i>l</i> ≤ 46
Reflections collected	198103	83918
Independent reflections	29451 [R _{int} = 0.0728, R _{sigma} = 0.0377]	24783 [R _{int} = 0.1420, R _{sigma} = 0.1237]
Data/restraints/parameters	29451/68/1240	24783/604/1019
GOF on F ²	1.053	1.388
Largest diff. peak and hole, eÅ ⁻³	0.88/-0.77	0.56/-1.25
R ₁ , [I > 2σ(I)]	0.0602	0.2025
wR ₂ , all data	0.1849	0.5691
CCDC Number	2071203	2071200

Table 7.4.3.5.5. Crystallographic data collection and refinement parameters for the metalated forms of **MnMOF-1**.

Sample	MnMOF-1·[Cu(H ₂ O)]OTf	MnMOF-1·[Cu(C ₂ H ₄)]BF ₄
Crystallographic Parameter		
Formula	C ₉₁ H ₉₆ Cu _{1.02} F ₃ Mn ₃ N ₁₂ O _{17.5} S	C ₇₇ H ₇₀ BCuF ₄ Mn ₃ N ₁₂ O ₁₂
FW	1956.48	1670.62
T, K	100(2)	100(2)
Wavelength, Å	0.71073	0.71073
Crystal system, space group	Triclinic, P-1	Monoclinic, P2 ₁ /c
Z	2	4
a, Å	12.456(3)	12.298(3)
b, Å	12.898(3)	34.353(7)
c, Å	35.140(7)	25.793(5)
α°	88.09(3)	90
β, °	85.82(3)	98.30(3)
γ°	79.80(3)	90
V, Å ³	5540(2)	10783(4)
d _{calc} , g/cm ³	1.173	1.029
Absorption coefficient, mm ⁻¹	0.612	0.594
F(000)	2027.0	3428.0
Crystal size, mm ³	0.23 × 0.14 × 0.03	0.2 × 0.07 × 0.02
2θ range for data collection	2.324 to 64.332	1.988 to 58.356
Index range	-16 ≤ h ≤ 16, -19 ≤ k ≤ 19, -47 ≤ l ≤ 47	-16 ≤ h ≤ 16, -45 ≤ k ≤ 45, -34 ≤ l ≤ 34
Reflections collected	96363	139847
Independent reflections	28163 [R _{int} = 0.0551, R _{sigma} = 0.0554]	23497 [R _{int} = 0.0750, R _{sigma} = 0.0444]
Data/restraints/parameters	28163/253/1191	23497/50/999
GOF on F ²	1.295	1.297
Largest diff. peak and hole, eÅ ⁻³	1.12/-1.21	1.59/-0.75
R ₁ , [I > 2σ(I)]	0.1100	0.1074
wR ₂ , all data	0.3711	0.3510
CCDC Number	2071202	2071199

7.4.4. Isotherm data

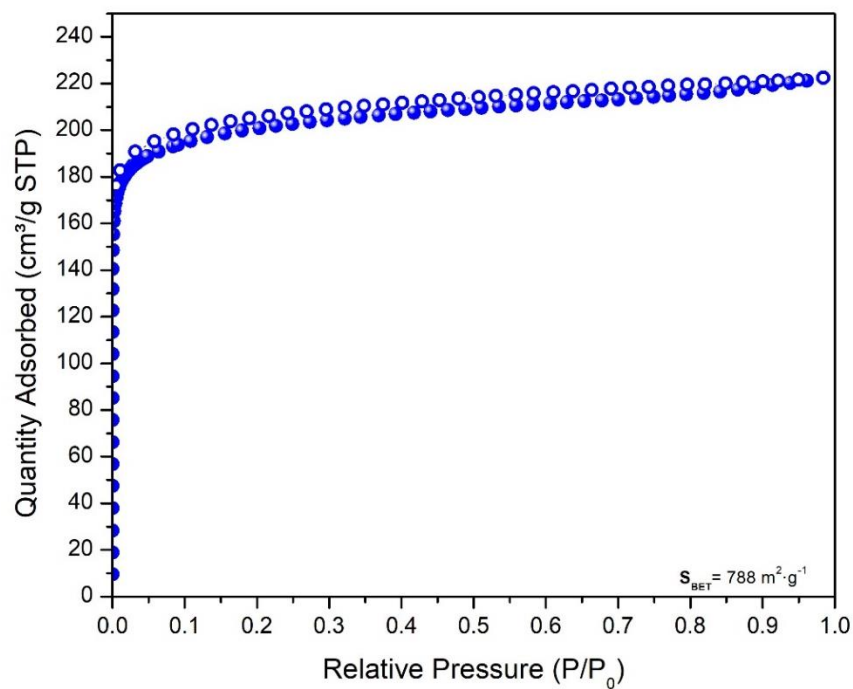


Figure 7.4.4.1: N_2 isotherm data collected on **MnMOF-1·[CuCO]BF₄** at 77K, after activation from dry pentane at RT for 2 hours. Coloured circles represent adsorption, open circles represent desorption.

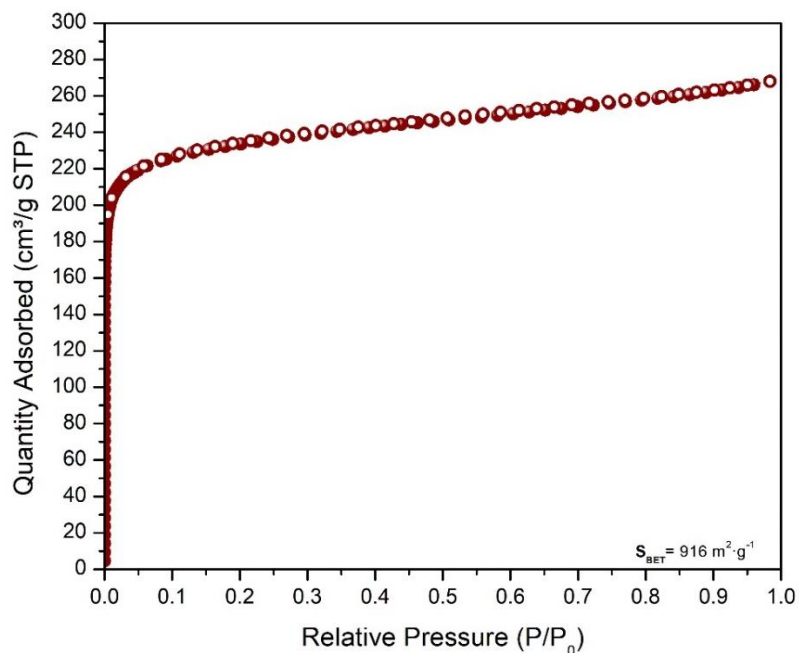


Figure 7.4.4.2: N_2 isotherm data collected on **MnMOF-1·[CuCO]PF₆** at 77K, after activation from dry pentane at RT for 2 hours. Coloured circles represent adsorption, open circles represent desorption.

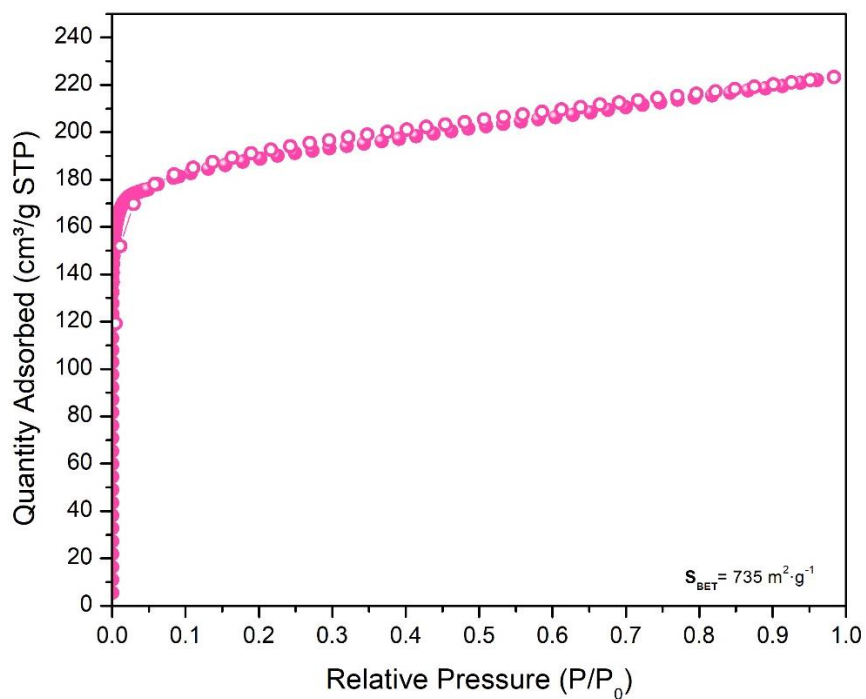


Figure 7.4.4.3: N₂ isotherm data collected on **MnMOF-1-[CuCO]OTf** at 77K, after activation from dry pentane at RT for 2 hours. Coloured circles represent adsorption, open circles represent desorption.

7.4.5. Infrared (IR) spectroscopy

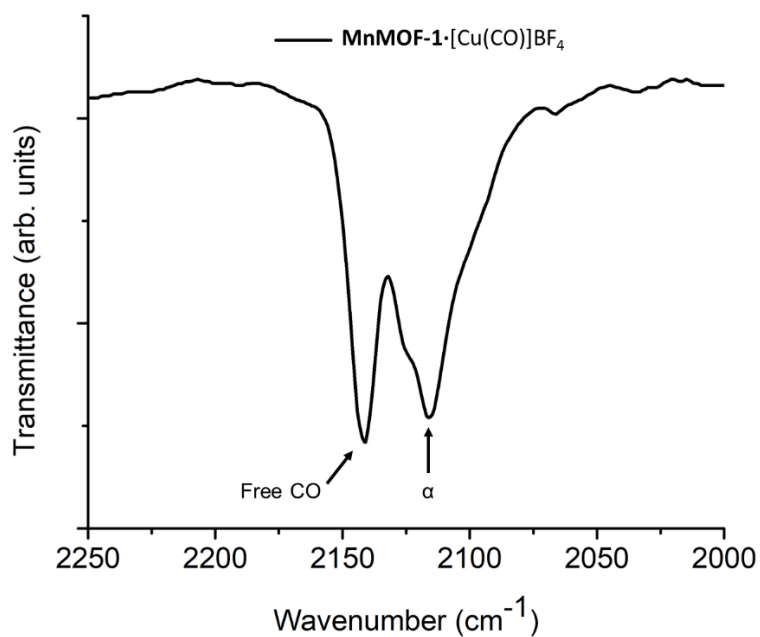


Figure 7.4.5.1: Infra-red spectrum (neat) of **MnMOF-1·[CuCO]BF₄** following exposure to vacuum for two hours (CO loss) and dosing with carbon monoxide to regenerate the **MnMOF-1·[Cu(CO)]BF₄**. To remove as much excess CO as possible, the sample chamber was briefly flushed with Argon. The IR spectrum displays the copper carbonyl stretch observed at 2105 cm⁻¹ and excess free CO trapped in the MOF pellet.

7.4.6. Formation of MnMOF-1·[Cu(OH₂)]OTf

We noted that when insufficiently dried triflate was used to perform the anion metathesis ligand exchange of **MnMOF-1**·[Cu(MeCN)Cl] in presence of CO, a trigonal planar Cu(I) aqua complex was formed. We postulate that water entered via the highly hygroscopic NaOTf salt during handling. As outlined in Chapter 7.4.3.2 and in Figure 7.4.3.3.4, **MnMOF-1**·[Cu(CO)]OTf features a mixture of trigonal planar Cu(CO) sites and trigonal planar Cu(OH₂) sites, indicating that complete prevention of water coordination (presumably from the hygroscopic NaOTf salt) is difficult. In one instance, presumably due to excessive moisture present in the NaOTf salt, a sample of **MnMOF-1**·[Cu(OH₂)]OTf was obtained in which negligible coordinated CO is present. The crystal structure revealed a trigonal planar Cu(OH₂) moiety, commensurate with the minor component observed in **MnMOF-1**·[Cu(CO)]OTf, with Cu-OH₂ bond length of 1.890(16). The triflate anion is located in the MOF pore as observed in **MnMOF-1**·[Cu(CO)]OTf.

Chapter 7

7.4.7. In-situ IR spectroscopy cell

The *In-situ* FTIR cell (Figure SI 6.1) used to assess the stability of $1 \cdot [\text{CuCO}]\text{BF}_4$ was developed in-house.

In-situ FTIR cell assembly:

65mm x 16mm, 304ss, 2 Port, OR, and Tapped, with an internal volume of 25 ml. Mini Ball Valve, BRS, N/P SCD M/ F ¼" 8MM connected to both ports. Stainless Steel Swagelok Tube Fitting, Male Elbow, 1/4 in. Tube OD x 1/4 in. Male ISO Tapered Thread connected to Mini Ball Valves.

Viewport Flange - 65mm x 16mm, 304ss, OR, and bolted to IR Sampling Chamber backside using M3 x 16 304ss Hex. Socket Cap Screws.

Lens – NaCl disks 25.4mm x 5.1mm and fitted to inside of Viewport Flange bore.

Lens Cap - 40mm x 16mm, 304ss, OR, and bolted to Viewport Flange outer face using M3 x 10 304ss Hex. Socket Cap Screws.

Lens: 25.4mm x 5.1mm Quartz and fitted to inside IR Sampling Chamber frontside bore.

Slide Holder - 50.4mm x 76.5mm x 5.5mm x 16mm BORE, 304ss, OR, and bolted to IR Sampling Chamber frontside using M3 x 10 304ss Countersink Head Hex. Screws.

Sample Holder Assembly:

Front Flange - 37mm x 16mm, Tapped, 304ss and bolted internally to IR Sampling Chamber using M2 x 8 304ss Hex. Socket Cap Screws. Back Flange – 37mm x 16mm, Clearance, 304ss 2 x 25.4mm x 5.1mm thick lenses clamped together, face to face, using M3 x 8 304ss Hex. Socket Cap Screws.

Notes: All parts thoroughly cleaned before assembly.

MS-PTS-50 Swagelok SWAK Anerobic Thread Sealant 50cm³ Tube was applied to all male threads before assembly and allowed to cure for 24 hours.

IR Sampling Cell Assembly pressure tested to 80psi (5.5bar) with compressed air and Helium Leak Tested.

To load the sample, a NaCl disk is placed into the chamber. One outlet is connected to a glass manifold pressurised with Argon (Hg pressure), an inverted funnel is placed over the chamber to maintain an Argon atmosphere while allowing access to the chamber for loading the sample. A narrow paper 'funnel' is positioned in the small opening of the inverted funnel, such that it rests on the middle of the NaCl disk. The dry sample is carefully dropped through the paper funnel onto in the middle of the NaCl disk (neat) while maintaining the Argon

blanket within the chamber. A second NaCl disk is placed on top of the sample. Maintaining constant Ar flow the chamber is sealed and an initial spectrum is collected before the chamber is placed under vacuum.



Figure SI 7.1: *In-situ* FTIR cell with double tap assembly.

7.4.8. References

1. McPhillips, T.; McPhillips, S.; Chiu, H.; Cohen, A. E.; Deacon, A. M.; Ellis, P. J.; Garman, E.; Gonzalez, A.; Sauter, N. K.; Phizackerley, R. P.; Soltis, S. M.; Kuhn, P., Blue-Ice and the Distributed Control System software for data acquisition and instrument control at macromolecular crystallography beamlines. *J. Synchrotron Radiat.* **2002**, *9*, 401-406.
2. Cowieson, N. P.; Aragao, D.; Clift, M.; Ericsson, D. J.; Gee, C.; Harrop, S. J.; Mudie, N.; Panjikar, S.; Price, J. R.; Riboldi-Tunnicliffe, A.; Williamson, R.; Caradoc-Davies, T., MX1: a bending-magnet crystallography beamline serving both chemical and macromolecular crystallography communities at the Australian Synchrotron. *J. Synchrotron Radiat.* **2015**, *22* (1), 187-190.
3. Aragao, D.; Aishima, J.; Cherukuvada, H.; Clarken, R.; Clift, M.; Cowieson, N. P.; Ericsson, D. J.; Gee, C. L.; Macedo, S.; Mudie, N.; Panjikar, S.; Price, J. R.; Riboldi-Tunnicliffe, A.; Rostan, R.; Williamson, R.; Caradoc-Davies, T. T., MX2: a high-flux undulator microfocus beamline serving both the chemical and macromolecular crystallography communities at the Australian Synchrotron. *J. Synchrotron Rad.* **2018**, *25* (3), 885-891.
4. Sheldrick, G., A short history of SHELX. *Acta. Crystallogr. A* **2008**, *64* (1), 112-122.
5. Sheldrick, G., SHELXT - Integrated space-group and crystal-structure determination. *Acta. Crystallogr. A* **2015**, *71* (1), 3-8.
6. Sheldrick, G. M., Crystal structure refinement with SHELXL. *Acta. Crystallogr. C* **2015**, *71* (Pt 1), 3-8.
7. Barbour, L. J., X-Seed — A Software Tool for Supramolecular Crystallography. *J. Supramol. Chem.* **2001**, *1* (4), 189-191.
8. Dolomanov, O. V.; Bourhis, L. J.; Gildea, R. J.; Howard, J. A. K.; Puschmann, H., OLEX2: a complete structure solution, refinement and analysis program. *J. Appl. Crystallogr.* **2009**, *42* (2), 339-341.
9. Spek, A. L., PLATON SQUEEZE: a tool for the calculation of the disordered solvent contribution to the calculated structure factors. *Acta. Crystallogr. C* **2015**, *71* (Pt 1), 9-18.